

**EXPERIMENTAL AND NUMERICAL STUDY OF MOLECULAR
MIXING DYNAMICS IN RAYLEIGH–TAYLOR UNSTABLE FLOWS**

A Dissertation

by

NICHOLAS J. MUESCHKE

Submitted to the Office of Graduate Studies of
Texas A&M University
in partial fulfillment of the requirements for the degree of

DOCTOR OF PHILOSOPHY

May 2008

Major Subject: Mechanical Engineering

**EXPERIMENTAL AND NUMERICAL STUDY OF MOLECULAR
MIXING DYNAMICS IN RAYLEIGH–TAYLOR UNSTABLE FLOWS**

A Dissertation

by

NICHOLAS J. MUESCHKE

Submitted to the Office of Graduate Studies of
Texas A&M University
in partial fulfillment of the requirements for the degree of

DOCTOR OF PHILOSOPHY

Approved by:

Chair of Committee,	Malcolm J. Andrews
Committee Members,	Oleg Schilling
	Bing Guo
	Sharath Girimaji
Head of Department,	Dennis O’Neal

May 2008

Major Subject: Mechanical Engineering

ABSTRACT

Experimental and Numerical Study of Molecular Mixing Dynamics in
Rayleigh–Taylor Unstable Flows. (May 2008)

Nicholas J. Mueschke, B.S., University of Louisiana at Lafayette;
M.S., Texas A&M University

Chair of Advisory Committee: Dr. Malcolm J. Andrews

Experiments and simulations were performed to examine the complex processes that occur in Rayleigh–Taylor driven mixing. A water channel facility was used to examine a buoyancy-driven Rayleigh–Taylor mixing layer. Measurements of fluctuating density statistics and the molecular mixing parameter θ were made for $Pr = 7$ (hot/cold water) and $Sc \sim 10^3$ (salt/fresh water) cases. For the hot/cold water case, a high-resolution thermocouple was used to measure instantaneous temperature values that were related to the density field via an equation of state. For the $Sc \sim 10^3$ case, the degree of molecular mixing was measured by monitoring a diffusion-limited chemical reaction between the two fluid streams. The degree of molecular mixing was quantified by developing a new mathematical relationship between the amount of chemical product formed and the density variance $\overline{\rho'^2}$. Comparisons between the $Sc = 7$ and $Sc \sim 10^3$ cases are used to elucidate the dependence of θ on the Schmidt number.

To further examine the turbulent mixing processes, a direct numerical simulation (DNS) model of the $Sc = 7$ water channel experiment was constructed to provide statistics that could not be experimentally measured. To determine the key physical mechanisms that influence the growth of turbulent Rayleigh–Taylor mixing layers, the budgets of the exact mean mass fraction \tilde{m}_1 , turbulent kinetic energy \tilde{E}'' , turbulent kinetic energy dissipation rate $\tilde{\epsilon}''$, mass fraction variance $\tilde{m}_1''^2$, and mass fraction variance dissipation rate $\tilde{\chi}''$ equations were examined. The budgets of the

unclosed turbulent transport equations were used to quantitatively assess the relative magnitudes of different production, dissipation, transport, and mixing processes.

Finally, three-equation $(\widetilde{E''}-\widetilde{\epsilon''}-\widetilde{m_1''^2})$ and four-equation $(\widetilde{E''}-\widetilde{\epsilon''}-\widetilde{m_1''^2}-\widetilde{\chi''})$ turbulent mixing models were developed and calibrated to predict the degree of molecular mixing within a Rayleigh–Taylor mixing layer. The DNS data sets were used to assess the validity of and calibrate the turbulent viscosity, gradient-diffusion, and scale-similarity closures *a priori*. The modeled transport equations were implemented in a one-dimensional numerical simulation code and were shown to accurately reproduce the experimental and DNS results *a posteriori*. The calibrated model parameters from the $Sc = 7$ case were used as the starting point for determining the appropriate model constants for the mass fraction variance $\widetilde{m_1''^2}$ transport equation for the $Sc \sim 10^3$ case.

To my wife

ACKNOWLEDGMENTS

I would like to thank my advisor Dr. Malcolm J. Andrews for making my graduate career a memorable experience. I would also like give my sincere gratitude to Dr. Oleg Schilling for his support, guidance, and countless hours he devoted to seeing this work to completion. I also owe my gratitude to David Youngs, Dr. Susan Daniel, and Dr. Fernando Albertorio for their helpful discussions on the chemistry aspects of this work. Thanks are due to Dr. Andrew Cook and Dr. William Cabot for the use of the Miranda code and to the High Energy Density Physics summer student program for supporting this collaboration.

Personally, I would like to thank my wife Lea Mueschke for helping me achieve my dreams. Without her constant support, laughter, friendship, and love, I would not be where I am today. I want to thank my parents H. Jay & Christine Mueschke for their guidance and always supporting my endeavors, academic and otherwise. Thanks are also due to Gary & Debra Melancon for their generous support (and food) over the years.

This research was sponsored by the U.S. Department of Energy National Nuclear Security Administration under the Stewardship Science Academic Alliances program through DOE Research Grant #DE-FG03-02NA00060. A portion of this work was also performed under the auspices of Lawrence Livermore National Security, LLC, (LLNS) under Contract No. DE-AC52-07NA27344.

TABLE OF CONTENTS

		Page
1.	INTRODUCTION	1
	1.1 Overview and Motivation	1
	1.2 The Rayleigh–Taylor Instability	3
	1.3 Previous Work	5
	1.3.1 Experimental studies of turbulent mixing	6
	1.3.2 Numerical simulations of buoyancy-driven tur- bulent mixing	10
	1.3.3 Modeling of buoyancy-driven turbulent mixing	12
	1.4 Research Objectives	14
	1.5 Outline of Dissertation	17
2.	EXPERIMENTAL MEASUREMENTS OF MOLECULAR MIXING	18
	2.1 Overview of Goals and Methodology	18
	2.2 Experimental Facility	19
	2.3 Hot/Cold Water Experiments	21
	2.3.1 Thermocouple diagnostics	22
	2.3.2 Density fluctuations measurement	26
	2.3.3 Statistical composition of mixed fluid	29
	2.3.4 Evolution of the density variance spectrum	32
	2.4 Salt/Fresh Water Experiments	39
	2.4.1 Reaction chemistry	40
	2.4.2 Optical imaging system and calibration	43
	2.4.3 Uncertainty analysis	46
	2.4.4 Measurement of mixing layer growth	47
	2.4.5 Measurements of chemical product formation	50
	2.4.6 Species diffusivity considerations	53
	2.4.7 Product thickness integrals	56
	2.4.8 Measurements of product formation mixing parameter	60
	2.4.9 Relationship between chemical product forma- tion measurements and fluctuating density statistics	62
	2.4.10 Measurement of molecular mixing parameters	66

	Page
2.4.11 Implications for turbulent transport and mixing modeling	74
2.5 Summary of Experimental Measurements	76
3. EXAMINATION OF TURBULENT TRANSPORT AND MIXING USING DNS DATA	79
3.1 Overview of Goals and Methodology	79
3.2 Direct Numerical Simulation of Rayleigh–Taylor Mixing: Hot/Cold Water Case	80
3.3 Statistical Averaging	85
3.4 Comparison with Water Channel Experimental Data	86
3.4.1 Qualitative observations and comparisons	86
3.4.2 Mixing layer growth rate	90
3.4.3 Statistical convergence	93
3.4.4 Fluctuating velocity and density statistics	96
3.4.5 Molecular mixing parameter θ	103
3.5 Measurements of Molecular Mixing	103
3.5.1 Reynolds number regimes	104
3.5.2 Chemical product measurements	115
3.5.3 Fluctuating density statistics	119
3.5.4 Statistical composition of mixed fluid	122
3.6 Budgets of Turbulent Transport and Mixing Equations	128
3.6.1 Mean continuity equation	129
3.6.2 Mean momentum transport	132
3.6.3 Mean mass fraction transport	135
3.6.4 Turbulent kinetic energy transport	137
3.6.5 Turbulent kinetic energy dissipation rate transport	154
3.6.6 Mass fraction variance transport	163
3.6.7 Mass fraction variance dissipation rate transport	172
4. REYNOLDS-AVERAGED NAVIER–STOKES MODEL FOR RAYLEIGH–TAYLOR TURBULENT MIXING	180
4.1 Overview of Goals and Methodology	180
4.2 Overview of Turbulent Viscosity-Based Reynolds-Averaged Turbulence Models	180
4.2.1 Eddy viscosity, gradient-diffusion, and scale-similarity hypotheses	180

	Page
4.2.2 Assumptions and limitations of eddy viscosity-based models	182
4.3 Determination of Model Parameters	185
4.3.1 Quantification of calibration quality	188
4.3.2 Boussinesq Reynolds stress model	189
4.3.3 Gradient-diffusion closures	194
4.3.4 Pressure transport closures	203
4.3.5 Scale-similarity closures	210
4.4 Numerical Implementation of the $\widetilde{E}''-\widetilde{\epsilon}''-\widetilde{m}_1''^2-\widetilde{\chi}''$ Model . . .	223
4.4.1 Model equations	225
4.4.2 Spatial discretization	227
4.4.3 Time integration	229
4.5 Model Validation	229
4.5.1 Comparison with Snider and Andrews (1996)	229
4.5.2 Self-Similar analysis	232
4.6 Mixing Model: $Sc = 7$ Case	236
4.6.1 Evolution of model profiles	236
4.6.2 Comparison of model with DNS and experiments . .	247
4.6.3 Production-to-dissipation ratios	249
4.6.4 Comparison with constant model parameters	252
4.7 Mixing Model: $Sc \sim 10^3$ Case	255
4.7.1 Calibration of C_{m2} for $Sc \sim 10^3$ experiments	255
4.7.2 Comparison with experiment	259
5. CONCLUSIONS	262
5.1 Summary	262
5.2 Future Work	268
REFERENCES	271
APPENDIX A	291
APPENDIX B	296
APPENDIX C	304
APPENDIX D	306
APPENDIX E	317

	Page
APPENDIX F	321
APPENDIX G	327
VITA	330

LIST OF FIGURES

FIGURE	Page	
1.1	Schematic of canonical arrangement of a Rayleigh–Taylor instability-driven turbulent mixing layer taken from slices of a three-dimensional direct numerical simulation. See § 3 for a detailed description of the DNS.	5
2.1	Schematic of the water channel facility, diagnostics, and associated coordinate system.	20
2.2	Photographic image of a hot/cold water experiment in the water channel. The mean flow is from left-to-right.	21
2.3	Evolution of the molecular mixing quantities B_0 , B_2 and θ on the centerplane for the $Pr = 7$ experiments. The values of B_2 all approach a value of 0.25 (dashed line), indicating that the measurements were taken at the centerplane of the mixing layer. The error bars on the measurements are also shown.	27
2.4	Evolution of the early-time (top) and late-time (bottom) volume fraction PDF $P(f_1)$ on the centerplane of the mixing layer.	31
2.5	Evolution of the volume fraction kurtosis on the centerplane.	32
2.6	Illustration of a smoothed density variance spectrum using the logarithmic binning procedure.	34
2.7	The normalized density variance spectrum at $\tau = 0.016$ or at $x = 0.5$ cm downstream (top-left), $\tau = 0.06$ or at $x = 2.0$ cm downstream (top-right), $\tau = 0.204$ or at $x = 6.0$ cm downstream (bottom-left), and at $\tau = 0.473$ or at $x = 15.0$ cm downstream (bottom-right).	36

FIGURE	Page	
2.8	The normalized density variance spectrum at $\tau = 0.865$ or at $x = 25.0$ cm downstream (top-left). The compensated spectrum (top-right) at $\tau = 0.865$ indicates a short range of apparent $k^{-5/3}$ scaling. The normalized density variance spectrum at $\tau = 1.36$ or at $x = 40.0$ cm downstream (bottom-left). The compensated spectrum (bottom-right) at $\tau = 1.36$ indicates a short range of apparent $k^{-5/3}$ scaling.	37
2.9	Spectral molecular mixing fraction $\theta(k)$ versus dimensionless wavenumber at $\tau = 1.36$	39
2.10	Fraction of dissociation for the colored form of the chemical indicator In_{IV}	43
2.11	Calibration of molar absorptivity coefficient ε_{In} for phenolphthalein. A fiducial for $\varepsilon_{\text{In}} = 2.935 \times 10^{-4} (\text{M} \cdot \text{cm})^{-1}$ is shown (dashed line).	45
2.12	Photograph of the buoyancy-generated mixing layer in a typical water channel experiment. Nigrosine dye was added to the top stream (contrast enhanced for visualization).	49
2.13	Mean volume fraction profiles across the mixing layer at dimensionless times $\tau = 0.25, 0.50, 0.75, 1.00, 1.25,$ and 1.50 . Two fiducials indicating the boundaries of the mixing layer are shown.	49
2.14	Measurement of the mixing layer growth parameter α for the $Sc \sim 10^3$ case. The half-width of the mixing layer is plotted against $Ag\tau^2$ with 95% confidence interval bounds. An alternative measure of α is obtained by normalizing \dot{h} (right). In both cases, a fiducial is shown for $\alpha = 0.085$ (dashed line).	50
2.15	Photograph of the buoyancy-generated mixing layer in a typical water channel experiment. Phenolphthalein was added to the bottom stream, which changes to its pink form as the two streams molecularly mix.	51
2.16	Normalized colored indicator concentration profiles across the mixing layer at dimensionless times $\tau = 0.25, 0.50, 0.75, 1.00, 1.25,$ and 1.50 for the $\text{pH}_2 = 7.02$ (left) and $\text{pH}_2 = 2.44$ (right) cases. For both experiments, $\text{pH}_1 = 11.5$	52

FIGURE	Page	
2.17	Normalized colored indicator concentration profiles across the mixing layer at $\tau = 0.25, 0.50, 0.75, 1.00, 1.25,$ and 1.50 for the hot/cold water case.	55
2.18	Equivalent chemical product thickness, P/δ , for the case of a liquid-phase, turbulent shear layer.	58
2.19	Equivalent product thickness measurements for a liquid-phase buoyancy-driven mixing layer, P/h , and shear-driven mixing layers, P/δ , at various velocity ratios r . Outer-scale Reynolds numbers are $Re_h = 0.35\sqrt{Agh^3}/\nu$ for the Rayleigh–Taylor case and $Re_{\delta_{vis}} = \Delta U \delta_{vis}/\nu$ for the shear case.	59
2.20	Schematic of $[\overline{\text{In}_{IV}}]$ formation as a function of \bar{f}_1 and the equivalence ratio φ_{In} . The maximum product formed occurs when the stoichiometric ratio of reactants are available at $(\bar{f}_1)_{st} = \varphi_{\text{In}}/(1 + \varphi_{\text{In}})$	61
2.21	Fraction of dissociation for In_{IV} as a function of the volume fraction f_2 and pH_2 of the acidic stream.	64
2.22	Values of colored indicator concentration C for $f_2^{50\%=0.471}$ (left: $\text{pH}_1 = 11.52$ and $\text{pH}_2 = 2.44$) and $f_2^{50\%=0.471}$ (right: $\text{pH}_1 = 11.48$ and $\text{pH}_2 = 7.02$) at different downstream locations.	66
2.23	Profiles of $\bar{f}_1'^2$ across the mixing layer at dimensionless times $\tau = 0.25, 0.50, 0.75, 1.00, 1.25,$ and 1.50	67
2.24	Profiles of θ across the mixing layer at dimensionless times $\tau = 0.25, 0.50, 0.75, 1.00, 1.25,$ and 1.50	68
2.25	Relative uncertainties in the $\bar{f}_1'^2$ (left) and θ (right) profiles at dimensionless times $\tau = 0.25, 0.50, 0.75, 1.00, 1.25,$ and 1.50	69
2.26	Evolution of θ on the centerplane of the mixing layer for various Schmidt numbers. Uncertainty bounds for the $Sc \sim 10^3$ measurements are indicated by the dashed lines. Measurements for the $Sc = 0.7$ case are taken from Banerjee <i>et al.</i> (2008), and measurements for the $Pr \equiv Sc = 7$ case are taken from Mueschke <i>et al.</i> (2006).	70

FIGURE	Page
2.27	Evolution of the global mixing parameters Θ and Ξ for the $Sc \sim 10^3$ case. 72
2.28	Evolution of mixing parameters as a function of Reynolds number $Re_h = 0.35\sqrt{Ag}h^3/\nu$. A fiducial is indicated at $Re_h = 300$ indicating the onset of nonlinear, transitional dynamics. 73
2.29	Self-similar collapse of the colored indicator concentration (left) and the volume fraction variance (right) profiles. Parabolic profiles are shown as a reference (dotted line). 76
3.1	Schematic of computational domain for the DNS with associated axes and direction of gravity. The iso-surface of initial interfacial perturbations $\zeta(x, y)$ is shown at the centerplane ($z = 0$). 82
3.2	Early-time evolution of the $f_1 = 0.5$ volume fraction iso-surface at $\tau = 0.21$ (top) and $\tau = 0.50$ (bottom). 88
3.3	Late-time evolution of the $f_1 = 0.5$ volume fraction iso-surface at $\tau = 1.01$ (top) and $\tau = 1.52$ (bottom). 89
3.4	Photograph of the initial development of a Rayleigh–Taylor mixing layer in the water channel, where a small amount of milk has been added to the bottom stream for visualization purposes. The flow is from left-to-right. 90
3.5	Bubble and spike penetration (in cm) from the DNS (black) and water channel (dashed) (Wilson 2002). 91
3.6	Measurement of growth parameter α from the DNS using the mixing layer half-width (left) and from (3.16) and (3.17) (right). Fiducials denoting $\alpha = 0.07$ are shown in each figure. 93
3.7	Dominant wavelengths in x - and y -directions on the centerplane based upon each velocity component and density field from the DNS. 95
3.8	Number of turbulent structures on the centerplane of the mixing layer based upon the dominant wavelengths λ_ρ and λ_w 96

FIGURE	Page	
3.9	Comparison of fluctuating velocity statistics on the centerplane of the mixing layer from the DNS and the water channel. Uncertainty estimates (95% confidence interval bounds) are denoted by dashed and dotted lines.	97
3.10	Cumulative energy distributions of the vertical velocity and density variance spectra from the DNS.	99
3.11	Comparison of $E_w^*(k_x)$ from the DNS and water channel experiment on the centerplane of the mixing layer at $\tau = 0.31$ (top), $\tau = 0.58$ (middle), and $\tau = 0.92$ (bottom).	100
3.12	Comparison of $E_\rho^*(k_x)$ from the DNS and water channel experiment on the centerplane of the mixing layer at $\tau = 0.17, 0.4, 0.87,$ and 1.36 (left-to-right, top-to-bottom).	102
3.13	Comparison of θ on the centerplane of the mixing layer from the water channel experiment ($Pr = 7$) and the DNS ($Sc = 7$). Uncertainty estimates (95% confidence interval bounds) are shown by dashed lines.	104
3.14	Evolution of integral-scale Reynolds number calculated using the mixing layer width h , based upon 5–95% (black) and 1–99% (grey) volume fraction thresholds.	106
3.15	Evolution of the Taylor–Reynolds number Re_λ based upon the centerplane u , v , and w velocity fields.	107
3.16	Vertical slices of the density field at $Re_h \approx 10^1, 10^2, 10^3,$ and 1710 , corresponding to dimensionless times $\tau = 0.10, 0.43, 1.16,$ and 1.52 . The heavy and light fluids are denoted by the color red and blue, respectively. Mixed fluid is denoted by intermediate shades, <i>i.e.</i> green and yellow.	109
3.17	Evolution of centerplane density slices corresponding to the vertical slices shown in figure 3.2. Centerplane slices are at $\tau = 0.10$ (top-left), $\tau = 0.43$ (top-right), $\tau = 1.16$ (bottom-left), and $\tau = 1.52$ (bottom-right).	110
3.18	Evolution of the diagonal components of the Reynolds stress anisotropy tensor on the centerplane.	111

FIGURE	Page
3.19	Profiles of the diagonal components of the Reynolds stress anisotropy tensor b_{11} (top), b_{22} (middle), and b_{33} (bottom). 112
3.20	Evolution of centerplane density and velocity variance at $\tau = 0.21$, $\tau = 0.50$, $\tau = 1.01$, and $\tau = 1.52$. The initial spectra (when available) are shown in grey and the final spectra are bold. 114
3.21	Compensated vertical velocity variance and density variance spectra at $\tau = 1.52$ 115
3.22	Profiles of mean product concentration $\overline{[C]}/[B]$ for $\varphi \rightarrow 0$ (left) and $\varphi = 1$ (right) across the mixing layer at various times. 117
3.23	Equivalent product thickness for the $Sc = 7$, $\varphi \rightarrow 0$ case. Shear- and buoyancy-driven results at $Sc \sim 10^3$ and $Sc = 0.7$ are shown as a reference. 117
3.24	Evolution of equivalent product thickness P/h and mixing parameter Ξ as a function of Re_h and φ obtained from the DNS. 119
3.25	Evolution of centerplane volume fraction variance (left) and profiles across the mixing layer (right) obtained from the DNS. 120
3.26	Evolution of molecular mixing parameters Θ and $\theta(z = 0)$ (left), and profiles of θ across the mixing layer (right) obtained from the DNS. 121
3.27	Evolution of θ on the centerplane of the mixing layer from gas-phase (Banerjee <i>et al.</i> 2008) and liquid-phase Rayleigh–Taylor experiments, and from DNS. 122
3.28	Probability density function $P(f_1)$ across the mixing layer at $\tau = 0.21$, 0.50 , 1.01 , and 1.52 124
3.29	Profiles of average mixing fluid composition \bar{f}_1^m across the mixing layer at various times. 127
3.30	Profiles of the skewness and kurtosis of $P(f_1)$ across the mixing layer at various times. 128
3.31	Evolution of the global volume fraction probability density function $\overline{P}(f_1)$ at various times. 129

FIGURE	Page
3.32	Divergence of the Favre-averaged velocity field (left) and advection by the mean velocity field (right) across the Rayleigh–Taylor mixing layer at various times. 130
3.33	Profiles of the Favre-averaged velocity components \tilde{u}_i across the Rayleigh–Taylor mixing layer at various times (left column) obtained from the DNS. Profiles of the relative magnitudes of the mean-square velocities with respect to the turbulent velocity fluctuations (right column). 131
3.34	Profiles of fluctuation velocity correlations $\widetilde{u''_i u''_j}$ across the Rayleigh–Taylor mixing layer at various times obtained from the DNS. 133
3.35	Profiles of the terms in the \tilde{w} -component of the mean momentum equation across the Rayleigh–Taylor mixing layer at various times. . . 134
3.36	Profiles of the mean heavy-fluid mass fraction \tilde{m}_1 across the Rayleigh–Taylor mixing layer at various times obtained from the DNS. 137
3.37	Profiles of the mean mass fraction turbulent transport term $T^{\tilde{m}_1}$ across the Rayleigh–Taylor mixing layer at various times. 138
3.38	Profiles of the mean mass fraction flux terms in the transport term $T^{\tilde{m}_1}$ across the Rayleigh–Taylor mixing layer at $\tau = 0.034, 0.21, 1.01,$ and 1.52 (left-to-right, top-to-bottom). 139
3.39	Profiles of the turbulent kinetic energy $\widetilde{E''}$ across the Rayleigh–Taylor mixing layer at various times. 140
3.40	Evolution of potential energy released, turbulent kinetic energy, mean kinetic energy, and cumulative turbulent kinetic energy dissipated (left). Ratio of turbulent kinetic energy to potential energy released (right). 141
3.41	Ratio of mean kinetic energy to turbulent kinetic energy within the mixing layer. 142
3.42	Profiles of the dominant terms in the turbulent kinetic energy transport equation across the Rayleigh–Taylor mixing layer at $\tau = 0.21, 0.50, 1.01,$ and 1.52 (left-to-right, top-to-bottom). 143

FIGURE	Page
3.43	Profiles of the buoyancy and shear production terms $P_b^{\widetilde{E}''}$ and $P_s^{\widetilde{E}''}$ in the turbulent kinetic energy transport equation across the Rayleigh–Taylor mixing layer at various times. 144
3.44	Profiles of the pressure dilatation term $\Pi^{\widetilde{E}''}$ in the turbulent kinetic energy transport equation across the Rayleigh–Taylor mixing layer at various times. 145
3.45	Profiles of the transport term $T^{\widetilde{E}''}$ in the turbulent kinetic energy transport equation across the Rayleigh–Taylor mixing layer at various times. 146
3.46	Early-time profiles of the turbulent kinetic energy flux terms in the transport term $T^{\widetilde{E}''}$ across the Rayleigh–Taylor mixing layer at $\tau = 0.034, 0.10, 0.21,$ and 0.29 (left-to-right, top-to-bottom). . . . 147
3.47	Intermediate- and late-time profiles of the turbulent kinetic energy flux terms in the transport term $T^{\widetilde{E}''}$ across the Rayleigh–Taylor mixing layer at $\tau = 0.41, 0.50, 1.01,$ and 1.52 (left-to-right, top-to-bottom). 148
3.48	Profiles of the normalized pressure transport term across the Rayleigh–Taylor mixing layer at early-times (left) and intermediate-times (right). The bifurcation point for the sign of $\overline{p'w''}$ within the core of the mixing layer is seen at $\tau = 0.288$ 150
3.49	Vertical slices of the density field with red and blue pressure contours indicating high and low pressure regions (left-column), respectively, and fluctuating pressure regions (right-column) show the formation of secondary vortical instabilities at $\tau \approx 0.3$. The slices are shown at $\tau = 0.206, 0.288, 0.405,$ and 0.674 151
3.50	Profiles of the turbulent dissipation term $D^{\widetilde{E}''}$ in the turbulent kinetic energy transport equation across the Rayleigh–Taylor mixing layer at various times. 152
3.51	Evolution of buoyancy and shear production, and dissipation integrals (left). Evolution of production-to-dissipation ratios (right). . . 153
3.52	Profiles of the turbulent kinetic energy dissipation rate $\overline{\epsilon'}$ (black) and $\widetilde{\epsilon''}$ (grey) across the Rayleigh–Taylor mixing layer at various times. 155

FIGURE	Page
3.53	Profiles of the dominant terms in the turbulent kinetic energy dissipation rate transport equation across the Rayleigh–Taylor mixing layer at $\tau = 0.21, 0.50, 1.01,$ and 1.52 (left-to-right, top-to-bottom). 157
3.54	Profiles of the production terms $P_b^{\overline{\epsilon'}}$, $P_s^{\overline{\epsilon'}}$, $P_t^{\overline{\epsilon'}}$, and $P_c^{\overline{\epsilon'}}$ in the turbulent kinetic energy dissipation rate transport equation across the Rayleigh–Taylor mixing layer at various times. 158
3.55	Profiles of the transport term $T^{\overline{\epsilon'}}$ in the turbulent kinetic energy dissipation rate transport equation across the Rayleigh–Taylor mixing layer at various times. 159
3.56	Early-time profiles of the turbulent kinetic energy flux terms in the transport term $T^{\overline{\epsilon'}}$ across the Rayleigh–Taylor mixing layer at $\tau = 0.034, 0.10, 0.21,$ and 0.29 (left-to-right, top-to-bottom). 161
3.57	Intermediate- and late-time profiles of the turbulent kinetic energy flux terms in the transport term $T^{\overline{\epsilon'}}$ across the Rayleigh–Taylor mixing layer at $\tau = 0.41, 0.52, 1.01,$ and 1.52 (left-to-right, top-to-bottom). 162
3.58	Profiles of the viscous dissipation term $D^{\overline{\epsilon'}}$ in the turbulent kinetic energy dissipation rate transport equation across the Rayleigh–Taylor mixing layer at various times. 163
3.59	Evolution of buoyancy, shear, turbulent production, and dissipation integrals (left). Evolution of production-to-dissipation ratios (right). 164
3.60	Profiles of the Favre-averaged mass fraction variance $\widetilde{m_1''^2}$ across the Rayleigh–Taylor mixing layer at various times. 165
3.61	Profiles of the terms in the mass fraction variance transport equation across the Rayleigh–Taylor mixing layer at $\tau = 0.21, 0.50,$ $1.01,$ and 1.52 (left-to-right, top-to-bottom). 166
3.62	Profiles of the production term $P^{\widetilde{m_1''^2}}$ in the mass fraction variance transport equation across the Rayleigh–Taylor mixing layer at various times. 167

FIGURE	Page
3.63	Evolution of the density-velocity correlation coefficient $R_{w''m_1''}$ on the centerplane of the Rayleigh–Taylor mixing layer. 168
3.64	Profiles of the transport term $T^{m_1''2}$ in the mass fraction variance transport equation across the mixing layer at various times. 169
3.65	Profiles of the mean mass fraction flux terms in the transport term $T^{m_1''2}$ across the Rayleigh–Taylor mixing layer at $\tau = 0.034, 0.21, 1.01,$ and 1.52 (left-to-right, top-to-bottom). 170
3.66	Profiles of the molecular dissipation term $D^{m_1''2}$ in the mass fraction variance transport equation across the Rayleigh–Taylor mixing layer at various times. 171
3.67	Evolution of production and dissipation integrals (left). Evolution of production-to-dissipation ratios (right). 171
3.68	Profiles of the mass fraction variance dissipation rate $\widetilde{\chi}''$ across the Rayleigh–Taylor mixing layer at various times. 173
3.69	Profiles of the dominant terms in the mass fraction variance dissipation rate transport equation across the Rayleigh–Taylor mixing layer at $\tau = 0.21, 0.50, 1.01,$ and 1.52 (left-to-right, top-to-bottom). . . 174
3.70	Profiles of the production terms $P_m^{\widetilde{\chi}''}, P_s^{\widetilde{\chi}''}, P_t^{\widetilde{\chi}''},$ and $P_c^{\widetilde{\chi}''}$ in the mass fraction variance dissipation rate transport equation across the Rayleigh–Taylor mixing layer at various times. 175
3.71	Profiles of the transport term $T^{\widetilde{\chi}''}$ in the mass fraction variance dissipation rate transport equation across the Rayleigh–Taylor mixing layer at various times. 176
3.72	Profiles of the mean mass fraction flux terms in the transport term $T^{\widetilde{\chi}''}$ across the Rayleigh–Taylor mixing layer at $\tau = 0.034, 0.21, 1.01,$ and 1.52 (left-to-right, top-to-bottom). 178
3.73	Profiles of the molecular dissipation term $D^{\widetilde{\chi}''}$ in the mass fraction variance dissipation rate transport equation across the Rayleigh–Taylor mixing layer at various times. 179

FIGURE	Page
3.74	Evolution of mean gradient, shear and turbulent production, and dissipation integrals (left). Evolution of production-to-dissipation ratios (right). 179
4.1	Profiles of the turbulent viscosity ν_t across the Rayleigh–Taylor mixing layer from the DNS at various times. The physical viscosity $\nu \approx 0.01$ is indicated by a dashed line. 189
4.2	Profiles of the unclosed velocity variance $\widetilde{u''^2}$ and its eddy viscosity closure across the Rayleigh–Taylor mixing layer at $\tau = 0.21, 0.50, 1.01,$ and 1.52 (left-to-right, top-to-bottom). 191
4.3	Profiles of the unclosed velocity variance $\widetilde{v''^2}$ and its eddy viscosity closure across the Rayleigh–Taylor mixing layer at $\tau = 0.21, 0.50, 1.01,$ and 1.52 (left-to-right, top-to-bottom). 192
4.4	Profiles of the unclosed velocity variance $\widetilde{w''^2}$ and its eddy viscosity closure across the Rayleigh–Taylor mixing layer at $\tau = 0.21, 0.50, 1.01,$ and 1.52 (left-to-right, top-to-bottom). 193
4.5	Evolution of correlation and amplitude coefficients for the Reynolds stress closures shown in figures 4.2–4.4. 194
4.6	Profiles of the unclosed turbulent flux $\bar{\rho} \widetilde{w'' m_1''}$ and its gradient-diffusion closure across the Rayleigh–Taylor mixing layer at $\tau = 0.21, 0.50, 1.01,$ and 1.52 (left-to-right, top-to-bottom). 195
4.7	Profiles of the unclosed turbulent flux $\bar{\rho} \widetilde{w'' E''}$ and its gradient-diffusion closure across the Rayleigh–Taylor mixing layer at $\tau = 0.21, 0.50, 1.01,$ and 1.52 (left-to-right, top-to-bottom). 196
4.8	Profiles of the unclosed turbulent flux $\bar{\rho} \widetilde{w' e'}$ and its gradient-diffusion closure across the Rayleigh–Taylor mixing layer at $\tau = 0.21, 0.50, 1.01,$ and 1.52 (left-to-right, top-to-bottom). 197
4.9	Profiles of the unclosed turbulent flux $\bar{\rho} \widetilde{w'' m_1''^2}$ and its gradient-diffusion closure across the Rayleigh–Taylor mixing layer at $\tau = 0.21, 0.50, 1.01,$ and 1.52 (left-to-right, top-to-bottom). 198

FIGURE	Page	
4.10	Profiles of the unclosed turbulent flux $\bar{\rho} \widetilde{w'' \chi''}$ and its gradient-diffusion closure across the Rayleigh–Taylor mixing layer at $\tau = 0.21, 0.50, 1.01,$ and 1.52 (left-to-right, top-to-bottom).	199
4.11	Evolution of calibrated turbulent Schmidt numbers as a function of dimensionless time.	201
4.12	Evolution of calibrated turbulent Schmidt numbers as a function of integral-scale Reynolds number.	201
4.13	Evolution of the model correlation and magnitude coefficients for the turbulent flux terms in the $\widetilde{E''}$ and $\widetilde{\epsilon''}$ transport equations.	202
4.14	Evolution of the model correlation and magnitude coefficients for the turbulent flux terms in the scalar field transport equations.	203
4.15	Profiles of the unclosed vertical pressure transport $\overline{p' w''}$ and Lumley’s (1978) closure across the Rayleigh–Taylor mixing layer at $\tau = 0.21, 0.50, 1.01,$ and 1.52 (left-to-right, top-to-bottom).	205
4.16	Profiles of the unclosed pressure transport $F_p^{\overline{\epsilon'}}$ and Lumley’s (1978) closure across the Rayleigh–Taylor mixing layer at $\tau = 0.21, 0.50, 1.01,$ and 1.52 (left-to-right, top-to-bottom).	207
4.17	Evolution of calibrated pressure transport coefficients C_{pu} and C_{pu}^{ϵ} as a function of time (left) and integral-scale Reynolds number (right).	208
4.18	Evolution of the model correlation and magnitude coefficients for the Lumley pressure transport models in the $\widetilde{E''}$ and $\widetilde{\epsilon'}$ transport equations.	209
4.19	Profiles of the unclosed buoyancy production term $P_b^{\overline{\epsilon'}}$ and its scale-similarity closure across the Rayleigh–Taylor mixing layer at $\tau = 0.21, 0.50, 1.01,$ and 1.52 (left-to-right, top-to-bottom).	211
4.20	Profiles of the difference between the unclosed turbulent destruction and production term $D^{\overline{\epsilon'}} - P_t^{\overline{\epsilon'}}$ and its scale-similarity closure across the Rayleigh–Taylor mixing layer at $\tau = 0.21, 0.50, 1.01,$ and 1.52 (left-to-right, top-to-bottom).	213

FIGURE	Page
4.21	Evolution of calibrated scale-similarity coefficients for the $\overline{\epsilon'}$ transport equation as a function of time (left) and integral-scale Reynolds number (right). 214
4.22	Evolution of the model correlation and magnitude coefficients for the scale-similarity models in the $\overline{\epsilon'}$ transport equation. 215
4.23	Profiles of the mechanical time scale τ_m (left) and the scalar mixing time scale τ_s (right) across the Rayleigh–Taylor mixing layer at various times. 216
4.24	Profiles of the mechanical-to-scalar time scale ratio R across the Rayleigh– Taylor mixing layer at various times. 216
4.25	Profiles of the unclosed mass fraction variance destruction term $D\widetilde{m_1''^2}$ and its scale-similarity closure across the Rayleigh–Taylor mixing layer at $\tau = 0.21, 0.50, 1.01,$ and 1.52 (left-to-right, top-to-bottom). 218
4.26	Profiles of the unclosed mass fraction variance dissipation rate mean gradient production term $P_m^{\widetilde{\chi''}}$ and its scale-similarity closure across the Rayleigh–Taylor mixing layer at $\tau = 0.21, 0.50, 1.01,$ and 1.52 (left-to-right, top-to-bottom). 219
4.27	Profiles of the unclosed mass fraction variance dissipation rate turbulent production term $P_t^{\widetilde{\chi''}}$ and its scale-similarity closure across the Rayleigh– Taylor mixing layer at $\tau = 0.21, 0.50, 1.01,$ and 1.52 (left-to-right, top-to-bottom). 221
4.28	Profiles of the unclosed mass fraction variance dissipation rate destruction term $D\widetilde{\chi''}$ and its scale-similarity closure across the Rayleigh–Taylor mixing layer at $\tau = 0.21, 0.50, 1.01,$ and 1.52 (left-to-right, top-to-bottom). 222
4.29	Evolution of calibrated scale-similarity parameters for the $\widetilde{m_1''^2}$ transport equation as a function of time (top-left) and the integral-scale Reynolds number (top-right). Evolution of calibrated scale-similarity parameters for the $\widetilde{\chi''}$ transport equation as a function of time (bottom-left) and the integral-scale Reynolds number (bottom-right). 224

FIGURE	Page
4.30	Evolution of the model correlation and magnitude coefficients for the scale-similarity models in the $\widetilde{m_1''^2}$ and $\widetilde{\chi''}$ transport equations. 225
4.31	Comparison of DNS profiles (black) with self-similar solutions (red) across the mixing layer at various times. All parabolic profiles are normalized by their respective centerplane value. 234
4.32	Comparison of profiles from the model with their self-similar solutions (red). The initial model profile is denoted by a dotted line and the final profile is denoted by a blue line. All parabolic profiles have been normalized by their respective centerplane value. The model parameters are taken from Snider and Andrews (1996). 235
4.33	Comparison of profiles from the three-equation model with self-similar solutions (red). The initial profile is denoted by a dotted line and the final profile is denoted by a blue line. All parabolic profiles are normalized by their respective centerplane value. The model parameters are taken from the calibrations shown in figures 4.12, 4.21, and 4.29. 237
4.34	Comparison of profiles from the four-equation model with self-similar solutions (red). The initial profile is denoted by a dotted line and the final profile is denoted by a blue line. All parabolic profiles are normalized by their respective centerplane value. The model parameters are taken from the calibrations shown in figures 4.12, 4.21, and 4.29. 238
4.35	Profiles of \widetilde{m}_1 , $\widetilde{E''}$, $\widetilde{\epsilon''}$, $\widetilde{m_1''^2}$, and $\widetilde{\chi''}$ across the mixing layer from the DNS used as initial conditions in the model. 239
4.36	Evolution of \widetilde{m}_1 profiles as a function of the initial conditions. 241
4.37	Evolution of $\widetilde{E''}$ profiles as a function of the initial conditions. 242
4.38	Evolution of $\widetilde{\epsilon''}$ profiles as a function of the initial conditions. 243
4.39	Evolution of $\widetilde{m_1''^2}$ profiles as a function of the initial conditions. 244
4.40	Evolution of $\widetilde{\chi''}$ profiles as a function of the initial conditions. 245

FIGURE	Page
4.41	Comparison of the growth of the mixing layer (left) and late-time growth rate (right) from the model, DNS, and experiment using various initial conditions. 247
4.42	Comparison of $\theta(z = 0)$ from the model, DNS, and experiment using various initial conditions: three-equation model (left) and four-equation model (right). 248
4.43	Comparison of Θ from the model and DNS using various initial conditions: three-equation model (left) and four-equation model (right). 249
4.44	Comparison of production-to-dissipation ratios from the DNS (blue) and three-equation model (black) for various initial conditions. 250
4.45	Comparison of production-to-dissipation ratios from the DNS (blue) and four-equation model (black) for various initial conditions. 251
4.46	Comparison of the mixing layer growth rate (left) and $\theta(z = 0)$ from the model, DNS, and experiment for the constant parameters case. 253
4.47	Comparison of the production-to-dissipation ratios from the model and the DNS for the constant parameters case. 254
4.48	Evolution of the integrated production and dissipation profiles for the $Sc = 7$ and $Sc \sim 10^3$ cases. 258
4.49	Comparison of C_{m2} calibration for the $Sc = 7$ and $Sc \sim 10^3$ cases. The approximate model for the $Sc \sim 10^3$ case is shown by the dashed line. 258
4.50	Comparison of $\theta(z = 0)$ from the model using the high Schmidt number calibration of C_{m2} and the $Pr = 7$ and $Sc \sim 10^3$ experiments. 260
4.51	Comparison of the integrated dissipation rate profiles from the model and estimated integrals from figure 4.48. 261
D.1	Initial interfacial (top) and centerplane vertical velocity (bottom) perturbation isosurfaces. 310
D.2	Initial interfacial perturbation spectra in the x - and y -directions. 314

FIGURE	Page
D.3	Initial vertical velocity perturbation spectra at the centerplane of the mixing layer in the x -direction. 314
D.4	Comparison of the mixing layer growth rates for different initialization methods. 315
D.5	Comparison of centerplane velocity variances and molecular mixing parameter θ for different initialization methods. 315

LIST OF TABLES

TABLE	Page	
2.1	Downstream locations of centerplane temperature (density) measurements and the corresponding dimensionless times.	23
2.2	Ion and phenolphthalein diffusivities in water (Desai & Vadgama 1991; Lide 2006).	54
3.1	Parameters used in the direct numerical simulation of the water channel experiment.	83
3.2	Integral-scale and Taylor–Reynolds numbers for selected times. . . .	108
4.1	Model parameters for ‘standard’ \widetilde{E}'' , $\widetilde{\epsilon}''$, $\widetilde{m}_1''^2$ transport models (Jones & Launder 1972; Launder & Sharma 1974; Lumley 1978; Orszag <i>et al.</i> 1996; Pope 2000; Chassaing <i>et al.</i> 2002; Liu & Fox 2006; Wilcox 2006; Brinkman <i>et al.</i> 2006) and as used in Rayleigh–Taylor mixing (Spitz & Haas 1991; Snider & Andrews 1996; Grégoire & Souffland 1999).	187
4.2	Model parameters used by Snider and Andrews (1996) and for the current model validation.	230
4.3	Convergence of self-similar growth parameter α for various grid spacings and time steps. Model parameters were chosen to match Snider and Andrews (1996).	231
4.4	Dimensionless initialization times and integral-scale Reynolds numbers for the four initial conditions cases examined.	240
4.5	Model parameters used in the constant parameters case taken from an average of the final three Reynolds-number dependent parameter values. Calibrated model parameters that are still changing at the latest times calculated are denoted by †.	253

TABLE	Page
D.1	Table of selected three-dimensional Rayleigh–Taylor simulations. 307
E.1	Molecular mixing parameters from $Pr = 7$ experiments. 317
E.2	Molecular mixing parameters from $Sc \sim 10^3$ experiments. 318
E.3	Turbulent Schmidt numbers calculated from DNS. 319
E.4	Scale-similarity parameters calculated from DNS. 320
G.1	Figure data files. 327
G.2	Figure data files. 328
G.3	Figure data files. 329

1. INTRODUCTION

1.1 Overview and Motivation

A fundamental understanding of the physics of turbulence and its effects on molecular mixing processes is crucial to the development of predictive models of turbulent mixing. Historically, shear-driven turbulence, passive scalar mixing, and combustion have received extensive experimental, numerical, and theoretical attention (Warhaft 2000; Veynante & Vervisch 2002; Fox 2003; Dimotakis 2005). Mixing induced by buoyancy-driven turbulence remains an open area of research, especially when the complexity of the flow physics increases due to the dynamic coupling of the density field with the velocity field (Chassaing *et al.* 2002; Hanjalić 2002). The present work is motivated, in part, by the development of inertial confinement fusion (ICF) technology, where the implosion of target capsules is susceptible to acceleration-driven instabilities and turbulent mixing. Lindl (1995) noted that such hydrodynamic instabilities limit the upper bound implosion velocity, and hence the overall neutron yield from the thermonuclear reactions. Thus, a thorough understanding of the role of hydrodynamic instabilities in ICF is crucial to the development of viable capsule designs (Lindl 1998; Nakai & Takabe 1996; Nakai & Mima 2004; Atzeni & Meyer-ter-Vehn 2004; Pfalzner 2006). Hydrodynamic instabilities can also affect implosion symmetry, as well as introduce cold shell material into the high temperature core of the capsule during the implosion deceleration phase, thereby degrading (or possibly quenching) the burning of the capsule. Shock and acceleration-driven hydrodynamic instabilities, such as the Richtmyer–Meshkov instability (Richtmyer 1960; Meshkov 1969) and the Rayleigh–Taylor instability (Rayleigh 1884; Taylor 1950), respectively,

This dissertation follows the style of the *Journal of Fluid Mechanics*.

are a limiting factor in the overall thermonuclear yield of an ICF capsule (Takabe *et al.* 1988; Dittrich *et al.* 1994; Keane *et al.* 1995a,b; Radha *et al.* 2002; Li *et al.* 2002; Wilson *et al.* 2003). Their mitigation is, therefore, desirable and perhaps essential to the success of high-gain ICF.

The design of ICF capsules requires the optimization of a variety of design parameters. Typically, many simulations must be performed to adequately define the design phase-space. Direct numerical simulations (DNS) of the complete physics that occur in ICF implosions is not feasible with current computational capabilities. In particular, a complete physical description of the hydrodynamics of ICF implosions over the range of typical length scales and time scales remains difficult (Zhou *et al.* 2003), and thus hydrodynamic instability and turbulence models are required. Modeling of ICF capsule implosions requires hydrodynamic models to accurately predict the turbulent transport of mass, momentum, energy and materials across the entire range of Reynolds numbers, from quiescent material layers to high Reynolds number mixing layers. The present work is motivated by the challenge of developing more predictive and physically complete transport and mixing models for buoyancy-driven turbulence. This work used a combination of experiments, DNS, and mixing models to examine the physics of Rayleigh–Taylor generated turbulent mixing. Experiments were conducted to measure the degree of molecular mixing within a Rayleigh–Taylor mixing layer. A DNS of the water channel experiment was used to further diagnose the mixing dynamics which could not be experimentally-measured. The results from the experiments and DNS were then used to test the feasibility and predictive capability of Reynolds-averaged turbulent transport and mixing models for Rayleigh–Taylor driven mixing layers.

1.2 The Rayleigh–Taylor Instability

Buoyancy-driven hydrodynamic instabilities arise when one fluid of density ρ_1 is accelerated into another of density ρ_2 . Specifically, the Rayleigh–Taylor instability arises when a heavier fluid ρ_1 is unstably stratified above a lighter fluid ρ_2 in the presence of a gravitational field (Rayleigh 1884; Taylor 1950) such that $\nabla\rho\cdot\nabla p < 0$, where p is the pressure. The dynamics of the penetration of one fluid into another in a Rayleigh–Taylor instability-driven mixing layer can be classified into three regimes (Sharp 1984; Youngs 1984). First, in the presence of sufficiently small perturbations at the initial interface separating the two fluids, each mode grows exponentially and independently according to linear theory (Chandrasekhar 1961; Drazin & Reid 2004). As the amplitude of each mode reaches $\hat{\zeta}(k) \approx \lambda/2$, where $k = 2\pi/\lambda$ is the wavenumber, nonlinear interactions become important and neighboring structures begin to influence the growth of rising “bubbles” and falling “spikes” (Sharp 1984; Haan 1989). The extent of penetration of one fluid into another is defined as the distance between the centerplane of the mixing layer and the bubble and spike fronts, h_b and h_s , respectively. Following the onset of nonlinearity, secondary Kelvin–Helmholtz instabilities (Kelvin 1871; Helmholtz 1868) develop as regions of high vorticity form between rising bubbles and falling spikes. As the instabilities grow, an increase in the range of scales present in the mixing layer is driven by the nonlinear interactions between buoyant structures. Bubbles and spikes merge to form larger buoyant structures, while shearing forces generate smaller-scale structures, as well as more topologically-complex interfaces. Finally, as highly-nonlinear interactions continue to develop, the mixing layer eventually transitions to turbulence. In this turbulent regime, nonlinear extensions of classical linear instability theory (Youngs 1984), dimensional analysis (Anuchina *et al.* 1978; Cook & Dimotakis 2001), self-similar analysis (Ristorcelli &

Clark 2004), bubble merger or competition models (Shvarts *et al.* 1995; Rikanati *et al.* 2000; Dimonte *et al.* 2005), experiments (Andrews & Spalding 1990; Linden *et al.* 1994; Snider & Andrews 1996; Dimonte & Schneider 2000; Banerjee & Andrews 2006), and numerical simulations (Youngs 1994; Ramaprabhu *et al.* 2005; Cabot & Cook 2006) showed that the late-time penetration of the bubbles and spikes (for cases where dissipative, diffusive and surface tension effects can be neglected) scale as

$$h_{b,s} = \alpha_{b,s} A g t^2, \quad (1.1)$$

where $\alpha_{b,s}$ is dimensionless, $A \equiv (\rho_1 - \rho_2)/(\rho_1 + \rho_2)$ is the Atwood number, g is the acceleration, and t is time. For the small Atwood number mixing layers considered here $h_b = h_s$ and $\alpha_b = \alpha_s = \alpha$. A schematic of turbulent Rayleigh–Taylor mixing is shown in figure 1.1.

Rayleigh–Taylor instabilities occur in a variety of physical processes, and over a wide range of length- and time-scales. Buoyancy-driven hydrodynamic instabilities, including the Rayleigh–Taylor instability, may limit the formation of heavy elements during stellar implosions (Smarr *et al.* 1981). On a smaller scale, many oceanographic and atmospheric currents are buoyancy-driven due to temperature or concentration gradients (Molchanov 2004; Cui & Street 2004). On a yet smaller scale, the breakup of fuel droplets in internal combustion engines has been related to Rayleigh–Taylor instabilities, as the air-fuel interface is unstable when the droplets are accelerated by the local flow field (Thomas 2003; Marmottant & Villermaux 2004). As noted above, at the smallest scales, the acceleration and subsequent deceleration of an ICF capsule fuel-shell interface is susceptible to Rayleigh–Taylor driven instabilities and significantly affects the design and analysis of target capsules (Lindl 1995, 1998). Buoyancy-generated turbulence provides an efficient mechanism for mixing the constituent miscible fluids (Linden & Redondo 1991). Despite the importance that mole-

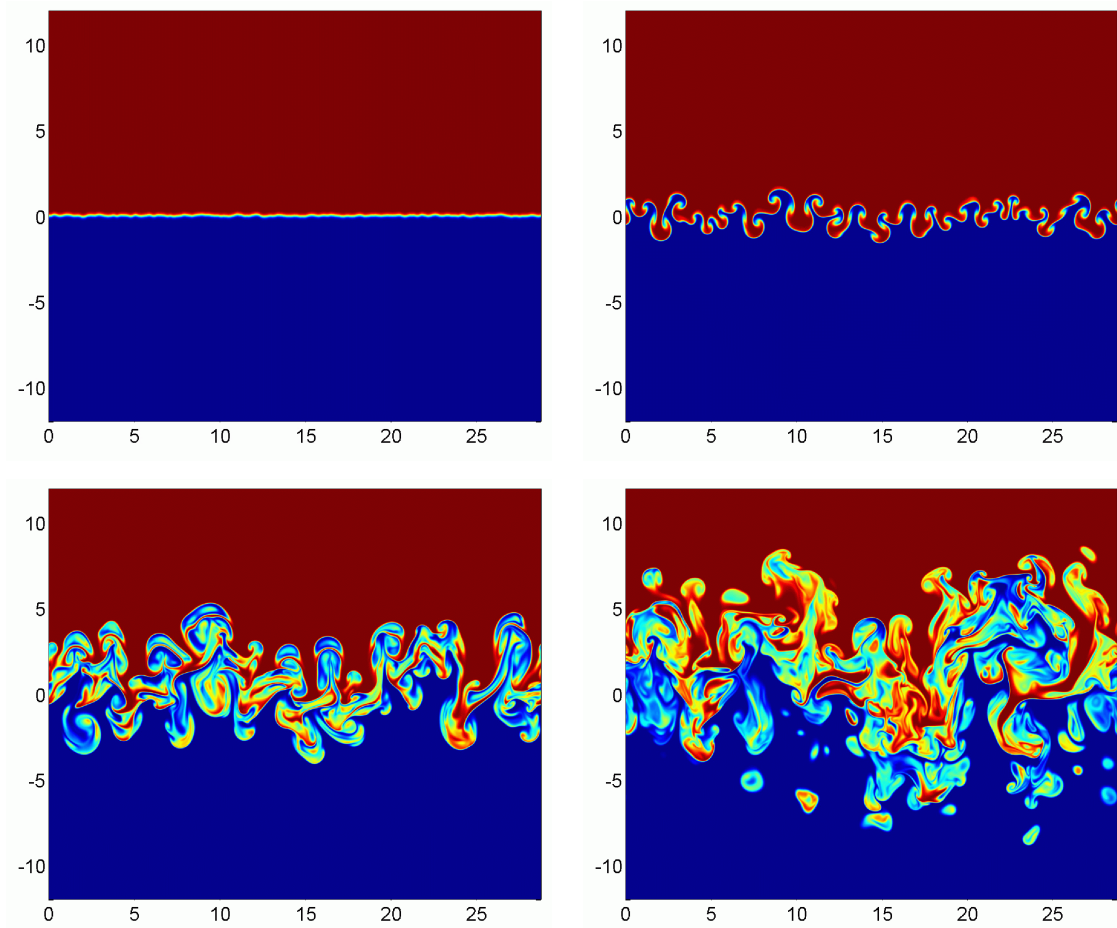


Figure 1.1 Schematic of canonical arrangement of a Rayleigh–Taylor instability-driven turbulent mixing layer taken from slices of a three-dimensional direct numerical simulation. See § 3 for a detailed description of the DNS.

cular mixing may have in these applications, a comprehensive understanding of the buoyancy-driven mixing process, the coupled molecular mixing, and the associated modeling remain largely unexplored.

1.3 Previous Work

The study, measurement, and modeling of turbulence-induced mixing has remained at the forefront of turbulence research due to its impact in such fields of study as cli-

mate dynamics (Adkins *et al.* 2002; Wunsch 2002), combustion and chemical reactor processes (Veynante & Vervisch 2002), pollutant dispersion (Britter & Hanna 2003), inertially-confined fusion (Lindl 1998; Betti *et al.* 2001; Atzeni & Meyer-ter-Vehn 2004), and cosmic and stellar dynamics (Colgate & White 1966). In this work, the terms ‘turbulent mixing’ and ‘molecular mixing’ imply the process of producing a homogenous mixture at the molecular level, as opposed to the intermingling of pockets of unmixed fluid produced by laminar stirring motions. The study of turbulent mixing can be broken down into three categories (Dimotakis 2005), where ‘Level 1’ mixing is categorized by the mixing of passive scalars, which do not influence the turbulent dynamics. ‘Level 2’ mixing is categorized by flows where there is an active feedback from the scalar field on the turbulent dynamics, such as in Rayleigh–Taylor mixing layers. Finally, ‘Level 3’ mixing is categorized by flows where the mixing produces changes in the fluid composition, such as in combustion. From Levels 1 to 3, the complexity of the theory, measurement, simulation, and modeling of the mixing processes increases. The historical study of turbulent mixing has been focused on the study of passive scalar mixing, with the assumption that various aspects of the simplified mixing dynamics may be used to model more complex flows.

1.3.1 *Experimental studies of turbulent mixing*

The history of experimental measurements of turbulent mixing have primarily focused on shear-driven flows, such as shear layers and jets. Far less attention has been given to the buoyancy-driven case, likely due to difficulties associated with the development of experimental facilities and the application of high-fidelity diagnostics to such experiments. A brief review of some pertinent shear-driven results are presented first, followed by a review of previous experimental measurements of molecular mixing in Rayleigh–Taylor driven turbulence.

Quantitative measurements of molecular mixing have been reported for many classical, shear-driven turbulent flows. In particular, a variety of experiments have been designed to monitor a diffusion-limited chemical reaction to quantify the degree of molecular mixing. Konrad (1977) examined gas-phase mixing in free-shear flows with an associated Schmidt number $Sc = \nu/D = 0.7$ (ν is the kinematic viscosity and D is the mass diffusivity). Breidenthal (1979, 1981) performed similar measurements in liquid-phase turbulent shear layers with $Sc \sim 10^3$. Both Konrad and Breidenthal quantified the degree of molecular mixing using backlit optical techniques to measure the absorption of light by a specific chemical species. A key result from these studies was an integral measure of the chemical product concentration, P/δ , where P is the equivalent thickness of chemical product across the mixing layer, and δ is the width (vorticity thickness) of the turbulent shear layer. It was reported that P/δ is a function of the Schmidt number, velocity ratio $r = U_1/U_2$, initial conditions, and Reynolds number up to a transition range after which the mixing layer became entrainment-limited, *i.e.* the turbulent motions generated sufficient surface area that molecular diffusion produced mixed fluid at a greater rate than pure fluid could be introduced into the mixing layer. Once the mixing layer crossed the threshold Reynolds number range, P/δ became independent of all parameters except the Schmidt number. For $Sc = 0.7$ experiments, Konrad (1977) reported $P/\delta \approx 0.65$ for $Re_\delta = \Delta U \delta/\nu < 5000$, and $P/\delta \approx 0.81$ at higher Reynolds numbers. This contrasts with much lower values reported for liquid-phase experiments (Breidenthal 1979, 1981), where $P/\delta = 0.05$ – 0.3 was measured in pre-transitional mixing layers at different velocity ratios, and $P/\delta = 0.365 \pm 0.02$ at $Re_\delta > 8000$. Koochesfahani and Dimotakis (1986) extended this work by using a combination of passive scalar and reacting flow techniques to quantify the amount of chemical product formed (measuring post-transition values of P/δ), and the probability density function (PDF) of the high-speed fluid. The statis-

tical composition of the mixed fluid was quantified by calculating the first moment of the interior portion of the high-speed fluid PDF. In summary, in all of these results, the scalar Schmidt number had a significant influence on the degree of molecular mixing both before and after the mixing transition in shear flows.

Reacting flow techniques have also been used to measure mixing in turbulent jets. Shea (1976) used chemically-reacting gases to measure the effects of the Reynolds number and equivalence ratio on the reduction of the initial chemical reactants. Zhang *et al.* (1995) and Zhang and Schneider (1995) used a similar liquid-phase configuration, phenolphthalein indicator, and experimental methods as Breidenthal (1979, 1981) to study how variations in exit geometry affected the degree of molecular mixing in turbulent jets. Analogous to the measurement of P/δ by Konrad (1977) and Breidenthal (1979, 1981), Zhang *et al.* (1995) also quantified the degree of molecular mixing by integrating the measured concentration chemical indicator across the span of the jet at downstream locations. It was concluded that the total amount of chemical product formed can be increased by adding ‘tabs’ near the jet exit, thereby increasing the turbulent fluctuations at the injection point of the jet.

Few measurements of molecular mixing have been reported for turbulent Rayleigh–Taylor driven mixing layers. Using a water channel (Wilson & Andrews 2002; Ramaprabhu & Andrews 2004a; Mueschke *et al.* 2006) analogous to the two-stream configurations used by Konrad (1977) and Breidenthal (1979, 1981), the degree of molecular mixing was measured for a buoyancy-driven mixing layer, where one stream was heated so that $T_1 \neq T_2$. A complete description of the water channel facility is provided in § 2. In this configuration, temperature was a marker for the density and $Pr = \nu/\Gamma \equiv Sc = 7$, where Γ is the thermal diffusivity of water. No chemical reaction was used in these experiments; instead a high resolution thermocouple system measured pointwise temperatures that were then related to density through an equa-

tion of state (Kukulka 1981). Mueschke *et al.* (2006) reported the time-evolution of the molecular mixing parameter θ , defined in (2.1) and analogous to the intensity of segregation parameter (Dankwerts 1952), along the centerplane of the mixing layer. Here, $\theta = 0$ when the two fluids are completely unmixed (*i.e.* an emulsion) and $\theta = 1$ when the two fluids are homogeneously mixed at the molecular level. Banerjee *et al.* (2007) used hot-wire techniques to measure late-time values of θ in analogous gas-phase experiments using air and helium, in which $Sc = 0.7$.

The water and gas channel experiments, discussed in the previous paragraph, provided measurements for moderate species diffusivities $Sc = 0.7$ and $Sc = 7$. A different set of experiments by Linden and Redondo (1991) and Linden *et al.* (1994) considered the degree of molecular mixing in a Rayleigh–Taylor mixing layer, in which the density difference was created by adding salt to the top fluid, such that $Sc \sim 10^3$. In these experiments, an unstable stratification of salt water over fresh water was created when a thin barrier separating the fluids was quickly removed. Linden *et al.* (1994) used two separate measurement techniques to quantify the degree of mixing. First, electrical conductivity probes were used to measure the salt concentration pointwise. In addition, methods similar to those used by Breidenthal (1979) and Zhang *et al.* (1995) were adopted to measure the formation of colored phenolphthalein indicator. However, the resulting product formation measurements were limited to the concentration profiles of the indicator for a single equivalence ratio [see (2.36)], and the time-evolution of the centerplane indicator concentration at several equivalence ratios. The present work extends these previous efforts by developing a relationship between the measured product concentrations, the molecular mixing parameter θ , and its global equivalent Θ , both defined in § 2.

1.3.2 Numerical simulations of buoyancy-driven turbulent mixing

Experimental studies of buoyancy-driven mixing that yield quantitative measurements of molecular mixing are limited due to difficulties generating unstable density interfaces, and applying the necessary high fidelity (in both time and space) diagnostics. In contrast, numerical studies of turbulent Rayleigh–Taylor mixing have been more numerous as computational resources have increased. Just as with the simulation of shear-driven turbulent mixing layers (Rogers & Moser 1994), simulation of Rayleigh–Taylor mixing requires a large domain so that the both horizontal and vertical turbulent structures can grow without the influence of the boundary conditions. As the Rayleigh–Taylor mixing layer Reynolds number Re_h increases, complete resolution of all spatial scales requires that the grid spacing scale as $Sc^{-1/2} Re_h^{-3/4}$ (Fox 2003), and thus, simulations of Rayleigh–Taylor mixing quickly become computationally-expensive and challenging for the combination of high Reynolds and high Schmidt number flows for at least several generations of computational power.

To relax the small-scale resolution requirements, increase the computational efficiency, increase the Reynolds numbers, and allow for a more robust treatment of initial conditions, implicit large eddy simulations (ILES) and monotone-integrated large eddy simulations (MILES) have been widely applied to numerical studies of Rayleigh–Taylor mixing (Linden *et al.* 1994; Youngs 1994; Dalziel *et al.* 1999; Dimonte *et al.* 2004; Ramaprabhu *et al.* 2005). Both the ILES and MILES methods represent a class of large eddy simulation (LES) methods that do not explicitly include subgrid-scale (SGS) models; rather, the diffusion inherent in the numerical algorithm damps small-scale fluctuations in the velocity and scalar field in a process similar to physical diffusion (Boris *et al.* 1992; Grinstein *et al.* 2007). Both ILES and MILES

exhibited similar late-time values $\theta(z = 0) \approx 0.8$ (Linden *et al.* 1994; Youngs 1994; Dimonte *et al.* 2004) and $\Theta = 0.77\text{--}0.84$ (Linden *et al.* 1994; Youngs 1994; Dalziel *et al.* 1999; Dimonte *et al.* 2004); however, Ramaprabhu *et al.* (2005) reported a range of late-time molecular mixing parameter values $\Theta = 0.63\text{--}0.82$, depending upon the exact initial conditions used. Cook *et al.* (2004) used an incompressible LES with an explicit SGS filter and hyperviscosity model to simulate an $A = 0.5$ Rayleigh–Taylor mixing layer, and reported a late time-value $\Theta = 0.78$. Mellado *et al.* (2005) used an LES to simulate a compressible Rayleigh–Taylor mixing layer. Despite the difference in flow physics and numerical schemes, a late time value $\Theta = 0.75$ was also found.

While good agreement was observed in the late-time degree of molecular mixing amongst all LES-type simulations, such methods are poorly suited for the simulation of flows where $Sc \neq 1$ without further modification or SGS modeling efforts (Pullin 2000; Hickel *et al.* 2007). In contrast, direct numerical simulation (DNS) of Rayleigh–Taylor mixing avoids SGS modeling by fully-resolving the smallest velocity and scalar fluctuations. DNS have been used to study Rayleigh–Taylor driven mixing, where Ristorcelli and Clark (2004) reported late-time values $\theta(z = 0) \approx 0.8$ for small Atwood number, $Sc = 1$ mixing layers with varying initial conditions. Cabot and Cook (2006) reported a late-time value $\Xi = 0.8$ (analogous to Θ) for a high Reynolds number, $Sc = 1$ Rayleigh–Taylor mixing layer. Young *et al.* (2001) performed a set of DNS of a small Atwood number Rayleigh–Taylor mixing layer where the density difference was induced by a temperature difference; however, the thermal diffusivity was taken to be equal to the viscosity $\Gamma = \nu$, so that $Pr = 1$. Livescu and Ristorcelli (2007) used DNS to examine homogeneous, variable-density turbulent mixing, which was intended to approximate the internal turbulent core of a Rayleigh–Taylor mixing layer. Due to the need for large computational facilities to account for the small scales associated with $Sc \gg 1$, this study examined a small range of Schmidt numbers, $0.1 \leq Sc \leq 2$, where

even small differences in the Schmidt number were found to affect the production and dissipation rates of both the turbulent kinetic energy and scalar variance.

1.3.3 *Modeling of buoyancy-driven turbulent mixing*

The complexity and range of scales involved in many realistic turbulent flows preclude the use of DNS, and thus, the turbulent and mixing dynamics must be modeled statistically (Pope 2000; Wilcox 2006). However, application of RANS-type models to buoyancy-driven turbulence has been hindered by an observed counter-gradient behavior in some variable-density flows (Veynante *et al.* 1997; Chassaing *et al.* 2002; Schmitt *et al.* 2003), complexity of the turbulent flow physics (Ristorcelli *et al.* 2005), and the interaction of the scalar and momentum fields (Hanjalić 2002). To model mixing dynamics, scalar variance (Fox 2003; Liu & Fox 2006; Ristorcelli 2006), scalar flux (Besnard *et al.* 1992; Fox 2003), and scalar variance dissipation rate (Veynante & Vervisch 2002; Mura *et al.* 2007) RANS-type transport models have been developed, but these additional transport models have only received cursory attention from the Rayleigh–Taylor community.

RANS models represent one of the most computationally economical approaches to turbulence modeling, but much of the RANS modeling effort has been focused on passive scalar mixing, reacting flow, and combustion applications. Only a small portion of turbulence modeling efforts have focused on the modeling of Rayleigh–Taylor and Richtmyer–Meshkov instability-induced turbulence. Youngs (1989) adopted a multiphase flow approach, where the required closures in the mean momentum, density, kinetic energy, and length-scale equations were closed by phenomenological observations of bubble and spike dynamics. The model coefficients were calibrated by comparing the model predictions with experimentally-measured growth rates *a posteriori* from a small Atwood number Rayleigh–Taylor mixing layer. Dimonte and

Tipton (2006) and Chiravalle (2006) used single-fluid k - L models, analogous to the two-fluid model of Youngs (1989), where the primary buoyancy terms in the k and L equations were modeled via a relation with buoyancy-drag type models (Dimonte 2000). Using a combination of buoyancy-drag model analysis and self-similar analysis of the transport equations, Dimonte and Tipton (2006) were able to calibrate their k - L model and demonstrated the ability of the model to reproduce both Rayleigh–Taylor and Richtmyer–Meshkov mixing layer growth rates. Besnard *et al.* (1992) also developed a k - L formulation (BHR) to model variable-density and buoyancy-driven turbulence, where eddy viscosity and scale-similarity moment closures were used to construct the modeled transport equations. Additional transport equations for the turbulent mass flux and density-specific volume correlation were also included in the model with the intent of increasing its physical accuracy and to predict the degree of molecular mixing. The only published results for a calibrated form of this model were reported by Valerio *et al.* (1999), where the model was used to predict the growth of a set of Richtmyer–Meshkov mixing layers in shock tube experiments.

For k - ϵ models, much of the research effort has investigated the calibration of the buoyancy source terms in the modeled k and ϵ equations, where the dimensionless model parameters σ_ρ and $C_{\epsilon 0}$ (see § 4.3.3 and 4.3.5 for a complete definition) have been the primary focus. Andrews (1984) examined self-similar solutions to the k - ϵ model equations to determine the proper calibration of the buoyancy production terms in the modeled k and ϵ equations. Andrews (1984) reported that $C_{\epsilon 0} = 0.9$ provided good agreement with the mixing layer growth measurements of Read (1984). Spitz and Haas (1991) also examined self-similar solutions to the k and ϵ equations. They reported that $\sigma_\rho = 1.48$ and $C_{\epsilon 0} = 0.815$, along with a set of canonical model closure parameters for the remaining terms (Wilcox 2006), best reproduced the growth of a small Atwood number Rayleigh–Taylor mixing layer (Read 1984). Snider and

Andrews (1996) also used self-similar analysis to examine the role of the buoyancy production of ϵ on the growth of an incompressible, small Atwood number mixing layer. They reported that $\sigma_T \equiv \sigma_\rho = 0.6$ and $C_{\epsilon 0} = 0.9$ produced favorable agreement between the model and water channel experiment mixing layer growth rate measurements. Gauthier and Bonnet (1990) demonstrated that a k - ϵ model with calibrated buoyancy source terms could reproduce the experimentally-measured growth of a Richtmyer–Meshkov mixing layer. Grégoire and Souffland (1999) expanded upon the model of Gauthier and Bonnet (1990) by developing a second-order Reynolds stress model in order to capture local anisotropy effects. Transport equations for the turbulent mass flux and density variance were also included to better capture buoyancy-driven effects and the turbulent mixing of the two fluids. Despite the inclusion of additional transport mechanisms, only fair agreement was found in comparisons of the model with experiments and simulations for both the Rayleigh–Taylor and Richtmyer–Meshkov cases.

1.4 *Research Objectives*

The objectives of this research are to examine the turbulent transport and molecular mixing processes within a Rayleigh–Taylor mixing layer. This research aims to answer the following questions:

1. To what degree are the constituent fluids mixed at the molecular level within a turbulent Rayleigh–Taylor mixing? How does the Schmidt number affect the amount of mixing, as measured by the molecular mixing parameter θ ?
2. What are the key physical processes that determine the degree of molecular mixing?

3. Provided the experimental and numerical results from the first two questions, how can the amount of molecular mixing be properly modeled within the framework of Reynolds-averaged Navier–Stokes (RANS) models?

These questions have been answered using a combination of experiments, direct numerical simulations and a four-equation $(\widetilde{E}''-\widetilde{\epsilon}''-\widetilde{m}_1''^2-\widetilde{\chi}'')$ turbulence model. The methods by which the above questions were answered are listed below. The primary experimental objectives of this work are as follows:

1. Measure the molecular mixing parameter θ in the water channel using a hot/cold water arrangement ($Pr \equiv Sc = 7$).
2. Develop the experimental techniques and associated optical diagnostics to measure the degree of chemical product formation using a chemically-reacting, salt/fresh water arrangement ($Sc \sim 10^3$).
3. Perform the necessary validation experiments to support the developed optical techniques used in the reacting flow experiments.
4. Develop a mathematical relationship between the total amount of chemical product formed in the reacting flow case and the density variance $\overline{\rho'^2}$. Combining the measurements of $\bar{\rho}$ and $\overline{\rho'^2}$, obtain a measurement of the molecular mixing parameters θ and Θ for the $Sc \sim 10^3$ case.

The primary numerical objectives of this work are as follows:

1. Develop a direct numerical simulation (DNS) model of the water channel experiment and, in addition, develop the methodology required to directly implement experimentally-measured initial conditions into the DNS. Note that computational requirements for a DNS preclude a simulation of the $Sc \sim 10^3$ experiment.

2. Validate the DNS by comparing results with experimental measurements made in the water channel.
3. Obtain quantitative measures of the degree of molecular mixing and statistical composition of the mixed fluid which cannot be measured experimentally.
4. Use the DNS data to evaluate the budgets of transport equations for the mean momentum \tilde{u}_i , mean mass fraction \tilde{m}_1 , turbulent kinetic energy $\widetilde{E''}$, turbulent kinetic energy dissipation rate $\tilde{\epsilon''}$, mass fraction variance $\widetilde{m_1''^2}$, and mass fraction variance dissipation rate $\widetilde{\chi''}$.

The primary modeling objectives of this work are as follows:

1. Directly compare transport equation budgets from the DNS *a priori* with their associated gradient-diffusion and scale-similarity based closures. Use the DNS data to calibrate the required closures in the turbulent transport equations for \tilde{m}_1 , $\widetilde{E''}$, $\tilde{\epsilon''}$, $\widetilde{m_1''^2}$ and $\widetilde{\chi''}$. Assess the validity and accuracy of such closures with respect to Rayleigh–Taylor driven turbulent mixing.
2. Numerically-implement the transport equations to test the predictive accuracy and initialization methods of RANS models when applied to Rayleigh–Taylor turbulent mixing. Validate the ability of the model to reproduce mixing layer growth and molecular mixing statistics in the water channel experiments.
3. Starting from the $Sc = 7$ calibration for the $\widetilde{m_1''^2}$ transport equation, determine the model parameters required to reproduce the $Sc \sim 10^3$ case. Examine the physical justification of the variation in the parameters with respect to turbulent and mixing time-scales.

1.5 *Outline of Dissertation*

First, experimental measurements of the degree of molecular mixing in a Rayleigh–Taylor instability-driven turbulent mixing layer are presented. Measurements have been made using hot and cold water as the working fluids, which use temperature as a fluid marker, resulting in a Prandtl number $Pr = \nu/\Gamma = 7$. Another set of experiments were performed using fresh and salt water, resulting in a Schmidt number $Sc = \nu/D \sim 10^3$, where D is the approximate mass diffusivity of the salt and chemical indicator in water. Measurements of molecular mixing for the different diffusivity cases are compared to illustrate the influence of the Schmidt number (or Prandtl number) on the degree of molecular mixing.

Second, a numerical model of the hot/cold water experiments is used to further examine the mixing dynamics of a turbulent Rayleigh–Taylor mixing layer. Numerical details of the DNS, initial conditions, and validation are presented and discussed. The DNS data set is then used to further quantify the degree of molecular mixing, measuring parameters that could not be obtained from the experiments. The dissertation concludes with the formulation of a numerical model of the turbulent and mixing dynamics, calibrated using the numerical results. It is demonstrated that the calibrated turbulent mixing model reproduces the mixing layer growth and the degree of mixing for the Schmidt number cases of interest.

2. EXPERIMENTAL MEASUREMENTS OF MOLECULAR MIXING

2.1 Overview of Goals and Methodology

For the experimental portion of this work, the relative degree of molecular mixing in a turbulent Rayleigh–Taylor mixing layer was quantified for the cases $Pr \equiv Sc = 7$ (hot/cold water) and $Sc \sim 10^3$ (fresh/salt water). In both cases, the degree to which the two constituent fluids are mixed is given by a combination of the measured mean density field $\bar{\rho}$ and the density variance $\overline{\rho'^2}$, where the overbar denotes Reynolds averaging and the prime indicates a fluctuation about the mean. Based on the intensity of segregation parameter (Dankwerts 1952), the molecular mixing parameter is

$$\theta = \frac{\overline{f_1 f_2}}{\bar{f}_1 \bar{f}_2} = 1 - \frac{\overline{f_1'^2}}{\bar{f}_1 \bar{f}_2}, \quad (2.1)$$

where

$$f_1 = \frac{\rho - \rho_2}{\rho_1 - \rho_2} \quad (2.2)$$

is the volume fraction of fluid 1 (dimensionless measure of density), $\overline{f_1'^2} = \overline{\rho'^2}/(\Delta\rho)^2$, and $\Delta\rho = \rho_1 - \rho_2$ (Youngs 1984). The molecular mixing parameter θ is a measure of homogeneity of a mixture such that $\theta = 1$ if the mixture is completely mixed at the molecular level and $\theta = 0$ if the mixture is stirred but no diffusive mixing has occurred, *e.g.* an immiscible emulsion.

In both the hot/cold and salt/fresh water experiments, θ was used to indicate the degree of molecular mixing, and thus a measurement of both the mean density and density variance was required. Such measurements were achieved directly in hot/cold water experiments, where a series of instantaneous density values was recorded and the necessary density statistics were calculated. However, due to the small size of the spatial scales in the $Sc \sim 10^3$ experiments, direct measurements of instantaneous density values within the mixing layer were not possible. Thus, an alternate approach

was taken, where image analysis techniques were applied to a series of reacting flow experiments to measure $\overline{\rho'^2}$. In addition to the measurement of θ , alternate means of quantifying the degree of molecular mixing, such as the equivalent product thickness integrals P/h [see (2.37)], the probability density function of the density fluctuations, and the global mixing parameters Θ and Ξ [see (2.53) and (2.39)], were also measured and are reported here.

2.2 Experimental Facility

The water channel is an open-loop facility in which two streams of water enter the channel horizontally. Each stream is initially separated by a 3.2 mm thick Plexiglas splitter plate. A schematic of the water channel, diagnostics, and reference axes is shown in figure 2.1. A density difference between the two streams is created by either increasing the temperature ($\Delta T \approx 5$ °C) or adding salt to one stream. The water channel is supplied from two 500 gallon tanks; a typical experiment has a running time of approximately ten minutes. Sump pumps in each tank ensure adequate stirring of the water to maintain temperature uniformity. The heavy and light streams are pumped into the entrance plenum and each stream flows through an arrangement of flow-straighteners, followed by a series of screen meshes (30×30 wires/in). The screen meshes reduce the free-stream velocity fluctuations, and reduce the momentum deficit caused by boundary layers along the walls of the channel and splitter plate. The splitter plate terminates at a 2.5° knife-edge followed immediately by another screen mesh (35×35 wires/in). This final screen mesh (end-screen) minimizes the momentum deficit at the end of the splitter plate, thereby reducing the magnitude and wavelength of the wake shed from the splitter plate (Koop 1976; Browand & Weidman 1976; Stillinger *et al.* 1983).

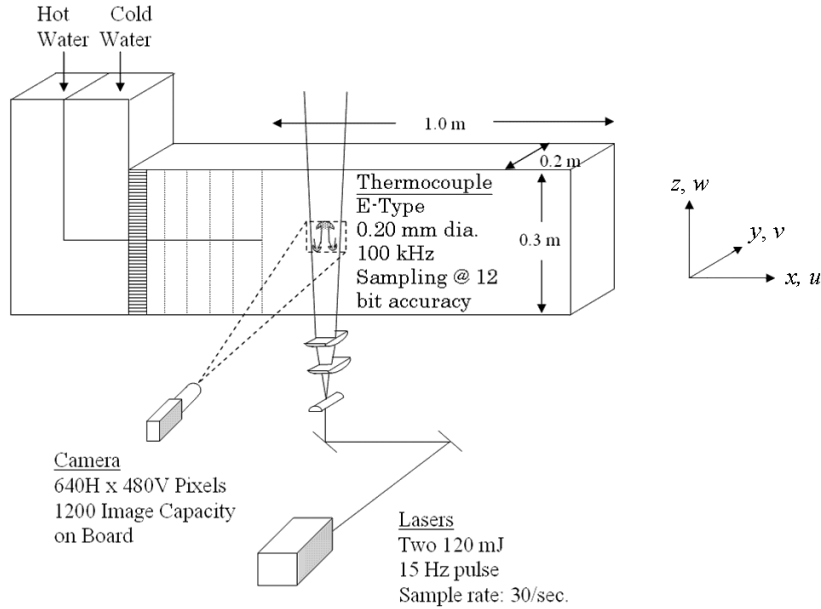


Figure 2.1 Schematic of the water channel facility, diagnostics, and associated coordinate system.

Upon entering the mixing section of the channel, an adverse density stratification exists between the two water streams and a Rayleigh–Taylor instability-driven mixing layer forms downstream. The mixing section is 100 cm long (x -direction) with cross-sectional dimensions of 20 cm \times 32 cm (width \times height). In the present experiments, the mean advection velocity is $U_m \approx 4.75$ cm/s, with the two stream velocities matched so that there is no shear due to mean velocity gradients. The time-evolution of the mixing layer was related to downstream distance by Taylor’s hypothesis $t = x/U_m$ (Pope 2000). Time was normalized as

$$\tau = t \sqrt{\frac{Ag}{H}}, \quad (2.3)$$

where $H = 32$ cm is the vertical height of the channel. The sidewalls were shown to have negligible influence on the growth rate of the mixing layer (Snider & An-



Figure 2.2 Photographic image of a hot/cold water experiment in the water channel. The mean flow is from left-to-right.

draws 1994). The water channel provides a unique facility for measuring turbulence statistics, as the mixing layer is statistically-stationary and long sampling times are available. Water channel measurements were shown to be statistically-stationary for higher-order moments of velocity and density fluctuations (Wilson 2002; Ramaprabhu 2003). A sample image from the experiment is shown in figure 2.2.

2.3 Hot/Cold Water Experiments

The first set of experiments involve the mixing of hot and cold water streams, where the temperature of the bottom stream is elevated such that a difference in density is created by thermal expansion (Snider & Andrews 1994; Wilson & Andrews 2002; Ramaprabhu & Andrews 2004a; Mueschke *et al.* 2006). The thermal diffusivity of heat in water gives a Prandtl number $Pr = \nu/\Gamma \approx 7$. Accordingly, pointwise temperature measurements become a marker for the local fluid density. Thus, the thermal diffusivity Γ is equivalent to the species diffusivity of the concentration of the bottom fluid; hence, the Prandtl number is equivalent to the Schmidt number $Sc = \nu/D$, where D is the equivalent mass diffusivity.

2.3.1 Thermocouple diagnostics

The measurement of the density perturbation in the streamwise (x) direction was performed using a high-resolution thermocouple measurement system. Temperature fluctuations were measured using E-type thermocouples positioned at multiple downstream locations from the splitter plate, as listed in Table 2.1. The thermocouples were constructed from 40 gauge wire (0.08 mm diameter) with a weld bead diameter of 0.16 mm—a smaller diameter than used by previous researchers in this water channel (Snider & Andrews 1994; Ramaprabhu & Andrews 2004a), resulting in a less intrusive diagnostic and improved spatial resolution. The time constant of the thermocouple was determined (Mills 1999) to be $t_c = 0.0047$ s with a corresponding frequency response of $(3t_c)^{-1}$, *i.e.* 71 Hz (corresponding to $kH = 1500$, where $k = 2\pi/\lambda$ is the wavenumber). Mueschke and Andrews (2006) showed that these spatial resolution enhancements reduced the uncertainty in the mixing statistics and scalar fluctuation spectra. The thermocouple wire, extension wire, and all connections were shielded and grounded to minimize external electromagnetic and radio frequency noise. Temperature measurements were recorded at a rate of 50 kHz using a 16-bit data acquisition system. Spurious noise from the temperature trace was eliminated using a 50-point averaging window, thus reducing the sampling rate to 1 kHz. Hence, the window averaging procedure did not affect the temperature fluctuations measured by the thermocouple. Using Taylor’s hypothesis, a sampling rate of 1 kHz and a mean advection velocity of $U_m \approx 4.75$ cm/s, each pointwise temperature measurement was separated by 0.048 mm, which is approximately 30% of the diameter of the probe volume. Fluctuations of the temperature measurements at the Nyquist frequency (500 Hz) were below the system noise, obviating the need for a more complex filtering algorithm that retains spectral resolution. Temperatures were

Downstream location x (cm)	Dimensionless time τ
0.5	0.016
2.0	0.061
5.0	0.166
6.0	0.204
8.0	0.255
10.0	0.342
11.3	0.334
12.5	0.400
15.0	0.473
16.0	0.552
20.1	0.694
25.0	0.865
27.0	0.924
40.0	1.363

Table 2.1 Downstream locations of centerplane temperature (density) measurements and the corresponding dimensionless times.

converted to density using the equation of state of water

$$\rho(T) = \frac{\left(999.8396 + 12.2249 T - 0.007922 T^2 - 55.448 \times 10^{-6} T^3 \right) + 149.756 \times 10^{-9} T^4 - 393.295 \times 10^{-12} T^5}{1 + 18.159 \times 10^{-3} T} \quad (2.4)$$

in units of kg/m^3 (Kukulka 1981). Hereafter, density and temperature are used interchangeably, as they are related by (2.4).

Three measurements were performed to ensure an accurate measurement of the dimensionless time τ , as x , U_m , and A are parameters that can vary from one ex-

periment to another and must be measured accurately to determine τ . First, the distance between the splitter plate and the probe volume was carefully measured. Second, the Atwood number was accurately measured using a digital temperature probe with a K-type thermocouple to measure the water temperature in each 500 gallon tank. Finally, the mean flow velocity in the channel was accurately measured as follows. First, the mean advection velocity of both streams was adjusted until no shear was present and $U_m \approx 4.5\text{--}5.0$ cm/s. The presence of a mean velocity gradient between the two streams was determined in several ways. The pumping system was regularly calibrated by injecting dye into the top and bottom streams and adjusting the flow rates to eliminate relative motion. In addition, dye was also injected onto the splitter plate just before the end-screen. Once the dye was entrained into the mixing layer, the ‘lean’ of developing Rayleigh–Taylor bubbles with respect to the vertical (z) axis was examined at downstream locations. In the absence of any ‘leaning’, the difference between the top and bottom stream velocities was shown to be at most $|U_1 - U_2| < 0.2$ cm/s or $\sim 5\%$ of the mean advection velocity (Ramaprabhu 2003). A final determination of the existence of shear was performed by examining the skew of the PDF of density (volume fraction) fluctuations. In the small Atwood number limit of the Rayleigh–Taylor instability, bubbles and spikes grow symmetrically. Due to the symmetry in the geometry of the apparatus, the PDF of the density fluctuations should also be symmetric, with no skew. Any measurement containing a skewed PDF due to excessive shear was discarded. To measure U_m , a syringe was used to inject fluid containing a high concentration of Nigrosine dye. The time t_m required for a blob of dye to travel a distance L_m from the end-screen to a marked downstream location was recorded, so that $U_m = L_m/t_m$.

To measure the density values, a thermocouple was mounted on a thin vertical rod that allowed fine adjustment of the probe location in the vertical (z) direction. All

measurements in the present study were performed at the centerplane of the mixing layer ($z = 0$), defined as the plane at which equal average volume fractions of hot and cold water exist, *i.e.* the centerplane corresponds to the z -location at which the average of the volume fraction of fluid 1 is

$$\bar{f}_1(z, t) = \frac{\bar{\rho}(z, t) - \rho_2}{\rho_1 - \rho_2} = \frac{1}{2}, \quad (2.5)$$

where the spatial (Reynolds) average of a scalar quantity ϕ is

$$\bar{\phi}(z, t) = \frac{1}{L_x} \int_0^{L_x} \phi(\mathbf{x}, t) dx. \quad (2.6)$$

Spatial averaging of pointwise measurements utilizes Taylor's hypothesis such that $x = U_m t$, $L = U_m N_{samp}/f_{samp}$ is the distance (cm) over which $\phi(\mathbf{x}, t)$ was measured in the x -direction, N_{samp} is the number of samples, and f_{samp} is the sampling rate (Hz).

The initial interface between the two fluids, and subsequent centerplane of the mixing layer that forms, is nominally a horizontal plane normal to the direction of gravity. As the splitter plate is not perfectly horizontal, the location of the centerplane drifts slightly with downstream distance; however, there is no evidence that the results are affected by this drift. In addition, it was concluded that a visual inspection of the thermocouple probe placement could not provide an accurate measure of the mixing layer centerline with respect to (2.6). Consequently, the following procedure was used to accurately position the probe: a set of temperature measurements was recorded at 200 Hz and \bar{f}_1 was evaluated; depending upon the value of \bar{f}_1 , the position of the probe was adjusted vertically until $\bar{f}_1 = 0.50 \pm 0.025$; once the probe was located at the centerplane, data collection commenced with a two minute interval of temperature measurements recorded at 50 kHz. A two minute collection period corresponds to the passage of approximately eighty large-scale (long-wavelength) plumes, ensuring

statistical convergence (Wilson & Andrews 2002; Ramaprabhu & Andrews 2004a).

2.3.2 Density fluctuations measurement

Measured density data was also used to determine an integral measure of the degree of molecular mixing $\theta(\tau)$ at a given downstream location. All molecular mixing measurements were taken at the centerplane of the mixing layer ($z = 0$), and thus do not represent the degree of molecular mixing over the entire mixing layer. The measure of molecular mixing used here was first introduced by Dankwerts (1952) as the degree of fluid segregation, and has been used by various researchers in a variety of forms (Youngs 1984; Dalziel *et al.* 1999; Wilson & Andrews 2002; Cook *et al.* 2004). The definition of θ requires two quantities, B_0 and B_2 :

$$B_0 = \overline{f_1'^2} = \frac{\overline{\rho'^2}}{(\Delta\rho)^2} \quad (2.7)$$

is the dimensionless density variance corresponding to two miscible fluids at a given downstream location, and

$$B_2 = \bar{f}_1 \bar{f}_2 = \bar{f}_1 (1 - \bar{f}_1) \quad (2.8)$$

is the maximum dimensionless density variance possible corresponding to two immiscible fluids (*i.e.* a pure two-fluid mixture) at a given downstream location, and is readily obtained from (2.7). In (2.7)–(2.8), the overbar indicates spatial averaging [see (2.6)] and the prime denotes a fluctuation about the mean, $\phi(x)' = \phi(x) - \bar{\phi}$.

The molecular mixing parameter at a given downstream location is then defined as

$$\theta(t) = 1 - \frac{B_0(t)}{B_2(t)}, \quad (2.9)$$

such that $\theta = 0$ when the two fluids are completely segregated, and $\theta = 1$ when they are completely molecularly mixed (*i.e.* when the density is uniform). The evolution

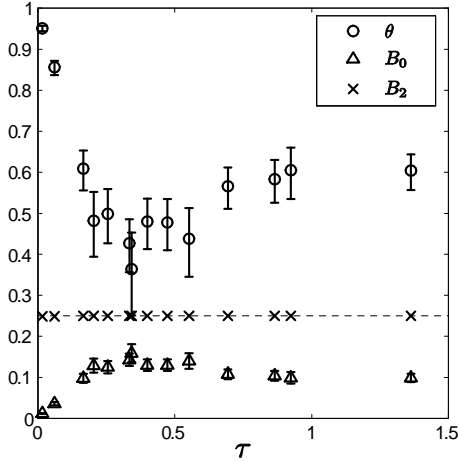


Figure 2.3 Evolution of the molecular mixing quantities B_0 , B_2 and θ on the centerplane for the $Pr = 7$ experiments. The values of B_2 all approach a value of 0.25 (dashed line), indicating that the measurements were taken at the centerplane of the mixing layer. The error bars on the measurements are also shown.

of the centerplane values of B_0 , B_2 and θ are shown in figure 2.3. All measurement points are taken at the centerplane where $\bar{f}_1 = \bar{f}_2 = 0.5$, so that $B_2 = \bar{f}_1 \bar{f}_2 = 0.25$ on the centerplane.

Figure 2.3 reveals two stages of evolution of the molecular mixing parameter θ . At early times ($\tau < 0.4$), θ decreases rapidly, which occurs during the early-time linear and weakly-nonlinear growth of the initial perturbations. The second stage is characterized by an increase in θ ($\tau > 0.4$). The evolution of θ suggests the following dynamical interpretation. A decrease in θ during the first stage is attributed to the initial growth of Rayleigh–Taylor unstable perturbations, leading to a straining of the initial density interface shed from the splitter plate. At the centerplane, the two fluids are ‘stirred’ with little molecular mixing. A subsequent increase in θ during the second stage is due to the flow complexity associated with

the development of strong nonlinearities. Secondary Kelvin–Helmholtz instabilities develop between rising bubbles and falling spikes, rapidly increasing the interfacial area between the fluids and the associated molecular diffusion. This transition is observed in the water channel experiments at $\tau \approx 0.4$, when θ attains its minimum value. Ristorcelli and Clark (2004) noted similar behavior in a DNS of a small Atwood number, miscible Rayleigh–Taylor instability-driven mixing layer.

In the present experiment, the degree of molecular mixing at the centerplane of the mixing layer varies significantly over the measurement times $0.016 \leq \tau \leq 1.36$. The time-evolution of the volume fraction PDF, volume fraction variance and kurtosis, and molecular mixing parameter is shown in figures 2.3–2.5, which indicate the same early-time imbalance between the rates of fluid engulfment and molecular mixing. The term ‘engulfment’ is used here in analogy with the term ‘entrainment’, typically used in shear layers in which the physical mechanism by which fluid enters the mixing layer is different from that in Rayleigh–Taylor instability-driven mixing. Comparison of figures 2.3–2.5 at $\tau \approx 0.4$ shows an early-time transition point in the development of the mixing layer when the rates of fluid engulfment and molecular mixing are comparable. Prior to the onset of strong nonlinearity, the growth of the initial buoyant structures engulfs unmixed fluid into the mixing layer before developing substantial surface area between the two fluids, thereby limiting the amount of molecular mixing. Beyond this transition point, the rate of molecular mixing due to turbulent fluctuations is greater throughout the mixing layer and, as a result, both the rate of molecular mixing and the amount of mixed fluid at the centerplane increase.

Molecular mixing in a miscible Rayleigh–Taylor mixing layer is difficult to measure due to the large number of samples required for the statistical convergence of \bar{f}_1 and $\overline{f_1'^2}$, with the measurement points taken with sufficient spatial resolution to resolve all density gradients (Mueschke & Andrews 2006). Other researchers have typically

reported $\theta(z)$ across the mixing layer or $\Theta(t)$ (a global measure of molecular mixing) for late times (Youngs 1991), rather than the evolution of $\theta(z = 0, t)$, as reported here. Ramaprabhu and Andrews (2004a) also measured $\theta(z = 0, t)$ in the same water channel used in the present investigation. In the present work, a minimum value of $\theta \approx 0.4$ was measured at $\tau \approx 0.4$ as in Ramaprabhu and Andrews (2004a), but is lower than their reported value $\theta = 0.68$. The difference between the measured values of θ reported here and by Ramaprabhu and Andrews (2004a) is attributed to the difference in the size of the thermocouple probes and to the noise elimination techniques used in the present work (Mueschke 2004; Mueschke & Andrews 2006). Ristorcelli and Clark (2004) reported a similar two-stage behavior of $\theta(z = 0, t)$; however, the exact time of transition and the minimum value of θ differ. The difference between the present early-time measured results and the simulation results of Ristorcelli and Clark may be due to the fact that the initial velocity field was zero in the numerical simulations.

2.3.3 *Statistical composition of mixed fluid*

To further examine the degree of molecular mixing, the probability density function (PDF) of the density fluctuations is examined. While θ is a function of the first and second moments of the density fluctuations, an infinite number of PDFs may be constructed of different shapes that yield the same value of θ . Thus, a better understanding of the composition of the mixed fluid within the mixing layer may be achieved by examining the PDF of f_1 directly. The PDF of a measured scalar quantity ϕ is defined discretely by

$$P(\phi) = \frac{F(\phi)}{N_{\text{samp}} \Delta\phi}, \quad (2.10)$$

where $F(\phi)$ is the discrete frequency distribution (histogram) of the scalar ϕ , N_{samp} is the number of samples, and $\Delta\phi$ is the bin width of $F(\phi)$. The kurtosis (fourth-order moment) of an ensemble of scalar measurements is

$$K_\phi = \frac{\overline{\phi^4}}{\left(\overline{\phi^2}\right)^2}. \quad (2.11)$$

The variance of the volume fraction fluctuations is a measure of the spread of volume fraction values away from the mean value $\bar{f}_1 = 0.5$, while the kurtosis is a measure of the sharpness of the volume fraction PDF. Kurtosis values $K_{f_1} < 1.8$ indicate a bimodal distribution with peaks at $f_1 = 0$ and $f_1 = 1$, whereas values $K_{f_1} > 1.8$ correspond to a centrally-peaked PDF, in this case at $\bar{f}_1 = 0.5$ (a Gaussian distribution has a value $K_{f_1} = 3$). The skewness (normalized third-order moment) of the density fluctuations was measured to be approximately zero on the centerplane, consistent with the expected symmetry of $P(f_1)$ in this small Atwood experiment, and is not discussed further.

Figure 2.4 shows both the early and intermediate time-evolution of $P(f_1)$. At early-times ($\tau = 0.016$ and 0.06) the volume fraction distributions are peaked at $f_1 = 1/2$, indicating that most of the fluid at the centerline is mixed. However, as the initial bubbles and spikes grow ($\tau = 0.204$ and 0.473), a large portion of the region near the centerplane becomes occupied by pockets of pure hot and cold water engulfed by the mixing layer, causing the distribution to become strongly bimodal. This trend is reversed at later times ($\tau > 0.473$), as a central peak reemerges in the distribution of $P(f_1)$ as τ and the Reynolds number increases. Similar volume fraction distributions were reported by Ramaprabhu and Andrews (2004a) using lower resolution thermocouples; however, a greater degree of bimodality is reported here. The present measurement refines those reported by Ramaprabhu and Andrews (2004a), as smaller

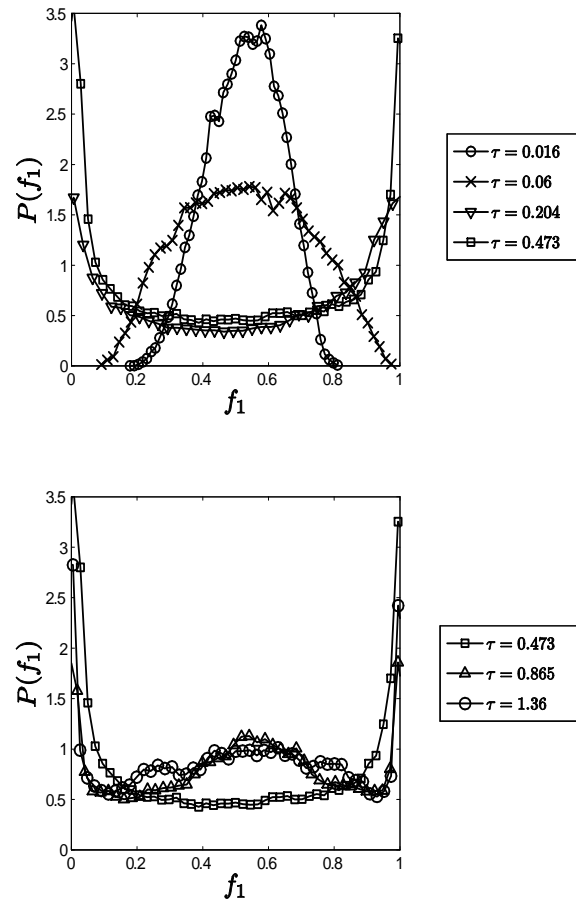


Figure 2.4 Evolution of the early-time (top) and late-time (bottom) volume fraction PDF $P(f_1)$ on the centerplane of the mixing layer.

thermocouples were used to better resolve the sharp density gradients present during the early stages of mixing (Mueschke & Andrews 2006).

The time-evolution of K_{f_1} shown in figure 2.5 quantifies the modality observed in figure 2.4. The initial, single-mode distribution of $P(f_1)$ evolves to a bimodal distribution, and the values of $K_{f_1}(\tau)$ correspondingly decrease below 1.8. This indicates a strong segregation of the two fluids at early and intermediate times $0.204 < \tau < 0.473$. As nonlinear interactions become increasingly dominant, the range of scales continues to increase, as do the associated interfacial areas between pockets of hot and cold

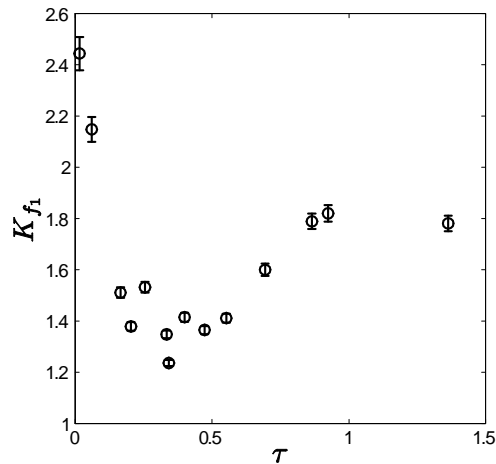


Figure 2.5 Evolution of the volume fraction kurtosis on the centerplane.

fluid. Thus, as the rate of molecular diffusion increases, so does the value of K_{f_1} .

2.3.4 Evolution of the density variance spectrum

A better understanding of the spatial scales within the mixing layer may be achieved by examining the spectrum of density fluctuations. The density variance spectrum is critical for the validation and calibration of spectral equilibrium models of mixing, such as the one proposed by Liu and Fox (2006). A brief review of the calculation of the density variance spectrum is given below; more details of the procedure are given in Appendix B.

The amplitudes of the density fluctuations are given by the one-dimensional Fourier transform of the density

$$\hat{\rho}(k, \tau) = \frac{2}{L_x} \int_0^{L_x} \rho(x, \tau) e^{-ikx} dx, \quad (2.12)$$

where $k \equiv 2\pi/\lambda$ is the wavenumber corresponding to wavelength λ , and L_x is the distance over which $\rho(x)$ was measured. The change from temporal variation to spatial

variation utilizes Taylor’s hypothesis to relate $\rho(t)$ and $\rho(x)$ (Pope 2000). As the probe volume records pointwise measurements, the dependence of the density field upon the other spatial and temporal dimensions is suppressed for brevity. The complex-valued amplitude and phase is given by (2.12), from which the one-dimensional energy spectrum is

$$E_\rho(k, \tau) = \frac{\hat{\rho}(k, \tau)^* \rho(k, \tau)}{4 \Delta k}, \quad (2.13)$$

where $\hat{\rho}^*$ is the complex conjugate of $\hat{\rho}$, and $\Delta k = 2\pi/L$ is the wavenumber bin width.

It follows that

$$\frac{\overline{\rho'^2}(\tau)}{2} = \int_0^\infty E_\rho(k, \tau) dk \quad (2.14)$$

in the continuum wavenumber limit.

In general, density variance spectra calculated from pointwise measurements are noisy for several reasons, including the finite recording time of data points and random errors due to electronic noise. The fluctuations in $E_\rho(k, \tau)$ render it difficult to accurately estimate the spectral slopes in various power-law regimes. In order to elucidate possible scaling laws of the density variance spectra, the original spectra must be smoothed. Ramaprabhu and Andrews (2004a) used Savitsky–Golay filtering techniques, which fit an n^{th} -order polynomial to a moving window ($2n + 1$ points wide) to perform smoothing. However, significant filtering is required to smooth the intermediate-to-large wavenumber variance spectra. The present study further improves upon this by implementing a smoothing procedure that conserves energy in local wavenumber regions by binning variance values into wavenumber bins, Δk , which increase in size logarithmically. This method is conservative by construction and significantly smooths the intermediate and large wavenumber spectra. As in standard discrete sampling theory, $E_\rho(k, \tau)$ is originally sorted in wavenumber bins of constant size $\Delta k = 2\pi/L$. To smooth the spectra, the density variance per unit wavenumber

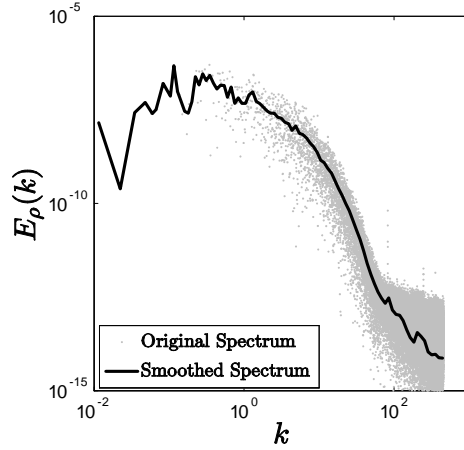


Figure 2.6 Illustration of a smoothed density variance spectrum using the logarithmic binning procedure.

from (2.13) was apportioned into wavenumber bins logarithmically increasing in size and normalized by the local wavenumber bin width: this results in a procedure that averages the density variance over a wavenumber bin width that increases in size at the same rate as the number of modes resolved at larger wavenumbers. This procedure conserves the energy content of the spectrum, which was confirmed by comparing the integrals of the original spectra with those of the smoothed spectra. Figure 2.6 illustrates the results of the smoothing procedure by plotting the unsmoothed and smoothed spectra.

Another characteristic of experimentally-measured variance spectra is the horizontal ‘tail’ at large wavenumbers, indicating the level at which the system noise is greater than the measured fluctuations. It is possible to improve the dynamic range of $E_\rho(k, \tau)$ measured by subtracting the system noise from the measured density variance spectrum using Wiener filtering (Press *et al.* 2002), requiring either an estimate or a measurement of the noise. In the present work, the background

noise was measured by filling the channel with water and allowing thermal equilibrium to be attained. A thermocouple probe was placed in the water channel and a two-minute sample of the background noise was measured at 50 kHz. Fluctuations in the temperature induced by EMF and RFI noise were converted to density using (2.4). The variance spectrum of the background noise was then calculated and subtracted from the measured density variance spectrum. This procedure provided an additional decade of measurable values at the largest wavenumbers. The subtraction of the background noise also eliminated a large portion of spurious noise from the initial density variance spectrum at $\tau = 0.016$, which will be discussed in detail next.

The early-time density variance spectra ($\tau = 0.016$) shown in figure 2.7 exhibit broad-banded perturbations at the onset of the instability. However, the spectrum at $\tau = 0.06$ contains considerably more energy in the dimensionless wavenumber range $kH < 100$. As the mixing layer develops, a steep decay in the energy spectrum is noted at larger dimensionless wavenumbers ($kH > 100$) as small-scale fluctuations are damped by diffusion, as shown in figure 2.7. However, definitive power-law scalings are difficult to determine due to the short interval over which the decay occurs (less than one decade). At later times ($\tau = 0.865$ and 1.36), a small range of scales exhibit an approximate $k^{-5/3}$ spectrum, as shown in figure 2.8. Compensated density variance spectra are also shown in figure 2.8, with an apparent inertial subrange over approximately one decade of wavenumbers. The slight deviation may be due to the limited Reynolds numbers attained in the experiment: Ramaprabhu and Andrews (2004a) also estimated the integral-scale Reynolds number $Re_h \approx 1000$ – 1450 at $\tau = 1.21$, depending upon the choice of length scale L and velocity-scale U (see § 2.4.7 for further details). Wilson and Andrews (2002) and Ramaprabhu and Andrews (2004a) reported a late-time $k^{-5/3}$ scaling. They also showed that an inertial subrange exists over approximately one decade of wavenumbers at $\tau = 2.08$, consistent with the

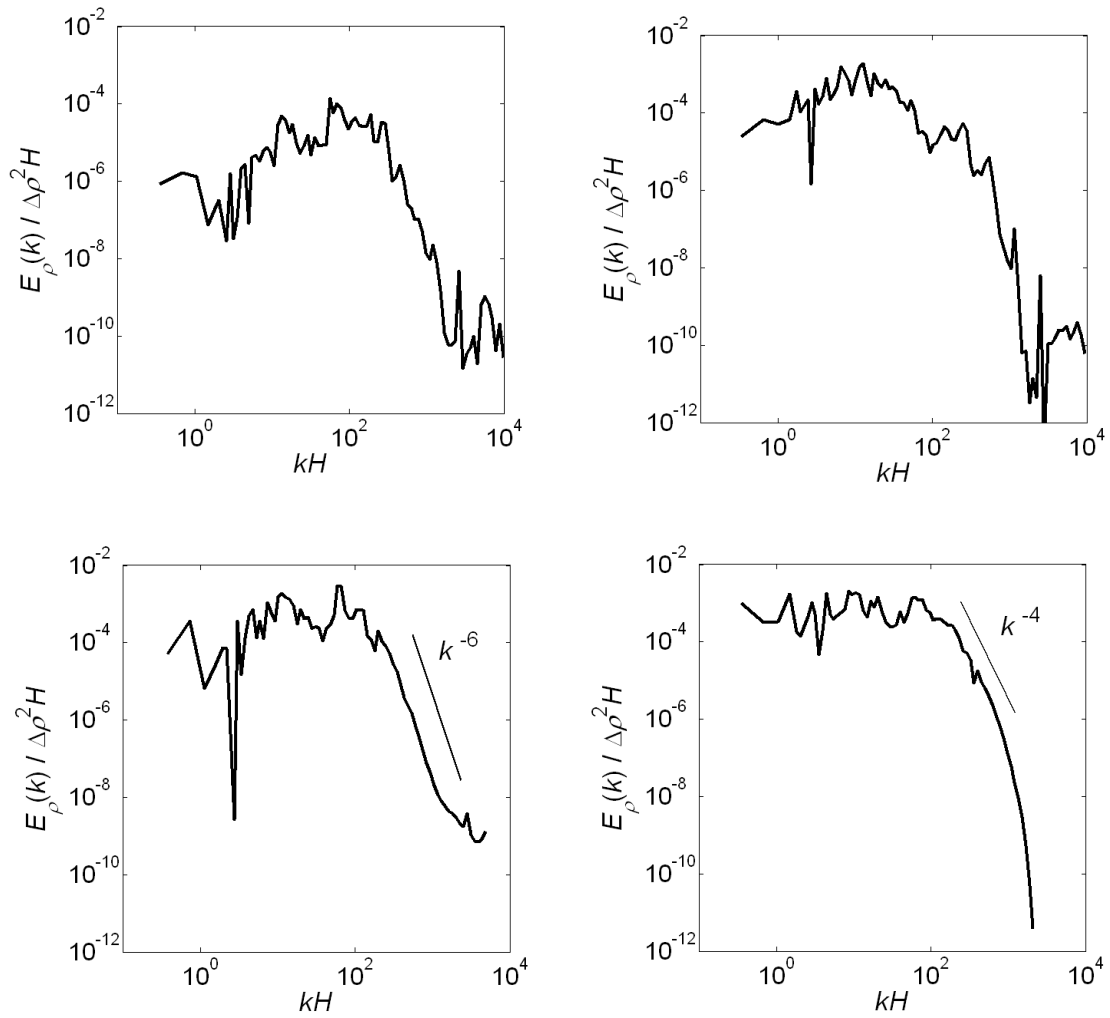


Figure 2.7 The normalized density variance spectrum at $\tau = 0.016$ or at $x = 0.5$ cm downstream (top-left), $\tau = 0.06$ or at $x = 2.0$ cm downstream (top-right), $\tau = 0.204$ or at $x = 6.0$ cm downstream (bottom-left), and at $\tau = 0.473$ or at $x = 15.0$ cm downstream (bottom-right).

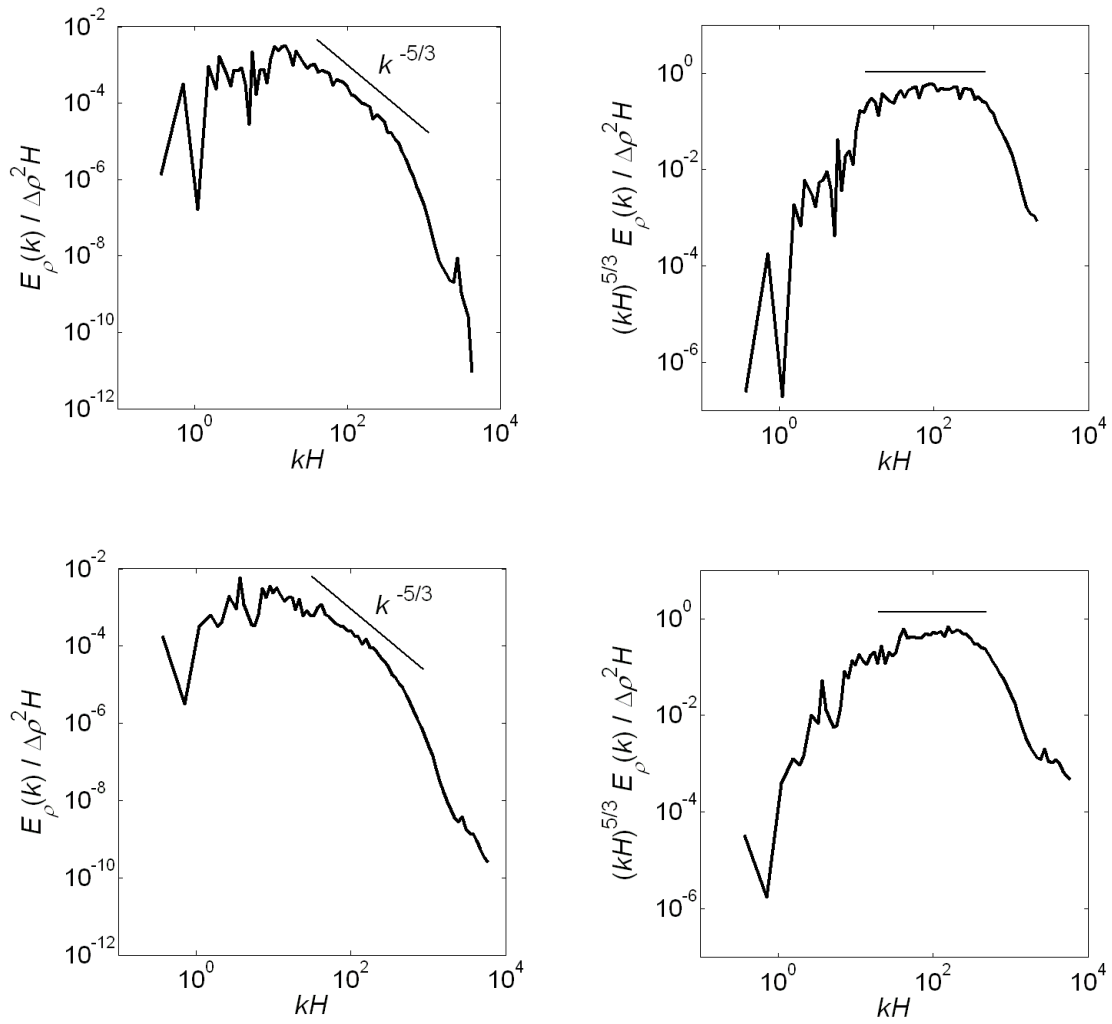


Figure 2.8 The normalized density variance spectrum at $\tau = 0.865$ or at $x = 25.0$ cm downstream (top-left). The compensated spectrum (top-right) at $\tau = 0.865$ indicates a short range of apparent $k^{-5/3}$ scaling. The normalized density variance spectrum at $\tau = 1.36$ or at $x = 40.0$ cm downstream (bottom-left). The compensated spectrum (bottom-right) at $\tau = 1.36$ indicates a short range of apparent $k^{-5/3}$ scaling.

current results.

An accurate measure of the density variance spectrum and of the molecular mixing parameter θ requires measurement times sufficient for statistical convergence of the larger scales, while adequately resolving the small-scale structures. As stated in § 2.3.1, the frequency response of the thermocouple probe is 71 Hz or $kH \approx 1500$, depending upon the exact mean flow velocity. Ramaprabhu and Andrews (2004a) estimated $Re_h = 1250$ at $\tau = 1.21$, resulting in a Kolmogorov scale $\eta_K = h_b Re_h^{-3/4} = 0.29$ mm ($kH = 6900$) and a Batchelor scale $\eta_B = \eta_K Pr^{-1/2} = 0.11$ mm ($kH = 18300$). Thus, the thermocouple measurement system is not capable of resolving approximately the final decade of wavenumbers in the dissipation subrange of the density variance spectrum. However, the error introduced by not resolving this final decade can be shown to be negligible. For example, taking $B_2 = 0.25$ at the centerplane (by definition) and substituting (2.7) and (2.14) into (2.9), θ can be written in terms of the density variance spectrum:

$$\theta(\tau) = 1 - \frac{8}{(\Delta\rho)^2} \int_0^\infty E_\rho(k, \tau) dk. \quad (2.15)$$

To examine the integral contribution of higher wavenumber density fluctuations to θ , consider the spectral molecular mixing parameter

$$\theta(k, \tau) = 1 - \frac{8}{(\Delta\rho)^2} \int_0^k E_\rho(k', \tau) dk'. \quad (2.16)$$

As additional wavenumbers are included in the integration of the measured $E_\rho(k, \tau)$, $\theta(k, \tau)$ converges to $\theta(\tau)$, as shown in figure 2.9. This demonstrates that the majority of the energy content is in the smaller wavenumbers of the spectrum. The same conclusion was reached by Wilson and Andrews (2002) by examining the cumulative energy distribution of density fluctuations. More importantly, $\theta(k, \tau)$ attains the asymptotic value of $\theta(\tau)$ before the measurement resolution limit $kH = 1500$. Thus,

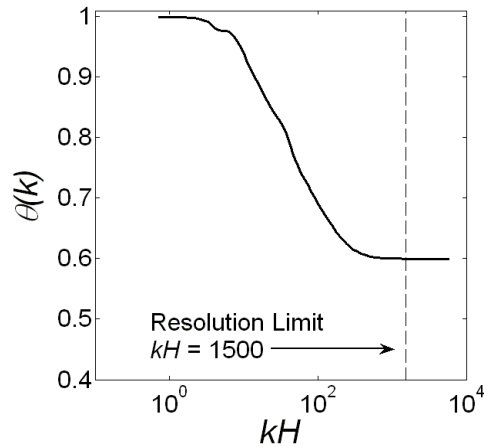


Figure 2.9 Spectral molecular mixing fraction $\theta(k)$ versus dimensionless wavenumber at $\tau = 1.36$.

the additional decade of energy in the dissipation subrange beyond the resolution limit of the probe can be assumed negligible in terms of the measurement of $\theta(\tau)$ for the mixing layer and Prandtl number considered here.

2.4 Salt/Fresh Water Experiments

In a different set of experiments, salt (NaCl) was added to the top stream of the channel to create a density difference. In this case, the concentration of salt served as a marker for the density field. The resulting species diffusivity of the Na^+ and Cl^- ions gave a Schmidt number $Sc = 620$ (Lide 2006). Direct measurements of the salt concentration field were not feasible due to the large magnitudes of the scalar gradients (Mueschke & Andrews 2006). Instead, a diffusion-limited chemical reaction between the two streams was monitored to measure the degree of molecular mixing. The pH of each stream was altered by adding either hydrochloric acid (HCl) or sodium hydroxide (NaOH) to each stream. As the two fluids mixed at the molecular

level, a neutralization reaction occurred and the local pH of the mixture reached a new equilibrium. The reaction was monitored by the addition of a pH-sensitive chemical indicator (phenolphthalein) to the acidic stream. As the local pH of the mixture changed, the transparent phenolphthalein changed color to a translucent shade of pink. The concentration of the colored form of the indicator was measured using backlit optical techniques. This section presents an overview of the prerequisite chemistry, optical measurement techniques, and estimated measurement uncertainty bounds.

2.4.1 Reaction chemistry

In the current experiments, fluid 1 is the heavier fluid with $\text{pH}_1 > 7$ (alkali) and fluid 2 is the lighter fluid with $\text{pH}_2 \leq 7$ (either acidic or neutral), where the subscript denotes either the top (heavy) or bottom (light) stream. In aqueous solutions, the concentration of hydrogen and hydroxide ions remains balanced according to the reversible reaction



with associated equilibrium constant

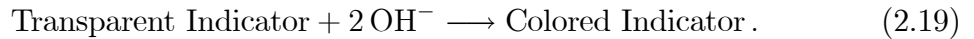
$$K_w = [\text{H}^+][\text{OH}^-] = 1 \times 10^{-14}, \quad (2.18)$$

where square brackets $[\bullet]$ denote molar concentration, *i.e.* moles per liter (Harris 2003). As fluid from each stream molecularly mix, the local concentrations of H^+ and OH^- adjust to a new equilibrium value satisfying (2.18). The pH of the resulting mixture is $\text{pH}_{mix} = -\log_{10}[\text{H}^+]_{mix}$. Further details on the neutralization reaction are given in Appendix C.

In this work, the pH is controlled by the addition of HCl or NaOH to either

stream. Given stoichiometric quantities of HCl and NaOH (*i.e.* both reactants are completely consumed in the reaction) the resulting mixtures will react according to the exothermic reaction $\text{HCl}(aq) + \text{NaOH}(aq) \longrightarrow \text{H}_2\text{O}(l) + \text{NaCl}(aq)$ with heat release $\Delta h_f^0 = -59.8 \text{ kJ/mol}$. Given a specific heat capacity of water $C_p = 4.179 \text{ J/g-K}$, the local temperature increase in the fluid is $\Delta T \approx 0.02^\circ \text{ C}$ for the case of $\text{pH}_1 = 11.5$ and $\text{pH}_2 = 2.5$. Accordingly, the local decrease in density due to thermal expansion is negligible and thus, the neutralization reaction has a negligible effect on the Atwood number or on the buoyancy effects driving the mixing.

To monitor the neutralization reaction, a small quantity of phenolphthalein ($\text{C}_{20}\text{H}_{14}\text{O}_4$) indicator was dissolved in the bottom (acidic) stream; In is used to denote the indicator. Typical concentrations $[\text{In}]_2 = 6 \times 10^{-6} \text{ M}$ were used, where the subscript indicates that the indicator was added to the bottom stream. While the chemistry of the neutralization reaction is straightforward, the chemistry of the pH-sensitive indicator is complex. Phenolphthalein is a weak acid, and will dissociate depending upon the local pH (Bishop 1972). Schematically, the indicator follows the reversible reaction



Phenolphthalein has multiple ionization states and, thus, several different chemical forms (denoted by Roman numeral subscripts):



All forms of the indicator in (2.20)–(2.22) are transparent with the exception of the

pink quinone phenolate form (In_{IV}). The equilibrium constants for the first two reactions are (Kolthoff 1937)

$$K_1 = \frac{[\text{In}_{III}][\text{H}^+]}{[\text{In}_I]} = 1.15 \times 10^{-9}, \quad (2.23)$$

$$K_2 = \frac{[\text{In}_{IV}][\text{H}^+]}{[\text{In}_{III}]} = 2.8 \times 10^{-10}. \quad (2.24)$$

As the pH of a mixture rises above pH = 8, the equilibria of the first two reactions in (2.20)–(2.21) move to the right according to Le Chatelier’s principle, and the colored form of the indicator is produced. However, as pH > 11.3, the equilibrium of the last reaction (2.22) also moves to the right and, as a result, less In_{III} is available to convert to the colored form In_{IV} . Zhang *et al.* (1995) reported a measurement of the equilibrium constant

$$K_3 = \frac{[\text{In}_{VII}][\text{H}^+]^2}{[\text{In}_{III}]} \approx 2.75 \times 10^{-23} \quad (2.25)$$

for this reaction. An expression for the fraction of indicator in its colored form can be obtained by substituting the equilibrium constant expressions (2.23)–(2.25) into the mass balance equation

$$[\text{In}] = [\text{In}_I] + [\text{In}_{III}] + [\text{In}_{IV}] + [\text{In}_{VII}]. \quad (2.26)$$

Solving for $[\text{In}_{IV}]/[\text{In}]$ gives a relative measure of concentration of In_{IV} as a function of the H^+ concentration (Harris 2003). The fraction of dissociation of In_{IV} ,

$$\alpha_{\text{In}_{IV}} = \frac{[\text{In}_{IV}]}{[\text{In}]} = \frac{K_1 K_2}{K_1 K_2 + K_1 [\text{H}^+] + [\text{H}^+]^2 + K_1 K_3 [\text{H}^+]^{-1}}, \quad (2.27)$$

is defined such that $\alpha_{\text{In}_{IV}} = 0$ when none of the indicator is in its colored form, and $\alpha_{\text{In}_{IV}} = 1$ when all of the indicator is in its colored form. Figure 2.10 shows the fraction of dissociation $\alpha_{\text{In}_{IV}}$ as a function of the pH.

The indicator reaction has been shown to be sufficiently fast to capture the

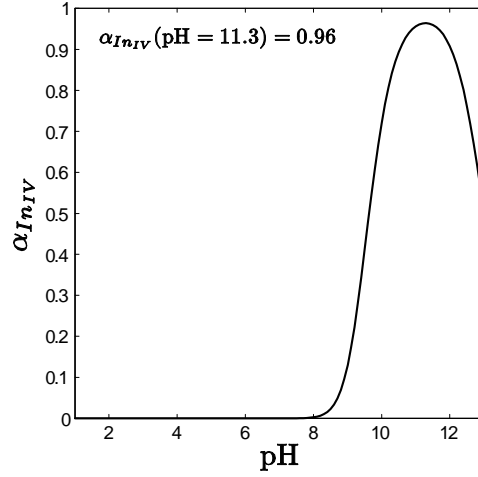


Figure 2.10 Fraction of dissociation for the colored form of the chemical indicator In_{IV} .

mixing dynamics of $Re_D = UD/\nu = 32,000$ jets (Zhang 1995). The Damköhler number (ratio of hydrodynamic to chemical reaction time scales) is defined as $Da_{ent} = \tau_{ent}/\tau_{chem}$, based upon the entrainment time scale τ_{ent} of the mixing layer, and $Da_{mix} = \tau_{mix}/\tau_{chem}$, based upon the mixing time scale of the layer. For the concentrations of indicator used in the water channel experiment, $\tau_{chem} = 2 \times 10^{-7}$ s (Caldin 1964; Zhang 1995), and $\tau_{ent} = (h_b - h_s) / \left[\frac{d}{dt}(h_b - h_s) \right] \approx 10$ s, based upon the mixing layer width measurements reported in § 2.4.4, and $\tau_{mix} = \tau_{ent} Re_h^{-1/2} \approx 0.18$ s. This results in $Da_{ent} = 5 \times 10^7$ and $Da_{mix} = 9 \times 10^5$, where $Da > 40$ for either definition is required to observe diffusion-limited mixing (Mungal & Frierler 1988). Thus, the use of phenolphthalein as a chemical indicator is well-suited for this flow.

2.4.2 Optical imaging system and calibration

All constituents of the mixing layer and forms of the chemical indicator are transparent except for the final product In_{IV} , which absorbs green light ($\lambda_{peak} = 552$ nm), and is therefore pink (Green 1990). The attenuation of a light ray passing through

the mixing layer is related to the concentration of colored indicator $[\text{In}_{IV}]$ through the Beer–Lambert law (Hecht 2002)

$$\sigma = \varepsilon \int_0^L [\text{In}_{IV}] dx, \quad (2.28)$$

where σ is the absorption of light, ε is a molar absorptivity constant for phenolphthalein, and L is the total path-length of the light ray through the absorbing medium. The absorption of light is related to the ratio of measured light intensity I to the back-lighting intensity I_0 by

$$\sigma = -\ln\left(\frac{I}{I_0}\right) = \varepsilon L \overline{[\text{In}_{IV}]}, \quad (2.29)$$

where $\overline{[\text{In}_{IV}]}$ is the spanwise average concentration of colored indicator. Thus, given a calibrated value of ε , $\overline{[\text{In}_{IV}]}$ is linearly related to a light absorption measurement. Colored indicator concentration measurements normalized by the free stream indicator concentration $C = \overline{[\text{In}_{IV}]} / [\text{In}]_2$ are presented in § 2.4.5.

In the present work, the molar absorptivity coefficient of phenolphthalein was measured by filling a Plexiglas wedge with a known concentration of indicator at a specified pH. The variation in light absorption across the wedge provided a measure of the light absorption versus depth of the wedge. The molar absorptivity coefficient was measured by calculating the slope of the absorption curve shown in figure 2.11. The calibration experiment was repeated using three different indicator concentrations: each produced similar slopes such that $\varepsilon = 2.935 \times 10^4 \pm 0.67\% \text{ (M}\cdot\text{cm)}^{-1}$, which agreed well with the value $\varepsilon = 2.934 \times 10^4 \text{ (M}\cdot\text{cm)}^{-1}$ measured by Zhang *et al.* (1995). It was found that at absorptions $\sigma > 1.5$ the system response became nonlinear, so the phenolphthalein concentration in the acidic stream was limited to exclude absorptions $\sigma > 1.2$.

To measure the concentration of the colored form of phenolphthalein in the chan-

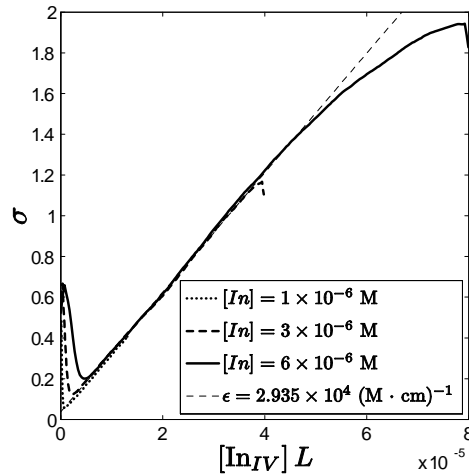


Figure 2.11 Calibration of molar absorptivity coefficient ϵ_{In} for phenolphthalein. A fiducial for $\epsilon_{\text{In}} = 2.935 \times 10^4 \text{ (M} \cdot \text{cm)}^{-1}$ is shown (dashed line).

nel, the experiment was backlit by multiple fluorescent lights. Prismatic panels and sheets of translucent velum were placed between the light source and the mixing section of the channel to create a uniform backlighting source. Attenuation of the background lighting by the colored phenolphthalein indicator was measured using an 8-bit, three-channel CCD array. The total amount of backlighting scattered by the mixing layer (due to the index of refraction difference) is negligible compared with the absorption by the indicator for the small Atwood numbers considered here. A green optical filter was used to minimize the transmission of wavelengths above and below the peak absorption wavelength of phenolphthalein to the CCD array. Approximately two hundred photographs were used to measure the average light absorption by the indicator, and thus, through the Beer–Lambert law (2.29), the average concentration of $\overline{[\text{In}_{IV}]}$ at downstream locations.

2.4.3 Uncertainty analysis

The density difference between the two fluids was created by adding salt to the top stream. The density of each fluid was obtained by measuring the mass of a 50 ml sample in a high-accuracy flask on an electronic balance. Multiple samples were measured ($N \approx 8-10$) and the density of each fluid stream $\rho_r = m_r/V$ (where $r = 1,2$ denotes the top and bottom streams) was determined. The 95% confidence interval bounds were obtained from

$$w_{m_r} = \pm 1.96 \sqrt{\frac{s_{m_r}^2}{N}}, \quad (2.30)$$

where $s_{m_r}^2$ is the variance of the mass measurements, and N is the number of samples (Benedict & Gould 1996). The resulting uncertainty in the density of each fluid is

$$w_{\rho_r} = \pm \sqrt{\left(\frac{\partial \rho_r}{\partial m_r} w_{m_r}\right)^2 + \left(\frac{\partial \rho_r}{\partial V} w_V\right)^2}, \quad (2.31)$$

where $w_V = \pm 0.05$ ml is the uncertainty in the volume measurement. Similarly, the uncertainty in the Atwood number for a given experiment is

$$w_A = \pm \sqrt{\left(\frac{\partial A}{\partial \rho_1} w_{\rho_1}\right)^2 + \left(\frac{\partial A}{\partial \rho_2} w_{\rho_2}\right)^2} = \pm 1\%. \quad (2.32)$$

The velocity of each stream was measured by injecting dye into the top and bottom streams, and recording the time required for the dye to travel a measured distance. Using similar uncertainty propagation estimates as in (2.31) and (2.32), the mean advection velocity of the two streams was known to within $\pm 2\%$. The uncertainty in the mean advection velocity was the greatest contributor to the uncertainty of the dimensionless time τ [see (2.3)], which was also known to within $\pm 2\%$.

Uncertainties in the mean colored indicator concentration measurements were due to several sources, including the uncertainty in the free-stream concentration of the indicator $w_{[\text{In}]_2}$, the molar absorptivity coefficient w_ε , the light absorption mea-

surement w_σ , and the width of the channel w_{L_y} . Furthermore, uncertainty in the phenolphthalein concentration in the bottom stream was determined by uncertainties in the volume of phenolphthalein added (± 5 ml) and the volume of water in the bottom stream tank (1890 ± 38 liters). Taken together, this gives a relative uncertainty in the concentration of chemical indicator in the bottom stream of $\pm 1.4\%$. The molar absorptivity coefficient from the calibration experiments in § 2.4.2 was determined to have an uncertainty of $\pm 0.67\%$. Finally, uncertainty in the light absorption measurements were due to variations in the background lighting intensity and statistical uncertainty in the estimation of the mean light intensity measured from an ensemble average of ~ 200 images. The root-mean-square amplitude of the background lighting fluctuations was 0.8 intensity units on a scale from 0–255 from the 8-bit CCD. Accordingly, the intensity of the background lighting was steady to within $\pm 0.5\%$. Combining these gives an uncertainty of the measured chemical concentration C of

$$w_C = \pm \sqrt{\left(\frac{\partial C}{\partial \sigma} w_\sigma\right)^2 + \left(\frac{\partial C}{\partial \varepsilon} w_\varepsilon\right)^2 + \left(\frac{\partial C}{\partial L_y} w_{L_y}\right)^2 + \left(\frac{\partial C}{\partial [\text{In}]_2} w_{[\text{In}]_2}\right)^2} = \pm 3\%. \quad (2.33)$$

2.4.4 Measurement of mixing layer growth

As an initial check of the experimental facility and diagnostics, the mixing layer width was measured for the salt/fresh water configuration. Nigrosine dye (5 g) was added to the tank supplying the top stream and the absorption of light was measured using the techniques discussed in § 2.4.2. A sample image from an experiment using the inert dye is shown in figure 2.12, where no discernible differences between the high Schmidt number salt/fresh water mixing layer and moderate Prandtl number hot/cold water mixing layer (see figure 2.2) are visible. The dye absorptivity coefficient was measured using the same Plexiglas wedge and light absorption techniques discussed

in § 2.4.2. Experiments using the dye were then performed and the absorption of the backlighting was related to the mean dye concentration. The mean dye concentration was normalized by the free stream dye concentration and related to the mean heavy fluid (top stream) volume fraction by

$$\bar{f}_1 = \frac{\bar{\rho} - \rho_2}{\rho_1 - \rho_2} = \frac{[\overline{Dye}]}{[Dye]_1}, \quad (2.34)$$

where \bar{f}_1 is a dimensionless measure of the mean density field. Profiles of \bar{f}_1 at several downstream locations are shown in figure 2.13. As expected for small Atwood number Rayleigh–Taylor mixing (Youngs 1984; Snider & Andrews 1994), the growth of the layer is symmetric about $\bar{f}_1 = 0.5$ with approximately linear profiles. The mixing layer width was determined by identifying the 5–95% thresholds from the profiles. The growth parameter $\alpha = 0.085 \pm 0.005$, was obtained by measuring the slope of the half-width of the mixing layer plotted against Agt^2 , as shown in figure 2.14. Ristorcelli and Clark (2004) showed that a measurement of α directly from $h = \alpha Agt^2$ is not independent of additional terms that scale as t^1 and t^0 . The dependence on such additional terms can be minimized by measuring α from the time-derivative $\dot{h}_b = 2\alpha Agt$ instead, where $\dot{h}_b = dh_b/dt$. Thus, as a confirmation, the instantaneous value of $\alpha = \dot{h}_b/(2Agt)$ is also shown in figure 2.14, where a self-similar, asymptotic value $\alpha = 0.086 \pm 0.01$ is measured for $\tau \geq 1.1$. While this measure of α has a larger degree of statistical uncertainty due to the time-derivative of h_b , both values of α are consistent. The growth parameter for the salt/fresh water case is slightly larger than that for the hot/cold water case, where $\alpha = 0.07 \pm 0.011$ (Snider & Andrews 1994). Thus, the increase in α for the salt/fresh water case suggests that the Schmidt number may have only a minor influence on the late time growth rate of the mixing layer.

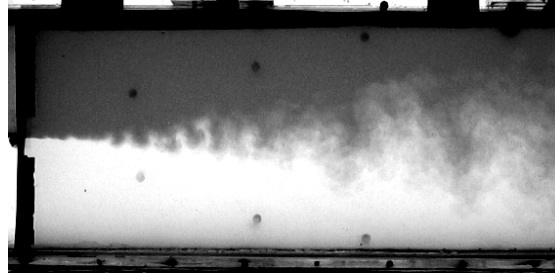


Figure 2.12 Photograph of the buoyancy-generated mixing layer in a typical water channel experiment. Nigrosine dye was added to the top stream (contrast enhanced for visualization).

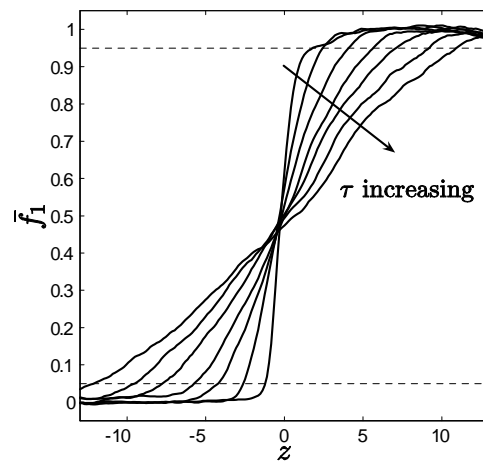


Figure 2.13 Mean volume fraction profiles across the mixing layer at dimensionless times $\tau = 0.25, 0.50, 0.75, 1.00, 1.25,$ and 1.50 . Two fiducials indicating the boundaries of the mixing layer are shown.

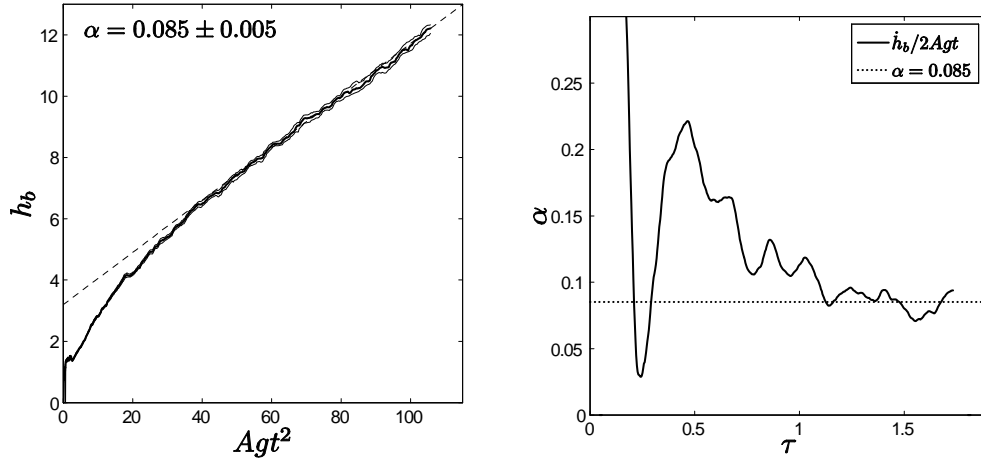


Figure 2.14 Measurement of the mixing layer growth parameter α for the $Sc \sim 10^3$ case. The half-width of the mixing layer is plotted against Agt^2 with 95% confidence interval bounds. An alternative measure of α is obtained by normalizing \dot{h} (right). In both cases, a fiducial is shown for $\alpha = 0.085$ (dashed line).

2.4.5 Measurements of chemical product formation

Using the backlit optical techniques described in § 2.4.2, the average concentration of the colored chemical indicator was measured in a turbulent Rayleigh–Taylor mixing layer. Figure 2.15 shows an image of the layer, where the pink chemical indicator represents regions of mixed fluid. Figure 2.16 shows the profiles of $C = \overline{[In]_{IV}}/[In]_2$ (the concentration of colored indicator normalized by the free stream concentration) for $pH_2 = 7.02$ and $pH_2 = 2.44$. The resulting profiles are approximately parabolic and, as expected, less chemical product is produced in the latter case. By decreasing the pH of the bottom stream, the concentration of H^+ ions is increased, so that the quantity of OH^- ions required to mix with the bottom stream to achieve a color change in the indicator is increased. Therefore, given the same degree of molecular mixing between the two streams, less colored indicator is produced when the pH of the bottom stream is lowered. In the $pH_2 = 7.02$ and $pH_2 = 2.44$ cases, the

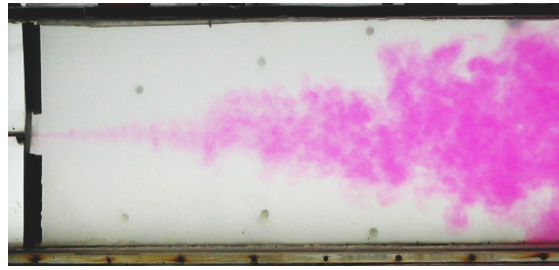


Figure 2.15 Photograph of the buoyancy-generated mixing layer in a typical water channel experiment. Phenolphthalein was added to the bottom stream, which changes to its pink form as the two streams molecularly mix.

measured concentration of the colored indicator increases as the mixing layer grows spatially downstream. This is expected, as the intensity of turbulence increases and the internal structure of the mixing layer becomes more complex with increasing Reynolds numbers. Turbulent fluctuations continuously stretch the interface between pockets of fresh and salt water, which increases the reaction surface area and brings fresh reactants into contact.

Previous researchers found that the quantity of indicator produced is a function of the equivalence ratio φ , and is a measure of balance or excess of reactants. Typically, the equivalence ratio for shear and jet flows is defined for the reaction involving the chemical indicator [see (2.19)] such that

$$\varphi_{\text{In}} = \frac{[\text{In}]/[\text{OH}^-]}{([\text{In}]/[\text{OH}^-])_{st}}, \quad (2.35)$$

where $([\text{In}]/[\text{OH}^-])_{st} = 1/2$ is the stoichiometric ratio of reactants in (2.19). In the limit $\varphi_{\text{In}} \rightarrow 0$, the quantity of colored chemical indicator C produced attains an asymptotic value and is a function only of the degree of molecular mixing between the two fluids (Shea 1977; Breidenthal 1979, 1981; Mungal & Dimotakis 1984; Zhang *et al.* 1995).

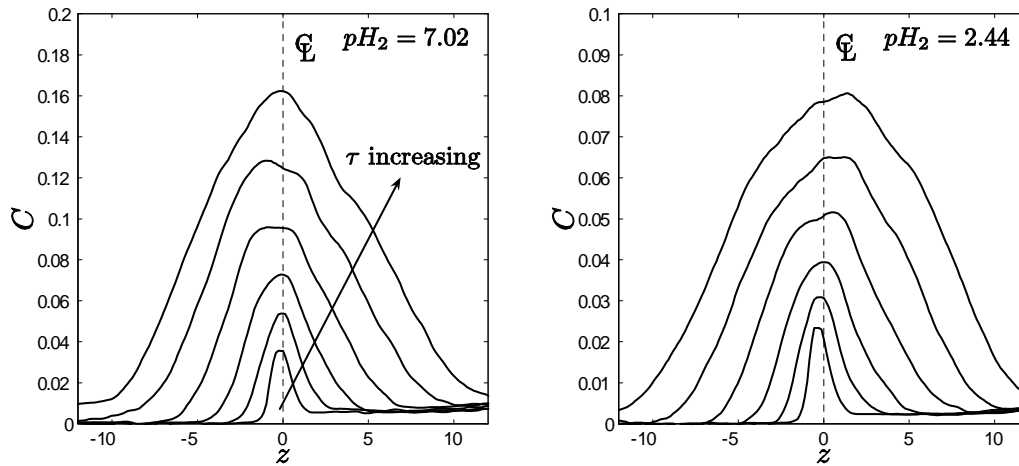


Figure 2.16 Normalized colored indicator concentration profiles across the mixing layer at dimensionless times $\tau = 0.25, 0.50, 0.75, 1.00, 1.25,$ and 1.50 for the $\text{pH}_2 = 7.02$ (left) and $\text{pH}_2 = 2.44$ (right) cases. For both experiments, $\text{pH}_1 = 11.5$.

The equivalence ratio for the indicator reaction neglects the neutralization reaction in (2.17) that occurs as fluid from each stream mixes. Accordingly, φ_{In} does not account for the reduced quantity of indicator formed in the $\text{pH}_2 = 2.44$ experiment. To account for this effect, it is more appropriate to examine the equivalence ratio of the neutralization reaction in (2.17), where

$$\varphi_n = \frac{[\text{H}^+]/[\text{OH}^-]}{([\text{H}^+]/[\text{OH}^-])_{st}} \quad (2.36)$$

and $([\text{OH}^-]/[\text{H}^+])_{st} = 1$ is the stoichiometric ratio of hydroxide and hydrogen ions. The neutralization equivalence ratio φ_n controls the volume fractions of fluid 1 and fluid 2 that must mix to achieve the pH increase required for the indicator to change color. For $\varphi_n \rightarrow 0$, a large excess of OH^- ions exists in the top stream and only a small fraction of fluid 1 must mix with fluid 2 to achieve a significant pH increase and resulting indicator color change. Conversely, for $\varphi_n \rightarrow \infty$, a large excess of H^+ ions exists and an infinite amount of fluid 1 is required to mix with fluid 2 to achieve the

required pH increase. As a result, no indicator will be converted to its colored form. For the pH combination $\text{pH}_1 = 11.5$ and $\text{pH}_2 = 7$, $\varphi_n = 3.2 \times 10^{-5} \ll 1$ and only a small fraction of fluid 1 is required to mix with fluid 2 to achieve a color change. Accordingly, a measure of C for $\varphi_{\text{In}} = 1.8 \times 10^{-3}$ and $\varphi_n = 3.2 \times 10^{-5}$ ($\text{pH}_1 = 11.5$, $\text{pH}_2 = 7$, $[\text{In}]_2 = 6 \times 10^{-6}$) should be insensitive to the exact equivalence ratio and representative of the degree of molecular mixing.

2.4.6 Species diffusivity considerations

In previous works examining high Schmidt number liquid-phase mixing (Breidenthal 1979, 1981; Koochesfahani & Dimotakis 1986; Linden *et al.* 1994; Zhang *et al.* 1995), acid-base neutralization reactions coupled with pH-sensitive chemical indicators quantified the degree of molecular mixing. While it is customary to estimate $Sc \sim 10^3$ in liquid-phase mixing, each specific molecule or ion within the mixture diffuses at a different rate. Table 2.2 lists the diffusivities of the species and their respective Schmidt numbers for the current experiments. It is important to note that the neutralization reaction front will precede the indicator reaction front because of the relatively high diffusivities of H^+ and OH^- . Accordingly, the total quantity of colored indicator is not limited by the diffusivities of the H^+ and OH^- ions. Larger ions (such as those of sodium and chloride) have lower mobilities, resulting in an effective Schmidt number $Sc_{\text{NaCl}} = \nu/D_{\text{NaCl}} = 620$ (Lide 2006). The diffusivity of phenolphthalein was measured by Desai and Vadgama (1991) and give an indicator Schmidt number $Sc_{\text{In}} = \nu/D_{\text{In}} = 1200$. Due to the difference in Sc_{NaCl} and Sc_{In} , the nominal Schmidt number of the experiments reported here is considered as $Sc \sim 10^3$.

An experiment was performed using a temperature increase in the bottom fluid stream ($\Delta T \approx 5$ °C) to create a density difference in order to demonstrate that the diffusivity of the chemical indicator determines the nominal Schmidt number

	D [cm ² /s]	Sc
Na ⁺	1.334×10^{-5}	750
Cl ⁻	2.032×10^{-5}	492
NaCl	1.611×10^{-5}	620
H ⁺	9.311×10^{-5}	107
OH ⁻	5.273×10^{-5}	190
Phenolphthalein	8.3×10^{-6}	1200

Table 2.2 Ion and phenolphthalein diffusivities in water (Desai & Vadgama 1991; Lide 2006).

of the experiment. For this reference experiment, the pH of each stream was set to $\text{pH}_1 \approx 11.5$ and $\text{pH}_2 \approx 7$ to match φ_{In} and φ_n of the baseline salt/fresh water experiments. No salt was added to the top stream, and thus the temperature of the water becomes a marker for the density field through an equation of state (Kukulka 1981). In this arrangement, the nominal Schmidt number of the scalar marking the density field is $Pr = 7 \equiv Sc$; however, the Schmidt number for the chemical indicator remains unchanged at $Sc_{\text{In}} = 1200$. Measurements of the colored indicator concentration for this hot/cold water case are shown in figure 2.17. These profiles indicate that similar amounts of colored chemical product are produced, despite the increased scalar diffusivity and presumably increased amount of mixed fluid within the layer. This experiment demonstrates that the diffusivity of the indicator limits its use to flows where the diffusivities of the scalar marking the density field are similar to the diffusivity of the indicator. It will be shown in § 2.4.10 that a factor of 10 difference in Schmidt numbers results in only a small change in the measurement of the molecular mixing parameter θ , and thus, a factor of two difference in the Schmidt numbers of salt and phenolphthalein is negligible.

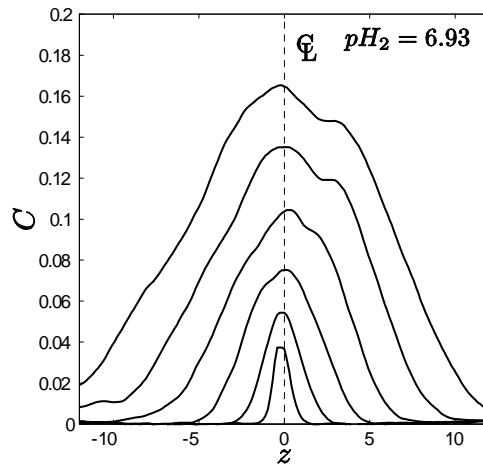


Figure 2.17 Normalized colored indicator concentration profiles across the mixing layer at $\tau = 0.25, 0.50, 0.75, 1.00, 1.25,$ and 1.50 for the hot/cold water case.

While the results in figure 2.17 demonstrate that the diffusivity of the scalar associated with the density field has a negligible effect on the production of colored indicator, another concern exists due to the diffusivities of hydrogen and hydroxide ions. As H^+ and OH^- ions diffuse down their respective concentration gradients at the interface between pure heavy and light fluids, the local pH on each side of the interface is altered. If the pH on the acidic side of the interface is sufficiently elevated, a color change in the chemical indicator may be induced. This effect is independent of the indicator Schmidt number, and may even occur when $Sc_{in} = \infty$. This effect has not been documented in any of the previous molecular mixing studies that use pH-sensitive chemical indicators to study high Schmidt number mixing (Breidenthal 1979, 1981; Koochesfahani & Dimotakis 1986; Corriveau & Baines 1993; Linden et al. 1994; Zhang et al. 1995; Karasso & Mungal 1996; Kastrinakis & Nychas 1998). It is believed that the production of colored indicator by this effect is small due to the continuous straining of the ion concentration gradients by three-dimensional

turbulent fluctuations; however, no means of quantifying the experimental bias has been developed and is recommended for future work.

2.4.7 Product thickness integrals

An integral measure quantifying the amount of chemical product formed (and representing the fraction of the mixing layer occupied by the colored indicator) is the equivalent product thickness

$$\frac{P}{h} = \frac{1}{h} \int_{h_s}^{h_b} \frac{[\text{In}_{IV}]}{[\text{In}]_2} dz, \quad (2.37)$$

which is analogous to P/δ for shear flows (Konrad 1977; Breidenthal 1979, 1981). For all experiments that used salt to create a density difference, a correction to (2.37) was applied to account for the absorption of light by the salt water from the measurement of P :

$$\frac{P}{h} = \frac{1}{h} \left[\int_{h_s}^{h_b} \frac{[\text{In}_{IV}]}{[\text{In}]_2} dz - \frac{h}{2} \xi \right], \quad (2.38)$$

where $\xi \approx 0.0075$ is the value of C measured outside the mixing layer in the salt water stream.

To validate the diagnostic techniques described in § 2.4.2, the water channel was used to create a reacting, turbulent shear layer similar to the flow created by Breidenthal (1979, 1981). The pH of each stream was set to $\text{pH}_1 = 11.73$ and $\text{pH}_2 = 7.04$ to match Breidenthal's conditions. The indicator concentration was set to $[\text{In}]_2 = 5 \times 10^{-6}$ M, whereas Breidenthal used $[\text{In}]_2 = 1 \times 10^{-5}$ M. The indicator concentration in the current experiments was lowered to keep the diagnostics in the linear range of the calibration. Salt was also added to the bottom stream as necessary to balance the increased density of the top stream due to the addition of NaOH, so that $\rho_1 = \rho_2$. The velocities of the top and bottom streams in the channel

were adjusted to $U_1 = 5.8$ and $U_2 = 3.5$ cm/s, respectively, giving a velocity ratio $r = U_2/U_1 = 0.61$. While Breidenthal reported results for $r = 0.38$ – 0.80 , the absolute velocities of each stream were much larger than those used in the current water channel. In Breidenthal’s work, the high speed stream was $U_1 = 300$ cm/s, with a resulting low speed stream velocity $U_2 = rU_1$. In addition, Breidenthal’s facility used a series of flow straighteners and meshes, and included a large cross-sectional area contraction to minimize boundary layers on the splitter plate and adjustable side walls to account for streamwise pressure gradients. The current water channel experiments also use a series of flow-straighteners and screen meshes to control boundary layers on the splitter plate, but no contraction was implemented. Due to differences in facility designs and flow velocities, the initial conditions for each experiment are not identical. Breidenthal reported that P/δ is a non-unique function of Reynolds number for $Re_\delta < 8000$. This was attributed to the observation that early-time, two-dimensional vorticity dynamics of the mixing layer was controlled by the initial vorticity in the high-speed fluid boundary layer. Remnants of initial conditions affected the value of P/δ until the mixing layer had completely transitioned to a fully-developed, three-dimensional state. Thus, slightly different initial conditions resulted in different measures of P/δ before the asymptotic value $P/\delta \approx 0.365$ for $Re_\delta > 8000$ was reached.

Figure 2.18 shows a comparison of P/δ for $r = 0.62$ and $r = 0.76$ from Breidenthal (1979) and a corresponding shear layer experiment conducted in the water channel as a function of shear layer Reynolds number $Re_\delta = \Delta U \delta/\nu$, where $\delta = \Delta U/(\partial u/\partial z)_{max}$ is the width (vorticity thickness) of the shear layer. In the absence of velocity measurements to obtain δ directly, the width of the shear layer was determined visually from the measured indicator concentration profiles. The visual width of the mixing layer is related to the vorticity thickness by $\delta_{vis}/\delta = 2.1$ (Brown & Roshko 1974; Koochesfahani & Dimotakis 1986). The water channel Reynolds numbers were lim-

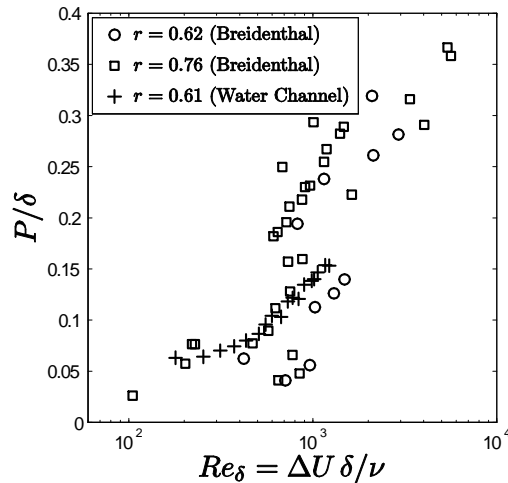


Figure 2.18 Equivalent chemical product thickness, P/δ , for the case of a liquid-phase, turbulent shear layer.

ited to $Re_\delta < 2000$. Thus, the asymptotic value of $P/\delta \rightarrow 0.365$ for $Re_\delta > 8000$ observed by Breidenthal could not be reproduced in the channel; however, over the range of comparable Reynolds numbers shown in figure 2.18, the measurements of P/δ are within the scatter of Breidenthal's results for comparable velocity ratios.

A measurement of the relative product thickness for the Rayleigh–Taylor case, denoted P/h , is shown in figure 2.19. For Rayleigh–Taylor mixing layers, any Reynolds number definition relies upon a choice of an integral-scale velocity and length. This work adopts $Re_h = 0.35\sqrt{Ag\bar{h}^3}/\nu$ (Ramaprabhu & Andrews 2004a), where the mixing layer width (5–95% volume fraction thresholds used) is the length-scale, and the terminal velocity of the dominant bubble is the velocity-scale. It is difficult to directly compare shear-driven mixing layers with the buoyancy-driven case due to the difference in Reynolds number definitions. For Rayleigh–Taylor mixing layers, the visual width of the layer defined the integral length scale that in-turn was used to define h , and hence P/h and Re_h . Thus, for comparison purposes in figure 2.19, the shear

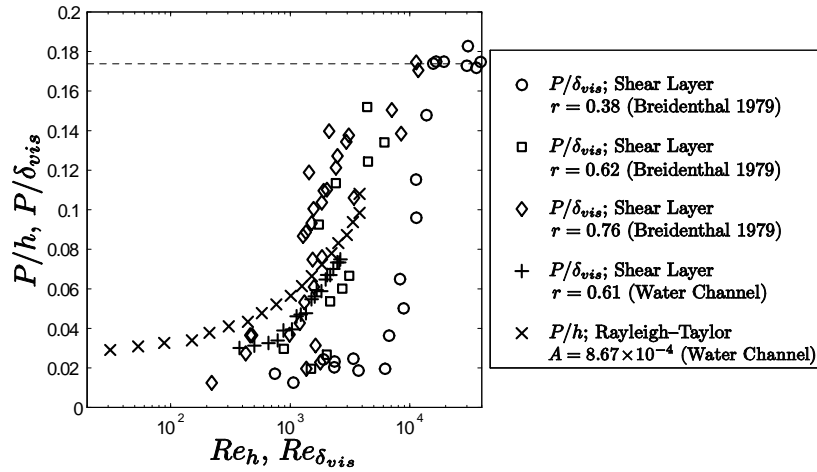


Figure 2.19 Equivalent product thickness measurements for a liquid-phase buoyancy-driven mixing layer, P/h , and shear-driven mixing layers, P/δ , at various velocity ratios r . Outer-scale Reynolds numbers are $Re_h = 0.35\sqrt{Agh^3}/\nu$ for the Rayleigh–Taylor case and $Re_{\delta_{vis}} = \Delta U \delta_{vis}/\nu$ for the shear case.

layer Reynolds numbers and product thicknesses have been defined using δ_{vis} instead of δ . For the shear layer cases in figure 2.19, it is evident that the time at which a significant rise in P/δ_{vis} occurs is a function of the Reynolds number, velocity ratio, and initial conditions. While the Reynolds number definitions are not completely equivalent for the buoyancy- and shear-driven cases, their comparison in figure 2.19 shows that the buoyancy-driven case exhibits an increasing trend in P/h , indicative of the onset of turbulence and a mixing transition at similar Reynolds numbers as the shear-driven case. However, higher Reynolds number experiments are needed to determine if buoyancy-driven turbulent mixing is capable of producing larger quantities of chemical product, and if P/h attains an asymptotic value. Extrapolation from the shear-driven experiments suggests that an asymptotic behavior of P/h may not be seen in Rayleigh–Taylor mixing until $Re_h \approx 8000$ – 10000 , necessitating a different

experimental facility for investigating asymptotic $Sc \sim 10^3$ mixing.

2.4.8 Measurements of product formation mixing parameter

The backlit optical technique described in § 2.4.2 provided measurements of the average concentration of colored indicator $\overline{[\text{In}_{IV}]}$ given two streams at pH_1 and pH_2 . While these measurements of chemical product formation are a function of the degree of molecular mixing at small equivalence ratios, it is desirable to relate C to more convenient measures of molecular mixing. In this section, the measured passive scalar and reacting scalar concentration field, \bar{f}_1 and C respectively, will be used to compute several parameters that quantify mixing.

The measured indicator concentration profiles can be used to compute integral measures of the total quantity of chemical product formed, such as P/h . However, such a measure does not indicate the maximum quantity of chemical product that may be formed for the same equivalence ratio. Koochesfahani and Dimotakis (1986) quantified the degree of mixing in a reacting shear layer by normalizing the amount of product formed by the maximum product that could be formed if the two fluids homogeneously mixed. Cook and Dimotakis (2001) extended this concept to define an integral mixing parameter

$$\Xi(\varphi_{\text{In}}) = \frac{\int_{h_s}^{h_b} \overline{[\text{In}_{IV}]} dz}{\int_{h_s}^{h_b} \overline{[\text{In}_{IV}]}_{max} dz}, \quad (2.39)$$

where $\overline{[\text{In}_{IV}]}_{max}$ is the maximum chemical product that can be produced if all fluid within the mixing layer was homogeneously mixed at a set equivalence ratio φ_{In} . This parameter is defined such that $\Xi = 0$ if no product is produced (*i.e.* the constituent fluids are completely segregated). Conversely, $\Xi = 1$ if all potential product has been produced (*i.e.* the mixing layer is homogeneously mixed). For the two-fluid case

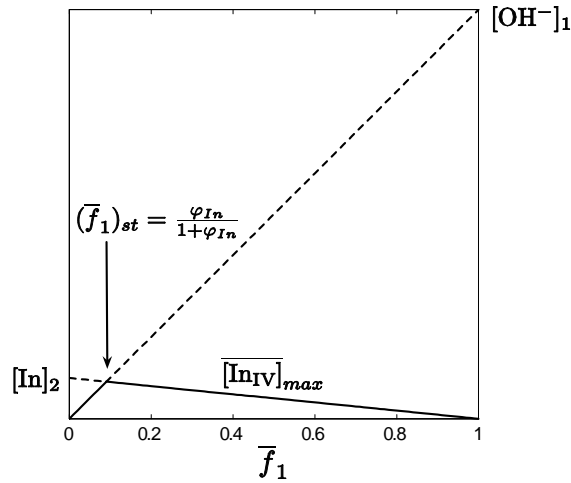


Figure 2.20 Schematic of $[\text{In}_{IV}]$ formation as a function of \bar{f}_1 and the equivalence ratio φ_{In} . The maximum product formed occurs when the stoichiometric ratio of reactants are available at $(\bar{f}_1)_{st} = \varphi_{\text{In}}/(1 + \varphi_{\text{In}})$.

(where $\bar{f}_1 + \bar{f}_2 = 1$), $[\text{In}_{IV}]_{max}$ depends upon the lean reactant such that

$$[\text{In}_{IV}]_{max} = \begin{cases} \bar{f}_1[\text{OH}^-]_1 & \bar{f}_1 \leq (\bar{f}_1)_{st} ; \\ (1 - \bar{f}_1)[\text{In}]_2 & \bar{f}_1 > (\bar{f}_1)_{st} , \end{cases} \quad (2.40)$$

where

$$(\bar{f}_1)_{st} = \frac{\varphi_{\text{In}}}{1 + \varphi_{\text{In}}} . \quad (2.41)$$

is the stoichiometric volume fraction of fluid 1 required to achieve a stoichiometric reaction, *i.e.* all reactants in (2.17) are entirely consumed. An illustration of the maximum product produced for a given equivalence ratio is shown in figure 2.20. The global mixing parameter Ξ is shown in figure 2.27, where it is compared with the global mixing parameter Θ defined in § 2.4.10.

2.4.9 *Relationship between chemical product formation measurements and fluctuating density statistics*

Measurements of the relative quantity of chemical product formed (given by Ξ) are dependent upon the equivalence ratio φ_{In} . An alternative description of molecular mixing is given by a combination of the mean and fluctuating density statistics, which are independent of the equivalence ratio. The mean density and density variance can be combined to form a molecular mixing parameter θ , which is defined in § 2.3.2.

The formation of colored chemical product can be related to the volume fraction variance $\overline{f_2'^2}$, or more specifically, the second moment of the volume fraction probability density function (PDF), where $\overline{f_2^2} = (\bar{f}_2)^2 + \overline{f_2'^2}$. Given a mixture with varying density (such as within a Rayleigh–Taylor mixing layer), the probability of finding a given fraction of fluid r is quantified by the PDF of the volume fraction fluctuations $P(f_2)$. Using $P(f_2)$, the quantity of chemical indicator and fraction of colored indicator within the mixing layer can be expressed as functions of the local fluid composition, *i.e.* the PDF of f_2 . As noted earlier, fluid 1 is the heavier fluid with a $\text{pH} > 7$ (alkali) and fluid 2 is the lighter fluid with $\text{pH} \leq 7$ (acidic or neutral) with a dilute amount of phenolphthalein added. Accordingly, the average concentration of indicator present within the mixing layer depends upon the indicator concentration in the lighter fluid (bottom stream) $[\text{In}]_2$ and \bar{f}_2 , which is equivalent to the first moment of $P(f_2)$,

$$\overline{[\text{In}]} = [\text{In}]_2 \int_0^1 f_2 P(f_2) \, df_2. \quad (2.42)$$

The total amount of indicator that is in its colored form depends on both the fraction of fluid 2 present and the fraction of dissociation α_{InIV} [see (2.27)]. Similar to (2.42),

the concentration of colored indicator is expressed as

$$\overline{[\text{In}_{IV}]} = [\text{In}]_2 \int_0^1 \alpha_{\text{In}_{IV}}(\text{pH}) f_2 P(f_2) \, df_2. \quad (2.43)$$

Consequently, $C = [\text{In}_{IV}]/[\text{In}]_2$ can be expressed as a function of the local composition of the mixed fluid, or $P(f_2)$. To relate C and $\overline{f_2^2}$, the integral on the right-hand side of (2.43) requires further evaluation.

While the right-hand side of (2.43) cannot be analytically evaluated, an approximation for $\alpha_{\text{In}_{IV}}$ can be obtained to allow an analytical treatment. If pH_1 is taken to be sufficiently large ($\text{pH}_1 \approx 11.5$ here), then $\alpha_{\text{In}_{IV}}$ becomes a function only of the local composition of the fluid, defined by f_1 , f_2 , and pH_2 . Only two-fluid systems are considered here, so that $\alpha_{\text{In}_{IV}}$ is a function of only f_2 and pH_2 . As pH_2 is decreased, a larger quantity of OH^- ions from the top stream is required [see φ_n in (2.36)], and hence a greater value of f_1 , to mix with the bottom stream to achieve the same rise in pH and indicator color change. Figure 2.21 shows $\alpha_{\text{In}_{IV}}(f_2, \text{pH}_2)$ as a function of local volume fraction f_2 with pH_2 as a parameter. The fraction of dissociation is then approximated by a step function

$$\alpha_{\text{In}_{IV}}(f_2, f_2^{50\%}) = \begin{cases} \alpha_{\text{In}_{IV}}^{max} = \alpha_{\text{In}_{IV}}(\text{pH} = 11.5) = 0.96 & f_2 \leq f_2^{50\%}; \\ 0 & f_2 > f_2^{50\%}, \end{cases} \quad (2.44)$$

where $f_2^{50\%}$ is the f_2 value where half of the indicator exists in its colored form, *i.e.* $\alpha_{\text{In}_{IV}} = 0.5$, for a specified pH_1/pH_2 combination. Note that $\alpha_{\text{In}_{IV}}^{max} = 0.96$ because $\alpha_{\text{In}_{IV}}$ does not attain unity at its maximum.

Substituting (2.44) into (2.43) allows the integral to be split into two parts and

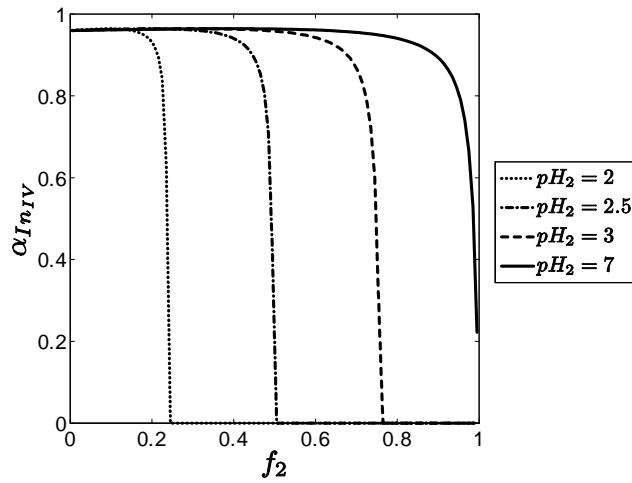


Figure 2.21 Fraction of dissociation for In_{IV} as a function of the volume fraction f_2 and pH_2 of the acidic stream.

simplified:

$$\begin{aligned}
 C(f_2^{50\%}) &= \int_0^{f_2^{50\%}} \alpha_{\text{In}_{IV}}(f_2, f_2^{50\%}) f_2 P(f_2) df_2 \\
 &\quad + \int_{f_2^{50\%}}^1 \alpha_{\text{In}_{IV}}(f_2, f_2^{50\%}) f_2 P(f_2) df_2 \\
 &= \alpha_{\text{In}_{IV}}^{\text{max}} \int_0^{f_2^{50\%}} f_2 P(f_2) df_2.
 \end{aligned} \tag{2.45}$$

Integrating over all values of $f_2^{50\%}$ gives

$$\frac{1}{\alpha_{\text{In}_{IV}}^{\text{max}}} \int_0^1 C(f_2^{50\%}) df_2^{50\%} = \int_0^1 \left\{ \int_0^{f_2^{50\%}} f_2 P(f_2) df_2 \right\} df_2^{50\%}. \tag{2.46}$$

Changing the order of integration on the right-hand side gives

$$\begin{aligned}
\frac{1}{\alpha_{\text{InIV}}^{\text{max}}} \int_0^1 C(f_2^{50\%}) \, df_2^{50\%} &= \int_0^1 \left\{ \int_{f_2}^1 f_2 P(f_2) \, df_2^{50\%} \right\} \, df_2 \\
&= \int_0^1 f_2 P(f_2) \left\{ f_2^{50\%} \Big|_{f_2}^1 \right\} \, df_2 \\
&= \int_0^1 (1 - f_2) f_2 P(f_2) \, df_2
\end{aligned} \tag{2.47}$$

and evaluating the remaining outer integral gives

$$\frac{1}{\alpha_{\text{InIV}}^{\text{max}}} \int_0^1 C(f_2^{50\%}) \, df_2^{50\%} = \bar{f}_2 - \overline{f_2^2}. \tag{2.48}$$

Since $\overline{f_2^2} = (\bar{f}_2)^2 + \overline{f_2'^2}$, the volume fraction variance becomes

$$\overline{f_2'^2} = \bar{f}_1 \bar{f}_2 - \frac{1}{\alpha_{\text{InIV}}^{\text{max}}} \int_0^1 C(f_2^{50\%}) \, df_2^{50\%}, \tag{2.49}$$

and the degree of molecular mixing becomes

$$\theta = 1 - \frac{\overline{f_1'^2}}{\bar{f}_1 \bar{f}_2} = \frac{\int_0^1 C(f_2^{50\%}) \, df_2^{50\%}}{\alpha_{\text{InIV}}^{\text{max}} \bar{f}_1 \bar{f}_2}. \tag{2.50}$$

At the centerplane of the mixing layer, $\bar{f}_1 = \bar{f}_2 = 1/2$, and θ reduces to

$$\theta = \frac{4}{\alpha_{\text{InIV}}^{\text{max}}} \int_0^1 C(f_2^{50\%}) \, df_2^{50\%}. \tag{2.51}$$

The integral of $C(f_2^{50\%})$ over $0 \leq f_2^{50\%} \leq 1$ in (2.49) may be physically interpreted as a sum of the chemical product produced given all possible equivalence ratios. Before this integral is evaluated for the flow considered here, several considerations regarding the bounding values of $C(f_2^{50\%})$ at $f_2^{50\%} = 0$ and $f_2^{50\%} = 1$ are discussed. For highly acidic streams, $[\text{H}^+]_2 \rightarrow \infty$ or $f_2^{50\%} \rightarrow 0$, and thus, no chemical indicator will exist in its colored form, *i.e.* $C(f_2^{50\%} = 0) = 0$. For the case of $\text{pH}_1 = \text{pH}_2 = 11.5$, no fluid from the top stream is required to mix with the bottom stream to achieve a color

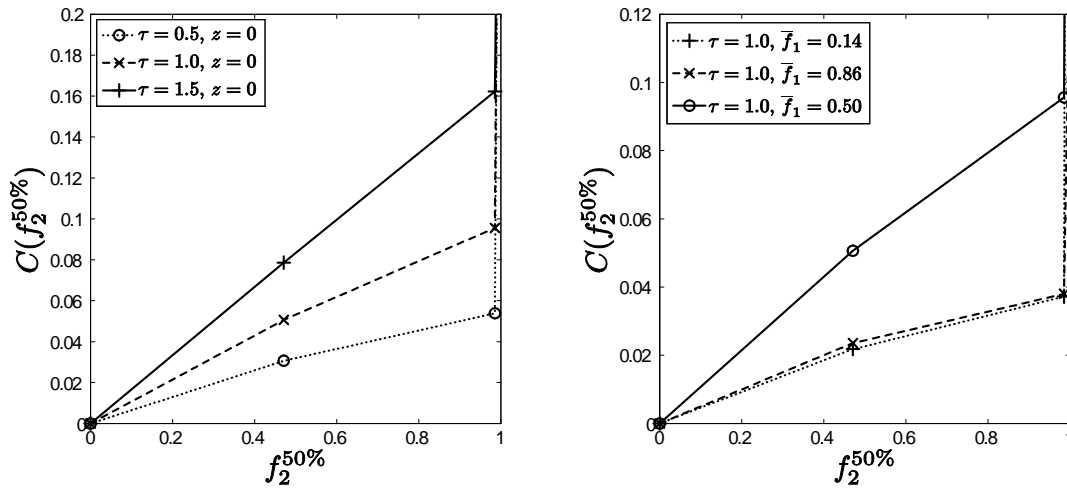


Figure 2.22 Values of colored indicator concentration C for $f_2^{50\%}=0.471$ (left: $\text{pH}_1 = 11.52$ and $\text{pH}_2 = 2.44$) and $f_2^{50\%}=0.471$ (right: $\text{pH}_1 = 11.48$ and $\text{pH}_2 = 7.02$) at different downstream locations.

change. Then, the chemical indicator acts as a passive scalar, such that

$$\begin{aligned} \overline{[\text{In}_{IV}]} &= [\text{In}]_2 \int_0^1 \alpha_{\text{In}_{IV}}(\text{pH}) f_2 P(f_2) df_2 \\ &= \alpha_{\text{In}_{IV}}^{\text{max}} [\text{In}]_2 \bar{f}_2. \end{aligned} \quad (2.52)$$

Thus, the two bounding values $C(f_2^{50\%} = 0)$ and $C(f_2^{50\%} = 1) = \alpha_{\text{In}_{IV}}^{\text{max}} \bar{f}_2$ are known *a priori*. To approximate the integral of $C(f_2^{50\%})$, the amount of colored product was measured for $\text{pH}_2 = 7.02$ and $\text{pH}_2 = 2.44$. Keeping $\text{pH}_1 \approx 11.5$, this gave $f_2^{50\%} = 0.986$ and $f_2^{50\%} = 0.471$, respectively. Several curves of $C(f_2^{50\%})$ are shown for various evolution times in figure 2.22, using the chemical product measurements shown in figure 2.16.

2.4.10 Measurement of molecular mixing parameters

The terms on the right-hand side of (2.49), which include mean volume fraction and mean chemical indicator product profiles, have been measured and are shown

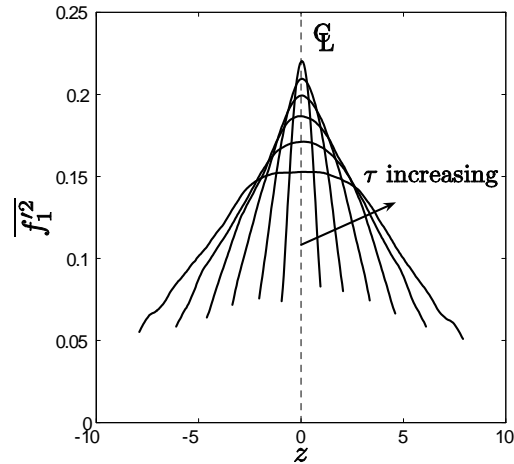


Figure 2.23 Profiles of $\overline{f_1'^2}$ across the mixing layer at dimensionless times $\tau = 0.25, 0.50, 0.75, 1.00, 1.25,$ and 1.50 .

in figures 2.13, 2.16, and 2.22. Combining these measured concentration profiles according to (2.49) provides a measure of the volume fraction variance profiles shown in figure 2.23 across the mixing layer from $\bar{f}_1 = 0.1$ to $\bar{f}_2 = 0.9$. The 10–90% volume fraction boundaries were used because measurements near the edges of the mixing layer are not converged due to a high degree of intermittency. The profiles in figure 2.23 are approximately parabolic in shape with peaks at the centerplane of the mixing layer. The magnitude of $\overline{f_1'^2}$ on the centerplane ($z = 0$) has bounding values of 0 (perfectly mixed) and 0.25 (perfectly segregated). As the mixing layer grows, $\overline{f_1'^2}(z = 0)$ decreases in time, moving away from the immiscible limiting value of 0.25, which indicates that a greater quantity of mixed fluid exists at later times.

The profiles of $\overline{f_1'^2}$ alone do not quantify the relative degree of molecular mixing, but such a measure is given by θ [see (2.1)]. To obtain profiles of θ , the volume fraction fluctuations (shown in figure 2.23) are combined with the mean volume fraction profiles (shown in figure 2.13) according to (2.49). Profiles of θ across the mixing layer

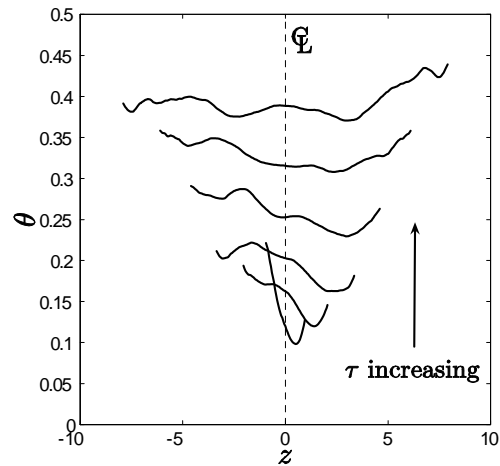


Figure 2.24 Profiles of θ across the mixing layer at dimensionless times $\tau = 0.25, 0.50, 0.75, 1.00, 1.25,$ and 1.50 .

are shown in figure 2.24 plotted between the 10–90% volume fraction thresholds. For the small Atwood number case considered here, the profiles of θ are expected to be approximately constant across the mixing layer, as found in experiments (Wilson & Andrews 2002) and in numerical simulations (Youngs 1994; Ristorcelli & Clark 2004). Indeed, the measured profiles of θ in figure 2.24 are approximately flat at later times across most of the mixing layer, and no conclusions can be drawn from the oscillations near the boundaries of the mixing layer because of increased uncertainty due to intermittency effects away from the centerplane.

Uncertainties in $\overline{f_1'^2}$ and θ are given by a combination of the uncertainties in the mean volume fraction and indicator concentration measurements. Uncertainties in the mean Nigrosine dye concentration measurements [as a result of (2.33)] contribute to uncertainties in the measured profiles of \bar{f}_1 and \bar{f}_2 . Similarly, uncertainties in the mean chemical indicator concentration profiles contribute to uncertainties in the integral of (2.48). Combined, the relative uncertainty in $\overline{f_1'^2}$ is less than $\pm 5\%$ within the core

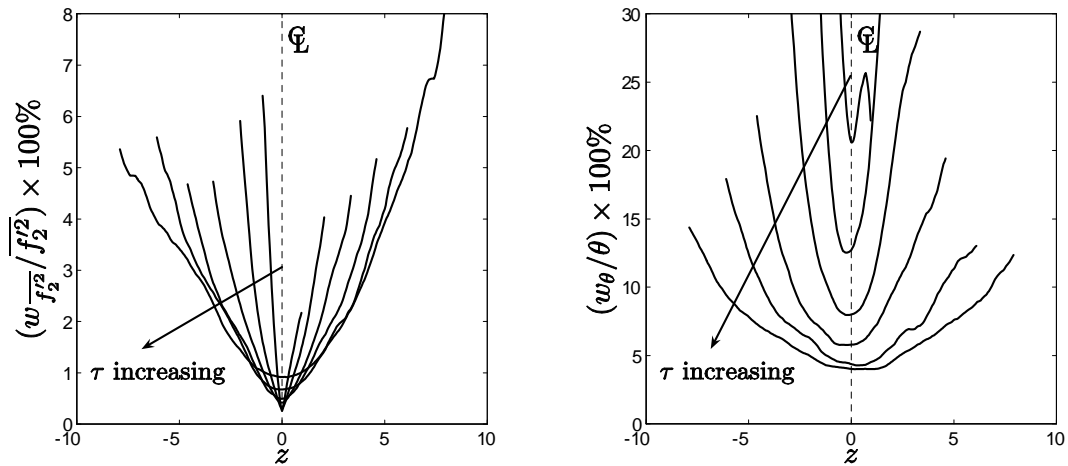


Figure 2.25 Relative uncertainties in the $\overline{f_1'^2}$ (left) and θ (right) profiles at dimensionless times $\tau = 0.25, 0.50, 0.75, 1.00, 1.25,$ and 1.50 .

of the mixing layer. However, the statistical uncertainty in the $\overline{f_1'^2}$ measurements increases near the mixing layer boundaries due to a greater degree of intermittency. Combining the uncertainties in the mean and fluctuating volume fraction statistics gives a relative measure of the uncertainty in the measurement of θ . Along the mixing layer centerplane, the absolute uncertainty in θ remains relatively unchanged for all times measured ($0.1 < \tau < 1.9$) at approximately $w_{\theta} \pm 0.015$. While this is a modest absolute uncertainty, the relative uncertainty is large at early times due to the small values of θ . Away from the centerplane, the uncertainty estimates in θ increase to $w_{\theta} \approx \pm 0.05$. Profiles of the relative uncertainties for $\overline{f_1'^2}$ and θ are shown in figure 2.25.

Measurements of θ on the centerplane ($z = 0$) of the mixing layer have been reported in previous water channel experiments (Wilson & Andrews 2002; Ramaprabhu & Andrews 2004; Mueschke *et al.* 2006) and in gas channel experiments (Banerjee *et al.* 2007). The current centerplane measurements of θ are plotted in figure 2.26 with measurements from the gas channel where $Sc = 0.7$ (Banerjee *et al.* 2008), and the

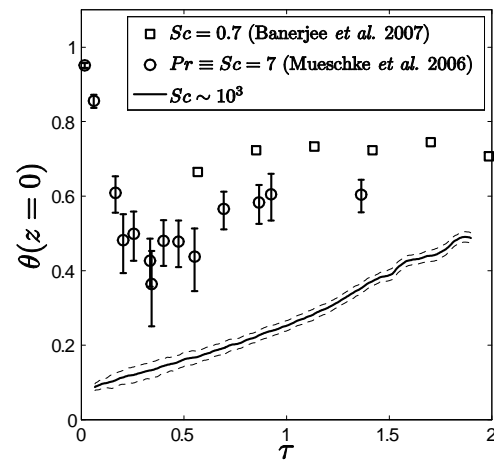


Figure 2.26 Evolution of θ on the centerplane of the mixing layer for various Schmidt numbers. Uncertainty bounds for the $Sc \sim 10^3$ measurements are indicated by the dashed lines. Measurements for the $Sc = 0.7$ case are taken from Banerjee *et al.* (2008), and measurements for the $Pr \equiv Sc = 7$ case are taken from Mueschke *et al.* (2006).

water channel for the hot/cold water case where $Pr \equiv Sc = 7$ (Mueschke *et al.* 2006). Inspection of figure 2.26 reveals that a factor of ten difference in Schmidt/Prandtl numbers between the water and gas channel experiments gives a small difference in θ over $0.5 < \tau < 1.5$. However, comparison of the moderate Schmidt number $Sc \sim 1$ results with the new $Sc \sim 10^3$ measurements results in a much larger and distinct difference. In particular, the minimum value of $\theta \approx 0.4$ was measured in the hot/cold water experiments at $\tau = 0.4$ before the mixing layer had transitioned to a fully three-dimensional, turbulent state. A similar value of $\theta \approx 0.4$ was only measured in the salt/fresh water experiments when the mixing layer reached $Re_h \approx 2000$ at $\tau = 1.5$. At the latest time measured ($\tau = 1.9$) $\theta \approx 0.5$, which begins to approach the late-time values of θ measured in the water channel. Thus, the current Rayleigh–Taylor measurements are similar to shear layer results (Konrad 1977; Breidenthal 1979, 1981), which indicates that the Schmidt number has a smaller effect on the degree of molecular mixing at higher Reynolds number.

Youngs (1994) introduced a global measure of mixing

$$\Theta = \frac{\int_{h_s}^{h_b} \overline{f_1 f_2} dz}{\int_{h_s}^{h_b} \overline{f_1} \overline{f_2} dz} = 1 - \frac{\int_{h_s}^{h_b} \overline{f_1'^2} dz}{\int_{h_s}^{h_b} \overline{f_1} \overline{f_2} dz} \quad (2.53)$$

which is analogous to the mixing parameter Ξ defined in § 2.4.8. As for θ and Ξ , $\Theta = 0$ when the two fluids are completely segregated, and $\Theta = 1$ when the two fluids are perfectly mixed. The mixing progress variables $\Xi(\varphi_{\text{In}} \rightarrow 0)$ and Θ were obtained from the present salt/fresh water experiments by integrating across the 10–90% volume fraction thresholds. The evolution of Ξ and Θ is shown in figure 2.27. For $\tau < 0.4$, $\Xi < 0.06$ and $\Theta < 0.15$, indicating that the majority of the fluid within the mixing layer exists as pockets of pure fluid that are stirred, but not molecularly mixed. Just as with the evolution of θ shown in figure 2.26, both parameters increase and

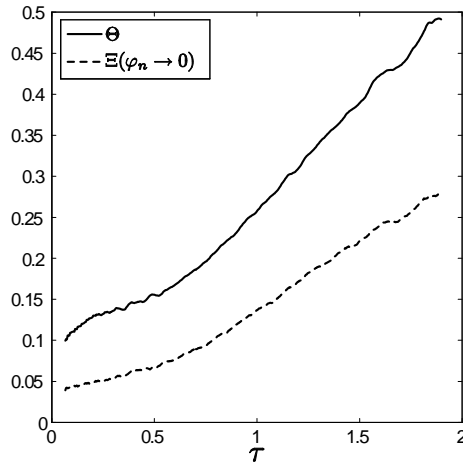


Figure 2.27 Evolution of the global mixing parameters Θ and Ξ for the $Sc \sim 10^3$ case.

reach late-time values $\Xi \approx 0.28$ and $\Theta \approx 0.5$, but neither appear to attain asymptotic values by $\tau = 1.9$. In comparison, Ramaprabhu *et al.* (2005) reported late-time values $\Theta \approx 0.7$ – 0.8 using monotone-integrated large-eddy simulations (MILES) to examine the influence of initial conditions on molecular mixing. Using a large-eddy simulation, Cook *et al.* (2004) obtained $\Theta \approx 0.78$ for a moderate Atwood number ($A = 0.5$), $Sc = 1$ mixing layer. Thus, it is unclear whether θ or Θ in the $Sc \sim 10^3$ case reach the same asymptotic values measured in $Sc \sim 1$ experiments.

As shown in figure 2.19, the relative fraction of chemical product formed remains small until the onset of a fully-turbulent regime, or equivalently, the Reynolds number attains sufficient magnitude. This effect can be seen clearly in figure 2.27, where a transition in the slopes of Θ and Ξ occurs at $\tau \approx 0.5$. Before this transition point, both Θ and Ξ exhibit shallow, approximately linear slopes. Following this transition ($\tau > 0.5$) the slopes of Θ and Ξ increase, indicating that the production rate of mixed fluid has increased. The weak effect of the Reynolds number before $\tau \approx 0.5$ is because the mixing layer contains little three-dimensional structure and is in a weakly

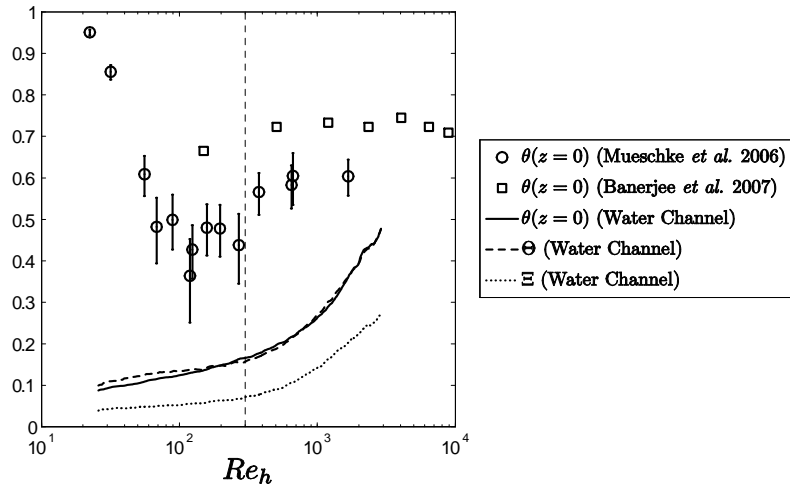


Figure 2.28 Evolution of mixing parameters as a function of Reynolds number $Re_h = 0.35\sqrt{Agh^3}/\nu$. A fiducial is indicated at $Re_h = 300$ indicating the onset of nonlinear, transitional dynamics.

nonlinear regime. However, as the bandwidths of velocity and spatial scales increase, stretching of the interface between the two fluids increases both the surface area and concentration gradients driving molecular diffusion. This Reynolds number effect on θ , Θ , and Ξ is shown more clearly in figure 2.28. As functions of Re_h , it is evident in figure 2.28 that the centerplane evolution of θ also exhibits the transition in slope at $\tau \approx 0.5$, corresponding to an integral-scale Reynolds number $Re_h \approx 300$. Before this Reynolds number threshold, the $Sc \sim 10^3$ mixing layer exists in a ‘stirred’ state with little molecular mixing. Beyond $Re_h \approx 300$, the production rate of mixed fluid increases.

As seen in the shear layer results of Konrad (1977) and Breidenthal (1979, 1981), a second transition is expected in the large Reynolds number limit, when each mixing parameter is expected to asymptote. Ristorcelli and Clark (2004) reported that the centerplane value of $\overline{f_1'^2}$ (and as a result θ) must be constant under the assumption

of self-similarity. Approximately asymptotic behavior in θ at the centerplane was observed in $Sc = 0.7$ gas-phase experiments (Banerjee *et al.* 2008) and in $Pr = 7$ liquid-phase experiments (Mueschke *et al.* 2007). Dalziel *et al.* (1999) used light-induced fluorescence (LIF) in a set of retracting plate experiments in a $Sc \sim 10^3$ salt/fresh water experiment and measured an approximately constant value $\Theta \approx 0.55$ over the range $0.4 < \tau < 1.5$ (when scaled to match the time normalization used in this work). However, LIF measurements are not resolution independent. The Batchelor scale for the analogous salt/fresh water experiments reaches $\eta_B = h Sc^{-1/2} Re_h^{-3/4}$ μm , and thus, under-resolved pointwise concentration measurements will over-predict the degree of molecular mixing (Mueschke & Andrews 2006). In the present work, where the measurement technique is free of optical resolution constraints, no such asymptotic behavior of the mixing parameters is observed by the largest Reynolds numbers achieved, $Re_h \approx 3000$. From figure 2.28, if buoyancy-driven mixing layers have an asymptotic value of P/h similar to that in shears layers, then an asymptotic behavior of θ and Θ in the $Sc \sim 10^3$ mixing layers may not be observed until $Re_h \approx 8000$ – 10000 .

2.4.11 *Implications for turbulent transport and mixing modeling*

Mathematical models of turbulent transport and mixing are designed to predict large-scale observables, such as the mixing layer width h and its late-time growth rate α . To predict the degree of mixing, such models must also accurately predict second-order turbulence statistics, including the turbulent kinetic energy and density variance. These quantities have been an important subject of study in the reacting flow and combustion communities (Fox 2003; Poinsoot & Veynante 2005), but have thus far received little attention in the Rayleigh–Taylor instability community. Anisotropy effects, statistical inhomogeneity, and nonequilibrium physics in Rayleigh–

Taylor mixing layers also complicate the modeling process. Predictive models should also encompass a large dynamic Reynolds number range. As shown in figure 2.28, mixing models must capture the small mixing rate (shallow slope of θ and Θ) at $Re_h < 300$. At higher Reynolds numbers, these models must account for an increased mixing rate, the expected self-similar collapse of the volume fraction variance profiles shown in figure 2.29, and the eventual asymptotic behavior of P/h , θ , and Θ . This suggests that the model parameters in the production and dissipation terms in the modeled density variance $\overline{\rho'^2}$ (or equivalently $\overline{f_1'^2}$) transport equation may strongly depend on an integral-scale Reynolds number Re_h or a turbulent Reynolds number $Re_t = (\overline{E'})^2 / (\nu \overline{\epsilon'})$, where $\overline{E'}$ and $\overline{\epsilon'}$ are the turbulent kinetic energy and its dissipation rate, respectively. Liu and Fox (2006) addressed this issue by analytically integrating model scalar spectra to determine the relationship between mechanical and scalar time-scales as a function of Re_t and Sc . However, the model proposed by Liu and Fox implies that the integral length scale is set by the bounding geometry (rather than the flow), which is not the case in Rayleigh–Taylor driven mixing. In addition, the model kinetic energy and scalar variance spectra neglect nonequilibrium effects (Pope 2000; Fox 2003). Thus, the dependence of the mixing rate on the initial perturbations at the fluid interface cannot be incorporated, which has been shown to have persisting effects out to at least $Re_h > 10^3$ (Cook & Dimotakis 2001; Ramaprabhu *et al.* 2005; Mueschke *et al.* 2006).

Accordingly, a complete calibration of transport models for high Schmidt number Rayleigh–Taylor mixing requires measurements of quantities such as $\overline{f_1}$ and $\overline{f_1'^2}$. However, there is currently little detailed data available from direct numerical simulations (DNS) and experiments (compared with shear-driven turbulence) to aid in the calibration and validation of such models for Rayleigh–Taylor mixing. While DNS studies of Rayleigh–Taylor driven mixing are available at $Sc = 1$ (Cook & Dimotakis

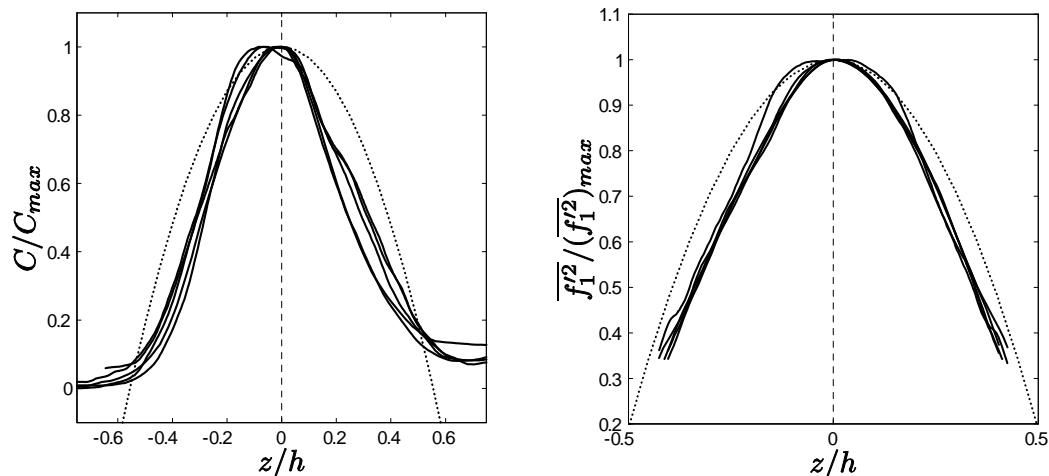


Figure 2.29 Self-similar collapse of the colored indicator concentration (left) and the volume fraction variance (right) profiles. Parabolic profiles are shown as a reference (dotted line).

2001; Ristorcelli & Clark 2004; Cabot & Cook 2006), no such data is available for the large Schmidt number case, for which DNS is too computationally expensive. In addition, there are few subgrid-scale models suitable for large-eddy simulation (LES) of large Schmidt number mixing (Pullin 2000; Burton 2008). Furthermore, monotone-integrated large-eddy simulation (MILES) and implicit large-eddy simulation (ILES) do not include molecular dissipation and diffusion terms [having a numerical Schmidt number of $O(1)$] and are thus poorly-suited to investigating Schmidt number effects on molecular mixing. Thus, the results of this work presently provide the sole experimental data for calibrating density variance transport models for high Schmidt number Rayleigh–Taylor mixing.

2.5 Summary of Experimental Measurements

The time-evolution of the volume fraction PDF, volume fraction variance and kurtosis, molecular mixing parameter, and density variance spectra were measured for a $Pr \equiv$

$Sc = 7$ Rayleigh–Taylor mixing layer. These measurements indicate that an early-time transition exists in the degree of molecular mixing in which (before the onset of strong nonlinearities and secondary Kelvin–Helmholtz instabilities) the interfacial area between the two fluids remains relatively small when compared to the area at later times. However, after the early-time onset of strong nonlinearities, the degree of molecular mixing within the flow steadily increases. It was shown that this increase in θ is associated with the decrease in $\overline{f_1'^2}$ and with the shift in the energy-containing modes to smaller wavenumbers. In addition, this work has investigated the linear and nonlinear growth of the Rayleigh–Taylor instability (depending on the initial perturbation amplitudes and wavelengths), mode-coupling and growth of successively larger scales, and the transition to a well-mixed state.

Experiments measuring the degree of molecular mixing in a liquid-phase, high Schmidt number, Rayleigh–Taylor instability-driven mixing layer have been performed using a salt/fresh water configuration in a water channel. Measurement of the mixing layer growth parameter α for this case indicates that the Schmidt number may have a minor influence on the late-time self-similar growth rate of the mixing layer. To quantify the degree of molecular mixing, the pH of each water stream was altered and a diffusion-limited neutralization reaction was monitored by the addition of a pH-sensitive chemical indicator. For the limiting case of the equivalence ratio $\varphi_{\text{In}} \rightarrow 0$, the chemical indicator concentration profiles indicate the degree of molecular mixing between the two fluids. As the buoyancy-driven mixing developed, the quantity of chemical indicator measured continued to increase, suggesting that the quantity of mixed fluid within the turbulent core of the mixing layer continued to increase with time. The degree of molecular mixing was further quantified by the equivalent product thickness P/h . At late times, P/h increased slightly with increasing Reynolds number. However, a mixing transition indicated by an increase

and eventual Reynolds number invariance in P/h (as previously observed in P/δ for shear-driven mixing layers) was not observed for the facility-limited, late-time Reynolds number $Re_h \approx 3000$.

The degree of molecular mixing was measured both by the relative fraction of chemical product formed and fluctuating density statistics. A mathematical relationship between the measured chemical indicator concentration profiles and the density variance was developed. Profiles of $\overline{f_1'^2}$ for $Sc \sim 10^3$ were obtained by integrating the total indicator formation over the range of equivalence ratios $0 < \varphi_n < \infty$ (or $0 < f_2^{50\%} < 1$). These profiles are approximately parabolic and the peak magnitude decreases in time, indicative of the greater volume of mixed fluid at later times. Combining measurements of \bar{f}_1 and $\overline{f_1'^2}$, the molecular mixing parameter θ was obtained for the $Sc \sim 10^3$ case and compared with lower Schmidt number (0.7 and 7) experiments. It was found that the increase in Schmidt number for the salt/fresh water experiments resulted in a significant decrease in θ for all times measured. In addition to the local mixing parameter θ , the global mixing parameters Ξ and Θ were also measured. At the latest time measured, all mixing parameters demonstrated an increasing trend. It remains unclear whether the $Sc \sim 10^3$ mixing layers reach the same asymptotic value of θ as in lower Schmidt number experiments.

3. EXAMINATION OF TURBULENT TRANSPORT AND MIXING USING DNS DATA

3.1 Overview of Goals and Methodology

To further examine Rayleigh–Taylor driven mixing dynamics, a direct numerical simulation (DNS) will be used to obtain measures of molecular mixing and turbulent statistics that are not readily measured in the water channel facility. As an outline of this section, the numerical methods, physical parameters used, and initial conditions are presented first. The DNS results are validated by comparing various integral-scale, turbulence, and mixing statistics with measurements from the water channel. The degree of molecular mixing is quantified by the mixing parameters P/h , θ , Θ , Ξ , the probability density function of the fluctuating density field $P(f_1)$, and the mean mixed fluid composition \bar{f}_1^m . Finally, the physics of Rayleigh–Taylor turbulent mixing is examined by evaluating the budgets of the relevant equations to quantify the relative importance of different physical transport and mixing processes.

The experiments discussed in § 2 reported measurements of mixing for $Sc = 7$ (hot/cold water) and $Sc \sim 10^3$ (salt/fresh water). Due to current computational limitations, the DNS of the water channel experiments is limited to the $Sc = 7$ case. Indeed, a DNS of the $Sc \sim 10^3$ experiments would require a twelve-fold increase in grid resolution in each coordinate direction, which is not currently feasible, and probably will not be for at least another 20 years. As a comparison, resolution requirements for $Sc \gg 1$ DNS imposes a severe limitation on the achievable Reynolds numbers. Schumacher *et al.* (2005) performed a 1024^3 DNS of isotropic, passive scalar mixing for $Sc = 32$, but were limited to a Taylor–Reynolds number $Re_\lambda = 24$. Yeung *et al.* (2004) performed a similar DNS of isotropic, passive scalar mixing for $Sc = 1024$, but were limited to $Re_\lambda = 8$. As an alternative to DNS, large-eddy simulations (LES)

require *a priori* knowledge of the physics of subgrid-scale mixing. Currently, DNS, LES, and MILES are not feasible for studying high Schmidt number Rayleigh–Taylor mixing.

3.2 Direct Numerical Simulation of Rayleigh–Taylor Mixing: Hot/Cold Water Case

This study uses the Miranda code (developed at the Lawrence Livermore National Laboratory) to solve the incompressible, variable-density conservation of mass and momentum equations (Cook & Dimotakis 2001)

$$\frac{\partial \rho}{\partial t} + \frac{\partial}{\partial x_j}(\rho u_j) = 0, \quad (3.1)$$

$$\frac{\partial}{\partial t}(\rho u_i) + \frac{\partial}{\partial x_j}(\rho u_i u_j) = \rho g_i - \frac{\partial p}{\partial x_i} + \frac{\partial \sigma_{ij}}{\partial x_j}, \quad (3.2)$$

where ρ is the density, v_i is the velocity field, g_i is the gravitational field, p is the pressure, and

$$\sigma_{ij} = \mu \left(\frac{\partial u_i}{\partial x_j} + \frac{\partial u_j}{\partial x_i} \right) - \frac{2}{3} \mu \delta_{ij} \frac{\partial u_k}{\partial x_k} \quad (3.3)$$

is the viscous stress tensor with dynamic viscosity $\mu = \rho\nu$ taken to be a linear function of the local density and average kinematic viscosity $\nu = (\mu_1 + \mu_2)/(\rho_1 + \rho_2)$. The divergence term in σ_{ij} is retained as the flow is not solenoidal due to density gradients that exist (Joseph 1990; Sandoval 1995). However, the velocity divergence term is expected to be relatively small compared with the other terms for the small Atwood number flow considered here.

In the hot/cold water experiments reported in § 2, a temperature difference was used to induce a density difference. However, the heat equation is not directly solved by the numerical algorithm. Instead, the mass fraction evolution equation is solved

in the Fickian diffusion approximation (Cook & Dimotakis 2001),

$$\frac{\partial}{\partial t}(\rho m_r) + \frac{\partial}{\partial x_j}(\rho m_r u_j) = \frac{\partial}{\partial x_j} \left(\rho D \frac{\partial m_r}{\partial x_j} \right), \quad (3.4)$$

where m_r is the mass fraction of fluid $r = 1, 2$, and D is the species mass diffusivity for both fluids, *i.e.* $D_{12} = D_{21}$. In the Fickian approximation, the analogy of temperature and species concentration is mathematically equivalent under the assumption of $D_{12} = D_{21} = D$. Thus, to simulate the water channel experiment, the species diffusivity D was equated to the thermal diffusivity of water, so that $Pr \equiv Sc = 7$.

The DNS code uses accurate, high-resolution methods to minimize numerical diffusion, which are required when fully-resolving density gradients in mixing applications. Specifically, a hybrid spectral/compact-differencing scheme was used to solve (3.1)–(3.4). Periodic boundary conditions were imposed in the x - and y -directions (orthogonal to gravity), which allowed the use of a spectral discretization with uniform grid spacing (Canuto *et al.* 2007). In the z -direction (parallel to gravity), free-slip boundary conditions were imposed at the top and bottom of the domain, and a tenth-order compact-differencing scheme was implemented (Lele 1992). As a result of the difference in resolving power of the spectral and compact-differencing schemes, the grid resolution in the vertical direction was set to $\Delta z = 0.75\Delta x$. Details on resolution considerations and the implementation of the boundary conditions can be found in Cook and Dimotakis (2001) and Cook *et al.* (2004).

A third-order Adams–Bashforth–Moulton predictor-corrector scheme was used to advance (3.1)–(3.4) in time. This two-step predictor-corrector scheme was further decomposed to advance the momentum equations, where an incompressible pressure-projection scheme was used to separate the advection/diffusion and acceleration/body force updates. First, the momentum field without pressure gradient or body forces was estimated at time step $n + 1$. Next, a pressure Poisson equation was solved to

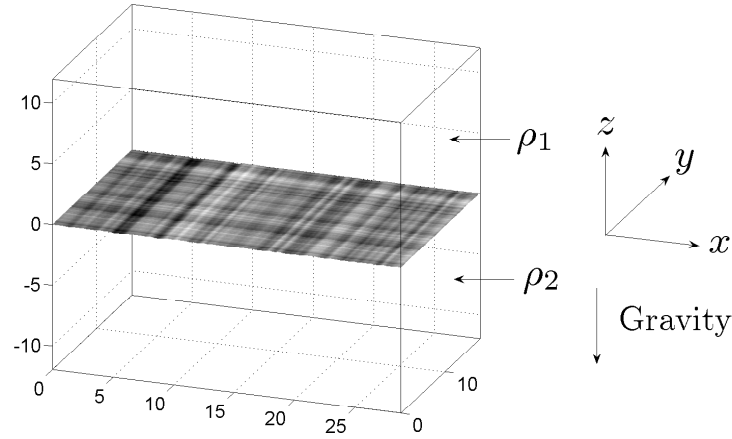


Figure 3.1 Schematic of computational domain for the DNS with associated axes and direction of gravity. The iso-surface of initial interfacial perturbations $\zeta(x, y)$ is shown at the centerplane ($z = 0$).

ensure mass conservation. The pressure gradient and body forces were then included to estimate the momentum field at time step $n + 1$, denoted $(\rho u_i)^*$. Applying the corrector step to $(\rho u_i)^*$ yields a final value of the momentum field $(\rho u_i)^{n+1}$.

The physical parameters in the DNS were chosen to closely match a typical water channel experiment, and are summarized in Table 3.1. The water channel has cross-sectional dimensions of 20 cm deep and 32 cm high (direction of gravity). With a typical mean advective velocity $U_m \approx 4.75$ cm/s and data capture times from 1–10 minutes in duration, the longest resolvable wavelengths in the streamwise direction are $\gtrsim 190$ cm. However, a computational domain size of 190 cm \times 20 cm \times 32 cm is not feasible due to resolution requirements and computational resource limitations. Thus, an acceptable domain size must be chosen such that resolution considerations could be met while also incorporating longer wavelengths that may influence the dynamics of the mixing layer (Linden *et al.* 1994; Dimonte *et al.* 2005).

Parameter	Value
ρ_1	0.9985986 g/cm ³
ρ_2	0.9970479 g/cm ³
A	7.5×10^{-4}
g_z	981 cm/s ²
μ_1	0.009 g/(cm s)
μ_2	0.011 g/(cm s)
$Sc \equiv Pr$	7

Table 3.1 Parameters used in the direct numerical simulation of the water channel experiment.

The chosen computational domain size was $L_x \times L_y \times L_z = 28.8 \text{ cm} \times 18 \text{ cm} \times 24 \text{ cm}$ and the grid resolution was $N_x \times N_y \times N_z = 1152 \times 760 \times 1280$. A schematic of the computational domain is shown in figure 3.1. The estimated Kolmogorov scale $\eta_K \approx h Re_h^{-3/4} \approx 0.055 \text{ cm}$ gives a lower bound resolution limit velocity field near the end of the simulation, where $h \approx 15 \text{ cm}$ and $Re_h \approx 1700$. As $Sc > 1$ in the DNS, the resolution requirements for the scalar field are even more stringent, where the smallest scalar fluctuations are given by the Batchelor scale $\eta_B = \eta_K Sc^{-1/2} \approx 0.021 \text{ cm}$. The DNS has a resolution of $\Delta x = \Delta y = 0.025 \text{ cm}$ and $\Delta z = 0.01875 \text{ cm}$, so that the flow is slightly under-resolved and aliasing errors will be generated as the Reynolds number increases towards the end of the simulation. Such aliasing errors (predominantly in the scalar density field) were filtered out using a sharp spectral low-pass filter at wavenumber $k_x = k_y = 113.8 \text{ cm}^{-1}$, or approximately at twice the grid spacing. While this filtering procedure effectively removed the aliasing errors, a small fraction of energy was also removed from the largest wavenumbers ($\approx 1 \times 10^{-7}\%$ of the total energy), which was found to have a negligible effect on the mixing dynamics.

More details on the filtering methods can be found in Cook *et al.* (2004).

The initial perturbations used in the DNS were parameterized from the data presented by Mueschke *et al.* (2006). The initial interface between the two fluids was perturbed in the x - and y -directions

$$\zeta(x, y) = \sum_{k_x=k_{\min}}^{k_{\max}} \hat{\zeta}(k_x) e^{ik_x x} + \sum_{k_y=k_{\min}}^{k_{\max}} \hat{\zeta}(k_y) e^{ik_y y}, \quad (3.5)$$

where $k_x = 2\pi/\lambda_x$ and $k_y = 2\pi/\lambda_y$ are the wavenumbers in the x - and y -directions. The amplitudes of the perturbations in each orthogonal direction, $\hat{\zeta}(k_x)$ and $\hat{\zeta}(k_y)$, were taken from experimental measurements of density and interfacial perturbations in the streamwise and spanwise directions just off the trailing edge of the splitter plate (Mueschke *et al.* 2006). In addition to interfacial perturbations, the initial velocity field of the DNS was perturbed to account for velocity fluctuations induced by the wake of the splitter plate. This was accomplished by defining a velocity potential field

$$\phi_r(\mathbf{x}, t = 0) = \sum_{k_x=k_{\min}}^{k_{\max}} \frac{\hat{w}(k_x)}{k_x} e^{ik_x x - k_x |z|}, \quad (3.6)$$

where the initial velocity field was taken to be the gradient of a potential field

$$u_i(\mathbf{x}, t = 0) = \frac{\partial \phi_r}{\partial x_i} - \frac{D}{\rho} \frac{\partial \rho}{\partial x_i}; \quad i = x, y, z. \quad (3.7)$$

In addition to the gradient of the potential field, the formulation of the initial velocity field accounted for diffusion velocity at the interface (Joseph 1990),

$$\frac{\partial u_i}{\partial x_i} = -\frac{\partial}{\partial x_i} \left(\frac{D}{\rho} \frac{\partial \rho}{\partial x_i} \right) \neq 0. \quad (3.8)$$

Further details on the implementation of the initial perturbations in the DNS can be found in Appendix D.

3.3 Statistical Averaging

Statistical analysis of Rayleigh–Taylor mixing requires averaging over an ensemble of realizations. Due to the extreme computational requirements of DNS, it is generally impractical to perform an ensemble of simulations for averaging purposes. However, the simple flow geometry implies statistical homogeneity in the x - and y -directions (orthogonal to the direction of gravity). Thus, ensemble averages are defined as the average over xy -planes (Youngs 1984). The Reynolds average (denoted by an overbar) of a field $\phi(\mathbf{x}, t)$ is then

$$\bar{\phi}(z, t) = \frac{1}{L_x L_y} \int_0^{L_x} \int_0^{L_y} \phi(\mathbf{x}, t) \, dy \, dx. \quad (3.9)$$

The instantaneous values of a given field can be decomposed into mean and fluctuating components according to

$$\phi(\mathbf{x}, t) = \bar{\phi}(z, t) + \phi'(\mathbf{x}, t). \quad (3.10)$$

As a consequence of this averaging, the fluctuation of a field (denoted by a prime) averages to zero in a given plane, $\overline{\phi'} = 0$.

To facilitate the analysis of variable-density effects, a mass-weighted (Favre) average is also considered (Chassaing *et al.* 2002; Wilcox 2006). The mean and fluctuating components are decomposed such that

$$\phi(\mathbf{x}, t) = \tilde{\phi}(z, t) + \phi''(\mathbf{x}, t), \quad (3.11)$$

where the Favre-average (denoted by a tilde) denotes a mass weighted two-dimensional average over xy -planes,

$$\tilde{\phi}(z, t) = \frac{\overline{\rho \phi}(z, t)}{\bar{\rho}(z, t)} = \frac{\int_0^{L_x} \int_0^{L_y} \rho(\mathbf{x}, t) \phi(\mathbf{x}, t) \, dy \, dx}{\int_0^{L_x} \int_0^{L_y} \rho(\mathbf{x}, t) \, dy \, dx}. \quad (3.12)$$

In the Favre-average case, the fluctuation of a field (denoted by a double prime) does not average to zero, $\overline{\phi''} \neq 0$; instead $\overline{\rho\phi''} = 0$ so that, as a consequence of (3.12), $\overline{\rho\phi} = \tilde{\rho}\tilde{\phi}$.

By defining statistical quantities on xy -planes, each statistic becomes a function of the z -coordinate and time only. All profiles presented are plotted along the z -axis and are normalized by the mixing layer width $h(t)$, as typically done in a self-similar scaling analysis (Ristorcelli & Clark 2004). In this work, the total mixing layer width $h(t)$ is based upon 5–95% volume fraction thresholds.

3.4 Comparison with Water Channel Experimental Data

In this section, the DNS is validated by comparing simulation results and experimental measurements from the water channel. Qualitative observations of the experiment and mixing layer show good agreement. Measurements of the mixing layer growth rate parameter α , fluctuating velocity statistics, and mixing statistics are also compared and exhibit favorable agreement.

3.4.1 Qualitative observations and comparisons

The initial velocity perturbations in the DNS were found to dominate the initial growth of the mixing layer in the water channel experiments (Mueschke *et al.* 2006). This was also observed in the DNS, where the initial growth of the mixing layer was primarily two-dimensional. In simulations employing isotropic initial conditions (see Appendix D for a more detailed discussion), the initial structures that develop from the unstable configuration are approximately spherical in shape (Laney *et al.* 2006). Each rising and falling structure roughly follows single-mode dynamics until secondary instabilities develop and nonlinear dynamics overtake the mixing layer (Youngs 1984;

Haan 1989). This is not the case here, where the initial growth of the mixing layer better resembles the early-time growth from two dimensional simulations (Cabot 2006). This is clearly seen in the early-time evolution of the $f_1 = 0.5$ isosurface shown in figure 3.2. Such growth is also observed in the water channel experiments, where little spanwise structure or variation is observed during the early-time development of the mixing layer.

At the onset of the instability, the initial velocity field model forms a vortex sheet with variations only in the x -direction. As a result, little structure exists in the spanwise or y -direction. The spanwise structure slowly develops due to the baroclinic production of vorticity in the x -direction that is a result of spanwise perturbations $\hat{\zeta}(k_y)$ [see (3.5) and Appendix D]. As the penetration rate of the initial structures grows in magnitude, the material surface area on the rising bubble and falling spikes is stretched. As a result, this stretches the vortex lines in the x -direction, increasing their strength and creating ‘rib-like’ structures along the cylindrical structures. Such rib-like structures are evident by $\tau = 0.5$, as shown in figure 3.2.

At approximately $\tau = 1$, the mixing layer transitions to a more three-dimensional flow. The late-time $f_1 = 0.5$ iso-surface shows the more three-dimensional flow structure in figure 3.3. This nonlinear transition to a more complex internal structure is also observed in the water channel experiments at approximately $\tau = 1$. This transition is more easily visualized in the DNS, where the nonlinear interactions of the stretched vortex lines in the x - and y -directions begin to contort the $f_1 = 0.5$ iso-surface in a direction not aligned with the x - and y -axes, as seen before $\tau = 0.5$. During this nonlinear transition, individual vortex lines are broken to form vortex rings creating more three-dimensional bubbles and spikes. At this time the bubbles and spikes appear to be closer to spherical in morphology than cylindrical.

The iso-surfaces of the density field can be qualitatively compared with the water

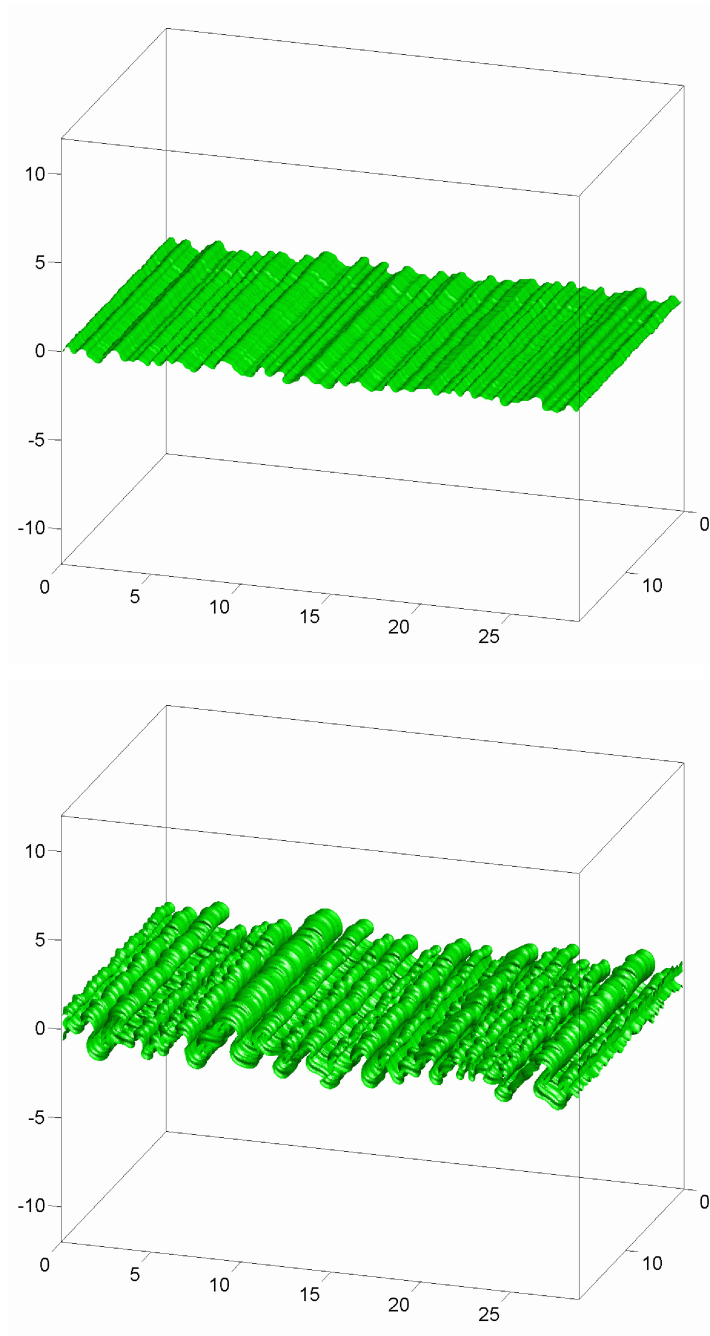


Figure 3.2 Early-time evolution of the $f_1 = 0.5$ volume fraction iso-surface at $\tau = 0.21$ (top) and $\tau = 0.50$ (bottom).

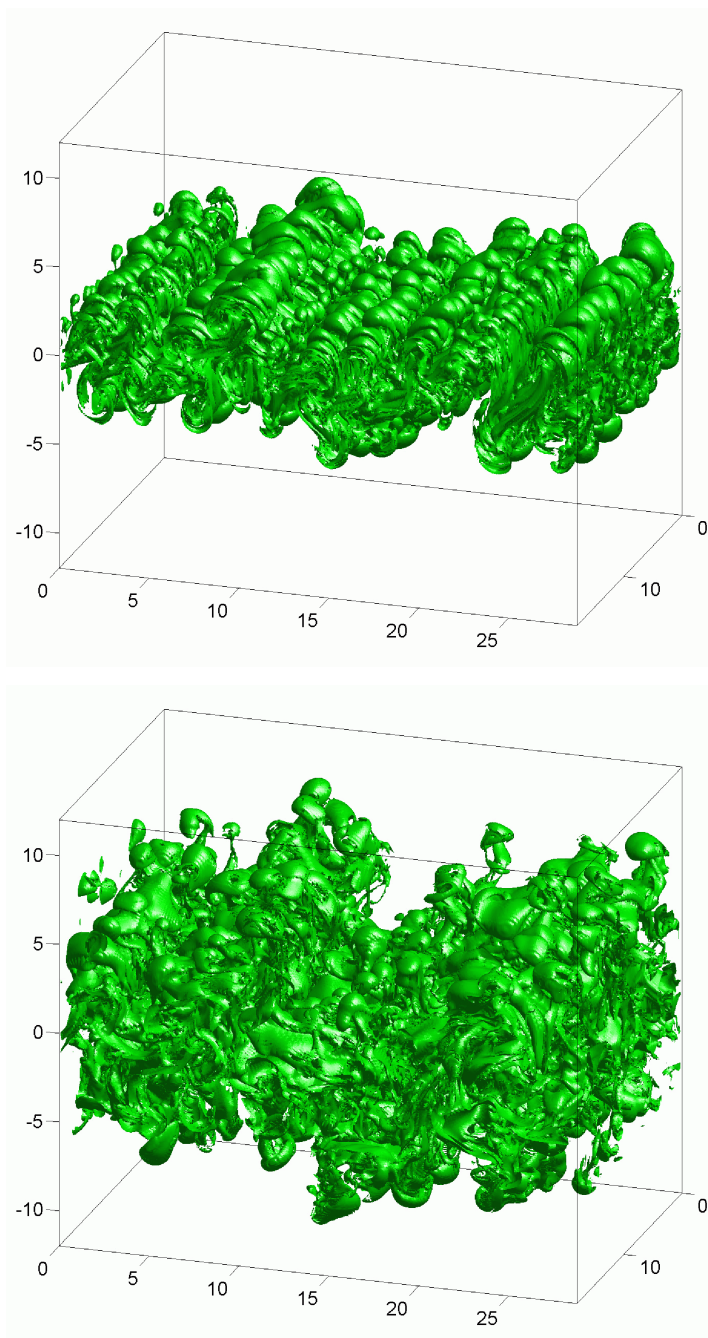


Figure 3.3 Late-time evolution of the $f_1 = 0.5$ volume fraction iso-surface at $\tau = 1.01$ (top) and $\tau = 1.52$ (bottom).

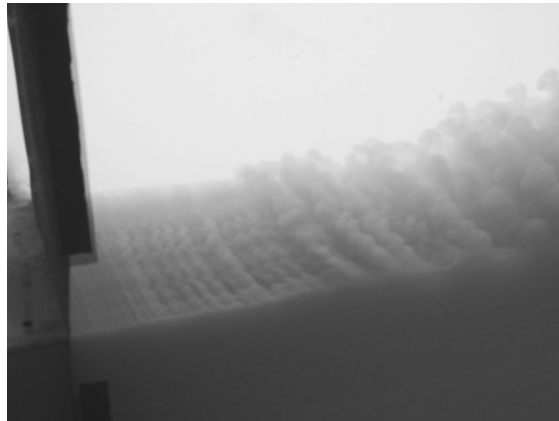


Figure 3.4 Photograph of the initial development of a Rayleigh–Taylor mixing layer in the water channel, where a small amount of milk has been added to the bottom stream for visualization purposes. The flow is from left-to-right.

channel experiments. An image of the initial development of the mixing layer in a water channel experiment is shown in figure 3.4. The initial, two-dimensional disturbance generated by the splitter plate is evident on the left-hand side of the figure, which is similar to the initial development observed in the DNS. As the Rayleigh–Taylor mixing layer grows, so do the perturbations in the spanwise direction as seen in both the DNS and the experiment. As the mixing layer continues to grow, ripples along the top edges of the rising structures break into individual bubbles, and more three-dimensional structure is evident at later times. This process is seen in both the water channel, on the right-hand side of figure 3.4, and in the DNS in figure 3.3.

3.4.2 *Mixing layer growth rate*

A first-order validation of the DNS results is given by a comparison of the mixing layer growth and its late-time growth rate. A comparison of mixing layer widths from the DNS and the $Sc = 7$ water channel experiment is shown in figure 3.5, where time has

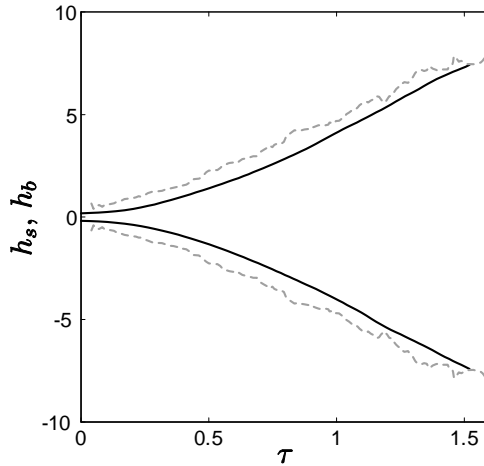


Figure 3.5 Bubble and spike penetration (in cm) from the DNS (black) and water channel (dashed) (Wilson 2002).

been normalized as in (2.3). This dimensionless time has been adopted to facilitate a comparison of the DNS results and water channel experiments; however, other time scales may be used. Other researchers have used the most unstable wavelength according to linear stability analysis (Chandrasekhar 1981)

$$\lambda_{max} \approx 4\pi \left(\frac{\nu^2}{Ag} \right)^{1/3} = 0.66 \text{ cm} \quad (3.13)$$

to normalize time according to (Cook *et al.* 2004; Kadau *et al.* 2007)

$$\tau_\lambda = t \sqrt{\frac{Ag}{\lambda_{max}}} \quad (3.14)$$

Another time scale can be used, where time is normalized by the growth rate of the most unstable wavelength s_{max} . Results are then characterized in terms of the number of e -folding periods

$$\tau_e = t s_{max} \quad (3.15)$$

This time scaling becomes advantageous when studying transitional flows, where ap-

proximately nine e -folding periods are required for temporal instabilities to transition to turbulence (Smith & Gamberoni 1957; van Ingen 1956). The relationship between these alternate time-scalings and (2.3) is given by $\tau_\lambda/\tau = 6.96$ and $\tau_e/\tau = 11.47$. Depending upon the dimensionless time used, the present DNS reaches $\tau = 1.52$, $\tau_\lambda = 10.6$, and $\tau_e = 17.4$. Thus, it may be possible to classify the final stages of the DNS as ‘turbulent’ according to the e -folding definition above. A more detailed discussion of the transitional and turbulent regimes observed in the DNS is given in § 3.5.1.

Both the DNS and the experiment show similar growth rates. In addition, the self-similar growth parameter α from (1.1) can be compared. Equation (1.1) is recovered for the late-time growth of a small Atwood number mixing layer by self-similar analysis (Youngs 1984; Ristorcelli & Clark 2004) or dimensional analysis (Cook & Dimotakis 2001). A more general expression for the self-similar growth of a mixing layer is given by the ordinary differential equation (Ristorcelli & Clark 2004; Cabot & Cook 2006)

$$\left(\frac{dh_b}{dt}\right)^2 = 4\alpha_b A g h_b, \quad (3.16)$$

Expanding (3.16), as shown by Ristorcelli and Clark (2004), shows that the mixing layer width is proportional to a sum of terms that scale as t^2 , t^1 , and t^0 .

While various methods for determining a late-time value of α are possible, three independent measurements of α are examined here. First, from (1.1), the late-time slope of $(h_b - h_s)/2$ plotted against Agt^2 is measured. While this method is robust, it is not free from the influence of t^1 and t^0 terms. The second method directly computes a time-dependent, effective α from the time derivative of (1.1),

$$\alpha(t) = \frac{1}{2Agt} \frac{dh_b}{dt}, \quad (3.17)$$

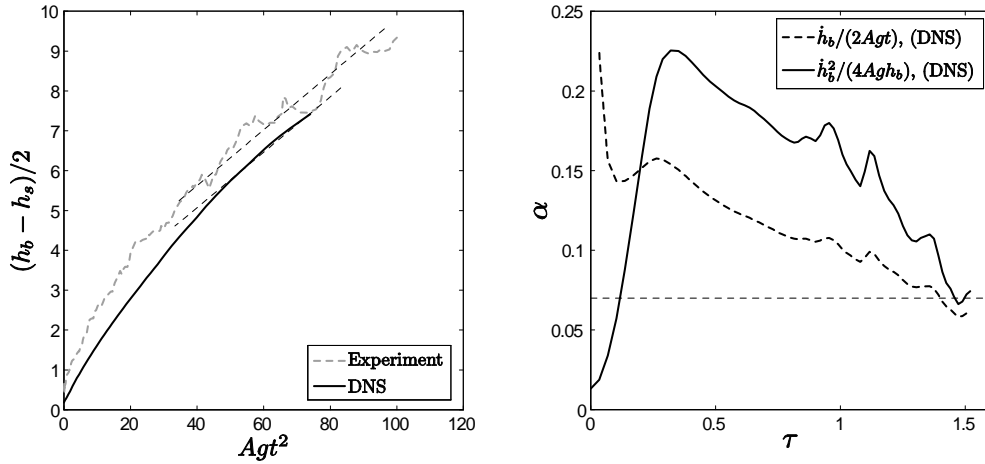


Figure 3.6 Measurement of growth parameter α from the DNS using the mixing layer half-width (left) and from (3.16) and (3.17) (right). Fiducials denoting $\alpha = 0.07$ are shown in each figure.

which eliminates the original t^1 dependence and reduces the t^0 dependence implicit in h . Finally, a time-dependent, effective α is directly calculated from the ordinary differential equation in (3.16). The various measures of α are shown in figure 3.6. The current DNS reaches a dimensionless time $\tau = 1.52$, which should be sufficiently late to realize self-similar growth as measured in the water channel. It has been noted that self-similar scaling of the mixing layer width (*i.e.* quadratic growth) is observed at $\tau \gtrsim 1.2$ (Snider & Andrews 1994). The growth parameter in the DNS appears to approach the experimentally reported value $\alpha \approx 0.07$ for $\tau > 1.3$; however, it is difficult to conclude if $\alpha = 0.07$ is the asymptotic growth parameter in the DNS due to the limiting domain size constraints.

3.4.3 Statistical convergence

Before a comparison of fluctuating velocity and density statistics is presented, a measure of the relative uncertainty in the measured statistics is required. The uncertainty

(95% confidence interval bounds) in the averaged statistics may be quantified by

$$w_\phi = \pm 1.96 \sqrt{\frac{s_\phi^2}{N_\phi}}, \quad (3.18)$$

where s_ϕ^2 is the sample variance of statistic ϕ and N_ϕ is the number of samples (*i.e.* turbulent structures) over which the average was taken (Benedict & Gould 1996). Accordingly, the statistical uncertainty in a given mean is proportional to $N_\phi^{-1/2}$. Thus, as the DNS evolves in time and the turbulent length scales grow, fewer structures are available to calculate a mean value, unlike in the water channel. Due to the decreasing number of turbulent structures at late-time, the bootstrap method of estimating statistical uncertainties is problematical and was not used in this work.

The dominant wavelength corresponding to a fluctuating scalar field $\phi(x, t)'$, based upon the energy content of its spectrum $E_\phi(k, z, t)$ is (Batchelor 1953)

$$\lambda_\phi(z, t) = 2\pi \frac{\int_{k_{min}}^{k_{max}} \frac{E_\phi(k, z, t)}{k} dk}{\int_{k_{min}}^{k_{max}} E_\phi(k, z, t) dk}, \quad (3.19)$$

where the factor of 2π results from defining wavenumbers as $k = 2\pi/\lambda$, $k_{min} = 2\pi/L_i$, and $k_{max} = \pi/\Delta x_i$. Due to the anisotropy of the implemented initial conditions, the turbulent scales of motion and statistics may not be equal in the x - and y -directions. Accordingly, the dominant wavelengths in both homogeneous coordinate directions are defined

$$\lambda_{\phi,x}(z, t) = 2\pi \frac{\int_{k_{min}}^{k_{max}} \frac{E_\phi(k_x, z, t)}{k_x} dk_x}{\int_{k_{min}}^{k_{max}} E_\phi(k_x, z, t) dk_x}, \quad \lambda_{\phi,y}(z, t) = 2\pi \frac{\int_{k_{min}}^{k_{max}} \frac{E_\phi(k_y, z, t)}{k_y} dk_y}{\int_{k_{min}}^{k_{max}} E_\phi(k_y, z, t) dk_y} \quad (3.20)$$

and examined separately. The evolution of the dominant wavelengths for all three velocity components and the density field at the centerplane ($z = 0$) of the mixing layer is shown in figure 3.7. As the Reynolds number increases, the dominant energy containing scales also increase in size. In general, the velocity and density

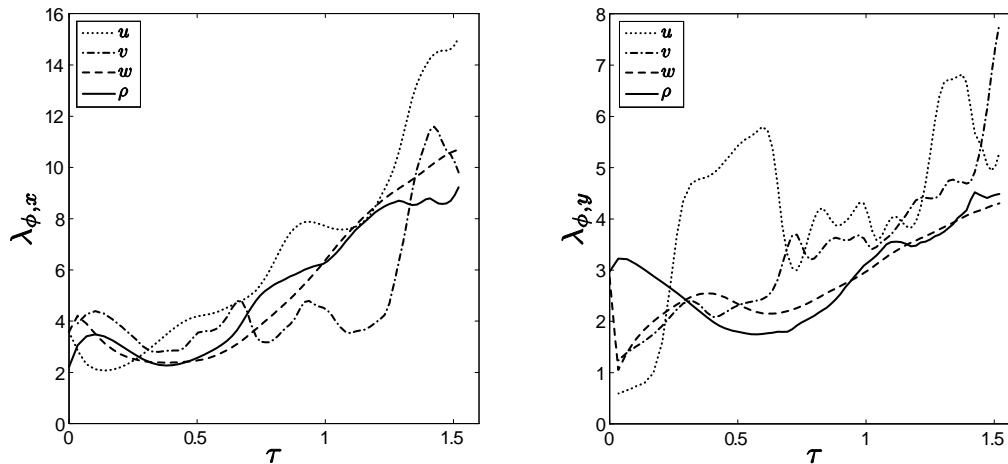


Figure 3.7 Dominant wavelengths in x - and y -directions on the centerplane based upon each velocity component and density field from the DNS.

fields yield similar dominant wavelength magnitudes. However, due to the sustained anisotropy resulting from the initial conditions, the dominant wavelengths in the x - and y -directions remain unequal even out to the final time of $\tau = 1.52$.

The total number of turbulent structures within the domain may be defined

$$N_{\phi} = \left(\frac{2L_x}{\lambda_{\phi,x}} \right) \left(\frac{2L_y}{\lambda_{\phi,y}} \right), \quad (3.21)$$

where two structures, one bubble and one spike, are taken per wavelength. It is important to note that as Re_h increases, the total number of dominant, energy-containing structures included in the ensemble averages in (3.9) decreases. The total number of turbulent structures in the DNS (based on the vertical velocity and density fields) as a function of the Reynolds number is shown in figure 3.8. As might be expected, in a flow with rising and falling structures, the strong correlation between the vertical velocity and density fluctuations results in $N_{\rho} \approx N_w$. The uncertainty in all statistics presented scales as $N_{\phi}^{-1/2}$, and thus, statistical oscillations in averaged quantities are expected to grow at late-time as there are $N_{\phi} \approx 50$ structures at

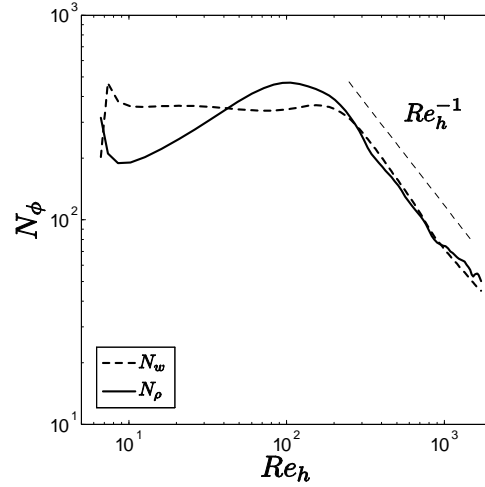


Figure 3.8 Number of turbulent structures on the centerplane of the mixing layer based upon the dominant wavelengths λ_ρ and λ_w .

$\tau = 1.52$.

3.4.4 Fluctuating velocity and density statistics

In addition to comparing integral-scale statistics, the evolution of fluctuating velocity statistics along the centerplane of the mixing layer are also compared in figure 3.9 and show good agreement with the experiment up to $\tau \approx 0.5$. Beyond $\tau = 0.5$, the DNS yields lower values of $\overline{w'^2}$ than measured in the experiment. This is likely attributed to the finite computational domain size, which limits the spectral dynamics of the larger scales of motion. The nonlinear velocity correlation in the advection term of the Navier–Stokes equation can be written in wavenumber space as

$$\mathcal{F}\left[\frac{\partial(u_i u_j)}{\partial x_j}\right] = i k_j \mathcal{F}(u_i u_j) = i k_j \sum_{\mathbf{k}'} \hat{u}_i(\mathbf{k}') \hat{u}_j(\mathbf{k}''), \quad (3.22)$$

where $\mathbf{k} = \mathbf{k}' + \mathbf{k}''$ (Pope 2000). Accordingly, energy is transferred from wavevectors \mathbf{k}' and \mathbf{k}'' , which are supported on the discrete numerical grid, to wavevector \mathbf{k} , which

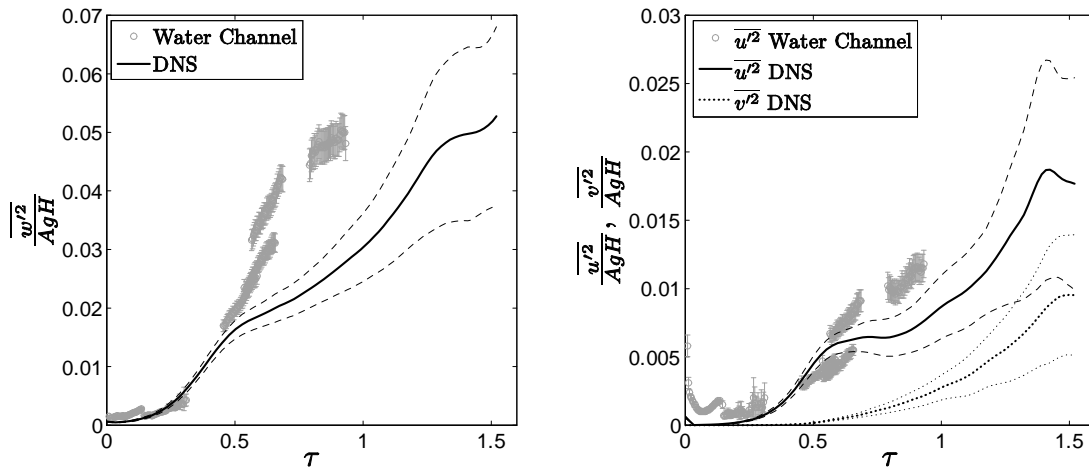


Figure 3.9 Comparison of fluctuating velocity statistics on the centerplane of the mixing layer from the DNS and the water channel. Uncertainty estimates (95% confidence interval bounds) are denoted by dashed and dotted lines.

may or may not be supported on the grid. This is analogous to the interaction of supergrid, cross, or subgrid scale triadic interactions in large-eddy simulations (Pope 2000; Cabot *et al.* 2004). When the magnitude of the wavevector satisfies $|\mathbf{k}| < \pi \Delta x$, the triadic wavevector interaction supplies energy to a scale too small to be supported on the grid and aliasing errors are generated. If properly resolved, this energy transfer is negligible and numerical filters are used to eliminate the influence of aliasing errors on the solution. At the other end of the spectrum, if $|\mathbf{k}| > 2\pi/L_x$ or $|\mathbf{k}| > 2\pi/L_y$, then energy from wavevectors \mathbf{k}' and \mathbf{k}'' is transferred to a wavelength too large to be supported by the numerical domain. In this event, the energy is entirely lost. Thus, two resolution requirements exist for fully-resolving a DNS of any experiment. First, the grid resolution must be fine enough to prevent the loss of energy to scales too small to be resolved, causing aliasing errors. Second, the domain must be large enough to allow the triadic interactions of the larger scales of motion. Thus, the domain size must be large enough to facilitate the creation of increasingly longer wavelengths,

minimizing the loss of energy to modes not supported by the discrete grid. These criteria are loosely satisfied by the current domain size and is further explored below.

To satisfy the first resolution requirement, the grid spacing must be the same size or smaller than the smallest dynamic scale in the flow. While this first requirement can typically be satisfied *a priori*, the second resolution requirement may not be for simulations of Rayleigh–Taylor mixing. The large-scale resolution requirement implies that the energy in the largest scales (low wavenumber regime of the spectrum) must constitute only a fraction of the total energy of the flow. Here, the normalized cumulative energy spectra

$$C_\phi(k) = \frac{\int_{k_{min}}^k E_\phi(k^*) dk^*}{\int_{k_{min}}^{k_{max}} E_\phi(k^*) dk^*} \quad (3.23)$$

are examined, which provides a measure of the cumulative energy in the spectrum of ϕ from mode 1 to mode $m = 2\pi/k$. If the spectrum of fluctuations for a given scalar is fully-resolved, including the small-wavenumber peak of the energy spectrum, then

$$\lim_{k \rightarrow 0} \frac{dC_\phi(k)}{dk} \approx 0. \quad (3.24)$$

If (3.24) is not satisfied, then the peak of the energy spectrum is not fully resolved and the energy transfer to larger scales cannot be assumed to be negligible. The normalized cumulative energy spectra for the vertical velocity fluctuations and density fluctuations on the centerplane from the DNS are shown in figure 3.10. At early times, $\tau < 0.5$, the slopes of $C_w(k)$ and $C_\rho(k)$ at $m = 1$ (*i.e.* $k = 2\pi/L_x$) are small. However, beyond $\tau \approx 0.5$, the criteria in (3.24) is not satisfied, especially for the velocity spectrum. Thus, the discrepancy between the DNS and the experimentally measured values of $\overline{w'^2}$ beyond $\tau \approx 0.5$ is due to the fact that the full dynamic range of $E_w(k)$ is not resolved.

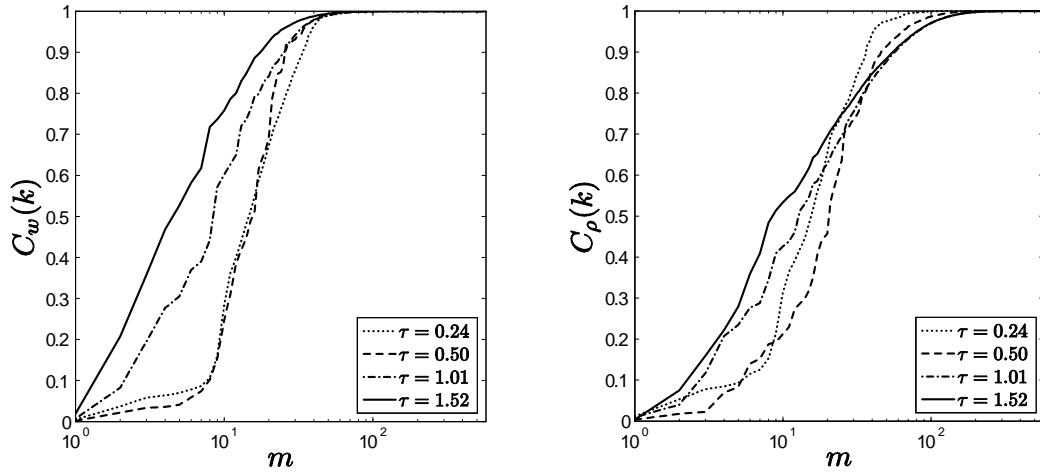


Figure 3.10 Cumulative energy distributions of the vertical velocity and density variance spectra from the DNS.

The velocity variance evolution shown in figure 3.9 can be further examined by comparing the centerplane vertical velocity variance spectra from the DNS and the water channel experiment, which are shown in figure 3.11. Caution must be exercised when comparing experimentally-measured spectra, which use a one-dimensional ‘flying-wire’ measurement technique (Pope 2000), and spectra from the DNS typically calculated from annular summations of energy within wavenumber rings (Dimonte *et al.* 2004; Ramaprabhu *et al.* 2005; Cabot & Cook 2006). The experimentally-measured spectra contain additional, low-wavenumber energy content from wavevectors not aligned with the x -axis. This spectral information cannot be distinguished or removed from the signal in a one-dimensional measurement (Pope 2000). However, it is possible to recreate an analogous spectrum from the two-dimensional spectrum calculated from the DNS. Starting with the Fourier transform of a scalar field ϕ ,

$$\hat{\phi}(k_x, k_y) = \frac{1}{L_x L_y} \int_0^{L_x} \int_0^{L_y} \phi(x, y) e^{-i(k_x x + k_y y)} dy dx, \quad (3.25)$$

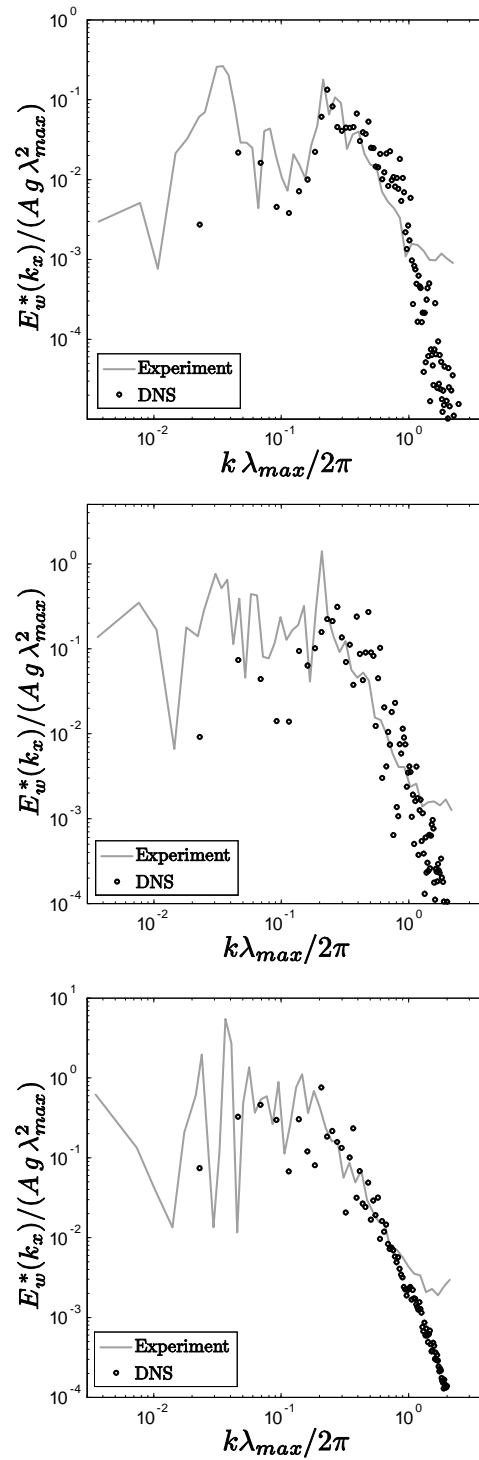


Figure 3.11 Comparison of $E_w^*(k_x)$ from the DNS and water channel experiment on the centerplane of the mixing layer at $\tau = 0.31$ (top), $\tau = 0.58$ (middle), and $\tau = 0.92$ (bottom).

the energy content may be calculated by

$$E_{\phi}(k_x, k_y) = \frac{\hat{\phi}(k_x, k_y) \hat{\phi}(k_x, k_y)^*}{2}, \quad (3.26)$$

where the superscript * indicates the complex conjugate of $\hat{\phi}$. The analogous flying-wire, one-dimensional spectra in the x -direction can be calculated by adding the off-axis energy content to the appropriate k_x wavenumber,

$$E_{\phi}^*(k_x) = \frac{2}{\Delta k_x} \sum_{k_y=-\pi/L_y}^{\pi/L_y} E_{\phi}(k_x, k_y). \quad (3.27)$$

A comparison of the one-dimensional vertical velocity variance spectra from the experiment and the DNS is shown in figure 3.11. For the overlapping range of wavenumbers, the DNS and the experiment exhibit good agreement. The largest discrepancy is seen in the longest wavelengths measured in the DNS. As shown in Appendix D and in figure 3.10, the domain size $L_x = 28.8$ cm limits the resolution of the long-wavelength content in the initial vertical velocity spectrum and the dynamic energy transfer amongst the largest scales. Thus, the DNS model of the water channel experiment well-represents the mixing layer dynamics with the exception of the very longest of wavelengths, *i.e.* modes 1 and 2. To better resolve wavelengths of size $\lambda \approx 15$ –30 cm, the domain size in the x -direction must be increased four- to eight-fold, which is not feasible with current computational facilities.

A similar comparison of the centerplane density variance spectrum can be made, where a similar operation is performed to calculate an estimated ‘flying-wire’ one-dimensional spectrum from the DNS. The comparison of $E_{\rho}^*(k_x)$ from the experiment and the DNS is shown in figure 3.12. Again, the longest wavelengths in the DNS exhibit less energy than the experimentally-measured spectra. As shown by the cumulative energy spectrum in figure 3.10, the total amount of energy in the first two

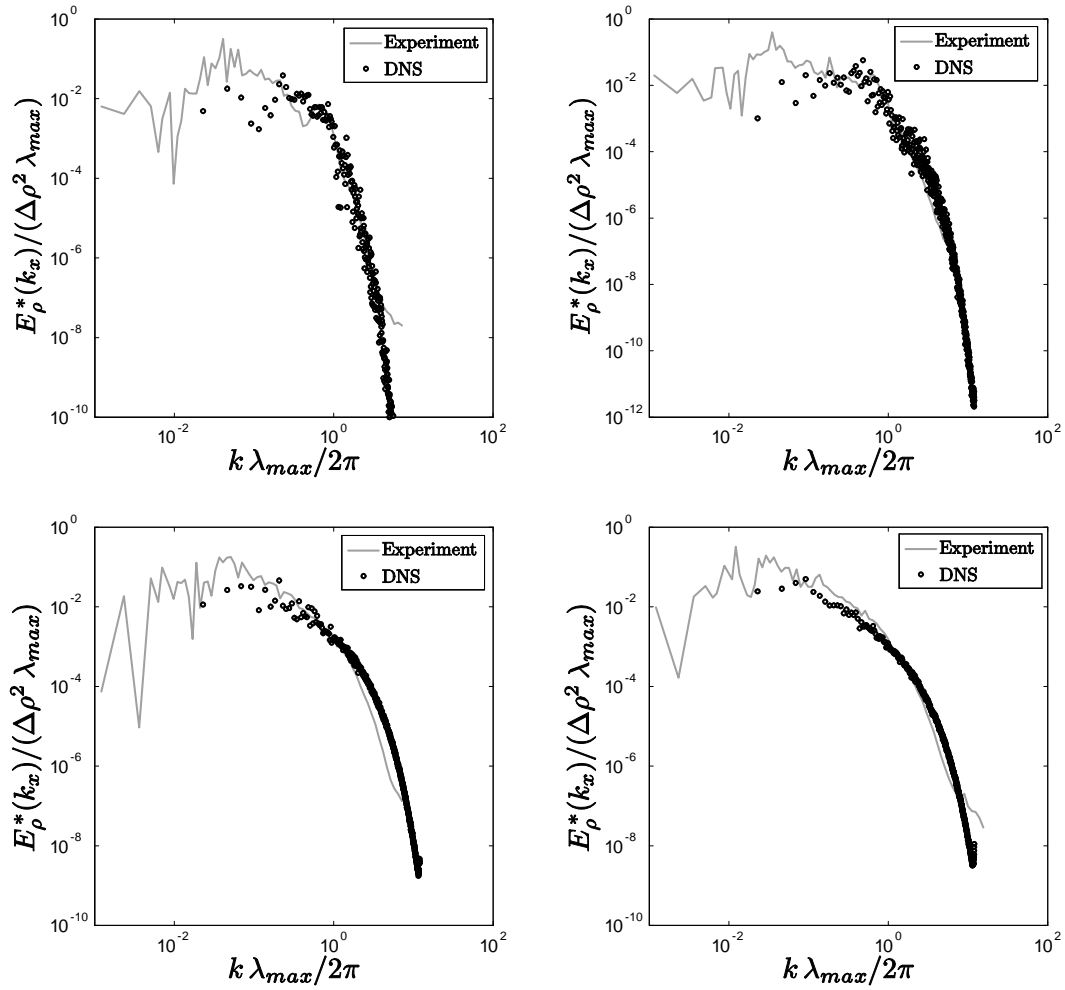


Figure 3.12 Comparison of $E_\rho^*(k_x)$ from the DNS and water channel experiment on the centerplane of the mixing layer at $\tau = 0.17, 0.4, 0.87,$ and 1.36 (left-to-right, top-to-bottom).

modes accounts for $< 5\%$ of the total variance of density fluctuations at early times ($\tau \leq 1$). Thus, the inability of the DNS to fully resolve the dynamics of the lowest two modes has little effect on the measurement of $\overline{\rho'^2}$. At the latest times in the simulation ($\tau = 1.52$), the energy deficit in the longest wavelengths remains; however, as shown in figure 3.10, the energy content in the first two modes is greater than 5% of the total variance, and thus, to better resolve the late-time mixing dynamics, a larger domain size in the x -direction is required.

3.4.5 *Molecular mixing parameter θ*

In addition to fluctuating velocity statistics, the degree of molecular mixing from the DNS and water channel experiment compare favorably. The evolution of the molecular mixing parameter θ [see (2.1) for the definition] on the centerplane of the mixing layer is shown in figure 3.13. Both the experiment and the DNS show the same dynamic trend of a decreasing θ at early times, followed by a slow rise to an approximately late-time asymptotic value $\theta \approx 0.6$. Both exhibit minimum values $\theta \approx 0.35$ at similar times $\tau \approx 0.4$ – 0.5 . The DNS exhibits a lower value of θ than reported by Mueschke *et al.* (2006); however, as shown in figure 3.13, uncertainties in the statistical measurements from the DNS and experiments overlap. More details on the measurement of mixing dynamics will be presented in the subsequent sections § 3.5 and 3.6.

3.5 *Measurements of Molecular Mixing*

In § 2, the degree of molecular mixing was quantified using parameters that depend upon measures of fluctuating density statistics or chemical product formation. In this section, measures of molecular mixing from the DNS data that are not readily mea-

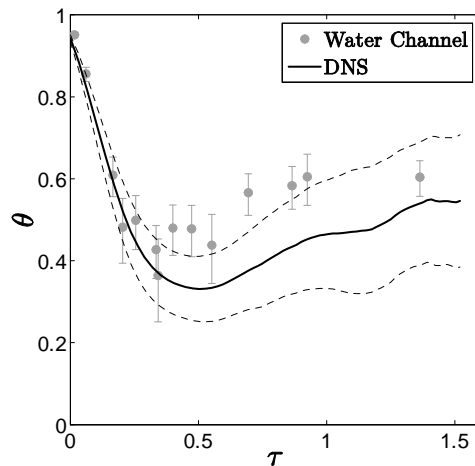


Figure 3.13 Comparison of θ on the centerplane of the mixing layer from the water channel experiment ($Pr = 7$) and the DNS ($Sc = 7$). Uncertainty estimates (95% confidence interval bounds) are shown by dashed lines.

sured in the hot/cold water experiment from § 2 are presented. This includes chemical product formation measurements, global measures of mixing, and the statistical composition of the mixed fluid across the mixing layer. These results are compared with results from gas-phase Rayleigh–Taylor mixing experiments at $Sc = 0.7$ (Banerjee *et al.* 2008), and the liquid-phase $Sc = 7$ and $Sc \sim 10^3$ experiments reported in § 2, as well as shear-driven results at $Sc = 0.7$ and $Sc \sim 10^3$.

3.5.1 Reynolds number regimes

As shown in § 2.4.10, the degree of molecular mixing is sensitive to the integral-scale Reynolds number of the mixing layer. The final Reynolds number reached in the DNS depends upon the choice of a length and velocity scale. Two definitions are considered here, both of which take the mixing layer width h as the integral length scale. Cook and Dimotakis (2001) used the growth rate of the mixing layer dh/dt as the integral

velocity scale. Ramaprabhu and Andrews (2004) used the terminal velocity of the dominant wavelength or bubble: relating the dominant wavelength or bubble diameter to the width of the mixing layer, $D_b \approx h_b \approx h/2$. Assuming symmetry of bubble and spike growth in the small Atwood number limit gives $v_\infty = 0.5C_\infty\sqrt{Ag h}$, where $C_\infty = 0.7$ depends on the Atwood number (Daly 1967). Based upon these choices of velocity scales, the corresponding Reynolds numbers are

$$Re_h^{\dot{h}} = \frac{h}{\nu} \frac{dh}{dt}, \quad (3.28a)$$

$$Re_h^\infty = \frac{h v_\infty}{\nu}, \quad (3.28b)$$

the evolution of which are shown in figure 3.14. Depending upon the volume fraction thresholds chosen to define the mixing layer width, the final Reynolds number ranges from $Re_h^\infty \approx 1700$ (5–95% thresholds) to $Re_h^{\dot{h}} \approx 4500$ (1–99% thresholds). The evolution of $Re_h^{\dot{h}}$ becomes non-monotonic at late times due to oscillations in the derivative of h . For this reason, Re_h^∞ is used henceforth and the superscript ∞ is implied.

While an integral-scale Reynolds number definition remains ambiguous, the turbulence within the mixing layer may be quantified by a Reynolds number which does not rely upon an arbitrary choice of a length or velocity scale. Studies of homogeneous turbulence, which have no geometric boundaries, define a Taylor–Reynolds number

$$Re_\lambda = \frac{\lambda_T^{u_i} \overline{u_i'^2}}{\nu}, \quad (3.29)$$

where

$$\lambda_T^{u_i} = \left[-\frac{1}{2} \frac{d^2 f_{u_i}}{dr^2} \Big|_{r=0} \right]^{-1/2} \quad (3.30)$$

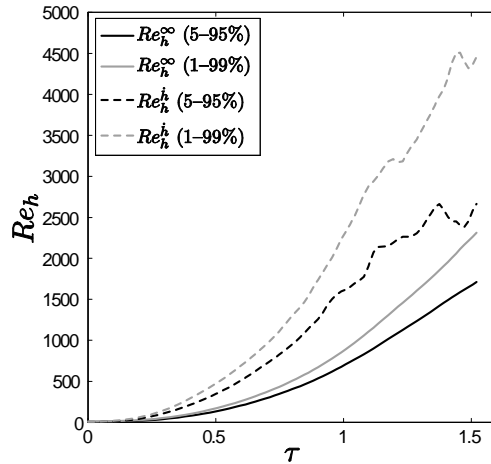


Figure 3.14 Evolution of integral-scale Reynolds number calculated using the mixing layer width h , based upon 5–95% (black) and 1–99% (grey) volume fraction thresholds.

is the Taylor microscale for the i^{th} -component of the velocity field, and

$$f_{u_i}(r, z) = \frac{\overline{u_i(\mathbf{x} + \mathbf{r})' u_i(\mathbf{x})'}}{\overline{u_i'^2(z)}} \quad (3.31)$$

is the autocorrelation of the velocity field u_i (Pope 2000). In anisotropic turbulence, the Taylor scales and velocity fluctuations in each coordinate direction are not necessarily equal, *i.e.* $\lambda_T^u \neq \lambda_T^v \neq \lambda_T^w$ and $\overline{u'^2} \neq \overline{v'^2} \neq \overline{w'^2}$. Thus, for the case of Rayleigh–Taylor mixing, the Taylor–Reynolds number can be defined in each coordinate. The evolution of Re_λ is shown in figure 3.15. Dimotakis (2000) suggested that a sustained Taylor–Reynolds number $Re_\lambda \gtrsim 100$ –140 must be achieved to realize entrainment-limited mixing dynamics. The current DNS reaches $Re_\lambda^w \approx 95$ at the latest time ($\tau = 1.52$). Thus, according to the criteria suggested by Dimotakis, the DNS cannot be used to determine the existence of (or observe) the mixing dynamics in an entrainment-limited Rayleigh–Taylor mixing layer.

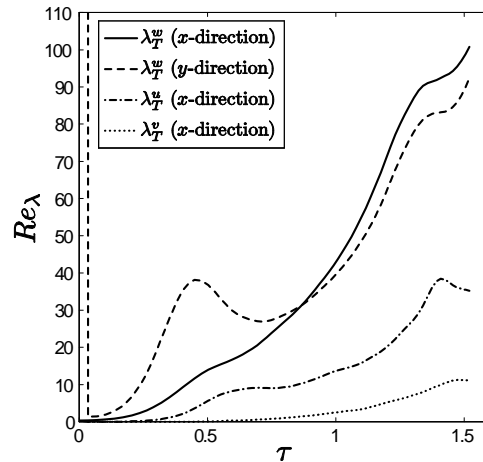


Figure 3.15 Evolution of the Taylor–Reynolds number Re_λ based upon the centerplane u , v , and w velocity fields.

Vertical slices of the density field from the DNS at $Re_h = 10, 100, 1000$, and 1710 are shown in figure 3.16, and the corresponding slices on the centerplane are shown in figure 3.17. A reference table of times and Reynolds numbers for the visualizations in figures 3.16 and 3.17 and the profiles in § 3 and 4 is given in Table 3.2. At the earliest times, the amplitudes of the initial perturbations are small with respect to the diffusion layer separating pure fluids. Accordingly, at $Re_h \approx 10$, the mixing layer width is approximately the same size as the diffusion layer thickness, and thus, the majority of the fluid within the 5–95% volume fraction thresholds can be viewed as mixed. As the growth rate of the initial perturbations increases, the interface between the two fluids remains relatively simple in topology, but the mixing layer width becomes much larger than the diffusion layer thickness separating the two fluids. Without the magnitude of velocity fluctuations found in higher Reynolds number mixing layers, there is only a marginal increase in surface area between the heavy and light fluids by $Re_h \approx 100$. At this point, the majority of the fluid within the 5–95%

t	τ	Re_h	Re_λ^w
0.68	0.10	10	0.6
1.36	0.21	21	1.7
2.82	0.43	94	11
3.32	0.50	137	14
6.65	1.01	708	44
7.62	1.16	978	64
10.03	1.52	1712	101

Table 3.2 Integral-scale and Taylor–Reynolds numbers for selected times.

volume fraction thresholds exists as pockets of pure, unmixed fluid. Beyond $Re_h \approx 200$, the mixing layer transitions to a nonlinear growth phase, where the topology of the interface separating the heavy and light fluids becomes very complicated. As a result, the surface area available for diffusion increases and the quantity of mixed fluid within the mixing layer continues to increase with Reynolds number.

Due to the moderate Reynolds numbers achieved in the DNS, the amount of mixed fluid is limited by the mass diffusion across density gradients. However, other researchers suggest that a final dynamic stage may exist, where the Reynolds number is sufficiently large that the mixing layer becomes entrainment-limited (Breidenthal 1981; Dimotakis 2000). Beyond this final transition, it has been demonstrated in shear-driven mixing layers that the equivalent product thickness [see (3.36)] becomes invariant with Reynolds number (Konrad 1977; Breidenthal 1979, 1981; Koochesfahani & Dimotakis 1986). However, for the Reynolds numbers achieved in the $Sc = 7$ DNS considered here, no such asymptotic behavior was realized by $Re_h = 1710$ or $Re_\lambda \approx 95$.

As observed in the visualizations of the density field shown in figures 3.16 and

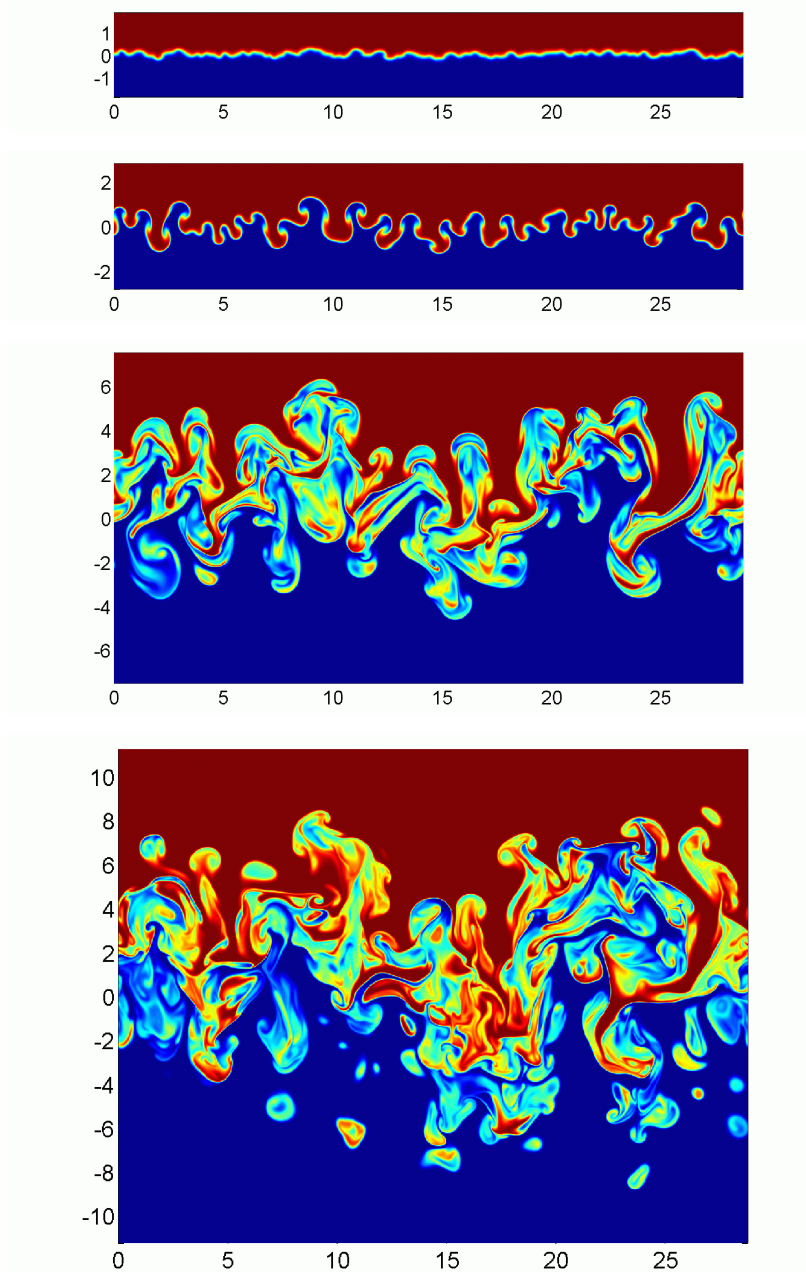


Figure 3.16 Vertical slices of the density field at $Re_h \approx 10^1$, 10^2 , 10^3 , and 1710, corresponding to dimensionless times $\tau = 0.10$, 0.43, 1.16, and 1.52. The heavy and light fluids are denoted by the color red and blue, respectively. Mixed fluid is denoted by intermediate shades, *i.e.* green and yellow.

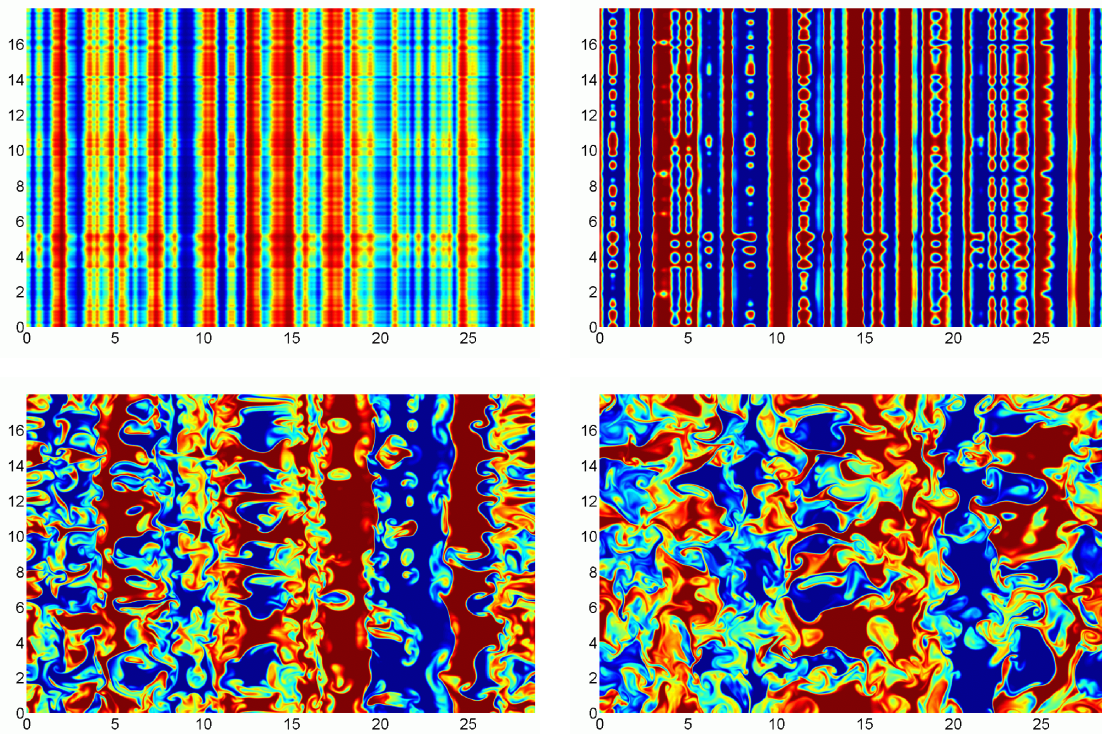


Figure 3.17 Evolution of centerplane density slices corresponding to the vertical slices shown in figure 3.2. Centerplane slices are at $\tau = 0.10$ (top-left), $\tau = 0.43$ (top-right), $\tau = 1.16$ (bottom-left), and $\tau = 1.52$ (bottom-right).

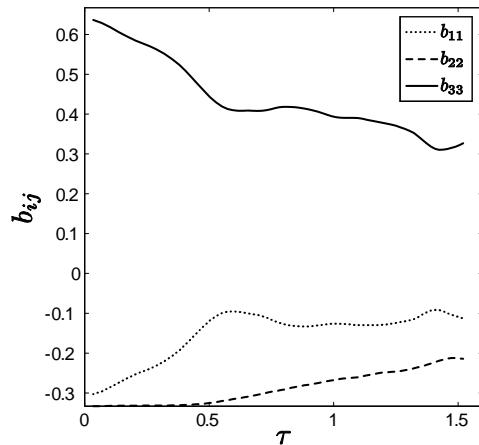


Figure 3.18 Evolution of the diagonal components of the Reynolds stress anisotropy tensor on the centerplane.

3.17, the initial structure of the mixing layer is highly anisotropic. The relative degree of anisotropy of the velocity fluctuations is quantified by the Reynolds stress anisotropy tensor

$$b_{ij} = \frac{\overline{u'_i u'_j}}{\overline{u'_k u'_k}} - \frac{1}{3} \delta_{ij}. \quad (3.32)$$

A maximum value of $b_{ij} = 2/3$ indicates that all of the energy in the turbulent fluctuations is in the Reynolds stress component $\overline{u'_i u'_j}$. The evolution of the centerplane values of b_{11} , b_{22} , and b_{33} is shown in figure 3.18. At early times, the bulk of the energy in the flow exists in vertical velocity fluctuations, with little energy in the u -component and zero in the v -component. As the mixing layer develops, the fluctuations move closer to an isotropic state with $b_{33} \approx 1/3$ at late time; however a fully-isotropic state of $b_{11} = b_{22} = b_{33}$ is not realized. Furthermore, the velocity fluctuations in the homogeneous directions remain anisotropic (i.e. $b_{11} \neq b_{22}$) out to $\tau = 1.52$, indicating that the turbulent mixing layer retains a memory of the initial conditions.

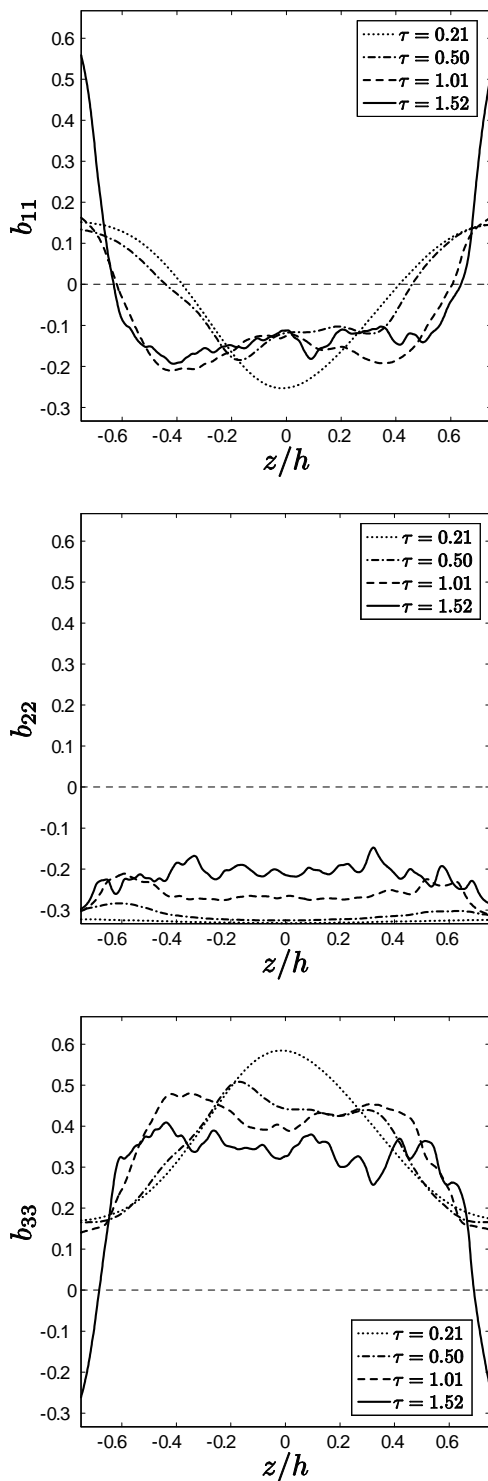


Figure 3.19 Profiles of the diagonal components of the Reynolds stress anisotropy tensor b_{11} (top), b_{22} (middle), and b_{33} (bottom).

In addition, the anisotropy of the velocity fluctuations from the DNS can be examined across the mixing layer. Profiles of the diagonal components of b_{ij} are shown in figure 3.19. Again, within the core of the mixing layer ($|z/h| < 0.5$), vertical velocity fluctuations dominate. Once the mixing layer transitions into a nonlinear, pre-turbulent state ($\tau > 0.5$), the profiles of b_{ij} from the DNS are approximately constant across the mixing layer, although they are not steady in time. It cannot be determined from the current DNS whether the degree of anisotropy within the mixing layer achieves steady, asymptotic values of b_{ij} . It is expected that fluctuations in the homogenous directions will continue to move towards a similar degree of anisotropy as memory of the initial conditions is lost.

As shown in figure 3.15, the mixing layer reaches a Taylor–Reynolds number $Re_\lambda \approx 95$, which approaches the value suggested by Dimotakis (2000) to realize entrainment-limited dynamics in shear-driven flows. However, the Reynolds number does not reach a large enough value that the largest and smallest scales are separated by a constant spectral cascade regime. Under these circumstances, the bandwidth of scales in the velocity variance and density variance spectra is large enough to support an inertial subrange scaling of $k^{-5/3}$ over a large range of scales. The evolution of the velocity and density variance spectra are shown in figure 3.20. Both the accumulation of energy in the longer wavelengths and expansion of scales at the longer wavelengths are observed, but the existence of a substantial inertial subrange is not.

To examine the separation of scales and inertial subrange scaling, the compensated spectra of $E_w(k)$ and $E_\rho(k)$ are shown in figure 3.21. The vertical velocity variance spectra exhibit an approximate $k^{-5/3}$ scaling for less than one decade of wavenumbers. The density variance spectra exhibit slightly different inertial subrange scaling of approximately $k^{-5/4}$ over a decade of wavenumbers. While the classical $k^{-5/3}$ scaling is not recovered for $E_\rho(k)$, it remains unknown whether the $k^{-5/4}$ scal-

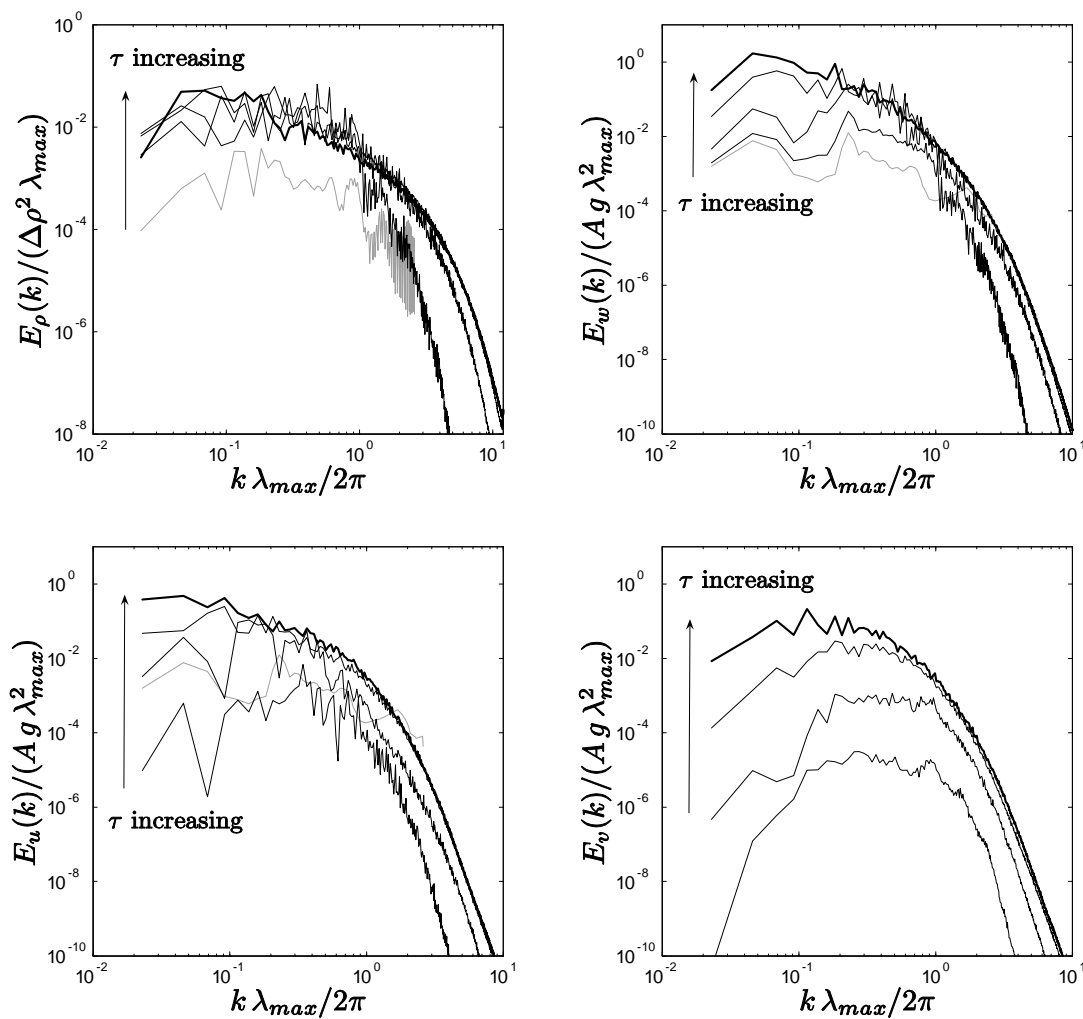


Figure 3.20 Evolution of centerplane density and velocity variance at $\tau = 0.21$, $\tau = 0.50$, $\tau = 1.01$, and $\tau = 1.52$. The initial spectra (when available) are shown in grey and the final spectra are bold.

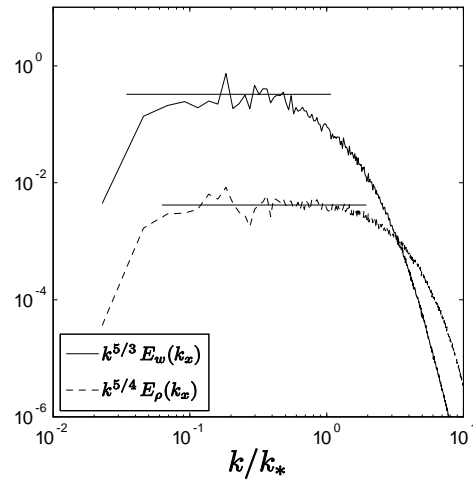


Figure 3.21 Compensated vertical velocity variance and density variance spectra at $\tau = 1.52$.

ing is a result of the moderate Reynolds number achieved or a $Sc > 1$ effect. In either case, the inertial subranges achieved in $E_w(k)$ and $E_\rho(k)$ are not wide enough that the effects of production and dissipation are sufficiently separated to exhibit Reynolds number independence with respect to the turbulence or the mixing dynamics (Zhou *et al.* 2003; Zhou 2007).

3.5.2 Chemical product measurements

There are canonical measurements of mixing that rely upon chemical product formation in a diffusion-limited mixing layer (Breidenthal 1979, 1981; Koochesfahani & Dimotakis 1986; Zhang & Schneider 1995; Karasso & Mungal 1996). The current DNS does not explicitly include reaction source terms in the conservation of mass fraction equations solved; however, it is possible to examine a hypothetical, infinitely-fast, reversible chemical reaction between two species,



This reaction is analogous to the phenolphthalein chemical indicator reaction in § 2.4.1, where the heavy and light fluids contain reactants A and B , respectively.

The equivalence ratio

$$\varphi = \frac{[A]/[B]}{([A]/[B])_{st}} \quad (3.34)$$

defines a measure of the balance or excess of reactants, where $([A]/[B])_{st} = 1$ is the stoichiometric ratio of the reactants for the reaction in (3.33). The local formation of product is a function of degree of mixing and φ , where

$$[C] = \begin{cases} f_1 [A]_1 & f_1 \leq \frac{\varphi}{\varphi+1} \\ (1 - f_1) [B]_2 & f_1 > \frac{\varphi}{\varphi+1} \end{cases}, \quad (3.35)$$

and $[A]_1$ and $[B]_2$ are the base concentrations of A and B in the top and bottom fluids, respectively. The chemical product concentration for the limiting case $\varphi \rightarrow 0$ and the stoichiometric case $\varphi = 1$ are shown in figure 3.22. The profiles of $\overline{[C]}$ for $\varphi \rightarrow 0$ exhibit a skew to the spike side of the mixing layer, while the $\varphi = 1$ profiles are more symmetric. This is expected as the maximum potential for product formation exists at the lower boundary of the mixing layer for the $\varphi \rightarrow 0$ case and at the centerplane for the $\varphi = 1$ case.

The total amount of chemical product formed can be obtained by integrating the profiles in figure 3.22 over the mixing layer width. Normalizing this integral by the mixing layer width gives the equivalent product thickness

$$\frac{P}{h} = \frac{1}{h} \int_{h_s}^{h_b} \frac{\overline{[C]}}{[B]_2} dz, \quad (3.36)$$

which measures the fraction of the mixing layer occupied with chemical product. The evolution of the equivalent production thickness for the $Sc = 7$, $\varphi \rightarrow 0$ case is shown in figure 3.23, where the DNS results are compared with both shear- and buoyancy-driven reacting flows at $\varphi \rightarrow 0$ (Konrad 1977; Breidenthal 1979; Mueschke *et al.*

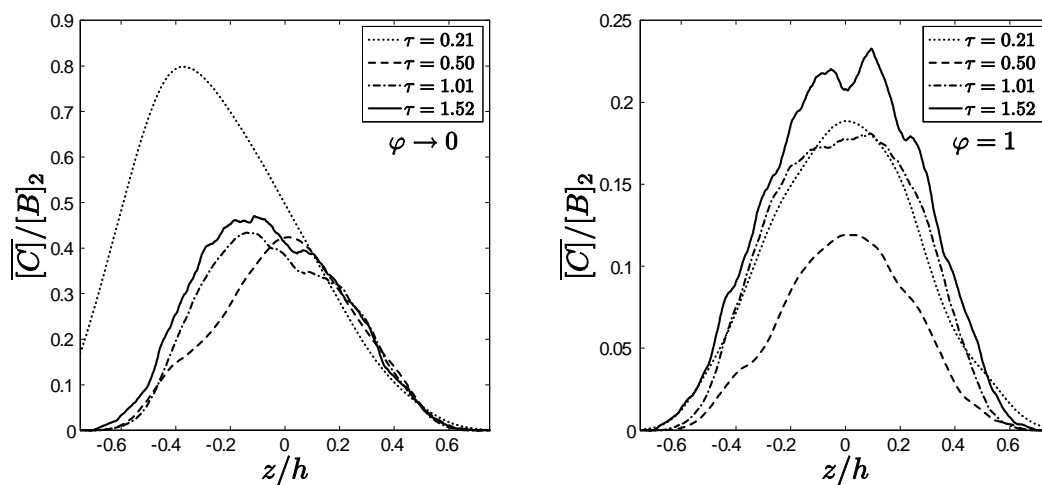


Figure 3.22 Profiles of mean product concentration $\overline{[C]}/[B]$ for $\varphi \rightarrow 0$ (left) and $\varphi = 1$ (right) across the mixing layer at various times.

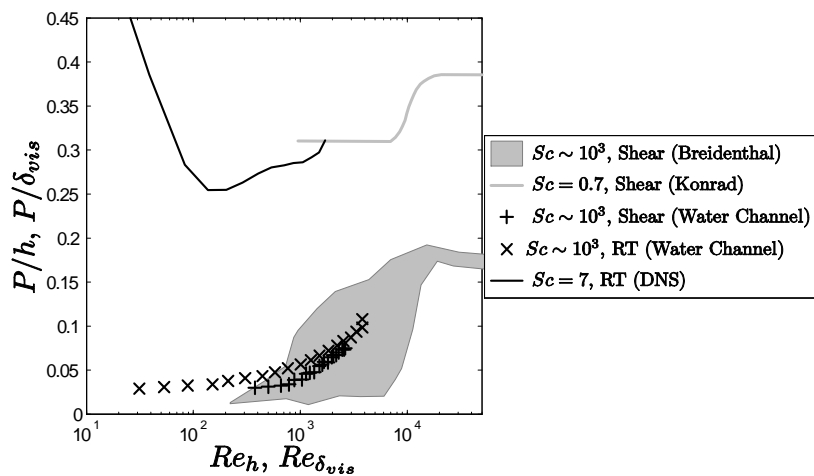


Figure 3.23 Equivalent product thickness for the $Sc = 7$, $\varphi \rightarrow 0$ case. Shear- and buoyancy-driven results at $Sc \sim 10^3$ and $Sc = 0.7$ are shown as a reference.

2008).

In the DNS, at small Reynolds numbers ($Re_h \ll 10^2$), mass diffuses across the species interface sufficiently to mix the majority of the fluid within the small mixing layer, resulting in a large P/h . This is in contrast with the $Sc \sim 10^3$ Rayleigh–Taylor measurements that do not exhibit a large quantity of product for $Re_h \ll 10^2$. Therefore, the amount of mixed fluid present at the onset of mixing is a strong function of the Schmidt number. In the DNS at $Re_h \approx 10^2$, the mixing layer has yet to develop sufficient turbulent fluctuations to mix the entrained fluid, and the penetrating bubbles and spikes exist primarily as pockets of unmixed fluid. As the Reynolds number increases, the relative fraction of chemical product increases slowly. By $Re_h = 1710$, the equivalent product thickness is approaching the pre-transitional values of P/δ_{vis} measured in gas-phase ($Sc = 0.7$) shear-driven mixing at moderate Reynolds numbers (Konrad 1977). However, as noted in § 3.5.1, an asymptotic measure of P/h is not expected in the current DNS at $Re_h = 1710$.

The equivalent product thickness provides a measure of the total amount of chemical product formed; however, a more meaningful measure of mixing is given by

$$\Xi = \frac{\int_{h_s}^{h_b} \overline{[C]} dz}{\int_{h_s}^{h_b} \overline{[C]}_{max} dz}, \quad (3.37)$$

which is the fraction of product formed relative to the maximum amount of product that may be formed for a given equivalence ratio. In (3.37), the maximum possible chemical product is defined

$$\overline{[C]}_{max} = \begin{cases} \bar{f}_1 [A]_1 & \bar{f}_1 \leq \frac{\varphi}{\varphi+1} \\ (1 - \bar{f}_1) [B]_2 & \bar{f}_1 > \frac{\varphi}{\varphi+1}. \end{cases} \quad (3.38)$$

The evolution of both P/h and Ξ for the cases $\varphi \rightarrow 0$ and $\varphi = 1$ are shown in figure 3.24 as a function of Re_h . Both P/h and Ξ have relatively high values at $Re_h \approx 10^1$,

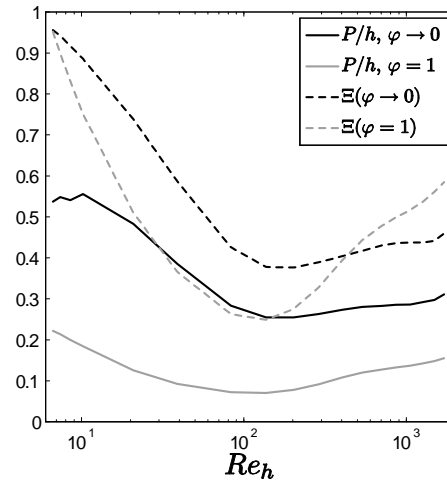


Figure 3.24 Evolution of equivalent product thickness P/h and mixing parameter Ξ as a function of Re_h and φ obtained from the DNS.

but then decrease rapidly to local minima at $Re_h \approx 10^2$. Above $Re_h \approx 200$, each mixing parameter increases with Reynolds number up to the final value $Re_h = 1710$. In addition, figure 3.24 illustrates that Ξ is a non-unique function of φ .

3.5.3 Fluctuating density statistics

The degree of molecular mixing in § 3.5.2 was quantified by the amount of chemical product formed within the mixing layer given a hypothetical chemical reaction. As shown in figure 3.16, it is also possible to quantify the degree of molecular mixing by a measurement of concentration or density fluctuations. In this section, two molecular mixing parameters are examined, including the local parameter θ [defined in (2.1)] and the global parameter Θ [defined in (2.53)]. The primary factor determining the values of θ and Θ is the volume fraction variance $\overline{f_1'^2}$, which is a measure of the intensity of segregation of two fluids (Dankwerts 1952). As the two fluids become homogeneously mixed, the density fluctuations about the mean will be small, and

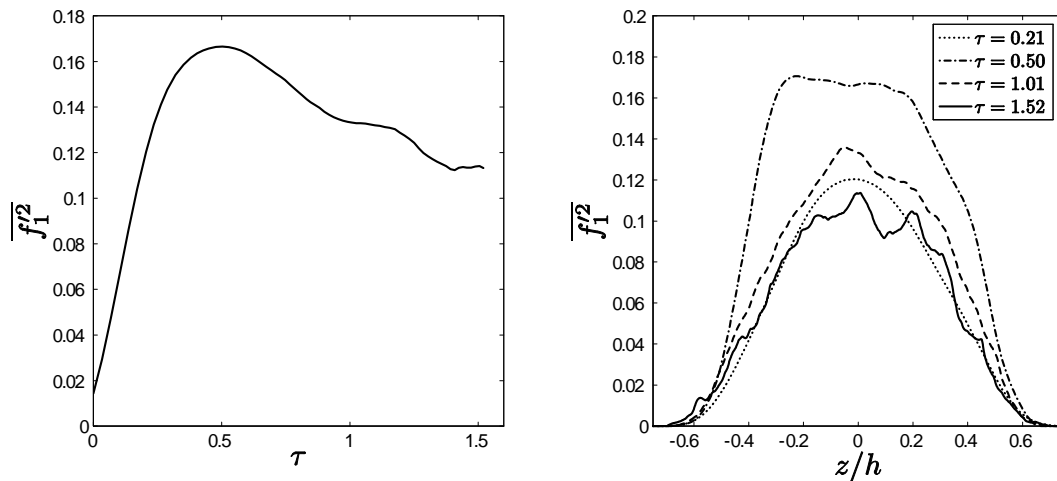


Figure 3.25 Evolution of centerplane volume fraction variance (left) and profiles across the mixing layer (right) obtained from the DNS.

hence, $\overline{f_1'^2}$ will be small. Conversely, if the two fluids are stirred but not mixed, the density fluctuations about the mean will be larger in magnitude, and hence, $\overline{f_1'^2}$ will be large.

The evolution of the volume fraction variance on the centerplane of the mixing layer and profiles of $\overline{f_1'^2}$ are shown in figure 3.25. At very early times, $\overline{f_1'^2}$ is very small. This agrees with the image of the $Re_h \approx 10$ density field shown in figure 3.16, where most of the mixing layer is mixed fluid. When $\tau \approx 0.5$, $\overline{f_1'^2}$ reaches a maximum value, which corresponds to the $Re_h \approx 100$ density field shown in figure 3.25. Similar to the mixing parameters P/h and Ξ , $\overline{f_1'^2}$ continues to decrease as the Reynolds number increases, indicating greater mixing.

Combining the mean and fluctuating volume fraction statistics gives the mixing parameters θ and Θ . The evolution of θ on the centerplane and Θ are shown in figure 3.26. Profiles of θ across the mixing layer are also shown in figure 3.26. Similar to the measures of mixing from § 3.5.2, both θ and Θ indicate that most of the fluid within the mixing layer is molecularly mixed at very early times. At $\tau \approx 0.5$, both

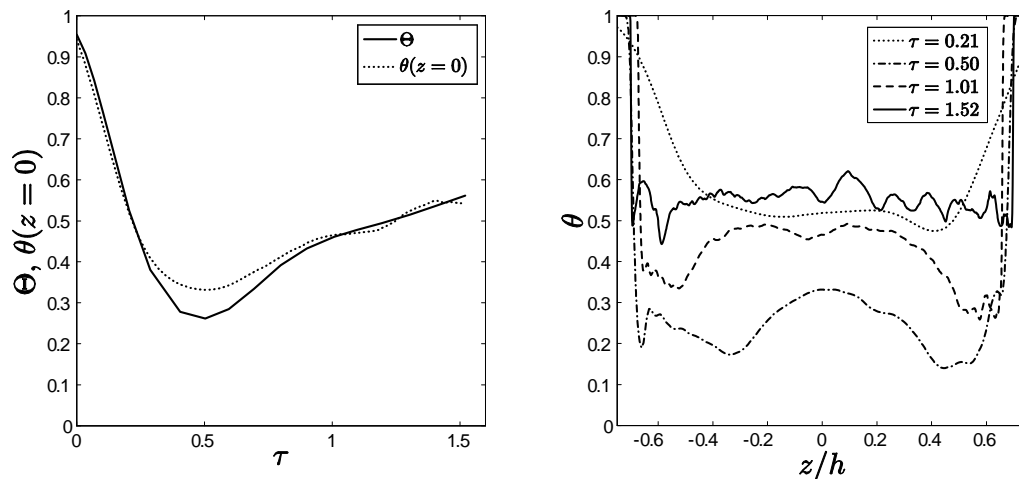


Figure 3.26 Evolution of molecular mixing parameters Θ and $\theta(z = 0)$ (left), and profiles of θ across the mixing layer (right) obtained from the DNS.

θ and Θ reach a minimum value, after which both parameters exhibit a gradual rise with Reynolds number. The profiles of θ indicate that the degree of molecular mixing remains relatively constant across the mixing layer. During the nonlinear transitional stage of the mixing layer development, $Re_h \approx 200$ – 1000 , the profiles of θ from the DNS are not perfectly constant. Instead, the fluid within the interior core, $|z/h| \lesssim 0.4$, has slightly larger values of θ . This greater degree of mixing is attributed to the onset of nonlinear, turbulent dynamics within the core of the mixing layer before the edges of the layer. As the Reynolds number increases, the inner turbulent core of the mixing layer occupies a greater fraction of the layer, as seen the difference between the θ profiles at $\tau = 0.5$ and 1.01 . At the latest time, the turbulent fluctuations are sufficiently large that θ remains approximately constant across the layer.

The mixing parameters shown in figure 3.26 were obtained from the $Sc = 7$ DNS, and are compared with measurements from the gas-phase experiments of Banerjee *et al.* (2008) and the liquid-phase experiments of § 2 in figure 3.27. At early times ($\tau < 0.2$), the species diffusivity in the $Sc = 7$ case is sufficiently large that the

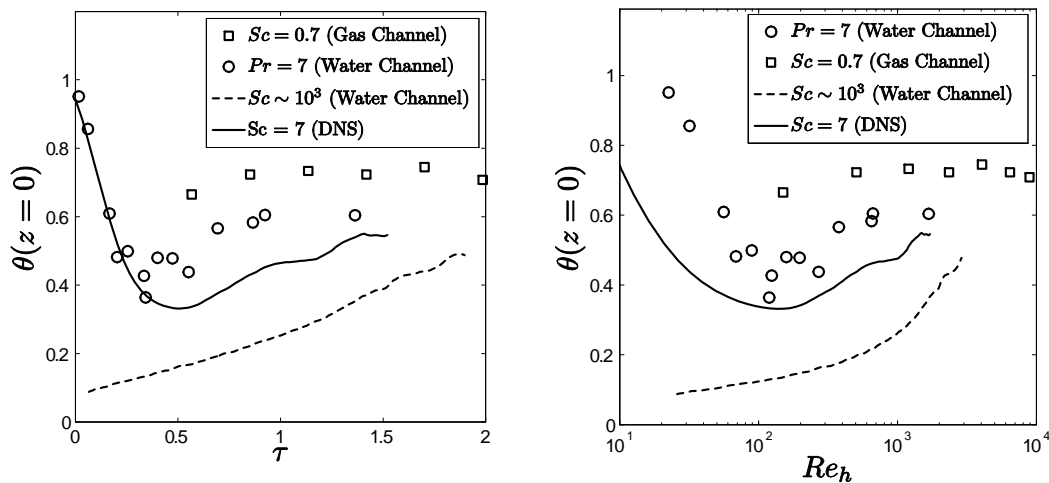


Figure 3.27 Evolution of θ on the centerplane of the mixing layer from gas-phase (Banerjee *et al.* 2008) and liquid-phase Rayleigh–Taylor experiments, and from DNS.

diffusion layer and mixing layer width are of similar size, resulting in a large value of θ . For the $Sc \sim 10^3$ case, the opposite is true, where the species diffusivity is sufficiently small that only a small fraction of the mixing layer exists in a mixed state. During the transition to turbulence, $0.5 < \tau < 1.5$, the degree of molecular mixing is a strong function of the Schmidt number. In addition, the higher Schmidt number results appear to require greater Reynolds numbers to achieve an approximately steady late-time value of θ . By $\tau \approx 0.8$, the $Sc = 0.7$ results appear to have reached a steady value $\theta \approx 0.7$. The $Sc = 7$ results show that a late-time value $\theta \approx 0.6$ is reached between $\tau \approx 0.9$ – 1.5 . For the $Sc \sim 10^3$ water channel experiments, an asymptotic value of θ has not been reached by $\tau = 1.9$.

3.5.4 Statistical composition of mixed fluid

In § 3.5.2, the degree of molecular mixing was quantified by measuring the amount of chemical product formed within the mixing layer, which implied molecular mixing.

In § 3.5.3, the degree of molecular mixing was further quantified by a statistical measurement of concentration fluctuations. The mixing parameters defined in (2.1) and (2.53) rely upon measurements of the mean density and density variance. However, it is possible to mathematically define an infinite number of probability distribution functions that yield the same mean and variance. Accordingly, a complete quantification of the degree of molecular mixing is provided by a measurement of the probability density function (PDF) of density or concentration fluctuations. A measure of the volume fraction PDF from the DNS across the mixing layer is given at several times in figure 3.28, where $P(f_1)$ is the probability of finding a concentrations of f_1 of heavy fluid and $1 - f_1$ of light fluid within a sample volume or grid cell.

At the earliest time shown in figure 3.28, a large fraction of the mixing layer exists as mixed fluid; however, $P(f_1)$ retains a bimodal profile across the mixing layer. At $\tau = 0.5$, where the least amount of mixed fluid is present, $P(f_1)$ continues to exhibit a bimodal distribution across the mixing layer. However, at $\tau = 0.5$, the probability of finding mixed fluid [*i.e.* $P(f_1) > 0$ for $\Delta f_1 < f_1 < 1 - \Delta f_1$] is lower than that at $\tau = 0.21$. By $\tau = 1.01$, the transition to a three-dimensional, turbulent mixing layer has begun. Accordingly, $P(f_1)$ reflects this transition by exhibiting a growing peak about $f_1 = 0.5 \pm 0.3$, that indicates a greater fraction of the fluid within the layer is mixed. By $\tau = 1.52$, this central peak of mixed fluid continues to grow in magnitude, indicating that the fraction of mixed fluid within the layer continues to increase at the latest times.

Another observation can be made about the final PDF at $\tau = 1.52$. The shape of $P(f_1)$ and location of its peak changes across the mixing layer. Above the centerplane ($z = 0$), the peak of $P(f_1)$ is located at $f_1 \approx 0.4$. This indicates that the composition of the mixed fluid primarily consists of the lighter fluid. Conversely, the peak of $P(f_1)$ below the centerplane occurs at $f_1 \approx 0.6$, indicating that the mixed fluid composition

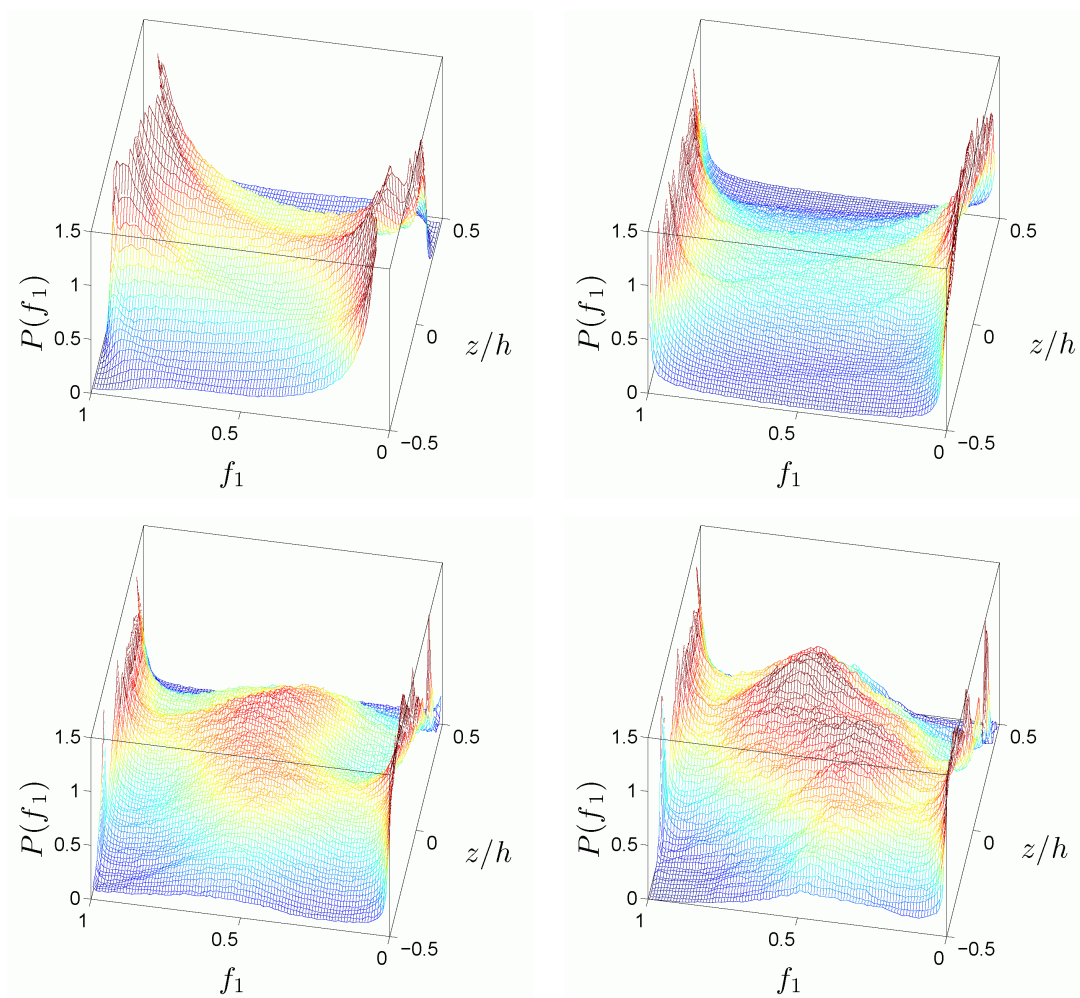


Figure 3.28 Probability density function $P(f_1)$ across the mixing layer at $\tau = 0.21$, 0.50, 1.01, and 1.52.

favors the heavy fluid. This is physically rationalized by the following argument. Heavy fluid falling downward has little residence time within the mixing layer before it crosses the centerplane. Thus, the probability of finding pockets of pure heavy fluid is greater above the centerplane than lower below the centerplane. Conversely, the probability of finding pockets of pure light fluid is greater below the centerplane. The pockets of pure fluid require a finite time to be broken down into smaller eddies, where molecular diffusion processes efficiently mix the two fluids. As a result, the statistical composition of the mixed fluid favors the lighter fluid above the mixing layer and the heavier fluid below the mixing layer.

Karasso and Mungal (1996) presented a thorough overview of scalar PDF measurements in shear-driven mixing layers. They reported that the shape of $P(\phi)$, where ϕ represents either instantaneous concentration or volume fraction measurements, across the mixing layer is a function of both the Reynolds number (even beyond the mixing transition threshold) and the entrainment ratio. At Reynolds numbers just beyond the mixing transition threshold, the location of the inner peak of $P(\phi)$ remains relatively unchanged across the mixing layer, where such a PDF was labeled a ‘non-marching’ type PDF (Konrad 1977; Koochesfahani & Dimotakis 1986; Frieler 1992; Karasso & Mungal 1996). However, some results and models predicted that the location of the peak within the mixing changes as the mixing layer is traversed (Batt 1977; Karasso & Mungal 1996). Such a model PDF is labeled a ‘marching’ PDF. A combination of the marching and non-marching PDF shapes was also measured (Frieler 1992; Karasso & Mungal 1996), and is labeled as a ‘tilted’ PDF.

Measurements in shear-driven mixing have examined the statistics of solely the mixed fluid, where the peak values at $P(f_1 = 0)$ and $P(f_1 = 1)$ that represent unmixed fluid are removed from the statistical measurement of \bar{f}_1 (Koochesfahani & Dimotakis 1986; Karasso & Mungal 1996; Dimotakis 2005; Meyer *et al.* 2006).

As a consequence of removing the unmixed fluid contribution of $P(f_1)$ from \bar{f}_1 , the influence of intermittency effects may also be removed as the entrained pockets of unmixed fluid are primarily irrotational. The average composition of the mixed fluid \bar{f}_1^m , denoted by the superscript m , quantifies the location of such a peak and the statistical composition of the mixed fluid by calculating the first moment of $P(f_1)$ without the pure-fluid contributions of $P(f_1 = 0)$ and $P(f_1 = 1)$, such that

$$\bar{f}_1^m = \frac{\int_{\Delta f_1}^{1-\Delta f_1} f_1 P(f_1) df_1}{\int_{\Delta f_1}^{1-\Delta f_1} P(f_1) df_1}, \quad (3.39)$$

where $\Delta f_1 = 0.05$ was selected to parallel the analysis of shear-driven mixing by Koochesfahani and Dimotakis (1986). The mean mixed fluid composition was calculated using several values above and below $\Delta f_1 = 0.05$ and was found to have a negligible dependence on the exact value of Δf_1 . Profiles of \bar{f}_1^m across the mixing layer are shown in figure 3.29. Once the mixing layer enters a nonlinear transition to turbulence stage ($Re_h > 200$), the mean mixed fluid composition remains relatively constant with an oscillatory behavior about $\bar{f}_1^m = 0.5 \pm 0.1$. However, at the highest Reynolds number achieved, the mixed fluid PDF relaxes into a tilted form, as seen by the continuous increase in \bar{f}_1^m across the mixing layer ($|z/h| < 0.4$). It remains unclear whether the mixing layer reverts to a non-marching PDF after the mixing transition is reached, as seen in post-mixing transition shear layers (Karasso & Mungal 1996).

The statistical composition of the mixed fluid within the mixing layer, shown in figure 3.28, can be further quantified by calculating the skewness and kurtosis of $P(f_1)$. The skewness

$$S_\phi = \frac{\overline{\phi^3}}{\left(\overline{\phi^2}\right)^{3/2}} \quad (3.40)$$

measures the asymmetry of $P(\phi)$. The kurtosis K_ϕ [see (2.11) for a complete defi-

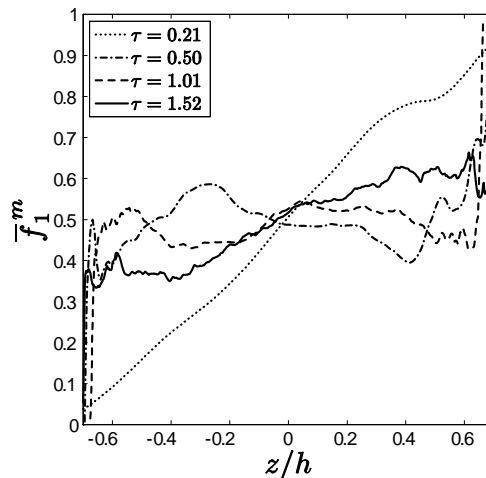


Figure 3.29 Profiles of average mixing fluid composition \bar{f}_1^m across the mixing layer at various times.

tion] measures the ‘peakedness’ of $P(\phi)$. Profiles of S_{f_1} and K_{f_1} , measured from $P(f_1)$, are shown in figure 3.30. The skewness S_{f_1} indicates a bias towards the heavier fluid above the centerplane of the mixing layer and the lighter fluid below the centerplane. This is expected as pockets of unmixed, irrotational fluid are entrained into the layer at the boundaries of the layer. These pockets of unmixed fluid are subsequently broken up and mixed as they cross through the turbulent layer. The kurtosis of $P(f_1)$ indicates highly non-Gaussian behavior; $S_{f_1} = 0$ and $K_{f_1} = 3$ indicate a Gaussian distribution.

The statistical composition of the mixed fluid across the mixing layer is shown in figures 3.28 and 3.29. The statistical composition of the entire fluid within the layer may be examined by calculating the global volume fraction PDF

$$\bar{P}(f_1) = \frac{1}{h} \int_{h_s}^{h_b} P(f_1) dz. \quad (3.41)$$

The evolution of the global volume fraction PDF is shown in figure 3.31. At $\tau = 0.21$

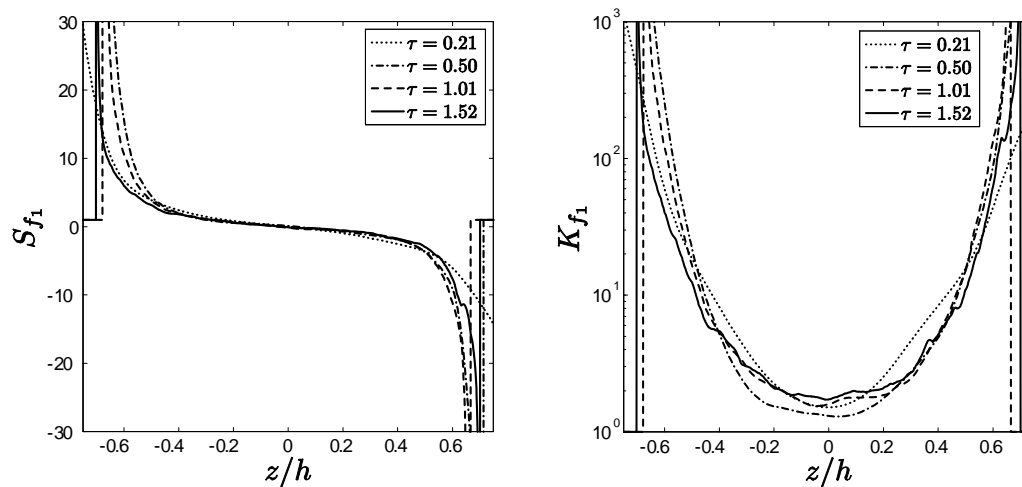


Figure 3.30 Profiles of the skewness and kurtosis of $P(f_1)$ across the mixing layer at various times.

and 0.5, the bimodal distribution of $P(f_1)$ seen in figure 3.28 at the same times, becomes more evident. Once the flow transitions into a turbulent mixing layer, greater quantities of mixed fluid are found.

3.6 Budgets of Turbulent Transport and Mixing Equations

The mixing measurements shown in § 3.5 are a result of the complex interactions of a turbulent velocity field and scalar density field. Thus, to predictively model the mixing dynamics, a complete understanding of both the stochastic velocity and density field dynamics is required. Here, the appropriately-averaged turbulent transport equations are examined and the dominant mechanisms in the transport and mixing processes are identified. As noted in § 3.3, the flow is statistically-homogeneous in the x - and y -directions; thus, the three-dimensional flow is reduced to a statistically one-dimensional system for analysis. The exact unclosed transport equations for pertinent statistics will be presented in the following subsections.

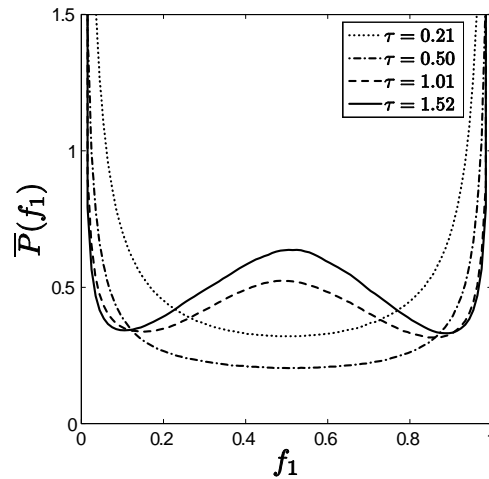


Figure 3.31 Evolution of the global volume fraction probability density function $\bar{P}(f_1)$ at various times.

3.6.1 Mean continuity equation

In general, buoyancy-driven turbulence does not satisfy the Boussinesq (1903) approximation. Accordingly, the Favre-averaged transport equations are typically employed when examining Rayleigh–Taylor mixing layers. While the Boussinesq approximation remains valid for the small Atwood numbers considered in this work, the Favre-averaged framework is retained for generality. As a result, the mean velocity field is not assumed to satisfy the incompressible velocity field constraint $\partial \tilde{u}_i / \partial x_i = 0$. The Reynolds-averaged continuity equation is

$$\frac{D\bar{\rho}}{Dt} = \frac{\partial \bar{\rho}}{\partial t} + \tilde{u}_j \frac{\partial \bar{\rho}}{\partial x_j} = 0, \quad (3.42)$$

where

$$\frac{D}{Dt} = \frac{\partial}{\partial t} + \tilde{u}_j \frac{\partial}{\partial x_j}. \quad (3.43)$$

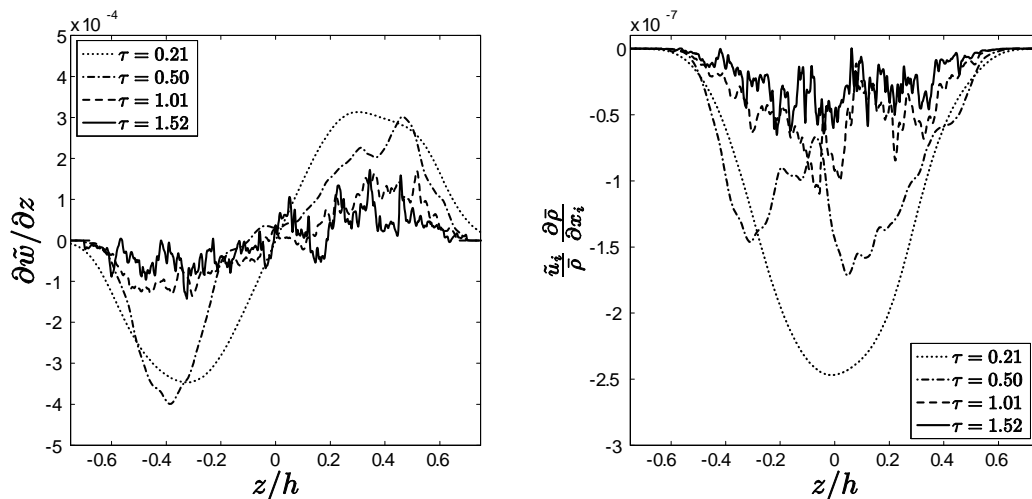


Figure 3.32 Divergence of the Favre-averaged velocity field (left) and advection by the mean velocity field (right) across the Rayleigh–Taylor mixing layer at various times.

The advection by the mean velocity \tilde{u}_j term is negligible for this small Atwood number flow, as shown in figure 3.32 and in § 3.6.2. The divergence of the Favre-averaged velocity field is shown in figure 3.32.

The existence of a non-zero mean (Favre-averaged) vertical velocity is a result of turbulent flux of mass, where $\tilde{w} = \bar{w} + \overline{\rho'w'}/\bar{\rho}$. For small Atwood number, incompressible flows the mean (Reynolds-averaged) vertical velocity is not zero due to the diffusive miscibility of the mixing layer (Joseph 1990), but is still negligible,

$$\bar{w} = -\frac{\bar{D}}{\bar{\rho}} \frac{\partial \bar{\rho}}{\partial z} \approx 0, \quad (3.44)$$

where $\bar{D} = \bar{\nu}/Sc$. Thus for the incompressible, miscible Rayleigh–Taylor mixing layer considered here, $\tilde{w} \approx \overline{\rho'w'}/\bar{\rho}$. While the divergence of the Favre-averaged mean velocity field is non-zero, it will be shown in § 3.6.2 that the magnitude of \tilde{w} is small when compared with the turbulent fluctuations and that the mean advection of transport quantities by \tilde{w} is negligible.

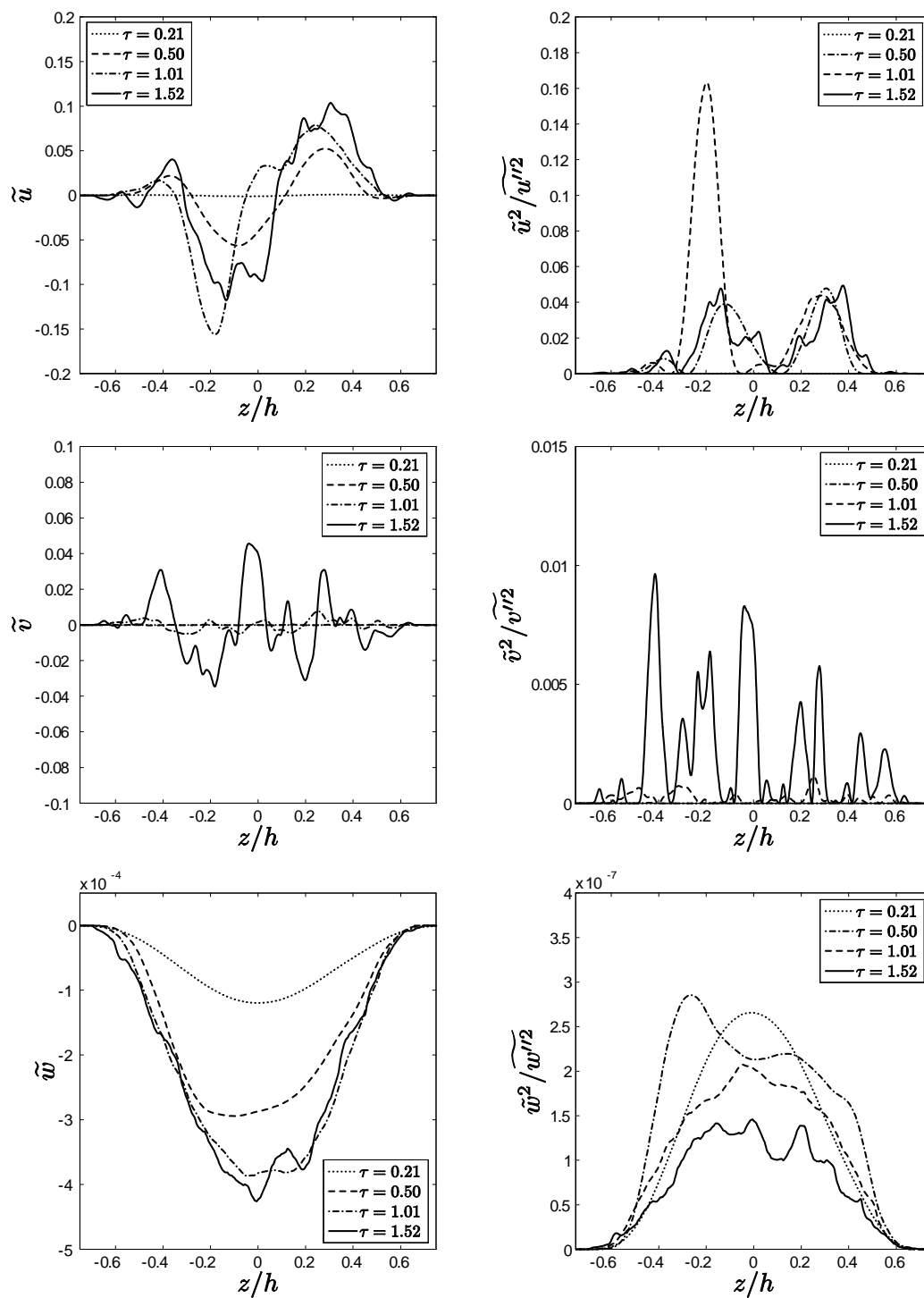


Figure 3.33 Profiles of the Favre-averaged velocity components \tilde{u}_i across the Rayleigh–Taylor mixing layer at various times (left column) obtained from the DNS. Profiles of the relative magnitudes of the mean-square velocities with respect to the turbulent velocity fluctuations (right column).

3.6.2 Mean momentum transport

The averaged Navier–Stokes equations are

$$\bar{\rho} \frac{D\tilde{u}_i}{Dt} = \bar{\rho} g_i - \frac{\partial \bar{p}}{\partial x_i} + \frac{\partial}{\partial x_j} (\bar{\sigma}_{ij} - \tau_{ij}) , \quad (3.45)$$

where $\tau_{ij} = \bar{\rho} \widetilde{u_i'' u_j''}$ is the Reynolds stress tensor. Unlike shear-driven turbulence, where velocity gradients are the driving force, Rayleigh–Taylor mixing layers have no mean velocity or mean velocity gradients in their canonical arrangement. Figure 3.33 shows the mean profiles for each velocity component and its relative magnitude compared with the velocity variance $\widetilde{u_i''^2}$ at various times. The mean velocities in the homogeneous directions are small and oscillatory. The departure of \tilde{u} and \tilde{v} from zero is a result of the departure from statistical convergence, as noted in § 3.4.3. While the mean advective velocities are not identically zero, it will be shown that the influence of all mean velocity gradients is negligible on both the turbulence and mixing dynamics. The Favre-averaged velocity in the z -direction is not oscillatory; rather, it is small in magnitude and negative. This is a result of $\tilde{w} = \bar{w} + \overline{\rho' w'} / \bar{\rho}$, where $\overline{\rho' w'}$ is the turbulent mass flux of the heavy fluid in the downward direction.

While the mean velocity field and its gradients are of minimal importance to the mixing dynamics, the Reynolds stress tensor is responsible for the turbulent transport of momentum. All six components of $\widetilde{u_i'' u_j''}$ are shown in figure 3.34. The diagonal components are clearly dominant, as expected in the absence of any significant mean velocity gradient. The vertical velocity fluctuations $\widetilde{w''^2}$ are also the largest, as τ_{33} is aligned with the forcing term $\bar{\rho} g_3$. For the case considered in the DNS, where the mixing layer has only one direction of statistical inhomogeneity, the vertical velocity fluctuations are the most important redistribution mechanism. The influence of the turbulent velocity fluctuations will be further examined in § 3.6.3–3.6.7.

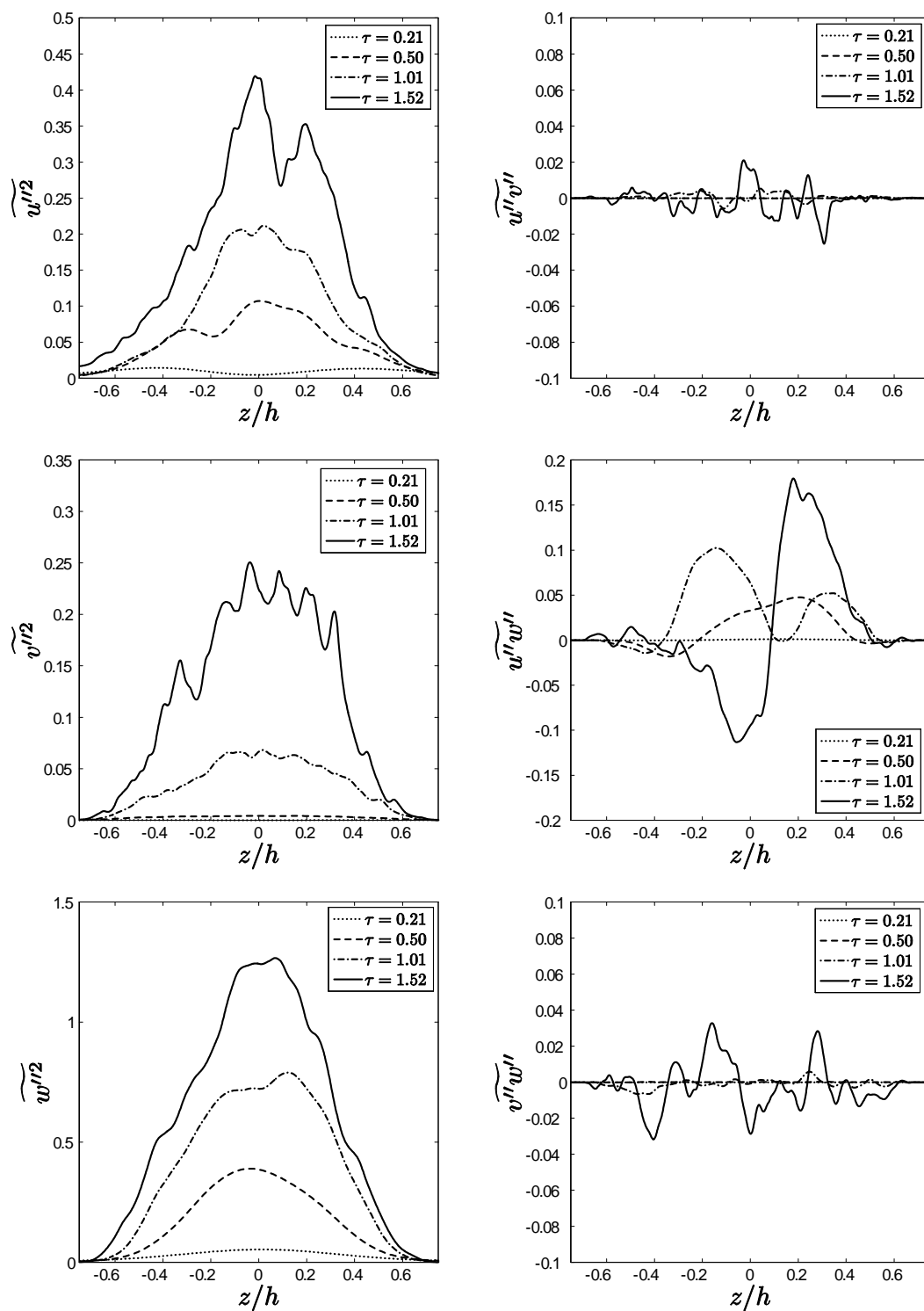


Figure 3.34 Profiles of fluctuation velocity correlations $\overline{u_i' u_j'}$ across the Rayleigh–Taylor mixing layer at various times obtained from the DNS.

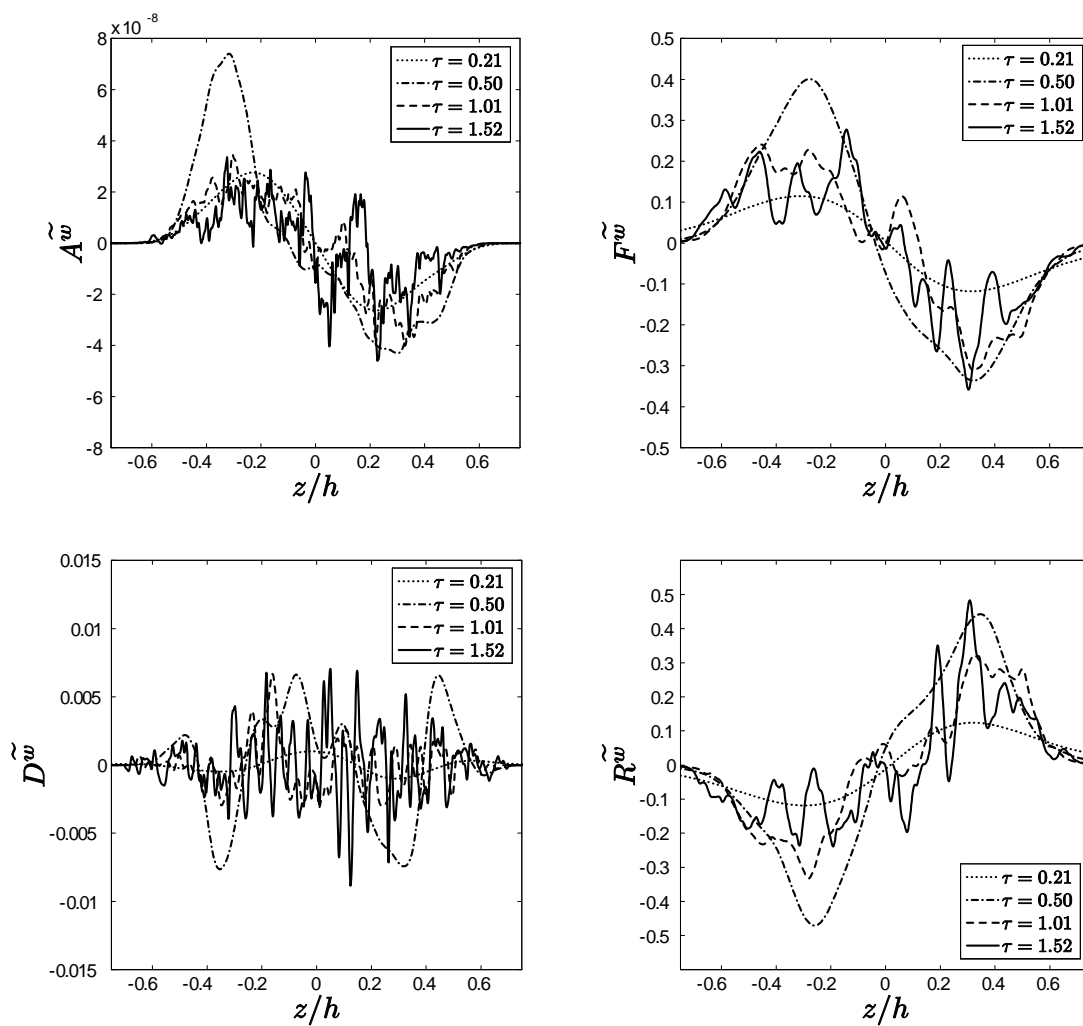


Figure 3.35 Profiles of the terms in the \tilde{w} -component of the mean momentum equation across the Rayleigh–Taylor mixing layer at various times.

While the mean velocity in the vertical direction is small, it is related to the downward turbulent flux of the heavy fluid. For completeness, the budget of the \tilde{w} -component of the mean momentum equation is examined here. The advection, forcing, diffusive, and Reynolds stress terms for the mean vertical velocity are

$$A^{\tilde{w}} = \bar{\rho} \tilde{w} \frac{\partial \tilde{w}}{\partial z}, \quad (3.46a)$$

$$F^{\tilde{w}} = -\frac{\partial \bar{p}}{\partial z} - \bar{\rho} g, \quad (3.46b)$$

$$D^{\tilde{w}} = \frac{\partial \bar{\sigma}_{33}}{\partial z}, \quad (3.46c)$$

$$R^{\tilde{w}} = -\frac{\partial \tau_{33}}{\partial z}. \quad (3.46d)$$

Profiles of each term are shown in figure 3.35. In small Atwood number flows, the contribution of the advection term is negligible. The diffusive term smooths small fluctuations and gradients in the \tilde{w} field, which become larger at late time. However, the overall contribution of $D^{\tilde{w}}$ also remains negligible. As a result, the remaining forcing and Reynolds stress term are significant, but balance one another, $F^{\tilde{w}} = -R^{\tilde{w}}$. For the vertical velocity component, the mean pressure gradient does not balance the hydrostatic head alone; however,

$$-\bar{\rho} g - \frac{\partial \bar{p}}{\partial z} = \frac{\partial \tau_{33}}{\partial z}. \quad (3.47)$$

3.6.3 Mean mass fraction transport

While the mean momentum equation has little influence on the development of the mixing layer, the mean density field and its gradient serve as the potential energy source for the generated turbulence. The unclosed averaged heavy-fluid mass fraction transport equation is

$$\bar{\rho} \frac{D\tilde{m}_1}{Dt} = T^{\tilde{m}_1}, \quad (3.48)$$

where the turbulent transport term is

$$T^{\tilde{m}_1} = \frac{\partial}{\partial x_j} \left(\frac{\bar{\mu}}{Sc} \frac{\partial \tilde{m}_1}{\partial x_j} - \bar{\rho} \widetilde{u_j'' m_1''} \right), \quad (3.49)$$

where $\bar{\mu}$ is the average dynamic viscosity. In variable-density flows, fluctuations in the dynamic viscosity $\mu = \bar{\mu} + \mu'$ must be considered. However, in the limit of small density and viscosity fluctuations (*i.e.* $\overline{\mu' \phi''} \ll \bar{\mu} \tilde{\phi}$), the transport assumptions can be simplified (Vandromme & Ha Minh 1983; Chassaing *et al.* 2002)

$$\frac{\overline{\mu}}{Sc} \frac{\partial m_1}{\partial x_j} = \frac{\bar{\mu}}{Sc} \frac{\partial \tilde{m}_1}{\partial x_j}. \quad (3.50)$$

The mass fraction field has values $0 \leq \tilde{m}_1 \leq 1$ and, in the absence of chemical reactions, has no physical source or sink terms. As a result, the only physical mechanisms for the transport of \tilde{m}_1 are viscous diffusion (related to the gradient of \tilde{m}_1) and turbulent velocity fluctuations given by the flux $\widetilde{w'' m_1''}$. The mean heavy-fluid mass fraction profiles are shown in figure 3.36. Similar to the experimentally-measured volume fraction profiles in figure 2.13, the profiles of \tilde{m}_1 collapse to an approximately linear form. This is expected for small Atwood number mixing layers as the mean mass fraction is related to the volume fraction field by

$$\bar{\rho} \tilde{m}_1 = \rho_1 \bar{f}_1. \quad (3.51)$$

As a result, the diffusive transport of \tilde{m}_1 is only significant at very early times when $\partial \tilde{m}_1 / \partial z$ is significant and $\widetilde{w'' m_1''} \rightarrow 0$ as $Re_h \rightarrow 0$.

The transport term $T^{\tilde{m}_1}$ is shown in figure 3.37. Positive values of $T^{\tilde{m}_1}$ on the spike side of the mixing layer indicate an accumulation of heavy fluid, while the negative values of $T^{\tilde{m}_1}$ on the bubble side indicate a loss of heavy fluid. Physically, this is expected as the heavy fluid continues to fall into the lighter fluid. The transport

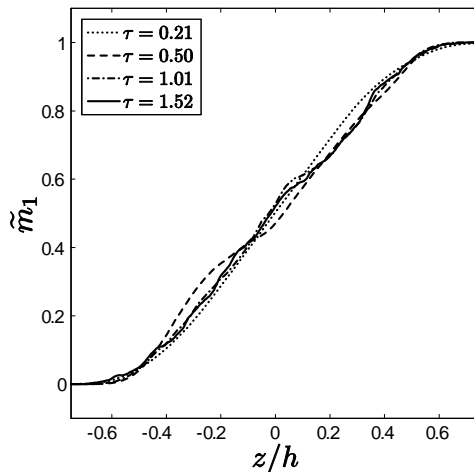


Figure 3.36 Profiles of the mean heavy-fluid mass fraction \tilde{m}_1 across the Rayleigh—Taylor mixing layer at various times obtained from the DNS.

term $T^{\tilde{m}_1}$ can be broken down into its diffusive and turbulent flux components

$$F_d^{\tilde{m}_1} = -\frac{\bar{\mu}}{Sc} \frac{\partial \tilde{m}_1}{\partial z}, \quad (3.52)$$

$$F_t^{\tilde{m}_1} = \overline{\bar{\rho} w'' m_1'}. \quad (3.53)$$

Profiles of each flux component at different times are shown in figure 3.38. The turbulent flux term dominates; however, the diffusive term cannot be neglected for $\tau \leq 0.2$.

3.6.4 Turbulent kinetic energy transport

While the mean momentum and mass fraction transport equations describe the growth of the mixing layer, they do not describe the nature of the turbulent flow field or the mixing dynamics. In addition, *a priori* knowledge of otherwise unknown turbulent correlations is required to close the mean field transport equations. In the following sections, the transport equations that govern the turbulent flow field and fluctuating

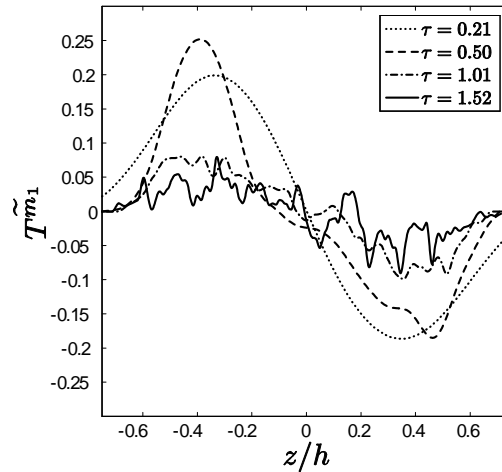


Figure 3.37 Profiles of the mean mass fraction turbulent transport term $T^{\tilde{m}_1}$ across the Rayleigh–Taylor mixing layer at various times.

density statistics are presented and analyzed.

The first equation examined is the turbulent kinetic energy transport equation. Profiles of the turbulent kinetic energy per unit mass $\tilde{E}'' = \tilde{u}_i''^2/2$ are shown in figure 3.39. As seen in the Reynolds stress tensor profiles, the profiles of \tilde{E}'' are peaked in the turbulent core of the mixing layer.

In classical turbulent flows, such as boundary layers, shear flows, wakes, and jets, there is steady exchange of energy between the mean and turbulent kinetic energy fields. Typically, energy is removed from the mean kinetic energy ($\tilde{E} = \tilde{u}_i^2/2$) by shearing forces, transferred to the turbulent kinetic energy ($\tilde{E}'' = \tilde{u}_i''^2/2$), and finally dissipated to thermal energy by viscous forces, *i.e.* into the mean temperature field. However, this is not the case in Rayleigh–Taylor driving mixing. Instead, the turbulent kinetic energy is driven directly by the release of potential energy from the

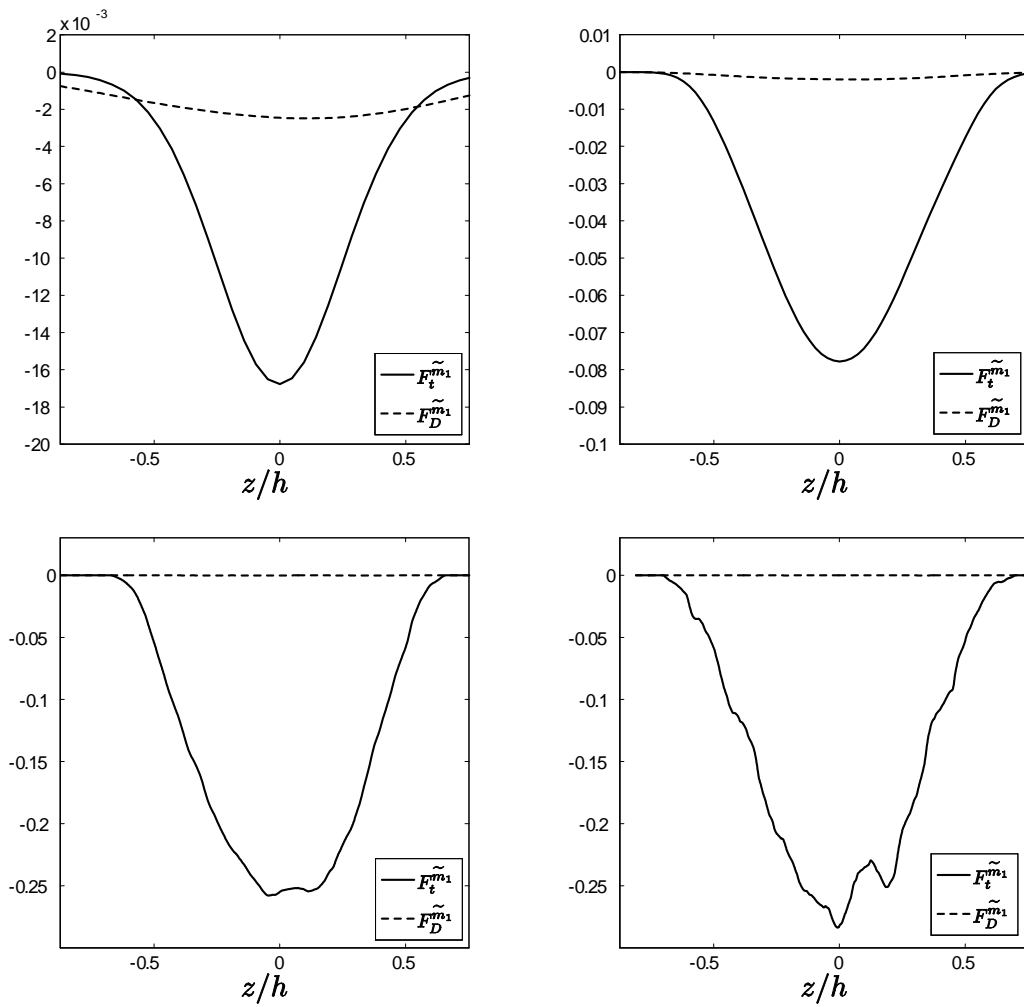


Figure 3.38 Profiles of the mean mass fraction flux terms in the transport term $T^{\tilde{m}_1}$ across the Rayleigh–Taylor mixing layer at $\tau = 0.034, 0.21, 1.01,$ and 1.52 (left-to-right, top-to-bottom).

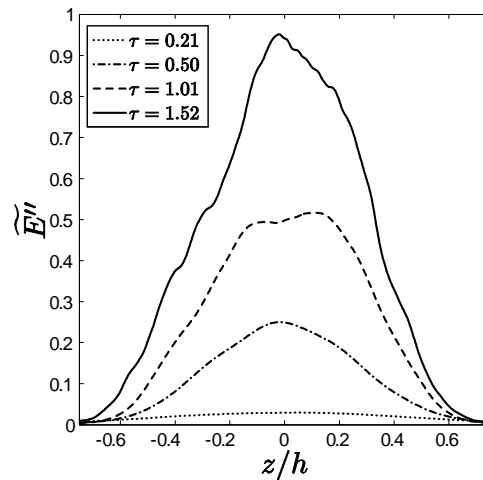


Figure 3.39 Profiles of the turbulent kinetic energy \widetilde{E}'' across the Rayleigh–Taylor mixing layer at various times.

falling heavy fluid. The total amount of potential energy per unit volume is

$$PE(t) = -\frac{1}{L_z} \int_{-L_z/2}^{L_z/2} \bar{\rho} g z \, dz, \quad (3.54)$$

and the cumulative amount of potential energy released $\delta PE(t) = PE(t=0) - PE(t)$ is shown in figure 3.40. The evolution of the total mean kinetic energy per unit volume

$$MKE(t) = \frac{1}{L_z} \int_{-L_z/2}^{L_z/2} \widetilde{E} \, dz, \quad (3.55)$$

total turbulent kinetic energy per unit volume

$$TKE(t) = \frac{1}{L_z} \int_{-L_z/2}^{L_z/2} \widetilde{E}'' \, dz, \quad (3.56)$$

and cumulative turbulent kinetic energy dissipated per unit volume

$$D(t) = \frac{1}{L_z} \int_0^t \int_{-L_z/2}^{L_z/2} D\widetilde{E}'' \, dz \, dt \quad (3.57)$$

are also shown in figure 3.40 [see (3.59a) below for a formal definition of the dis-

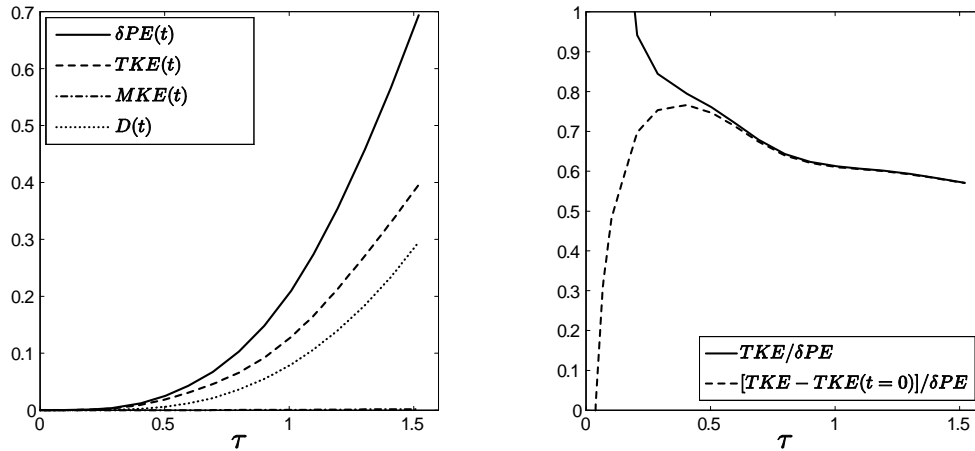


Figure 3.40 Evolution of potential energy released, turbulent kinetic energy, mean kinetic energy, and cumulative turbulent kinetic energy dissipated (left). Ratio of turbulent kinetic energy to potential energy released (right).

sipation rate]. The release of potential energy into the Rayleigh–Taylor mixing layer in the form of turbulent kinetic energy can be seen in figure 3.40. The ratio of turbulent kinetic energy to potential energy released is also shown in figure 3.40, where $TKE/\delta PE \approx 0.57$ at the latest time. This is larger than the values $TKE/\delta PE \approx 0.48$ – 0.52 from experimental measurements (Ramaprabhu & Andrews 2004; Banerjee 2006) and numerical simulations (Youngs 1994; Ramaprabhu *et al.* 2005; Cabot & Cook 2006); however, the ratio $TKE/\delta PE$ in the current DNS is still decreasing at $\tau = 1.52$. In addition, Ramaprabhu *et al.* (2005) demonstrated that the specific initial conditions can impact this ratio, where a range of $TKE/\delta PE \approx 0.48$ – 0.70 was reported.

As observed in § 3.6.2, the dynamics of the mean momentum equation are negligible for small Atwood number Rayleigh–Taylor mixing layers. This is also confirmed from the evolution of MKE in figure 3.40. The ratio of mean-to-turbulent kinetic energy is also shown in figure 3.41, where the mean field remains less than 1% of the turbulent field. Thus, the classical energy transfer phenomenology used to describe

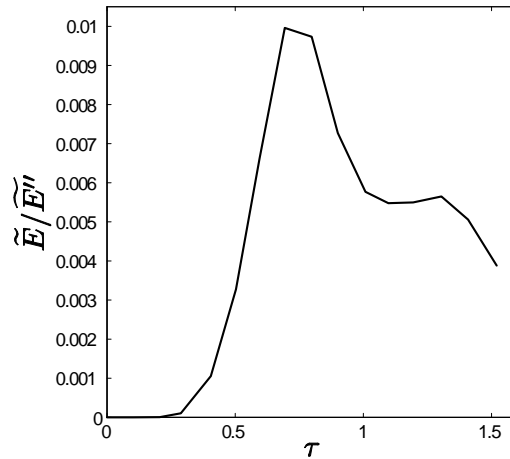


Figure 3.41 Ratio of mean kinetic energy to turbulent kinetic energy within the mixing layer.

shear-driven flows, where energy is exchanged between the mean and turbulent kinetic energy fields by shearing forces, does not apply to Rayleigh–Taylor driven mixing.

The exact, unclosed turbulent kinetic energy transport equation is

$$\bar{\rho} \frac{D\widetilde{E}''}{Dt} = P_b^{\widetilde{E}''} + P_s^{\widetilde{E}''} + \Pi^{\widetilde{E}''} + T^{\widetilde{E}''} - D^{\widetilde{E}''}, \quad (3.58)$$

where the buoyancy production, shear production, pressure dilatation, turbulent transport, and dissipation terms are (Chassaing *et al.* 2002; Wilcox 2006)

$$P_b^{\widetilde{E}''} = -\overline{u_j''} \frac{\partial \bar{p}}{\partial x_j}, \quad (3.59a)$$

$$P_s^{\widetilde{E}''} = -\bar{\rho} \overline{u_i'' u_j''} \frac{\partial \widetilde{u}_i}{\partial x_j}, \quad (3.59b)$$

$$\Pi^{\widetilde{E}''} = \overline{p' \frac{\partial u_i''}{\partial x_i}}, \quad (3.59c)$$

$$T^{\widetilde{E}''} = -\frac{\partial}{\partial x_j} \left(\overline{\rho u_j'' \widetilde{E}''} + \overline{p' u_j''} - \overline{u_i'' \sigma_{ij}''} \right), \quad (3.59d)$$

$$D^{\widetilde{E}''} = \bar{\rho} \widetilde{\epsilon}'' = \overline{\sigma_{ij}'' \frac{\partial u_i''}{\partial x_j}} + \overline{u_j'' \frac{\partial \widetilde{\sigma}_{jk}}{\partial x_k}}. \quad (3.59e)$$

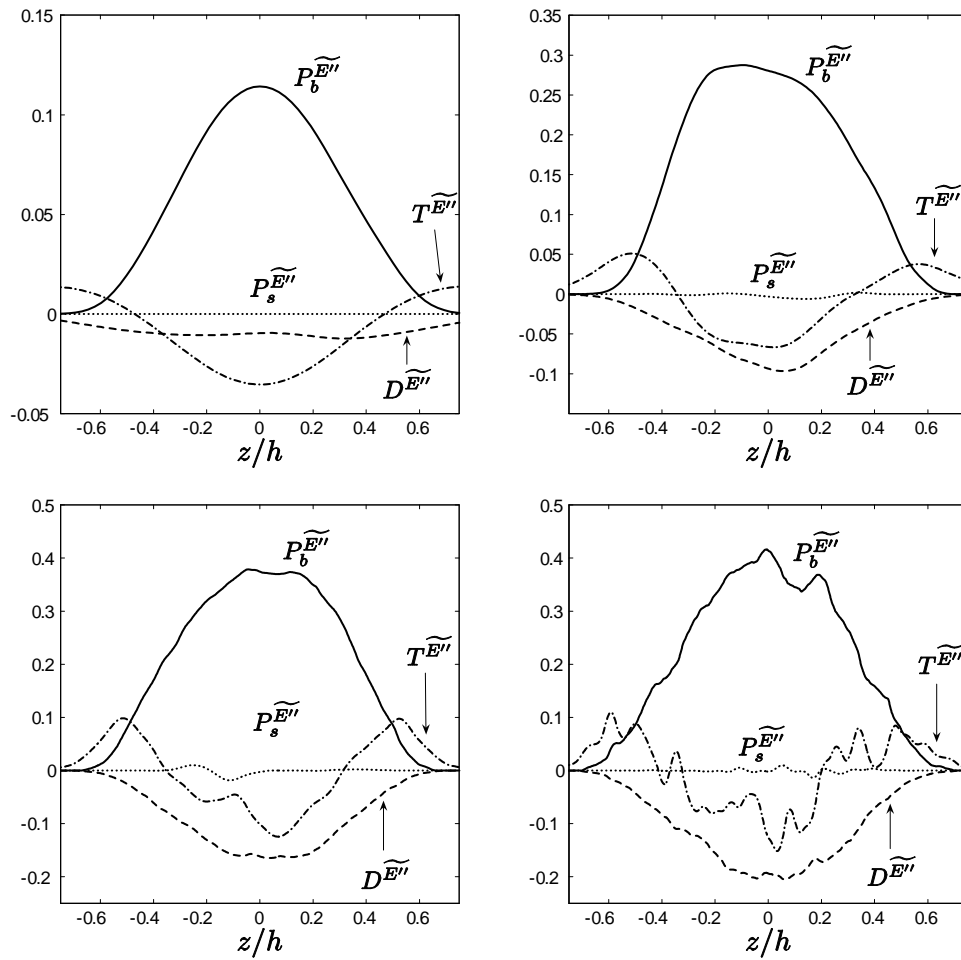


Figure 3.42 Profiles of the dominant terms in the turbulent kinetic energy transport equation across the Rayleigh–Taylor mixing layer at $\tau = 0.21, 0.50, 1.01,$ and 1.52 (left-to-right, top-to-bottom).

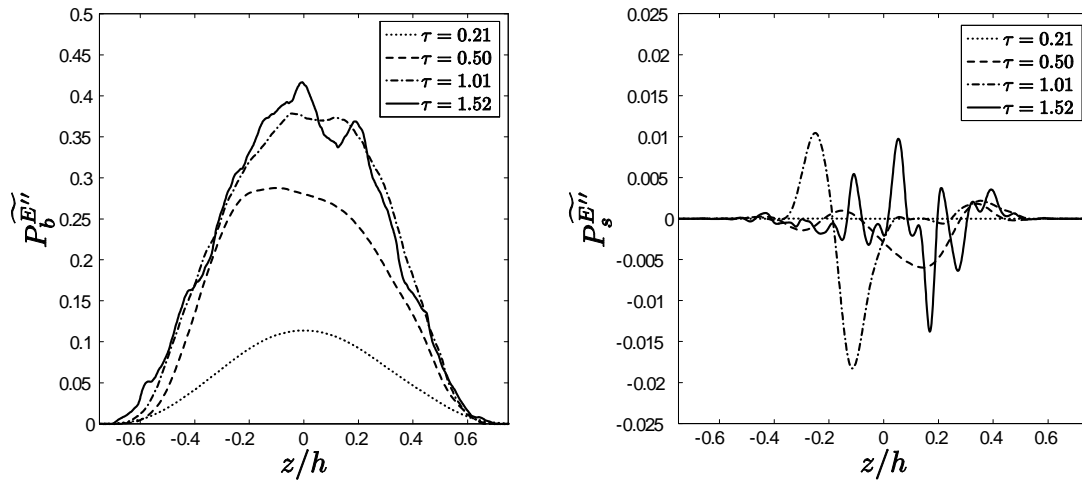


Figure 3.43 Profiles of the buoyancy and shear production terms $P_b^{\widetilde{E}''}$ and $P_s^{\widetilde{E}''}$ in the turbulent kinetic energy transport equation across the Rayleigh–Taylor mixing layer at various times.

Profiles across the mixing layer of the dominant terms from the \widetilde{E}'' transport equation are shown in figure 3.42 at various times. The overall form of the transport terms remain similar for all times observed, where the buoyancy production remains positive and generates turbulent kinetic energy within the core of the mixing layer ($|z/h| < 0.5$). The viscous dissipation term is negative definite and removes turbulent kinetic energy from the core. The transport term has a more complex shape, where it is negative within the core of the mixing layer ($|z/h| \lesssim 0.4$) and positive near the outer regions of the mixing layer ($|z/h| \gtrsim 0.4$), demonstrating that energy is removed from the turbulent core and transported to the edges of the layer.

Profiles of the buoyancy and shear production terms are shown in figure 3.43. As noted in § 3.6.2, the mean velocity gradient contribution to the overall production of turbulent kinetic energy is negligible. The primary source of kinetic energy for this flow arises from the mean pressure gradients in $P_b^{\widetilde{E}''}$. In models of $P_b^{\widetilde{E}''}$, the mean pressure gradient is a known mean field quantity. Therefore, an accurate closure for

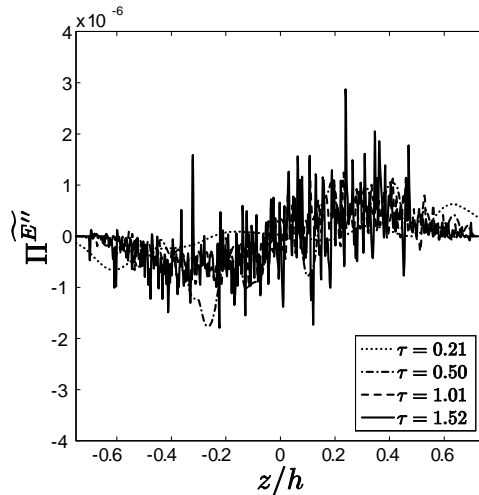


Figure 3.44 Profiles of the pressure dilatation term $\Pi^{\widetilde{E''}}$ in the turbulent kinetic energy transport equation across the Rayleigh–Taylor mixing layer at various times.

the density-velocity correlation $\overline{u_i''} = -\overline{\rho' u_i'} / \bar{\rho}$ is critical when modeling Rayleigh–Taylor mixing.

In compressible flows, energy may be transferred between turbulent kinetic energy and internal energy (thermal energy) by the compression or expansion of a volume of fluid. Profiles of $\Pi^{\widetilde{E''}}$ are shown in figure 3.44. The flow considered here is incompressible, but $\Pi^{\widetilde{E''}} \neq 0$ as a result of miscibility of the two fluids (Joseph 1990). However, while the divergence of the velocity field is not zero, it does scale with the local density gradients. Thus, for the small Atwood numbers considered in this work, $\Pi^{\widetilde{E''}}$ remains negligible.

The conservative redistribution of $\widetilde{E''}$ throughout the mixing layer is given by the turbulent transport term $T^{\widetilde{E''}}$, shown in figure 3.45. Regions of positive $T^{\widetilde{E''}}$ indicate a gain of $\widetilde{E''}$, whereas negative regions of $T^{\widetilde{E''}}$ indicate loss of $\widetilde{E''}$. Profiles of $T^{\widetilde{E''}}$ show that energy is transferred from the central core of the mixing layer, $|z/h| \lesssim 0.3$,

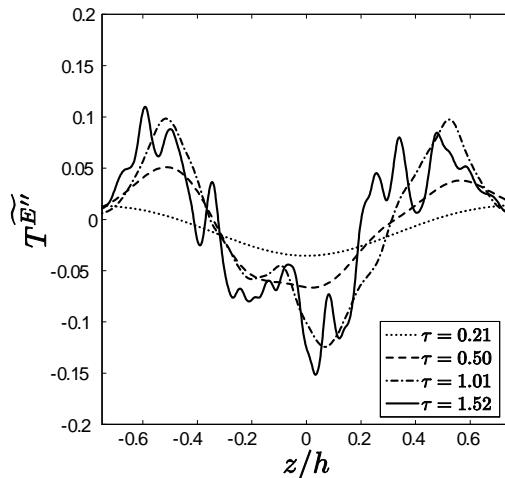


Figure 3.45 Profiles of the transport term $T^{\widetilde{E}''}$ in the turbulent kinetic energy transport equation across the Rayleigh–Taylor mixing layer at various times.

to the outer edges. Thus, the turbulent kinetic energy migrates in a down-gradient manner from regions of higher energy within the core of the mixing layer to regions of lower energy at the edges of the layer.

While the total transport term $T^{\widetilde{E}''}$ is shown in figure 3.45, this term can be decomposed into its turbulent kinetic energy flux components due to turbulent, pressure, and viscous transport

$$F_t^{\widetilde{E}''} = \overline{\bar{\rho} w'' E''}, \quad (3.60a)$$

$$F_p^{\widetilde{E}''} = \overline{p' w''}, \quad (3.60b)$$

$$F_d^{\widetilde{E}''} = -\overline{w'' \sigma_{33}''} \quad (3.60c)$$

These terms are examined in detail as canonical closure phenomenology typically neglects $F_d^{\widetilde{E}''}$ and groups $F_t^{\widetilde{E}''} + F_p^{\widetilde{E}''}$ into a single gradient-diffusion closure (Wilcox 2006). As shown here, these assumptions are not entirely accurate for Rayleigh–Taylor driven mixing layers. Early-time profiles ($\tau \leq 0.3$) of each flux are shown in

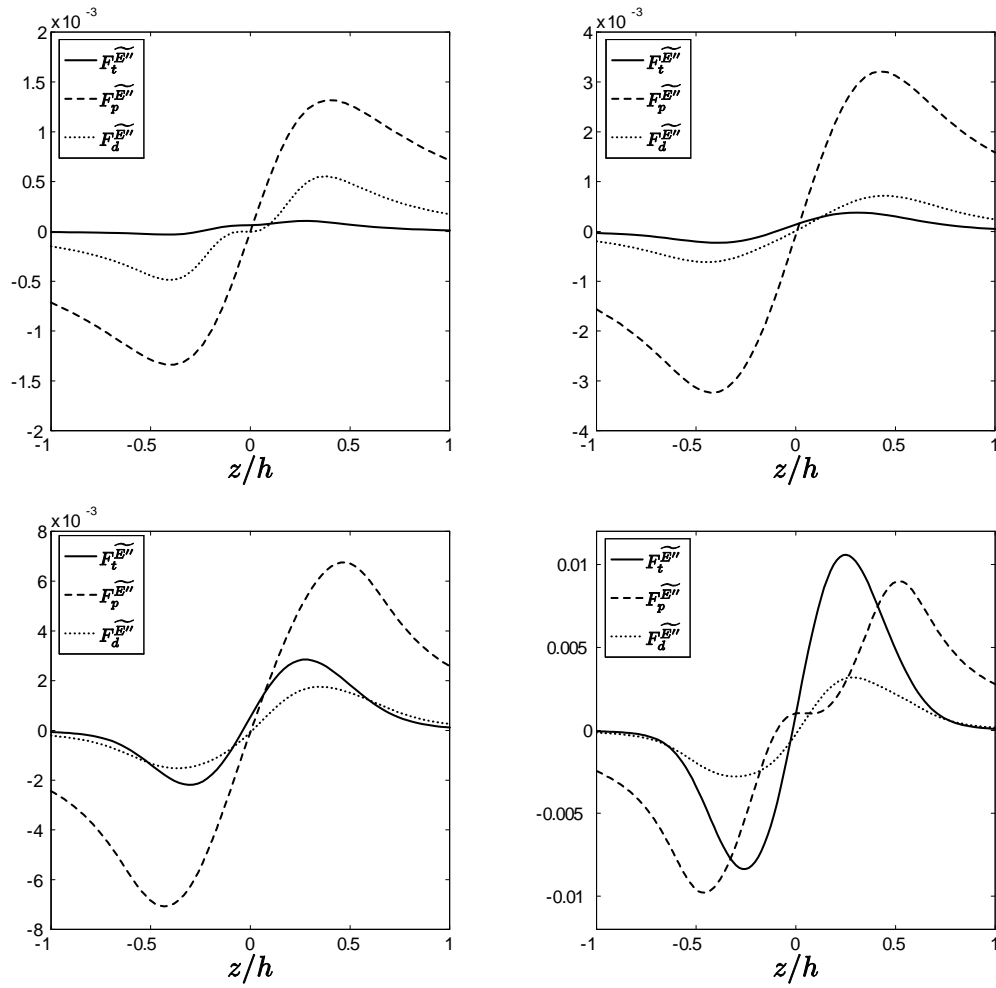


Figure 3.46 Early-time profiles of the turbulent kinetic energy flux terms in the transport term $T_tilde^{E''}$ across the Rayleigh–Taylor mixing layer at $\tau = 0.034, 0.10, 0.21,$ and 0.29 (left-to-right, top-to-bottom).

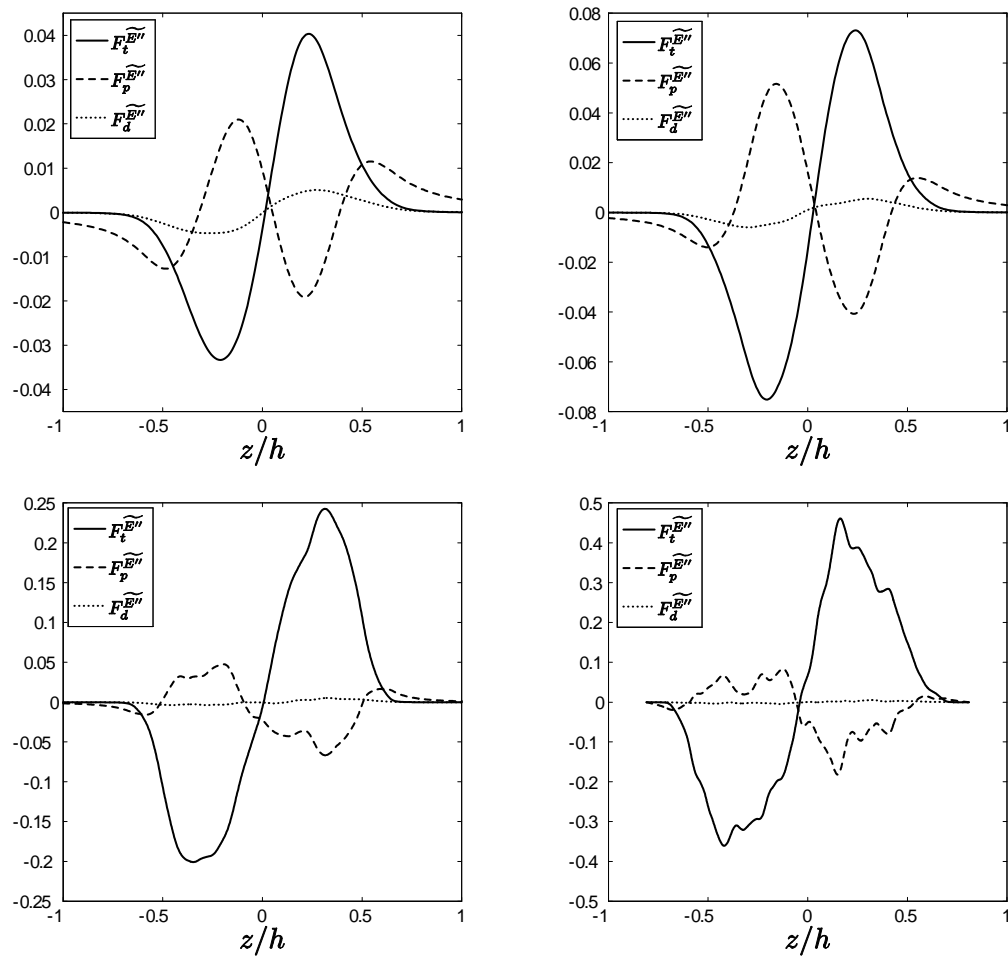


Figure 3.47 Intermediate- and late-time profiles of the turbulent kinetic energy flux terms in the transport term $T^{E''}$ across the Rayleigh–Taylor mixing layer at $\tau = 0.41, 0.50, 1.01,$ and 1.52 (left-to-right, top-to-bottom).

figure 3.46. Figure 3.47 shows the same profiles at later times ($\tau > 0.4$). Several qualitative observations can be made about the early-time flux components. First, all flux components follow a similar profile, transferring energy away from the centerplane of the mixing layer. Second, the turbulent flux $F_t^{\widetilde{E}''}$ is least important at $\tau \leq 0.1$. Accordingly, standard gradient-diffusion models are not expected to capture the transport physics accurately. Finally, the pressure transport has a significant, non-zero energy flux at the boundaries of the mixing layer and beyond. While the fluid outside the mixing layer remains nearly inviscid, instantaneous velocity fluctuations outside the layer exist due to the fluctuating pressure field created by the rising bubbles and falling spikes. Accordingly, all fluctuations outside the mixing layer are driven by pressure fluctuations resulting from the incompressible nature of the flow. This is the same process noted by Bradshaw (1994), where irrotational velocity fluctuations are induced at the free stream edges of shear layers and jets by pressure fluctuations.

For $\tau \geq 0.4$, $F_t^{\widetilde{E}''}$ becomes the dominant flux, transferring turbulent kinetic energy away from the central core of the mixing layer by means of velocity fluctuations. All other fluxes are negligible with the exception of the pressure transport term $F_p^{\widetilde{E}''}$, which has a more complex behavior. Within the core of the Rayleigh–Taylor mixing layer ($|z/h| \leq 0.5$), $F_p^{\widetilde{E}''}$ opposes the turbulent flux of kinetic energy in a counter-gradient manner. However, outside the core of the Rayleigh–Taylor mixing layer ($|z/h| > 0.5$), the pressure-flux term becomes re-aligned with the down-gradient flux of \widetilde{E}'' . Similar to results shown at early time, $F_p^{\widetilde{E}''}$ is the only significant mechanism for the transport of velocity fluctuations outside of the mixing layer.

To further examine $F_p^{\widetilde{E}''}$, profiles of the normalized pressure transport are shown in figure 3.48. The early-time bifurcation is clearly seen as $F_p^{\widetilde{E}''}$ transports energy away from the centerplane of the Rayleigh–Taylor mixing layer at $\tau < 0.288$, and

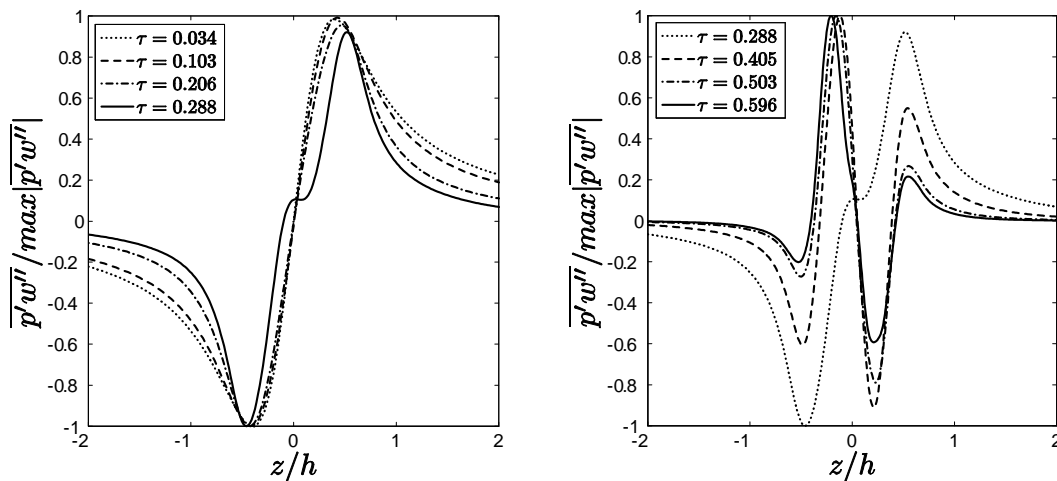


Figure 3.48 Profiles of the normalized pressure transport term across the Rayleigh—Taylor mixing layer at early-times (left) and intermediate-times (right). The bifurcation point for the sign of $\overline{p'w''}$ within the core of the mixing layer is seen at $\tau = 0.288$.

quickly switches to opposing $F_t^{\widetilde{E}''}$ at $\tau > 0.288$. This bifurcation corresponds to the initial formation of secondary vortices in-between rising and falling structures. As a result, pockets of low pressure form in the centers of the vortices. Figure 3.49 shows the early-time evolution of a slice of the density and pressure fields, where the formation of the secondary instabilities is visible. This transition at $\tau = 0.288$, however, does not affect the behavior of $F_p^{\widetilde{E}''}$ at the edges of the mixing layer and beyond ($|z/h| \geq 0.5$), where $F_p^{\widetilde{E}''}$ continues to remove energy from the mixing layer to induce velocity fluctuations in the quiescent pure fluid above and below the mixing layer. This behavior complicates the formulation of models of $T^{\widetilde{E}''}$ and will be further discussed in § 4.3.4.

The final term in the transport equation of \widetilde{E}'' is the turbulent dissipation term $D^{\widetilde{E}''} = \bar{\rho}\widetilde{e}''$. Profiles of $D^{\widetilde{E}''}$ are shown in figure 3.50. Similar to the buoyancy-production profiles, the viscous dissipation term is also approximately parabolic with a peak around $z \approx 0$. In Rayleigh–Taylor driven mixing, the turbulent kinetic energy

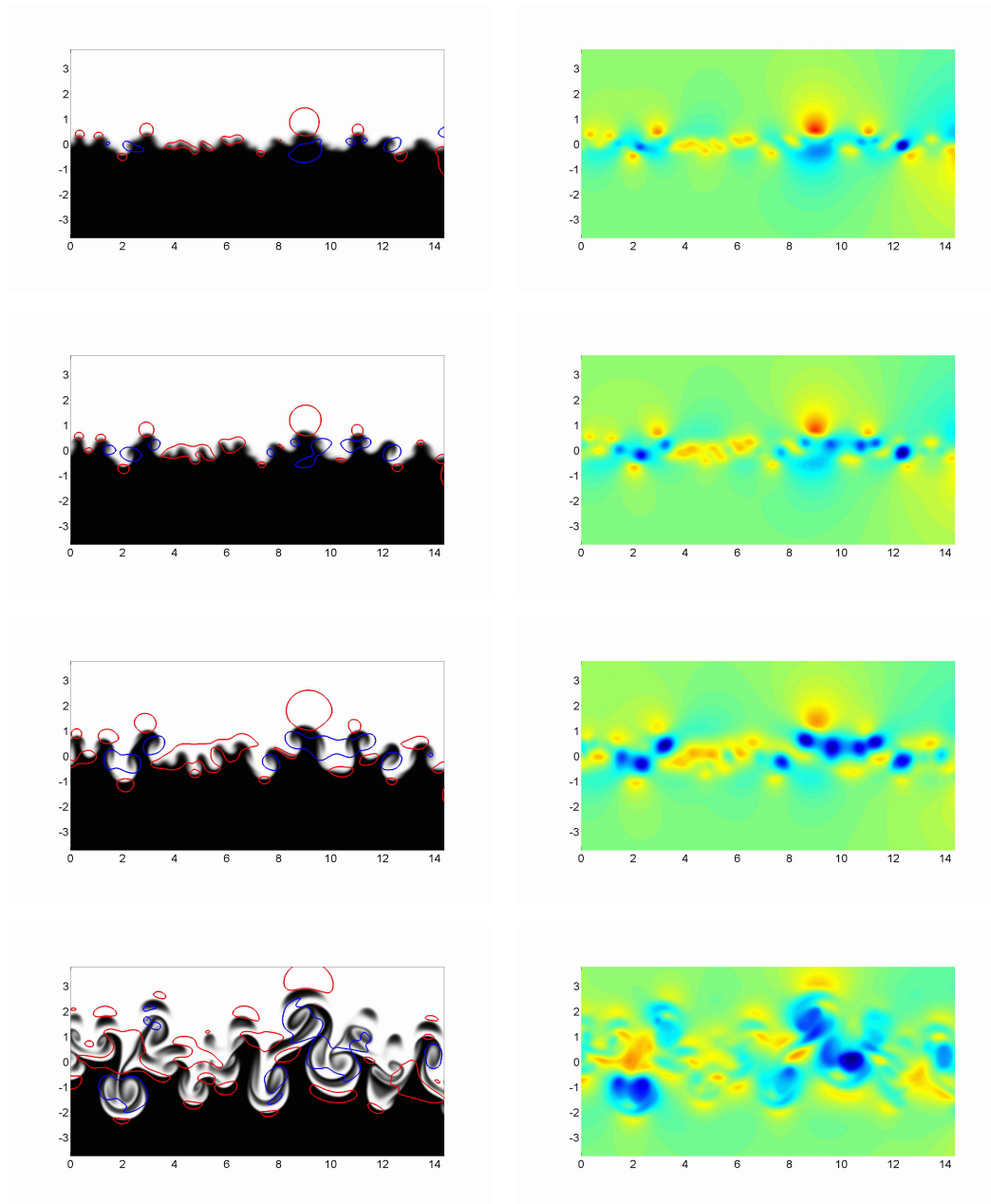


Figure 3.49 Vertical slices of the density field with red and blue pressure contours indicating high and low pressure regions (left-column), respectively, and fluctuating pressure regions (right-column) show the formation of secondary vortical instabilities at $\tau \approx 0.3$. The slices are shown at $\tau = 0.206, 0.288, 0.405,$ and 0.674 .

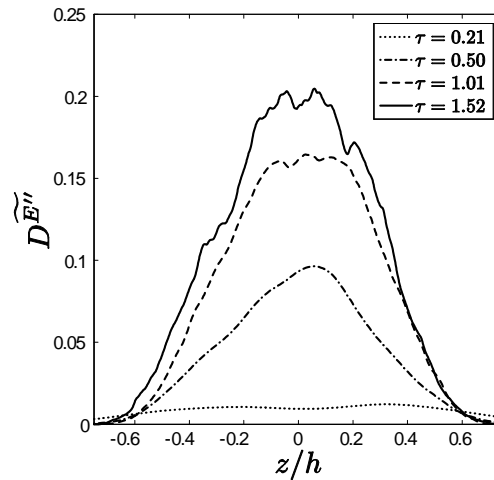


Figure 3.50 Profiles of the turbulent dissipation term $D^{\widetilde{E}''}$ in the turbulent kinetic energy transport equation across the Rayleigh–Taylor mixing layer at various times.

within the mixing layer grows due to the continual release of potential energy. As a result, the production of \widetilde{E}'' does not equal dissipation, and the production-to-dissipation ratio is not constant. Figure 3.51 shows the evolution of the production and dissipation terms integrated over the entire domain. The buoyancy production-to-dissipation ratio for both the integral case and on the centerplane is also shown in figure 3.51. At $\tau < 0.7$, the ratio $P_b^{\widetilde{E}''}/D^{\widetilde{E}''}$ is unsteady, which makes the modeling of such processes more difficult. At later times, $\tau > 0.7$, the mixing layer reaches an approximate steady-state ratio $P_b^{\widetilde{E}''}/D^{\widetilde{E}''} \approx 2.2$.

In general, two-equation modeling of turbulent flows requires that the production-to-dissipation ratio remain close to unity, *i.e.* turbulent statistics vary slowly in time with respect to mean flow changes. This is one reason why standard \widetilde{E}'' - $\widetilde{\epsilon}''$ type models (Jones & Launder 1972) perform adequately in simple flows, such as round jets with $P^{\widetilde{E}''}/D^{\widetilde{E}''} \approx 0.8$ (Pope 2000), homogenous shear flows with $P^{\widetilde{E}''}/D^{\widetilde{E}''} \approx 1.4$ –1.8

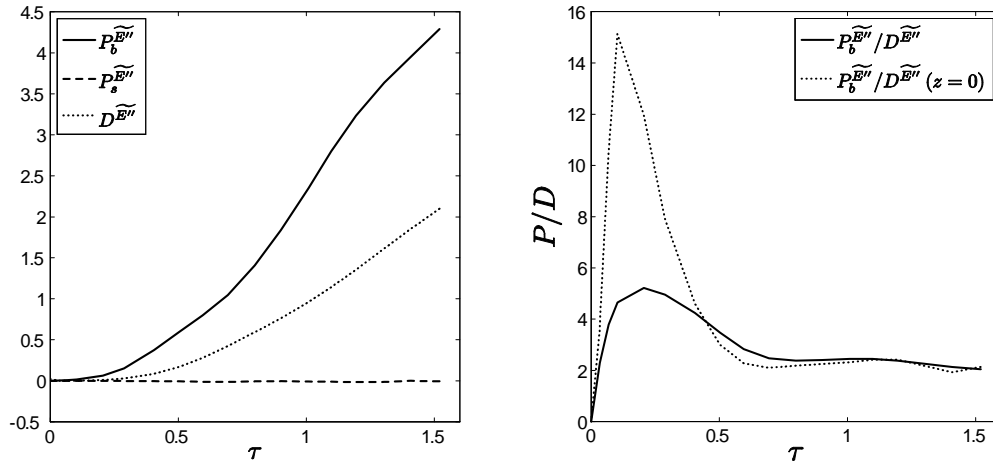


Figure 3.51 Evolution of buoyancy and shear production, and dissipation integrals (left). Evolution of production-to-dissipation ratios (right).

(Rogers & Moin 1987; Tavoularis & Corrsin 1981), and shear-driven mixing layers with $P^{\widetilde{E}''}/D^{\widetilde{E}''} \approx 1.4$ (Rogers & Moser 1994). Rayleigh–Taylor driven mixing layers exhibit larger production-to-dissipation ratios $P^{\widetilde{E}''}/D^{\widetilde{E}''} \approx 2$ –2.4 as reported here. Mellado *et al.* (2005) reported $P^{\widetilde{E}''}/D^{\widetilde{E}''} \approx 2$ –2.5 for a compressible, miscible, $A = 0.5$ Rayleigh–Taylor mixing layer. Ristorcelli and Clark (2004) reported even larger values of $P^{\widetilde{E}''}/D^{\widetilde{E}''} \approx 3.5$ for an $A = 0.01$, $Sc = 1$ Rayleigh–Taylor mixing layer. The difference between the Rayleigh–Taylor and shear-driven production-to-dissipation ratios is likely attributed to the difference in the production mechanisms of the turbulent fluctuations, where turbulent kinetic energy is created from mean density gradients and not from mean velocity gradients.

The departure from $P^{\widetilde{E}''}/D^{\widetilde{E}''} = 1$ indicates that turbulent statistics are rapidly changing with respect to the mean density field. In the early-time growth stage ($\tau < 0.5$), the production-to-dissipation ratio exhibits a large dynamic range. As the growth rate of the initial perturbations increases, $P^{\widetilde{E}''}/D^{\widetilde{E}''}$ continues to rise until a peak $P^{\widetilde{E}''}/D^{\widetilde{E}''} \approx 5$ is reached at $\tau \approx 0.25$. The peak $P^{\widetilde{E}''}/D^{\widetilde{E}''}$ corresponds with the

nonlinear transition time, where secondary vortices begin to form in between rising and falling structures. With the onset of nonlinear dynamics comes the bifurcation of the pressure transport $\overline{p'w''}$. Also, this represents the earliest time in which phenomenological turbulence concepts can be appropriately applied to the mixing layer, albeit in the low Reynolds number limit. After the onset of the transition at $\tau = 0.25$, the mixing layer begins to relax to the asymptotic state $P^{\widetilde{E}''}/D^{\widetilde{E}''} \approx 2.2$. This process occurs more rapidly until $\tau \approx 0.5$, after which turbulent statistics begin to change more slowly.

3.6.5 Turbulent kinetic energy dissipation rate transport

To construct turbulent viscosity models, one other quantity in combination with \widetilde{E}'' is required. In this work, the transport equation for the turbulent kinetic energy dissipation rate $\widetilde{\epsilon}''$ is examined. Profiles of $\widetilde{\epsilon}''$ are shown in figure 3.52. While the Favre-averaged framework is adopted here, the complete Favre-averaged $\widetilde{\epsilon}''$ transport equation contains many complicated terms, and thus, the budget of the turbulent kinetic energy dissipation rate transport equation is evaluated instead, where

$$\overline{\epsilon'} = \nu \overline{\left(\frac{\partial u'_i}{\partial x_j}\right)^2}. \quad (3.61)$$

Profiles of the incompressible dissipation rate $\overline{\epsilon'}$ and the general dissipation rate

$$\widetilde{\epsilon}'' = \frac{1}{\bar{\rho}} \overline{\sigma''_{ij} \frac{\partial u''_i}{\partial x_j}} \quad (3.62)$$

are shown in figure 3.52 at different times. It was observed in the DNS that the solenoidal and general formulations show similar profiles, as expected for small Atwood number Rayleigh–Taylor mixing layers. Thus, the resulting budgets and analysis of the Reynolds-averaged transport equation should be similar for incompressible, small Atwood number mixing layers.

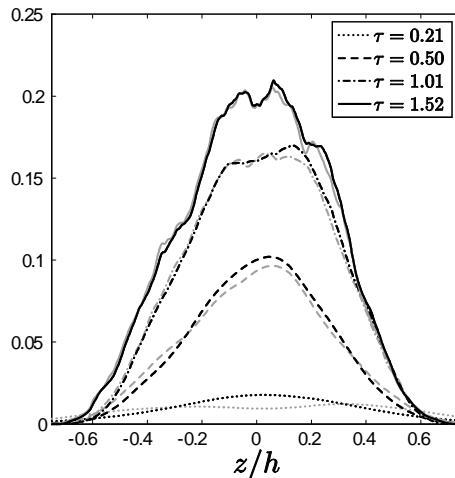


Figure 3.52 Profiles of the turbulent kinetic energy dissipation rate $\overline{\epsilon'}$ (black) and $\widetilde{\epsilon'}$ (grey) across the Rayleigh–Taylor mixing layer at various times.

The complete, unclosed transport equation for $\overline{\epsilon'}$ (Wilcox 2006; Jakirlić & Hanjalić 2002), generalized to include a buoyancy production term is

$$\bar{\rho} \frac{D\overline{\epsilon'}}{Dt} = P_b^{\overline{\epsilon'}} + P_s^{\overline{\epsilon'}} + P_t^{\overline{\epsilon'}} + P_c^{\overline{\epsilon'}} + T^{\overline{\epsilon'}} - D^{\overline{\epsilon'}}, \quad (3.63)$$

where

$$P_b^{\overline{\epsilon'}} = 2\bar{\nu} g_i \overline{\frac{\partial u'_i}{\partial x_j} \frac{\partial \rho'}{\partial x_j}}, \quad (3.64a)$$

$$P_s^{\overline{\epsilon'}} = -2\bar{\mu} \left(\overline{\frac{\partial u'_i}{\partial x_k} \frac{\partial u'_j}{\partial x_k}} + \overline{\frac{\partial u'_k}{\partial x_i} \frac{\partial u'_k}{\partial x_j}} \right) \frac{\partial \bar{u}_i}{\partial x_j}, \quad (3.64b)$$

$$P_t^{\overline{\epsilon'}} = -2\bar{\mu} \overline{\frac{\partial u'_i}{\partial x_k} \frac{\partial u'_i}{\partial x_m} \frac{\partial u'_k}{\partial x_m}}, \quad (3.64c)$$

$$P_c^{\overline{\epsilon'}} = -\bar{\mu} \overline{u'_k \frac{\partial u'_i}{\partial x_m} \frac{\partial^2 \bar{u}_i}{\partial x_k \partial x_m}}, \quad (3.64d)$$

$$T^{\overline{\epsilon'}} = \frac{\partial}{\partial x_j} \left(\bar{\mu} \frac{\partial \overline{\epsilon'}}{\partial x_j} - \bar{\rho} \overline{u'_j \epsilon'} - 2\bar{\nu} \overline{\frac{\partial p'}{\partial x_m} \frac{\partial u'_j}{\partial x_m}} \right), \quad (3.64e)$$

$$D^{\overline{\epsilon'}} = -2\bar{\rho} \bar{\nu}^2 \overline{\left(\frac{\partial u'_i}{\partial x_k \partial x_m} \right)^2}. \quad (3.64f)$$

The four production mechanisms of $\bar{\epsilon}'$ are given by the buoyancy production $P_b^{\bar{\epsilon}'}$, shear production $P_s^{\bar{\epsilon}'}$, turbulent production $P_t^{\bar{\epsilon}'}$, and mean velocity curvature production $P_c^{\bar{\epsilon}'}$. Analogous to the \widetilde{E}'' transport equation, the conservative transport and turbulent destruction of $\bar{\epsilon}'$ are given by $T^{\bar{\epsilon}'}$ and $D^{\bar{\epsilon}'}$, respectively. Unlike the budgets of \widetilde{E}'' in § 3.6.4 which have been reported for Rayleigh–Taylor mixing layers (Ristorcelli & Clark 2004; Mellado *et al.* 2005), the budgets of the $\bar{\epsilon}'$ transport equation shown in figures 3.54–3.59 are novel for Rayleigh–Taylor flows.

Figure 3.53 shows profiles of the dominant transport terms from the $\bar{\epsilon}'$ equation across the mixing layer at various times. Similar to the \widetilde{E}'' transport equation, the buoyancy production term remains positive-definite and the viscous destruction term remains negative-definite. In addition to the buoyancy forcing, an additional turbulent production term $P_t^{\bar{\epsilon}'}$ exists and becomes the dominant production mechanism at late time. The turbulent transport of $\bar{\epsilon}'$ exhibits a structure similar to the transport of \widetilde{E}'' , where $\bar{\epsilon}'$ is transported away from the centerplane to the edges of the mixing layer.

Similar to the production of turbulent kinetic energy, $\bar{\epsilon}'$ may be created by both buoyancy forces and mean velocity gradients. However, two additional production mechanisms exist which do not parallel the transport equation of \widetilde{E}'' . The dissipation rate $\bar{\epsilon}'$ may be produced by turbulent fluctuations alone, free of mean field influences, and by a curvature term which is proportional to the second derivative of the mean velocity field. However, as noted in § 3.6.2, the mean velocity profiles are negligible and so is the curvature production $P_c^{\bar{\epsilon}'}$. Profiles of each production mechanism are shown in figure 3.54. Similar to the shear production of \widetilde{E}'' , $P_s^{\bar{\epsilon}'}$ negligibly contributes to the overall production of $\bar{\epsilon}'$. The buoyancy production dominates at early times, but begins to diminish in magnitude at later times. The turbulent production term remains nearly negligible until $\tau > 0.5$, when the mixing layer begins to transition

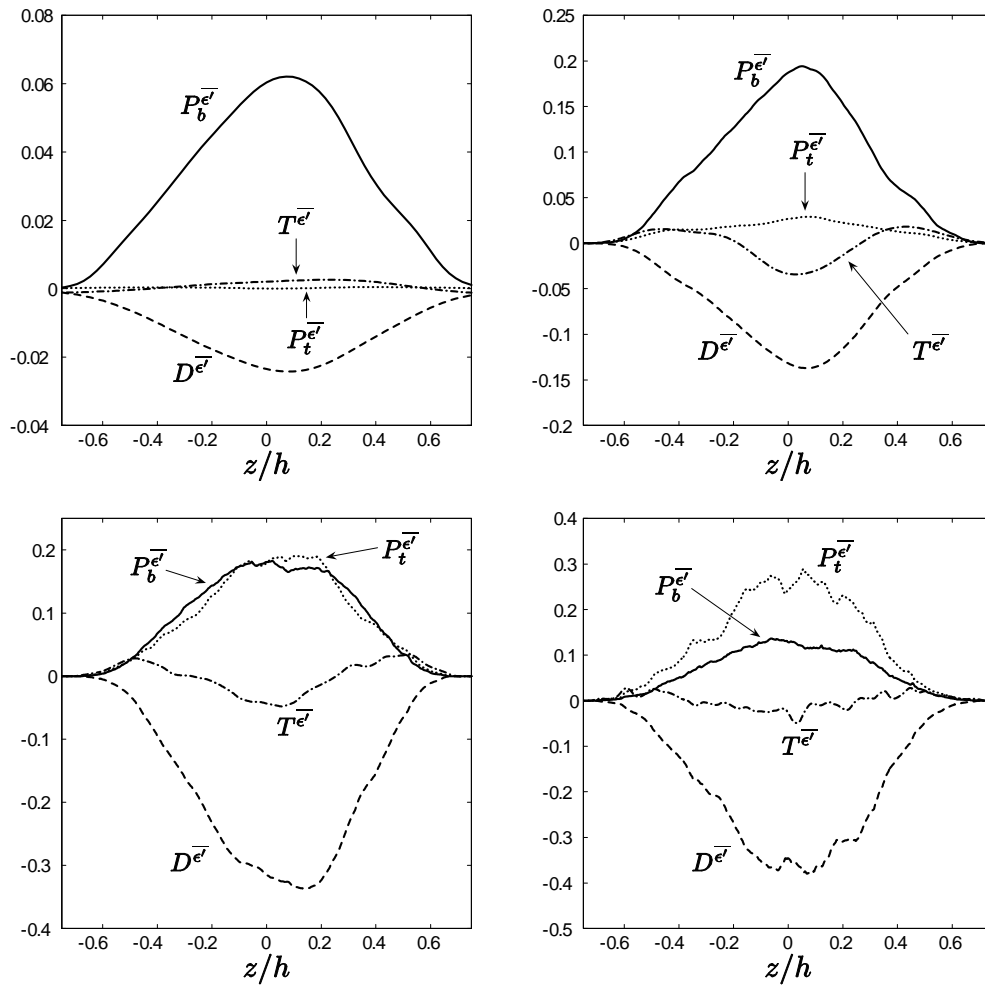


Figure 3.53 Profiles of the dominant terms in the turbulent kinetic energy dissipation rate transport equation across the Rayleigh–Taylor mixing layer at $\tau = 0.21, 0.50, 1.01,$ and 1.52 (left-to-right, top-to-bottom).

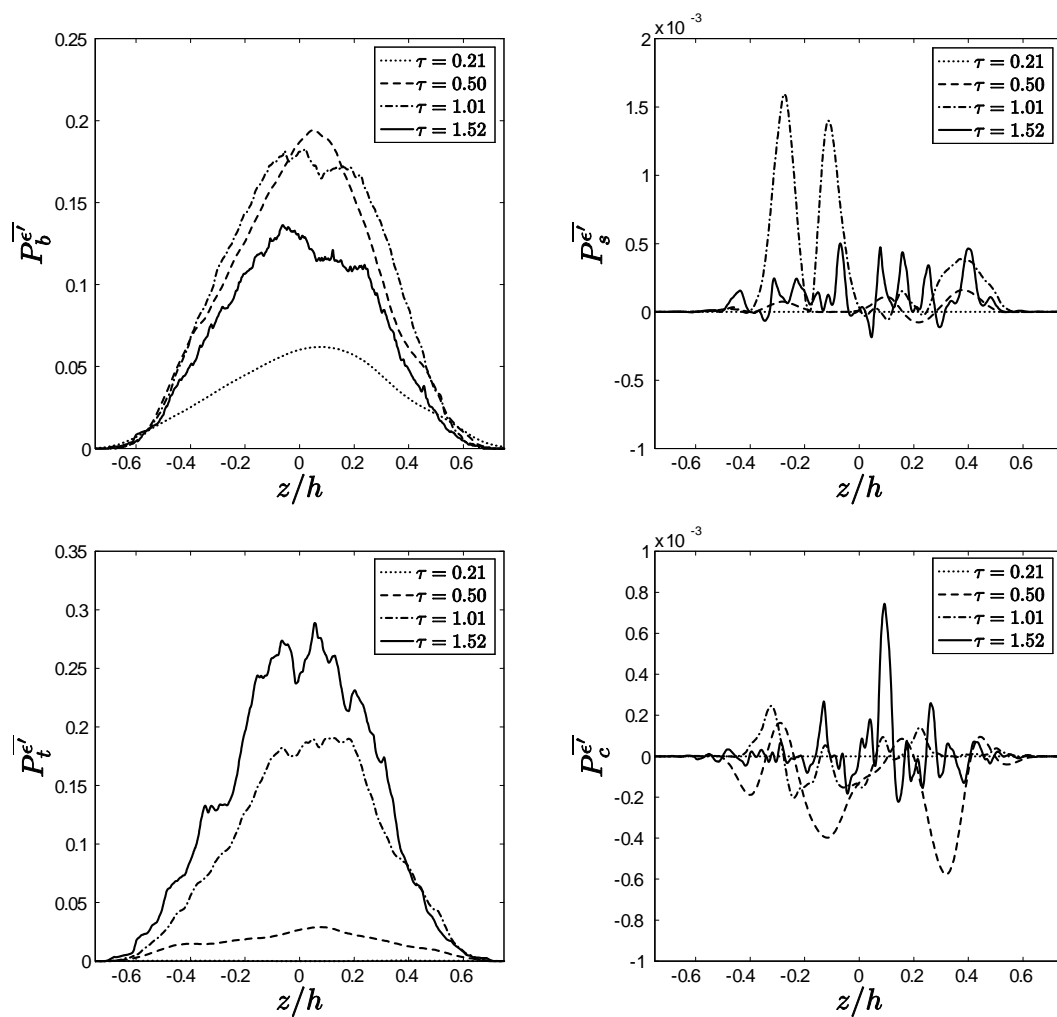


Figure 3.54 Profiles of the production terms $P_b^{e'}$, $P_s^{e'}$, $P_t^{e'}$, and $P_c^{e'}$ in the turbulent kinetic energy dissipation rate transport equation across the Rayleigh—Taylor mixing layer at various times.

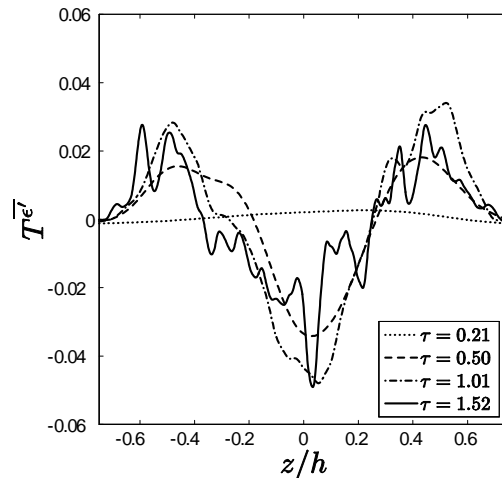


Figure 3.55 Profiles of the transport term $T^{\overline{\epsilon'}}$ in the turbulent kinetic energy dissipation rate transport equation across the Rayleigh–Taylor mixing layer at various times.

into a fully three-dimensional mixing layer. By $\tau = 1$, $P_t^{\overline{\epsilon'}}$ becomes the dominant production mechanism.

The conservative transport of $\overline{\epsilon'}$, given by $T^{\overline{\epsilon'}}$, occurs in a similar manner to the transport of $\widetilde{E''}$: $\overline{\epsilon'}$ is transported away from the turbulent centerplane of the Rayleigh–Taylor mixing layer in an approximately down-gradient manner. The turbulent transport term $T^{\overline{\epsilon'}}$, shown in figure 3.55, can be subdivided into contributions from three different physical mechanisms, where

$$F_d^{\overline{\epsilon'}} = -\bar{\mu} \frac{\partial \overline{\epsilon'}}{\partial z}, \quad (3.65)$$

$$F_t^{\overline{\epsilon'}} = \overline{w' \epsilon'}, \quad (3.66)$$

$$F_p^{\overline{\epsilon'}} = 2\bar{\nu} \overline{\frac{\partial p'}{\partial x_m} \frac{\partial w'}{\partial x_m}} \quad (3.67)$$

are the flux components due to molecular diffusion, turbulent transport, and pressure transport. The early-time ($\tau \leq 0.3$) profiles of each flux are shown in figure 3.56, and

the late-time ($\tau \geq 0.4$) profiles are shown in figure 3.57. In the early-time profiles, the flux of $\bar{\epsilon}'$ due to molecular diffusion remains non-negligible. Again, as $Re_h \rightarrow 0$, the turbulent flux is either negligible or of the same order of magnitude as the other fluxes. At later times, as shown in figure 3.57, the turbulent flux of $\bar{\epsilon}'$ becomes the sole dominant flux contributing to $T^{\bar{\epsilon}'}$.

The pressure transport at early times compliments the turbulent flux, transporting $\bar{\epsilon}'$ away from the centerplane. However, a similar bifurcation is seen in the pressure transport of $\bar{\epsilon}'$ as seen in the pressure transport of \widetilde{E}'' : $F_p^{\bar{\epsilon}'}$ opposes the down-gradient flux of $\bar{\epsilon}'$ within the core of the Rayleigh–Taylor mixing layer after $\tau = 0.5$. Unlike the pressure transport of \widetilde{E}'' , the overall contribution of $F_p^{\bar{\epsilon}'}$ to $T^{\bar{\epsilon}'}$ is relatively small, especially at late time. Additional complicating physics, such as the transport of $\bar{\epsilon}'$ beyond the edges of the mixing layer as seen in $F_p^{\widetilde{E}''}$, was not observed in the DNS. Due to the minimal impact of $F_p^{\bar{\epsilon}'}$, especially at late time, it may not be critical for turbulent transport models to capture the influence of the fluctuating pressure field on $\bar{\epsilon}'$.

Finally, profiles of the viscous destruction of $\bar{\epsilon}'$ are shown in figure 3.58. Similar to the production profiles shown in figure 3.54, the viscous destruction of $\bar{\epsilon}'$ occurs primarily within the turbulent core of the mixing layer and only becomes significant when nonlinear, three-dimensional, turbulent fluctuations begin to form after $\tau \approx 0.5$. The total contributions of the dominant production and viscous destruction terms were calculated by integrating each profile over the entire domain. The evolution of the production and destruction integrals are shown in figure 3.59. As noted earlier, the shear production is negligible. Buoyancy production dominates at early times ($\tau < 1$), and while non-negligible, becomes less important as the Reynolds number increases. Both the turbulent production and destruction terms are small until the mixing layer transitions into a nonlinear, three-dimensional phase at $\tau \approx 0.5$. The

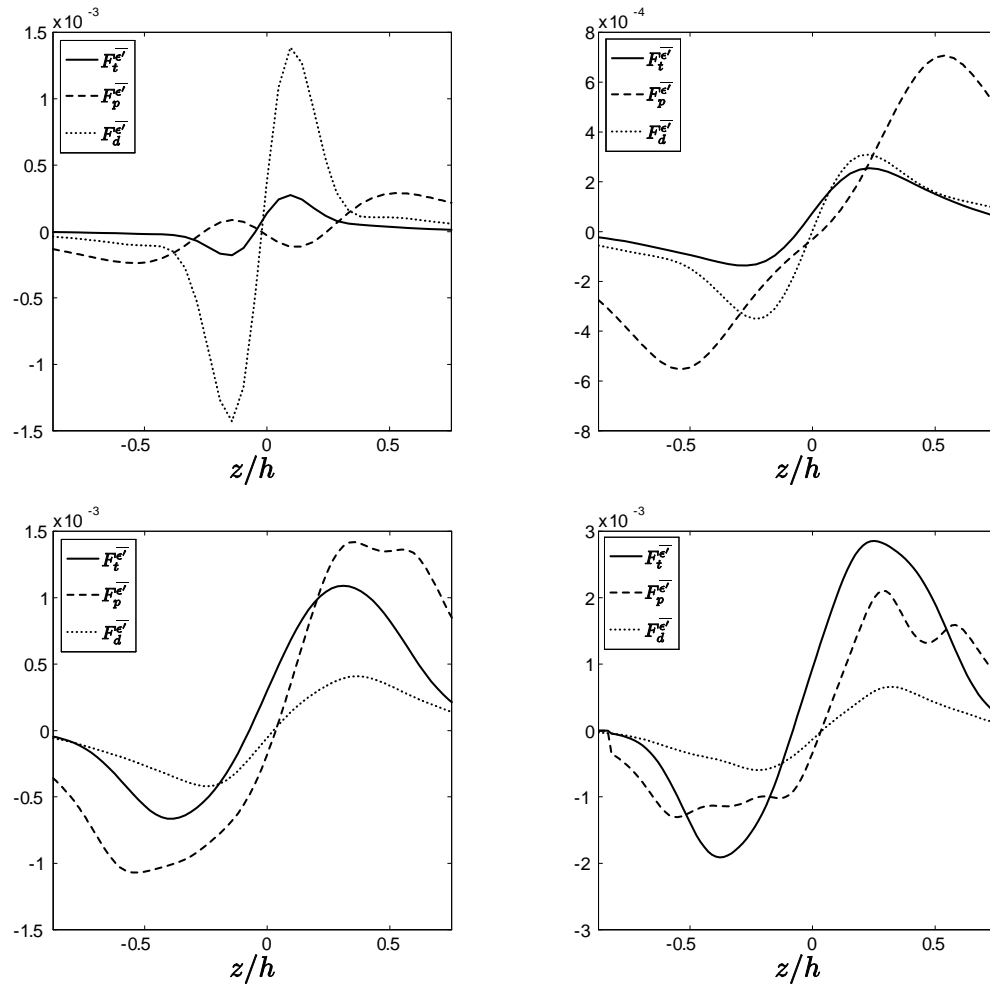


Figure 3.56 Early-time profiles of the turbulent kinetic energy flux terms in the transport term T^e across the Rayleigh–Taylor mixing layer at $\tau = 0.034, 0.10, 0.21,$ and 0.29 (left-to-right, top-to-bottom).

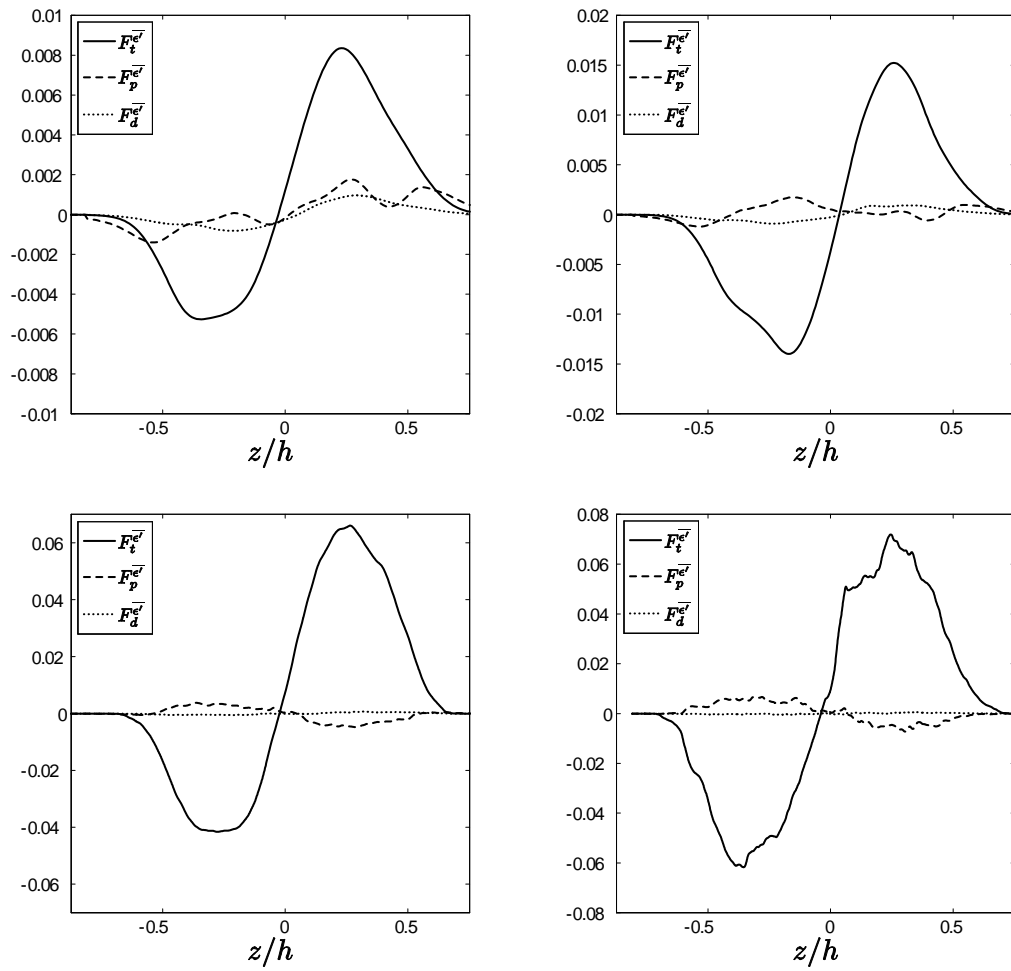


Figure 3.57 Intermediate- and late-time profiles of the turbulent kinetic energy flux terms in the transport term $T^{\overline{e'}}$ across the Rayleigh–Taylor mixing layer at $\tau = 0.41, 0.52, 1.01,$ and 1.52 (left-to-right, top-to-bottom).

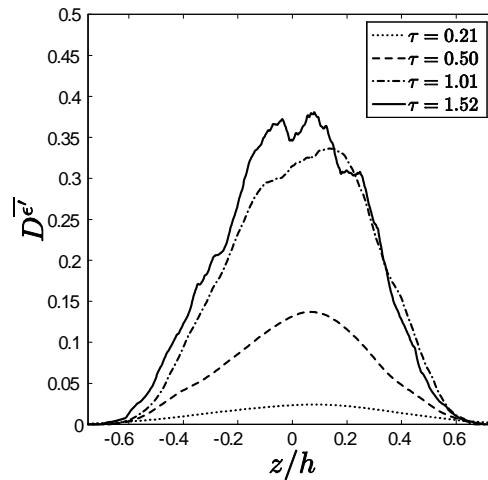


Figure 3.58 Profiles of the viscous dissipation term $D^{\epsilon'}$ in the turbulent kinetic energy dissipation rate transport equation across the Rayleigh–Taylor mixing layer at various times.

production-to-dissipation ratios for the entire mixing layer and on the centerplane are also shown in figure 3.59. Again, the turbulent flow field is highly non-stationary before $\tau \approx 0.7$; however, $P^{\epsilon'}/D^{\epsilon'}$ approaches unity after. This late-time value of $P^{\epsilon'}/D^{\epsilon'} \approx 1$ is expected in the high Reynolds number limit, as the spectral cascade rate of turbulent kinetic energy becomes equivalent to the turbulent kinetic energy dissipation rate.

3.6.6 Mass fraction variance transport

In § 3.6.4 and 3.6.5, the turbulent transport dynamics of the mixing layer were investigated by evaluating the budgets of the $\widetilde{E''}$ and $\bar{\epsilon'}$ transport equations. To properly model the mixing dynamics, additional correlations must also be included, such as the fluctuating density variance $\overline{\rho'^2}$. In scalar mixing and reacting flows, a dimensionless approach is taken where the mass fraction variance or volume fraction variance

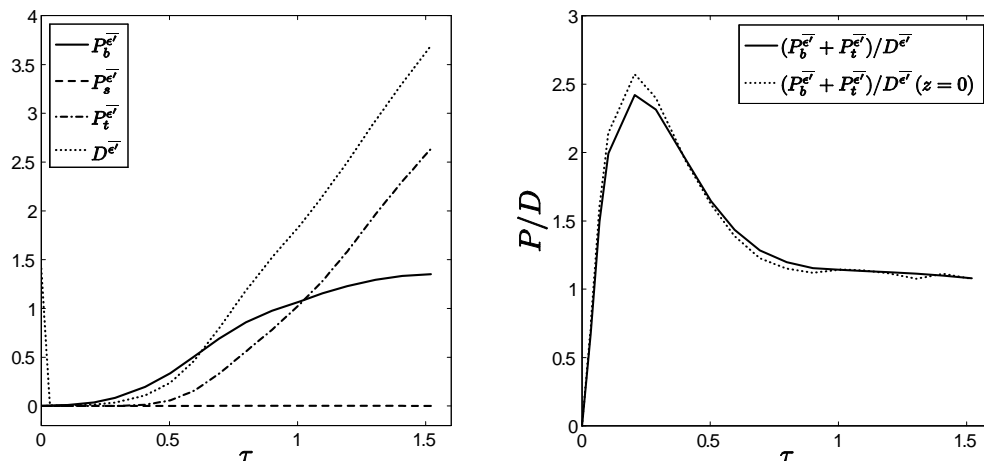


Figure 3.59 Evolution of buoyancy, shear, turbulent production, and dissipation integrals (left). Evolution of production-to-dissipation ratios (right).

transport equation are advanced (Veynante & Vervisch 2002). To retain the most general approach suitable for both incompressible and compressible flows, the budget of the averaged mass fraction variance transport is examined. The difference between $\overline{f_1'^2}$ and $\widetilde{m_1''^2}$ remains under 0.3% for the small Atwood number considered here. Thus, the difference between the transport budgets of $\overline{f_1'^2}$ and $\widetilde{m_1''^2}$ should be negligible. The exact relationship between $\widetilde{m_1''^2}$ and $\overline{f_1'^2}$ does not formally exist without some degree of approximation. Using the relationship between the mass and volume fractions, it is possible to write the relationship between the mass fraction variance and fluctuating volume fraction-specific volume correlation,

$$\begin{aligned} \widetilde{m_1''^2} &= \frac{\rho_1^2}{\bar{\rho}} \left[\overline{f_1'^2} \left(\frac{1}{\rho} \right) + 2 \overline{f_1'} \left(\frac{f_1'}{\rho} \right) + \overline{\left(\frac{f_1'^2}{\rho} \right)} - \frac{\overline{f_1'^2}}{\bar{\rho}} \right] \\ &\approx \frac{\rho_1^2}{\bar{\rho}} \overline{\left(\frac{f_1'^2}{\rho} \right)} + \text{higher order terms} . \end{aligned}$$

Thus, without introducing approximations for the specific volume term under the averaging operator as done in some models (Besnard *et al.* 1992), the mass fraction variance is not linearly related to the volume fraction variance.

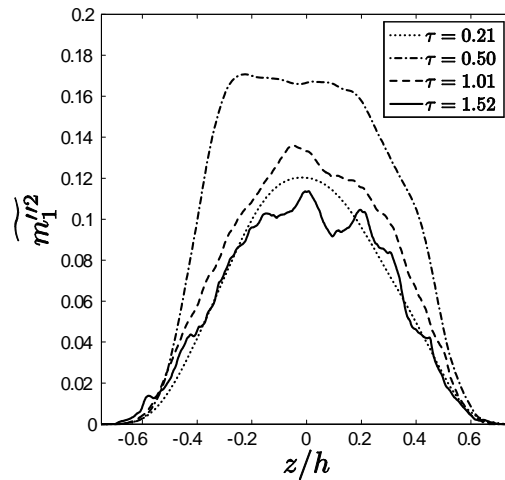


Figure 3.60 Profiles of the Favre-averaged mass fraction variance $\widetilde{m_1''^2}$ across the Rayleigh–Taylor mixing layer at various times.

Profiles of $\widetilde{m_1''^2}$ are shown in figure 3.60. The mass fraction variance transport equation is (Veynante & Vervisch 2002)

$$\bar{\rho} \frac{D\widetilde{m_1''^2}}{Dt} = P^{\widetilde{m_1''^2}} + T^{\widetilde{m_1''^2}} - D^{\widetilde{m_1''^2}}, \quad (3.68)$$

where

$$P^{\widetilde{m_1''^2}} = -2\bar{\rho} \widetilde{u_j'' m_1''} \frac{\partial \widetilde{m_1}}{\partial x_j}, \quad (3.69a)$$

$$T^{\widetilde{m_1''^2}} = \frac{\partial}{\partial x_j} \left(\overline{\rho D \frac{\partial m_1''^2}{\partial x_j}} - \bar{\rho} \widetilde{u_j'' m_1''^2} \right), \quad (3.69b)$$

$$D^{\widetilde{m_1''^2}} = -2\bar{\rho} \widetilde{\chi''} = -2\rho D \left(\frac{\partial m_1''}{\partial x_j} \right)^2. \quad (3.69c)$$

The turbulent production and destruction of $\widetilde{m_1''^2}$ are given by $P^{\widetilde{m_1''^2}}$ and $D^{\widetilde{m_1''^2}}$, respectively. The conservative transport of $\widetilde{m_1''^2}$ across the mixing layer is given by $T^{\widetilde{m_1''^2}}$. Profiles of the terms in the mass fraction variance transport equation across the mixing layer at various times are shown in figure 3.61, where a similar production,

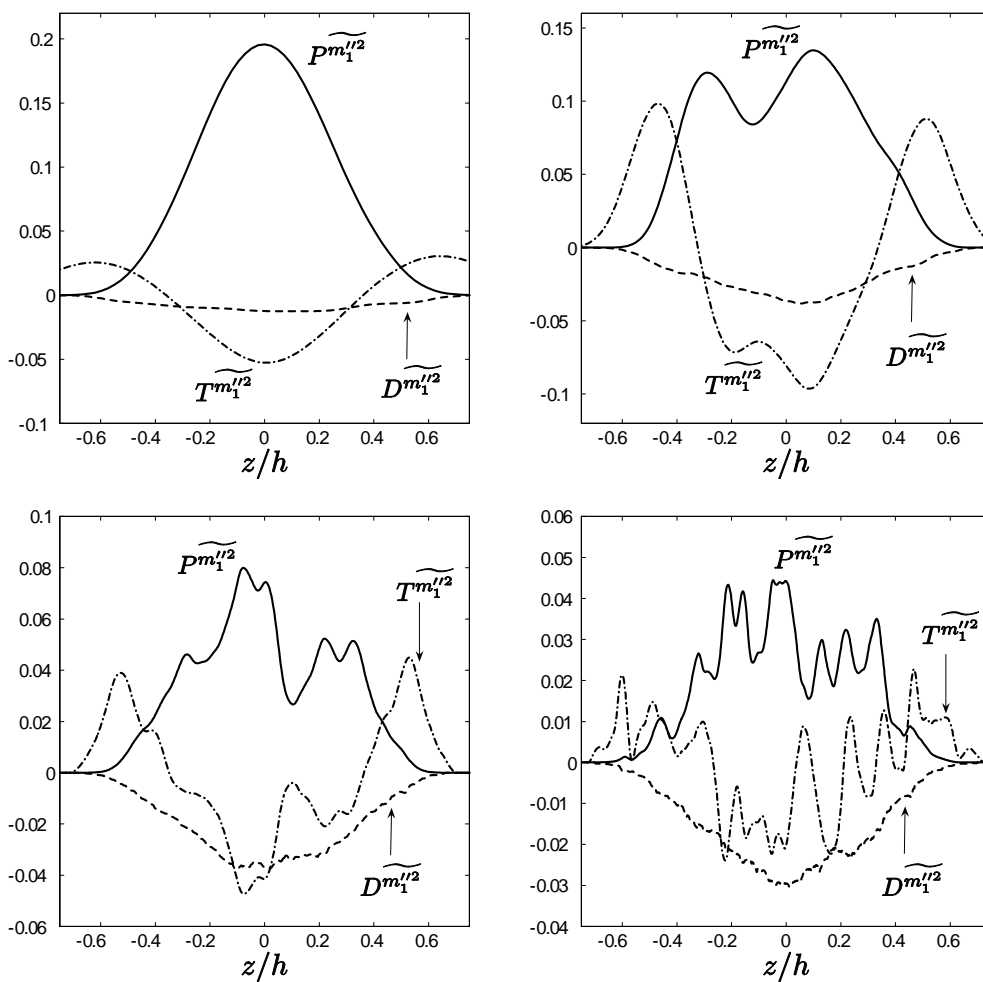


Figure 3.61 Profiles of the terms in the mass fraction variance transport equation across the Rayleigh–Taylor mixing layer at $\tau = 0.21, 0.50, 1.01,$ and 1.52 (left-to-right, top-to-bottom).

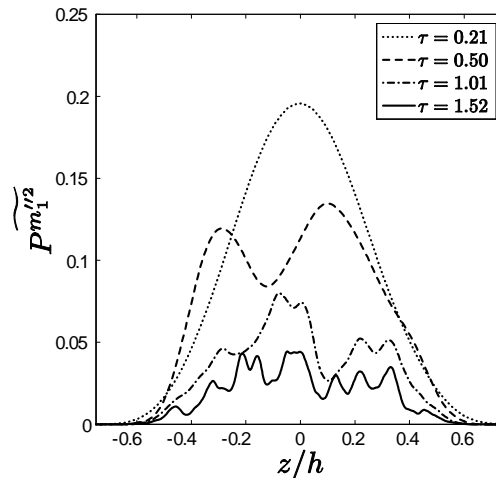


Figure 3.62 Profiles of the production term $P^{\widetilde{m}_1''^2}$ in the mass fraction variance transport equation across the Rayleigh–Taylor mixing layer at various times.

transport, and dissipation structure is observed as in the \widetilde{E}'' and $\overline{\epsilon}'$ transport equations. The late-time oscillations in the production and transport terms are remnants of the gradient of the mean mass fraction field.

Profiles of $P^{\widetilde{m}_1''^2}$, which is physically related to the entrainment of unmixed fluid into the mixing layer, are shown in figure 3.62. At early times, before the onset of three-dimensional, nonlinear dynamics, the mixing layer directly entrains pockets of pure fluid with little mixing, and therefore $P^{\widetilde{m}_1''^2}$ is large at $\tau \leq 0.5$. This can also be seen in the evolution of the mass fraction-velocity correlation coefficient

$$R_{\widetilde{w}''\widetilde{m}_1''} = \frac{\widetilde{w}'' \widetilde{m}_1''}{\sqrt{\widetilde{w}''^2} \sqrt{\widetilde{m}_1''^2}} \quad (3.70)$$

shown in figure 3.63. Combining the large flux of fluid into the mixing layer (where $R_{\widetilde{w}''\widetilde{m}_1''}$ approaches unity at $\tau \approx 0.2$) and the large gradient of \widetilde{m}_1 at early times, the total production of $\widetilde{m}_1''^2$ is relatively large at $\tau \leq 0.5$. At later times, the density-velocity correlation relaxes to $R_{\widetilde{w}''\widetilde{m}_1''} \approx 0.75$ and the gradient of \widetilde{m}_1 scales as h^{-1} .

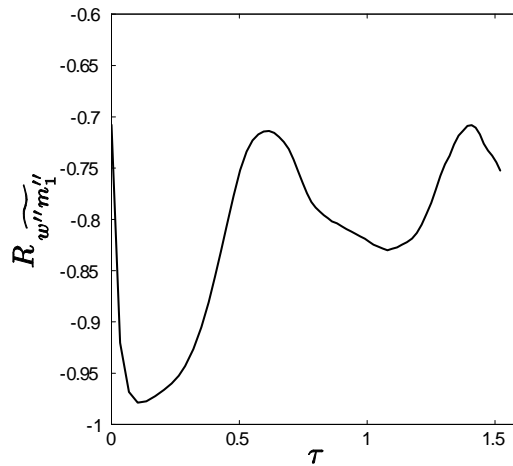


Figure 3.63 Evolution of the density-velocity correlation coefficient $R_{\widetilde{w''m_1''}}$ on the centerplane of the Rayleigh–Taylor mixing layer.

Accordingly, the production of $\widetilde{m_1''^2}$ decreases with time.

The conservative flux of $\widetilde{m_1''^2}$ is similar to the flux of $\widetilde{E''}$ and $\bar{\epsilon'}$, where $\widetilde{m_1''^2}$ is transferred away from the centerplane of the mixing layer in an approximately down-gradient manner. Unlike $\widetilde{E''}$ and $\bar{\epsilon'}$, which are unbounded quantities, $\widetilde{m_1''^2}$ is bounded by $[0, 1/4]$. Thus the magnitude of the transport term $T^{\widetilde{m_1''^2}}$ decreases with time. The individual flux components can be examined, where

$$F_d^{\widetilde{m_1''^2}} = -\overline{\rho D \frac{\partial m_1''^2}{\partial z}} \approx -\bar{\rho} \bar{D} \frac{\partial \widetilde{m_1''^2}}{\partial z}, \quad (3.71)$$

$$F_t^{\widetilde{m_1''^2}} = \bar{\rho} \widetilde{w'' m_1''^2}. \quad (3.72)$$

are the diffusive and turbulent fluxes of $\widetilde{m_1''^2}$. Figure 3.65 shows profiles of each flux component at various times. For all times examined, the turbulent flux of $\widetilde{m_1''^2}$ dominates the transport of $\widetilde{m_1''^2}$ to the exterior edges of the Rayleigh–Taylor mixing layer. As $Sc > 1$, the diffusive flux of $\widetilde{m_1''^2}$ is relatively small at all times, even at $\tau \approx 0$.

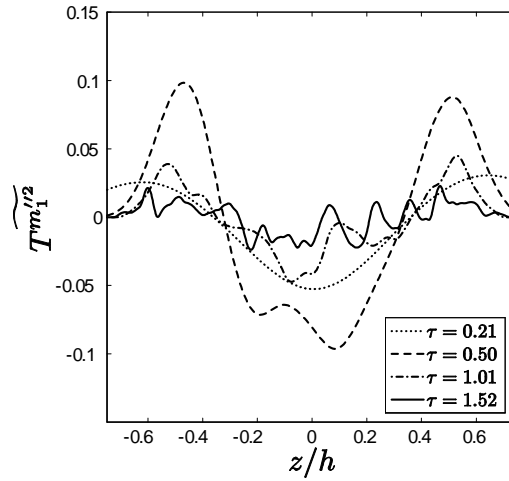


Figure 3.64 Profiles of the transport term $T^{\widetilde{m}_1''^2}$ in the mass fraction variance transport equation across the mixing layer at various times.

The production of $\widetilde{m}_1''^2$ represents the entrainment of unmixed fluid into the mixing layer, which increases the magnitude of $\widetilde{m}_1''^2$. Conversely, the destruction of $\widetilde{m}_1''^2$, given by $\widetilde{\chi}''$, represents the molecular diffusion of each fluid species into one another, homogenizing the fluid within the mixing layer and decreasing the magnitude of $\widetilde{m}_1''^2$. Profiles of the dissipation term $D^{\widetilde{m}_1''^2}$ are shown in figure 3.66. Analogous to $D^{\widetilde{E}''}$, the dissipation of $\widetilde{m}_1''^2$ primarily occurs within the turbulent core of the mixing layer. This is expected as \widetilde{E}'' is also peaked in the core, where the turbulent fluctuations increase the local strain rates at the fluid interface, which increases the magnitude of the local mass fraction gradients.

The production of $\widetilde{m}_1''^2$ is driven by the expansion of the mixing layer and entrainment of unmixed fluid. The destruction of $\widetilde{m}_1''^2$ depends upon the generation of sufficient turbulent fluctuations to generate the necessary surface area required for molecular diffusion to mix the constituent fluids. Figure 3.67 shows the evolution of $P^{\widetilde{m}_1''^2}$ and $D^{\widetilde{m}_1''^2}$ integrated over the numerical domain. At early times ($\tau < 0.4$),

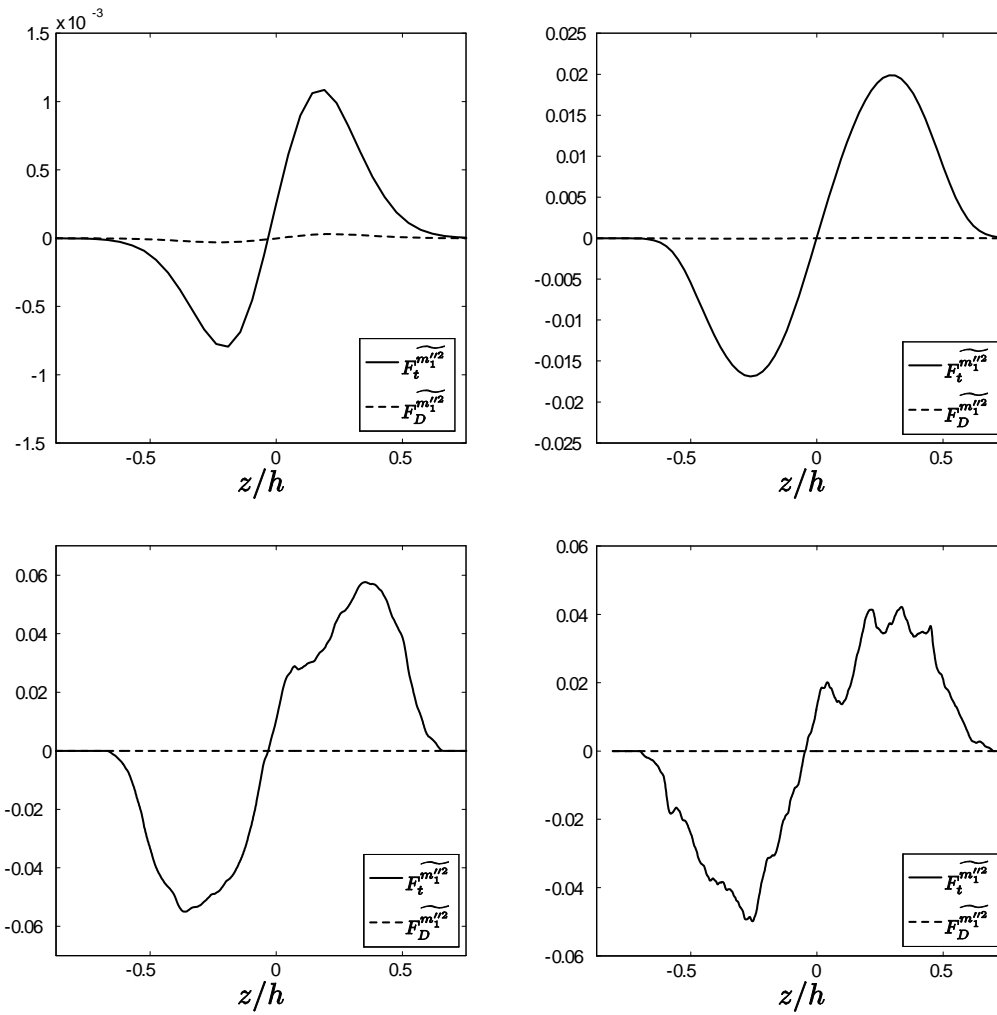


Figure 3.65 Profiles of the mean mass fraction flux terms in the transport term T_1^{m1r2} across the Rayleigh–Taylor mixing layer at $\tau = 0.034, 0.21, 1.01,$ and 1.52 (left-to-right, top-to-bottom).

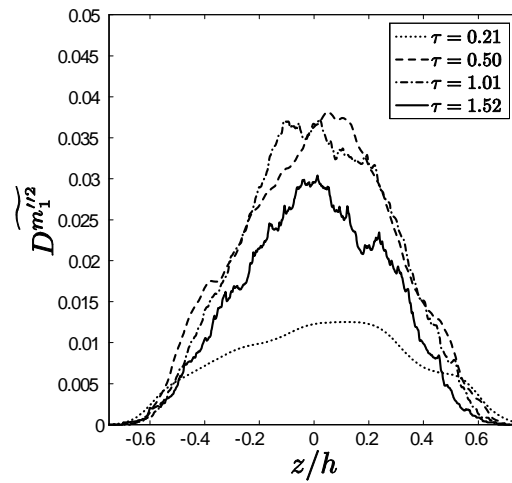


Figure 3.66 Profiles of the molecular dissipation term $D^{m_1^{1/2}}$ in the mass fraction variance transport equation across the Rayleigh–Taylor mixing layer at various times.

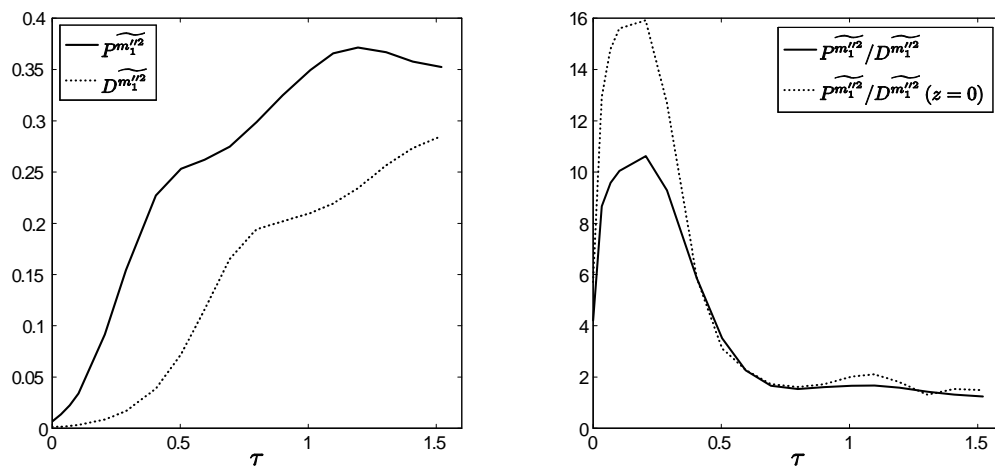


Figure 3.67 Evolution of production and dissipation integrals (left). Evolution of production-to-dissipation ratios (right).

the total production of $\widetilde{m_1''^2}$ is an order of magnitude larger than $D\widetilde{m_1''^2}$. As three-dimensional, turbulent structures within the mixing layer develop ($\tau > 0.7$), the ratio of $P\widetilde{m_1''^2}/D\widetilde{m_1''^2}$ approaches unity. A late-time ratio $P\widetilde{m_1''^2}/D\widetilde{m_1''^2} = 1.25$ is observed in the DNS, which is expected to remain greater than unity due to the continuous entrainment of unmixed fluid into the mixing layer.

3.6.7 Mass fraction variance dissipation rate transport

Similar to the dissipation rate of $\widetilde{E''}$, it is possible to derive a transport equation for the dissipation rate of $\widetilde{m_1''^2}$,

$$\widetilde{\chi''} = \bar{D} \left(\overline{\frac{\partial m_1''}{\partial x_j}} \right)^2.$$

Profiles of $\widetilde{\chi''}$ are shown in figure 3.68. The transport equation of $\widetilde{\chi''}$ may be written as (Mantel & Borghi 1994; Veynante & Vervisch 2002; Mura & Borghi 2003; Mura, Robin & Champion 2007)

$$\bar{\rho} \frac{D\widetilde{\chi''}}{Dt} = P_s^{\widetilde{\chi''}} + P_m^{\widetilde{\chi''}} + P_t^{\widetilde{\chi''}} + P_c^{\widetilde{\chi''}} + T^{\widetilde{\chi''}} - D^{\widetilde{\chi''}}, \quad (3.73)$$

where

$$P_m^{\widetilde{\chi''}} = -2\rho D \overline{\frac{\partial m_1''}{\partial x_i} \frac{\partial u_j''}{\partial x_i} \frac{\partial \widetilde{m}_1}{\partial x_j}}, \quad (3.74a)$$

$$P_s^{\widetilde{\chi''}} = -2\rho D \overline{\frac{\partial m_1''}{\partial x_j} \frac{\partial m_1''}{\partial x_i} \frac{\partial \widetilde{u}_j}{\partial x_i}}, \quad (3.74b)$$

$$P_t^{\widetilde{\chi''}} = -2\rho D \overline{\frac{\partial m_1''}{\partial x_j} \frac{\partial m_1''}{\partial x_i} \frac{\partial u_j''}{\partial x_i}}, \quad (3.74c)$$

$$P_c^{\widetilde{\chi''}} = -2\rho D \overline{u_j'' \frac{\partial m_1''}{\partial x_i} \frac{\partial^2 \widetilde{m}_1}{\partial x_i \partial x_j}}, \quad (3.74d)$$

$$T^{\widetilde{\chi''}} = -\frac{\partial}{\partial x_j} \left(\overline{\rho D \frac{\partial \chi''}{\partial x_j} - \bar{\rho} u_j'' \widetilde{\chi''}} \right), \quad (3.74e)$$

$$D^{\widetilde{\chi''}} = 2\rho D^2 \overline{\left(\frac{\partial^2 m_1''}{\partial x_i \partial x_j} \right)^2} \quad (3.74f)$$

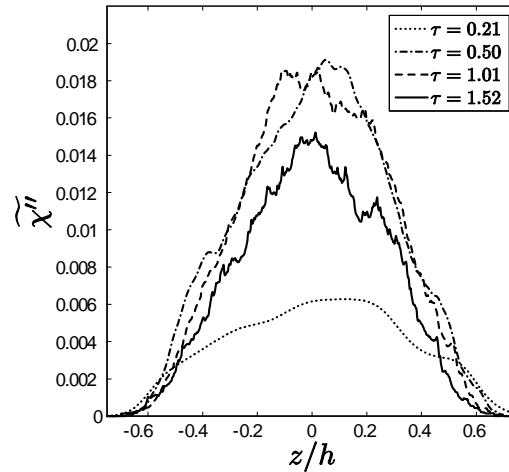


Figure 3.68 Profiles of the mass fraction variance dissipation rate $\overline{\chi''}$ across the Rayleigh–Taylor mixing layer at various times.

are the production, transport, and destruction terms. The four production mechanisms of $\overline{\chi''}$ are given by the mean gradient production $P_m^{\overline{\chi''}}$, shear production $P_s^{\overline{\chi''}}$, turbulent production $P_t^{\overline{\chi''}}$, and mean curvature production $P_c^{\overline{\chi''}}$. The conservative transport and turbulent destruction of $\overline{\chi''}$ are given by $T^{\overline{\chi''}}$ and $D^{\overline{\chi''}}$, respectively.

Profiles of the terms in the mass fraction variance dissipation rate transport equation across the mixing layer are shown in figure 3.69. Similar to the $\overline{\epsilon'}$ transport equation, the buoyancy and turbulent production terms are the primary production mechanisms of $\overline{\chi''}$ within the core of the mixing layer. The turbulent destruction of $\overline{\chi''}$ is also negative-definite across the mixing layer. The conservative transport of $\overline{\chi''}$ retains the expected profile, where $\overline{\chi''}$ is transported away from the centerplane; however, the relative role of turbulent transport in the dynamics of $\overline{\chi''}$ is smaller than observed in the other transport equations examined.

Figure 3.70 shows profiles of the mean gradient, shear, turbulent, and curvature production terms in (3.73). Similar to all transport budgets examined here, the shear

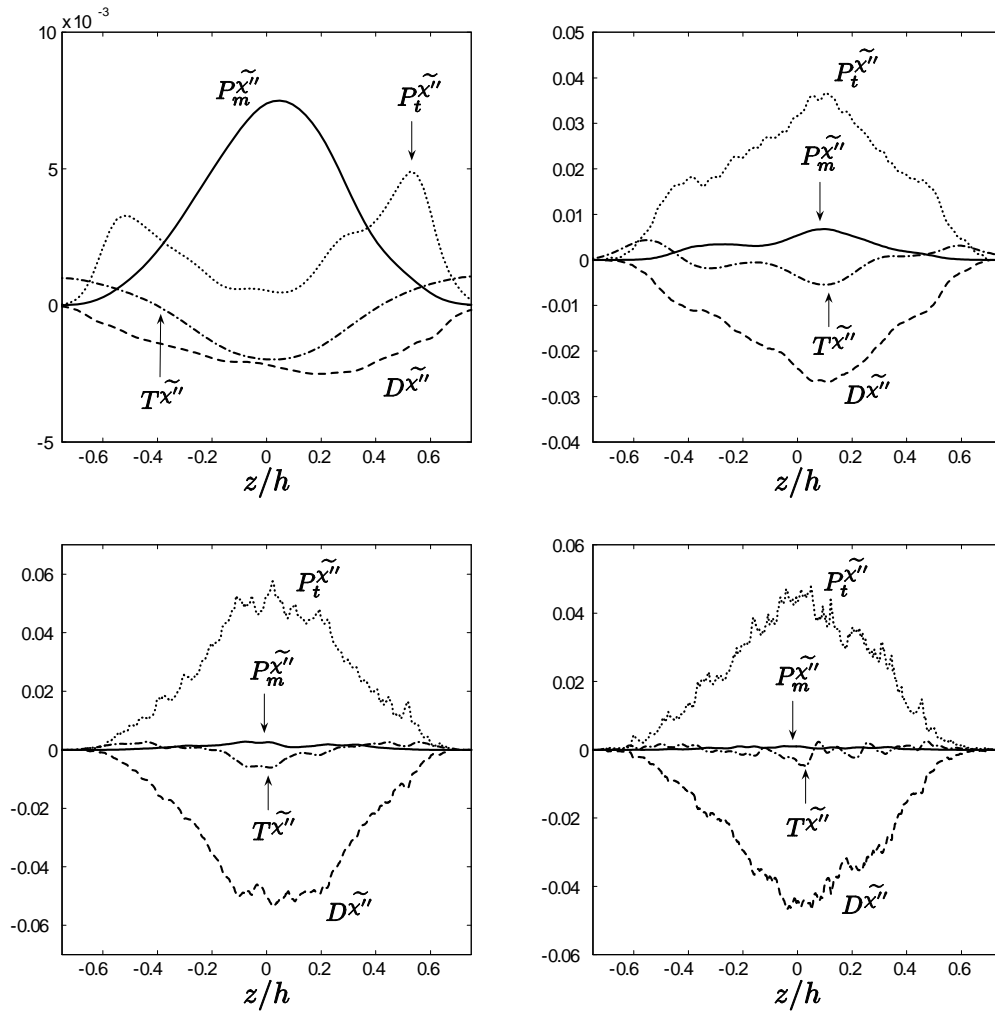


Figure 3.69 Profiles of the dominant terms in the mass fraction variance dissipation rate transport equation across the Rayleigh–Taylor mixing layer at $\tau = 0.21, 0.50, 1.01,$ and 1.52 (left-to-right, top-to-bottom).

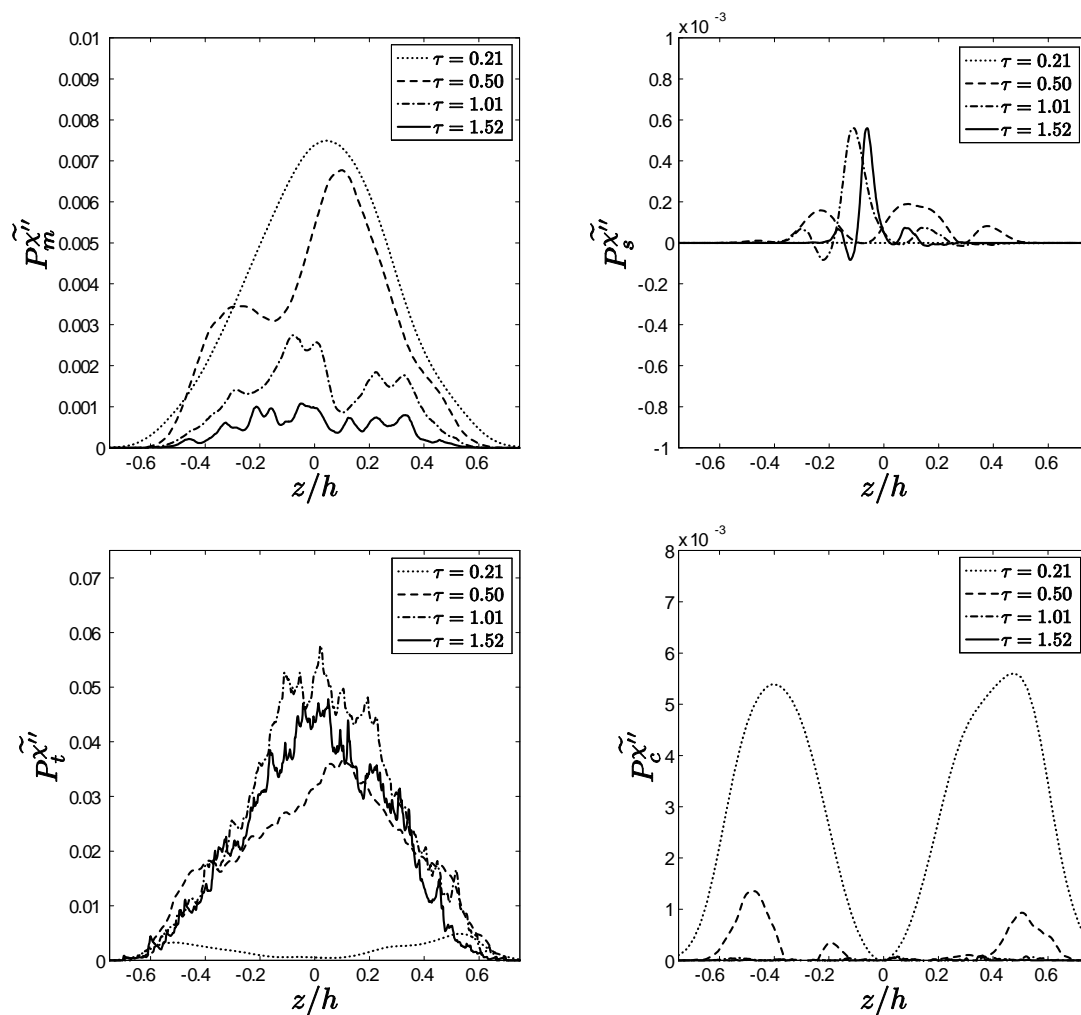


Figure 3.70 Profiles of the production terms $P_m^{\chi''}$, $P_s^{\chi''}$, $P_t^{\chi''}$, and $P_c^{\chi''}$ in the mass fraction variance dissipation rate transport equation across the Rayleigh–Taylor mixing layer at various times.

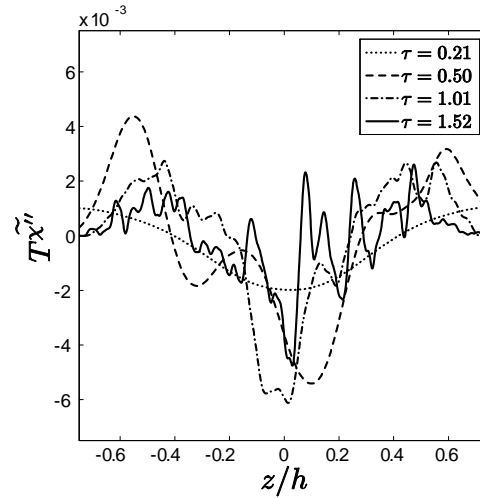


Figure 3.71 Profiles of the transport term $T^{\tilde{\chi}''}$ in the mass fraction variance dissipation rate transport equation across the Rayleigh–Taylor mixing layer at various times.

production of $\tilde{\chi}''$ is negligible, compared with the other production mechanisms. The curvature production $P_c^{\tilde{\chi}''}$ is larger in magnitude at early times when the layer width is small and $\partial^2 \tilde{m}_1 / \partial z^2$ is large at $|z/h| \approx 0.5$. Despite the large value of $P_c^{\tilde{\chi}''}$ at early times, it is still negligible when compared with the mean gradient production term $P_m^{\tilde{\chi}''}$ at all times. The mean gradient production decreases in time; however, the total contribution to the production of $\tilde{\chi}''$ remains approximately constant as shown in figure 3.74. This is the expected Re^0 scaling, as predicted by Mura and Borghi (2003). Beyond $\tau = 0.3$, the turbulent production term $P_t^{\tilde{\chi}''}$ becomes the dominant production mechanism. Fluctuating velocity gradients strain the existing density gradients, thereby increasing the total surface area available for mass diffusion. These combined processes result in an increased rate of molecular mixing.

The conservative transport of $\tilde{\chi}''$ is shown in figure 3.71. Similar to the transport terms of \tilde{E}'' , $\bar{\epsilon}'$, and $\tilde{m}_1''^2$, $\tilde{\chi}''$ is transferred away from the turbulent core of the mixing

layer in an approximately down-gradient manner. The individual flux components of $T^{\widetilde{\chi}''}$ can be broken down into their diffusive and turbulent fluxes,

$$F_d^{\widetilde{\chi}''} = -\overline{\rho D \frac{\partial \chi''}{\partial z}} \approx -\bar{\rho} \bar{D} \frac{\partial \widetilde{\chi}''}{\partial z}, \quad (3.75)$$

$$F_t^{\widetilde{\chi}''} = \bar{\rho} \overline{w'' \chi''}. \quad (3.76)$$

Profiles of each flux are shown in figure 3.72: at all times examined, the turbulent flux dominates. As $Sc > 1$, the diffusive fluxes of both $\widetilde{m_1''^2}$ and $\widetilde{\chi}''$ are negligible, even at the earliest times.

The destruction of $\widetilde{\chi}''$ by molecular diffusion, given by $D^{\widetilde{\chi}''}$, remains small until the mixing layer begins to develop significant velocity fluctuations at $\tau \approx 0.3$. Profiles of $D^{\widetilde{\chi}''}$ are shown in figure 3.73. As the mixing layer develops, $P_m^{\widetilde{\chi}''}$ decreases in magnitude, while $P_t^{\widetilde{\chi}''}$ and $D^{\widetilde{\chi}''}$ increase. The total contribution of the production and destruction terms is shown in figure 3.74. For all times examined, $P_t^{\widetilde{\chi}''} \approx D^{\widetilde{\chi}''}$. Similar to the turbulent kinetic energy dissipation rate $\bar{\epsilon}$, the total production of $\widetilde{\chi}''$ is greater than the destruction of $\widetilde{\chi}''$ until $\tau \approx 0.7$, after which the production-to-dissipation ratio remains approximately unity.

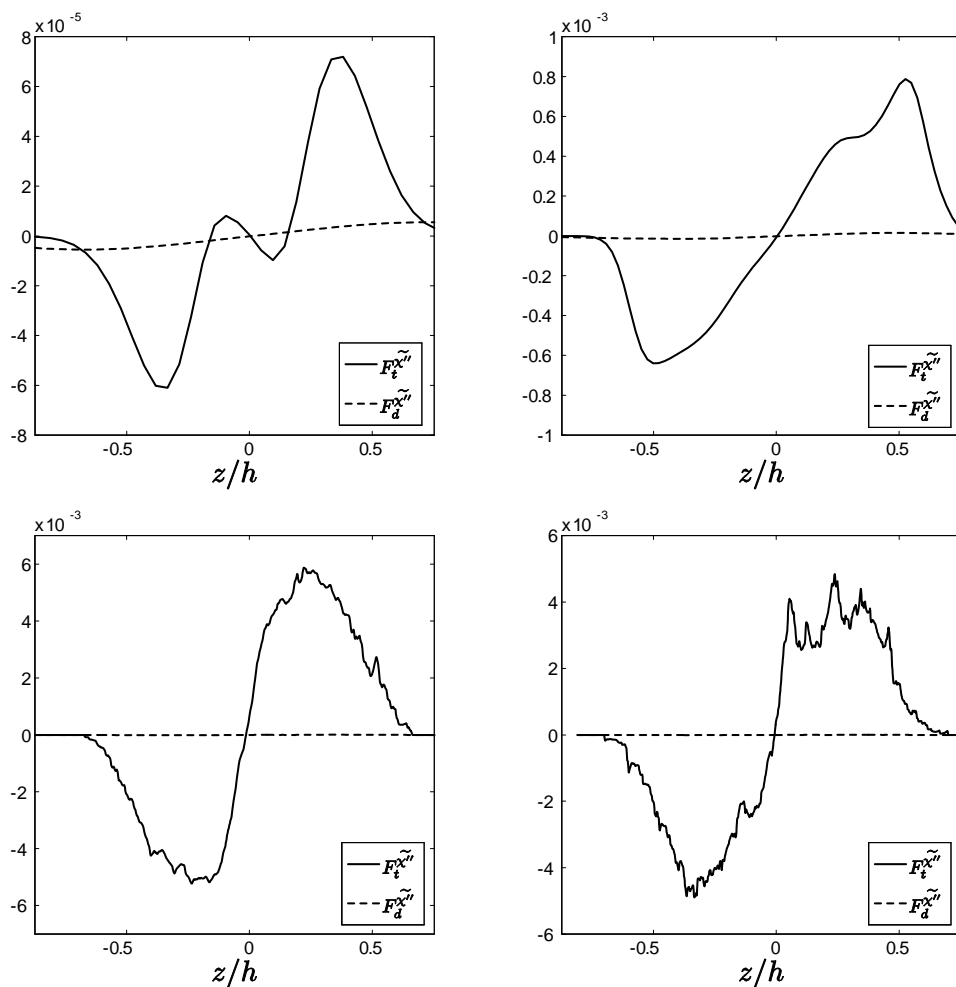


Figure 3.72 Profiles of the mean mass fraction flux terms in the transport term $T^{\chi''}$ across the Rayleigh–Taylor mixing layer at $\tau = 0.034, 0.21, 1.01,$ and 1.52 (left-to-right, top-to-bottom).

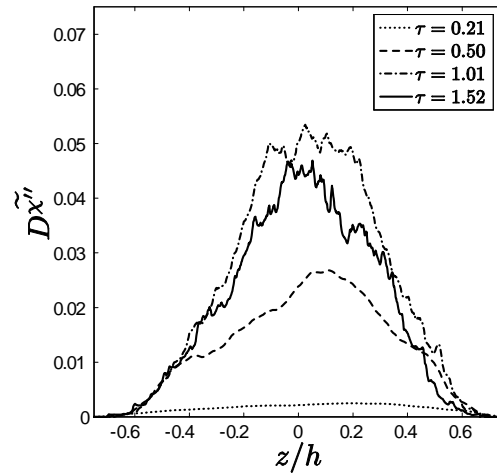


Figure 3.73 Profiles of the molecular dissipation term $D\tilde{\chi}''$ in the mass fraction variance dissipation rate transport equation across the Rayleigh–Taylor mixing layer at various times.

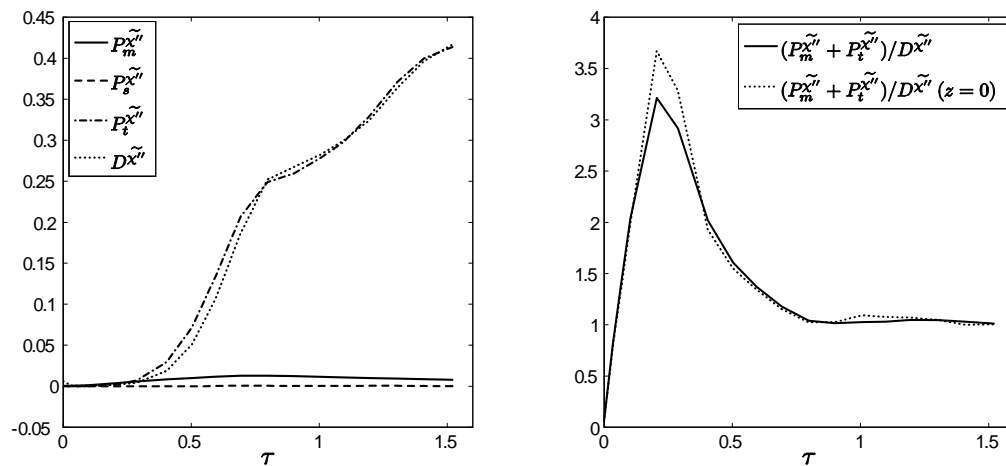


Figure 3.74 Evolution of mean gradient, shear and turbulent production, and dissipation integrals (left). Evolution of production-to-dissipation ratios (right).

4. REYNOLDS-AVERAGED NAVIER–STOKES MODEL FOR RAYLEIGH–TAYLOR TURBULENT MIXING

4.1 Overview of Goals and Methodology

The modeling of variable-density turbulent mixing by means of eddy viscosity-type turbulence models, such as the standard two-equation $\overline{E'}-\overline{\epsilon'}$ model (Jones & Lauder 1972), requires that the physics embodied in the closures accurately reflect the complex dynamics of the flow. In this work, fundamental assumptions of turbulent viscosity, gradient-diffusion, and scale-similarity closures are critically examined in the context of Rayleigh–Taylor turbulent mixing. First, an overview of turbulent viscosity models, gradient-diffusion, and scale-similarity approximations is presented. Next, in the spirit of Chen *et al.* (1991), budgets of unclosed terms in the mean and turbulent transport equations are compared with their respective closure models using the DNS data. From such comparisons, the applicability and accuracy of these closure models are assessed, and the model parameters providing the best agreement with the DNS are presented. Finally, the model parameters are tested by numerically implementing a one-dimensional, transient three- and four-equation turbulence and mixing model. The calibrated and validated model is then used to predict measurements of growth and mixing for the $Sc = 7$ experiment and DNS. Finally, the $Sc \sim 10^3$ experiment and the DNS are used to determine the necessary calibration required to accurately model the high Schmidt number experiments discussed in § 2.

4.2 Overview of Turbulent Viscosity-Based Reynolds-Averaged Turbulence Models

4.2.1 Eddy viscosity, gradient-diffusion, and scale-similarity hypotheses

First-order, single-point closure models of turbulent transport and mixing require expressions for various unclosed correlations such as the Reynolds stress tensor $\widetilde{u''_i u''_j}$ and

turbulent scalar fluxes $\widetilde{u_i''\phi''}$. Eddy viscosity closure formulations used in Reynolds-averaged Navier–Stokes (RANS) type turbulence models make use of the concept that a turbulent flow field will diffuse mass, momentum, and energy at a greater rate than by molecular processes alone. Accordingly, this enhanced diffusivity is expressed in terms of an additional turbulent stress. Boussinesq (1877) introduced the turbulent viscosity concept, drawing on an analogy from the kinetic theory of gases, by relating the deviatoric part of the Reynolds stress tensor to the mean strain-rate tensor by

$$\widetilde{u_i''u_j''} - \frac{2}{3}\widetilde{E''}\delta_{ij} \approx -2\nu_t \left(\widetilde{S}_{ij} - \frac{1}{3}\frac{\partial\tilde{u}_k}{\partial x_k}\delta_{ij} \right), \quad (4.1)$$

where $\nu_t = \mu_t/\bar{\rho}$ is a turbulent viscosity and

$$\widetilde{S}_{ij} = \frac{1}{2} \left(\frac{\partial\tilde{u}_i}{\partial x_j} + \frac{\partial\tilde{u}_j}{\partial x_i} \right) \quad (4.2)$$

is the mean strain-rate tensor. Dimensionally, the turbulent viscosity is the product of a characteristic turbulent velocity and a turbulent length scale, $\nu_t \propto u^*l^*$. Typically, the turbulent kinetic energy is used to determine the velocity scale $u^* = \sqrt{2\widetilde{E''}}$ and, thus, one other turbulent quantity is required for the length scale l^* . While many choices exist for l^* , the turbulent kinetic energy dissipation rate $\widetilde{\epsilon''}$ is often used to dimensionally construct

$$\nu_t = C_\mu \frac{\left(\widetilde{E''}\right)^2}{\widetilde{\epsilon''}}, \quad (4.3)$$

where C_μ is a dimensionless constant of proportionality (Jones & Launder 1972; Pope 2000; Wilcox 2006).

In addition to the eddy viscosity approximation for the Reynolds stress tensor, the turbulent viscosity is also used to define the gradient-diffusion hypothesis. Turbulent fluxes (*i.e.* velocity-scalar correlations) that appear in the averaged transport equations (see § 3.6) are not known *a priori* and must be modeled. The gradient-

diffusion hypothesis is phenomenologically analogous to Fourier's law of heat conduction, in that regions of high values of the mean scalar $\tilde{\phi}$ will diffuse in a 'down-gradient' manner proportional to the intensity of turbulent fluctuations

$$\widetilde{u_i'' \phi''} = -\frac{\nu_t}{\sigma_\phi} \frac{\partial \tilde{\phi}}{\partial x_i}, \quad (4.4)$$

where σ_ϕ is the dimensionless turbulent Schmidt number corresponding to $\tilde{\phi}$.

Additional closures are required for more complicated terms that appear in the $\bar{\epsilon}'$, $\widetilde{m_1''^2}$, and $\widetilde{\chi''}$ transport equations which are not implied directly by the turbulent viscosity or gradient-diffusion hypotheses, such as the buoyancy production and dissipation terms in the $\bar{\epsilon}'$ transport equation

$$P_b^{\bar{\epsilon}'} = 2 \bar{\nu} g_i \frac{\overline{\partial u_i'} \partial \rho'}}{\partial x_j \partial x_j}, \quad (4.5)$$

$$D^{\bar{\epsilon}'} = -2 \bar{\rho} \bar{\nu}^2 \left(\frac{\partial^2 u_i'}{\partial x_k \partial x_m} \right)^2. \quad (4.6)$$

While the gradient-diffusion hypothesis relates the fluctuating velocity-density correlation to known mean field quantities, no analogous hypothesis exists for relating the correlation in (4.5) or higher-order derivative correlations in (4.6). Accordingly, phenomenological similarities between the behaviors of the transport equations of $\widetilde{E''}$ and $\bar{\epsilon}'$ are made to construct closure hypotheses. For such phenomenological scale-similarity closures, a dimensionless constant of proportionality is used to relate the closures, *e.g.* $P_b^{\bar{\epsilon}'} = C_{\epsilon 0} \left(\bar{\epsilon}' / \widetilde{E''} \right) P_b^{\widetilde{E''}}$.

4.2.2 Assumptions and limitations of eddy viscosity-based models

Full-physics simulations of inertial confinement fusion capsule implosions require large computational resources, even when considering two-dimensional problems (Schurtz *et al.* 2000; Atzeni *et al.* 2005). Thus, it is advantageous to employ computationally-

economical hydrodynamics and mixing models. For this reason, engineering eddy-viscosity models similar to the standard $\overline{E'}-\overline{\epsilon'}$ model (Jones & Launder 1972) are examined here. However, several intrinsic assumptions embodied in eddy viscosity models are known to directly conflict with the dynamics of Rayleigh–Taylor driven mixing, several of which are outlined next.

First, in the standard Boussinesq approximation of the Reynolds stress tensor, it is assumed that all turbulent fluctuations are isotropic, *i.e.* $\widetilde{u'^2} = \widetilde{v'^2} = \widetilde{w'^2}$. While this assumption is violated by most turbulent flows, even in grid-generated turbulence often used to approximate decaying homogeneous isotropic turbulence (Ling & Huang 1970), this assumption clearly fails in Rayleigh–Taylor driven mixing where turbulent fluctuations and transport occurs primarily in the coordinate direction aligned with the gravitational forcing (see figure 3.19). A full account of the shortcomings of the Boussinesq eddy viscosity approximation with respect to Rayleigh–Taylor driven mixing is provided by Ristorcelli *et al.* (2005). However, it will be shown in § 4.4–4.7 that more advanced models of the Reynolds stress tensor may not be necessary to capture the fundamental turbulent transport and mixing dynamics for the small Atwood number flows considered here.

Another detracting property of eddy viscosity models is that both the Boussinesq approximation and the gradient-diffusion hypothesis rely upon a single scalar to relate vector quantities. In doing so, turbulent fluxes are assumed to be aligned with their respective mean field gradients. However, this assumption is not always correct (Deardorff 1966, 1972; Gerz & Schumann 1996; Chassaing 2001; Chassaing *et al.* 2002; Schmitt *et al.* 2003), and a more rigorous treatment of the gradient-diffusion hypothesis is required to achieve greater physical accuracy. One means of achieving

this is through the generalized gradient-diffusion hypothesis (Batchelor 1949),

$$\widetilde{u_i'' \phi''} = \Gamma_{ij} \frac{\partial \tilde{\phi}}{\partial x_j}, \quad (4.7)$$

where Γ_{ij} is the turbulent diffusivity tensor. Younis *et al.* (2005) demonstrated that Γ_{ij} is functionally-dependent on no less than ten terms for any general, incompressible, non-buoyant turbulent flow with a passive scalar. Many more terms are needed for buoyancy-driven flows with active scalars, compressible flows, or reacting flows. However, phenomenologically-simpler approaches have been proposed, most notably by Daly and Harlow (1970), where the turbulent diffusivity tensor was constructed only from the Reynolds stress tensor

$$\widetilde{u_i'' \phi''} = \frac{\widetilde{E''}}{\sigma'_\phi \widetilde{\epsilon''}} \widetilde{u_i'' u_j''} \frac{\partial \tilde{\phi}}{\partial x_j}, \quad (4.8)$$

where σ'_ϕ is a turbulent Schmidt number different from σ_ϕ defined above. Note that if the Reynolds stress tensor is modeled isotropically by $\tau_{ij} = (2/3) \bar{\rho} \widetilde{E''} \delta_{ij}$ and $\sigma'_\phi = (2/3) \sigma_\phi$, then (4.7) exactly reduces to (4.4).

Rayleigh–Taylor driven mixing further complicates the hydrodynamics modeling, in that shear production is no longer the sole source of turbulent kinetic energy. Instead, buoyancy production, which is proportional to the turbulent mass flux, becomes the most important production mechanism. This term is often modeled algebraically by the gradient-diffusion approximation, where the turbulent Schmidt number σ_ρ has a significant impact on the accurate prediction of the production rate of $\widetilde{E''}$. As noted by Chassaing *et al.* (2002), the scalar turbulent fluxes and their respective turbulent Schmidt numbers are strong functions of the particular flow being studied. For this reason, the predictive capability of gradient-diffusion closures for Rayleigh–Taylor driven mixing may be limited.

Another drawback of eddy viscosity models is the requirement that the flow be

weakly in a state of equilibrium, *i.e.* the production-to-dissipation ratios remain close to unity. The failure of RANS-type models in flows with large excursions from $P^{\widetilde{E}''}/D^{\widetilde{E}''} \approx 1$ has been well documented (Pope 2000; Jakirlić & Hanjalić 2002; Risorcelli & Clark 2004). As shown in § 3.6, the production-to-dissipation ratios for the transport equations of interest have values far from unity before $\tau \approx 0.7$. This requirement is due, in part, to the large Reynolds number assumption used to formulate scale-similarity closures, where there is a sufficient separation between the production and dissipation scales to facilitate the existence of an inertial cascade range of scales. However, Rayleigh–Taylor driven flows are initially-quiescent and transition through a number of stages before satisfying the high Reynolds number requirements of scale-similarity closures. Thus, at low and moderate Reynolds numbers, the model parameters are expected to exhibit some form of Reynolds number dependence until late-time asymptotic values are approached.

For the reasons above, the application of eddy viscosity models to Rayleigh–Taylor driven mixing may be problematic, and a complete analysis of the physics embodied in eddy viscosity, gradient-diffusion, and scale-similarity based closures is required to justify the application of such models. In the following sections, the closure models are tested by an *a priori* comparison of the profiles predicted by the models with the exact, unclosed profiles calculated in § 3.6. The model calibrations are then shown to predict the experimentally-measured degree of molecular mixing from the $Sc = 7$ and $Sc \sim 10^3$ experiments in § 2.

4.3 Determination of Model Parameters

In this section, budgets of the closed form of the transport equations examined in § 3.6 are presented to quantify the validity and accuracy of turbulent viscosity-based

closures for Rayleigh–Taylor turbulent mixing. This is important, as noted in § 4.2.2, where various phenomenological arguments used to formulate RANS-type models conflict with the flow physics that occur in buoyancy-driven mixing. In addition to justifying the predictive capabilities of the turbulent mixing models, it is possible to obtain a calibration of all model coefficients from the direct comparison of the unclosed and closed budgets. In doing so, a measure of the low-Reynolds number applicability of such models becomes evident. While the calibrated coefficients for canonical, shear-driven flows have been examined in great detail (Jones & Launder 1974; Launder & Sharma 1974; Orszag *et al.* 1996; Pope 2000; Wilcox 2006), far less attention has been given to a rigorous calibration of RANS-type models for Rayleigh–Taylor mixing (Spitz & Haas 1991; Besnard *et al.* 1992; Snider & Andrews 1996; Grégoire & Souffland 1999; Dimonte & Tipton 2006). A brief review of the commonly used values for the model parameters used in \widetilde{E}'' , $\widetilde{\epsilon}''$, and $\widetilde{m}_1''^2$ transport models is given in table 4.1.

Typically, for Rayleigh–Taylor mixing applications, the model parameters used were obtained from an *a posteriori* analysis of the model predictions compared with a limited selection of experimental data. In the work presented here, a different approach is used. Terms from the unclosed transport equation budgets will be compared *a priori* with their respective model closures (Chen *et al.* 1991; Pruett & Adams 2000). The closure model for each unclosed term was constructed from the quantities that would otherwise be available in a model (*e.g.* $\bar{\rho}$, \widetilde{E}'' , $\widetilde{\epsilon}''$, *etc.*) from the DNS, where the calibrated coefficient is given by the modeled profile that best matches the unclosed profile.

Parameter	Term	Canonical Values	Rayleigh–Taylor
C_μ	Turbulent viscosity	0.0845, 0.09	0.09
σ_ρ, σ_m	Turbulent mass flux	0.5–0.9	0.6–1.48
σ_k	Turbulent flux of \widetilde{E}''	0.72, 1.0	0.87–1.0
σ_ϵ	Turbulent flux of $\widetilde{\epsilon}''$	0.72, 1.3	1.3
σ_{m2}	Turbulent flux of $\widetilde{m_1''^2}$	0.7, 1.0	–
C_{pu}	Pressure transport of \widetilde{E}''	0.2	–
$C_{\epsilon 0}$	Buoyancy production of $\widetilde{\epsilon}''$	–	0.815–0.95
$C_{\epsilon 1}$	Shear production of $\widetilde{\epsilon}''$	1.44	1.44–1.47
$C_{\epsilon 2}$	Turbulent dissipation of $\widetilde{\epsilon}''$	1.68–1.92	1.9–1.92
C_{m2}	Turbulent dissipation of $\widetilde{m_1''^2}$	1	1.5

Table 4.1 Model parameters for ‘standard’ \widetilde{E}'' , $\widetilde{\epsilon}''$, $\widetilde{m_1''^2}$ transport models (Jones & Launder 1972; Launder & Sharma 1974; Lumley 1978; Orszag *et al.* 1996; Pope 2000; Chassaing *et al.* 2002; Liu & Fox 2006; Wilcox 2006; Brinkman *et al.* 2006) and as used in Rayleigh–Taylor mixing (Spitz & Haas 1991; Snider & Andrews 1996; Grégoire & Souffland 1999).

4.3.1 Quantification of calibration quality

Using the DNS data, the model parameters can be obtained through a direct comparison of the transport equation budgets presented in § 3.6 and their respective closures. In doing so, the optimum performance of the predictive closures can be achieved. Given the exact DNS profile $E(z, t)$ and the modeled profile $M(z, t; C_\phi)$ for a given model parameter C_ϕ , the calibrated parameter is given by the L_2 -norm minimization of the difference between $E(z, t)$ and $M(z, t; C_\phi)$. The L_2 norm is

$$L_2(t; C_\phi) = \int_{h_s}^{h_b} [E(z, t) - M(z, t; C_\phi)]^2 dz. \quad (4.9)$$

This method of calibrating model coefficients was found to be more robust than algebraically solving for C_ϕ , which can produce singularities in regions where $E(z, t)$ or $M(z, t; C_\phi)$ change sign.

Qualitative comparisons are carried out by plotting an unclosed term from the DNS against its respective closure model. A more quantitative assessment is given by calculating the correlation between the model and the DNS profile. In the spirit of Pruettt & Adams (2000), the model correlation coefficient

$$r(t; C_\phi) = \frac{\int_{h_s}^{h_b} [E(z, t) - \bar{E}(t)] [M(z, t; C_\phi) - \bar{M}(t; C_\phi)] dz}{\sqrt{\int_{h_s}^{h_b} [E(z, t) - \bar{E}(t)]^2 dz \int_{h_s}^{h_b} [M(z, t; C_\phi) - \bar{M}(t; C_\phi)]^2 dz}} \quad (4.10)$$

may be defined, where

$$\bar{E}(t) = \frac{1}{h(t)} \int_{h_s}^{h_b} E(z, t) dz, \quad \bar{M}(t; C_\phi) = \frac{1}{h(t)} \int_{h_s}^{h_b} M(z, t; C_\phi) dz \quad (4.11)$$

are the averages of $E(z, t)$ and $M(z, t; C_\phi)$ over the mixing layer width. The coefficient $r = 1$ for a perfect one-to-one correlation between the DNS data and the model prediction, $r = 0$ if there is no correlation, and $r = -1$ if the model and DNS are perfectly anti-correlated. However, the correlation coefficient only determines how

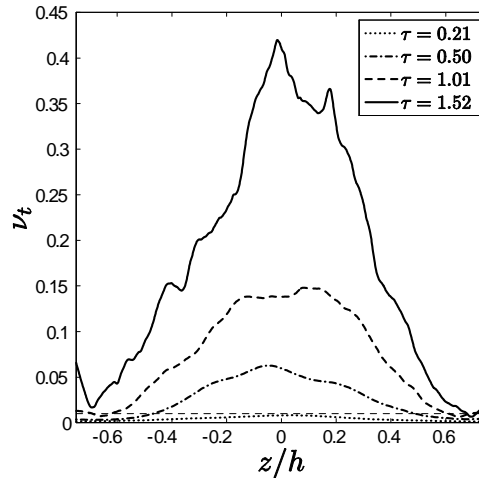


Figure 4.1 Profiles of the turbulent viscosity ν_t across the Rayleigh–Taylor mixing layer from the DNS at various times. The physical viscosity $\nu \approx 0.01$ is indicated by a dashed line.

well the model predictions are correlated with the DNS data, but does not provide information concerning how close the model predictions are in magnitude to the DNS data. Thus, a ratio of magnitude of the model to the DNS data is formulated as

$$a(t; C_\phi) = \sqrt{\frac{\int_{h_s}^{h_b} M(z, t; C_\phi)^2 dz}{\int_{h_s}^{h_b} E(z, t)^2 dz}}. \quad (4.12)$$

If $a > 1$, the model over-predicts the magnitude of the DNS data and if $a < 1$, the model under-predicts the data.

4.3.2 Boussinesq Reynolds stress model

In shear-driven flows, the ability of a model to capture the behavior of the Reynolds stress tensor is crucial for accurately modeling the mean flow dynamics. The Boussinesq eddy viscosity formulation of the Reynolds stress tensor [see (4.1)] relates the unknown velocity correlations to the known mean strain field \tilde{S}_{ij} through a turbulent

viscosity ν_t . Adopting the canonical value $C_\mu = 0.09$, profiles of ν_t from the DNS are shown in figure 4.1. While this algebraic model is phenomenologically simple, it has been shown to be sufficiently accurate for a wide range of flows. However, the Boussinesq model of the Reynolds stress tensor does not perform as well for Rayleigh–Taylor mixing due to the sustained anisotropy of the velocity fluctuations. Profiles of the diagonal components of $\widetilde{u''_i u''_j}$ from the DNS and the Boussinesq values from (4.1) are shown in figures 4.2–4.4.

In figures 4.2–4.4, the eddy viscosity model of the Reynolds stress predicts the overall shape of the profiles reasonably well; however, the magnitudes do not match. The model under-predicts the vertical velocity fluctuations and over-predicts the velocity fluctuations in the homogeneous directions. These qualitative observations can be seen more clearly in the evolution of the correlation and magnitude parameters [see (4.10) and (4.12)], shown in figure 4.5. Beyond $\tau \approx 0.2$, $r \approx 1$ for the predicted $\widetilde{w''^2}$ profiles. Similarly, $r \approx 1$ for the predicted $\widetilde{u''^2}$ and $\widetilde{v''^2}$ profiles beyond $\tau \approx 0.5$. Thus, the Boussinesq approximation models the *shape* of the diagonal Reynolds stress components well once the mixing layer transitions into a nonlinear development stage, *i.e.* $\tau > 0.5$ or $Re_h > 140$. The evolution of the magnitude coefficient in figure 4.5 shows the degree to which the Boussinesq model under- or over-predicts the total magnitude of the velocity fluctuations. However, the Boussinesq representation of $\widetilde{u''_i u''_j}$ is not expected to be valid for Rayleigh–Taylor mixing applications. Highly-accurate predictions of the Reynolds stress tensor anisotropy may not be a necessary component of a sufficiently-accurate model of Rayleigh–Taylor mixing. Fundamentally, the mean momentum transport equation and the shear production rates of $\widetilde{E''}$ and $\bar{\epsilon}'$ depend upon an accurate model of τ_{ij} . However, as shown in § 3.6, these aspects of the flow physics were found to be negligible for Rayleigh–Taylor driven mixing.

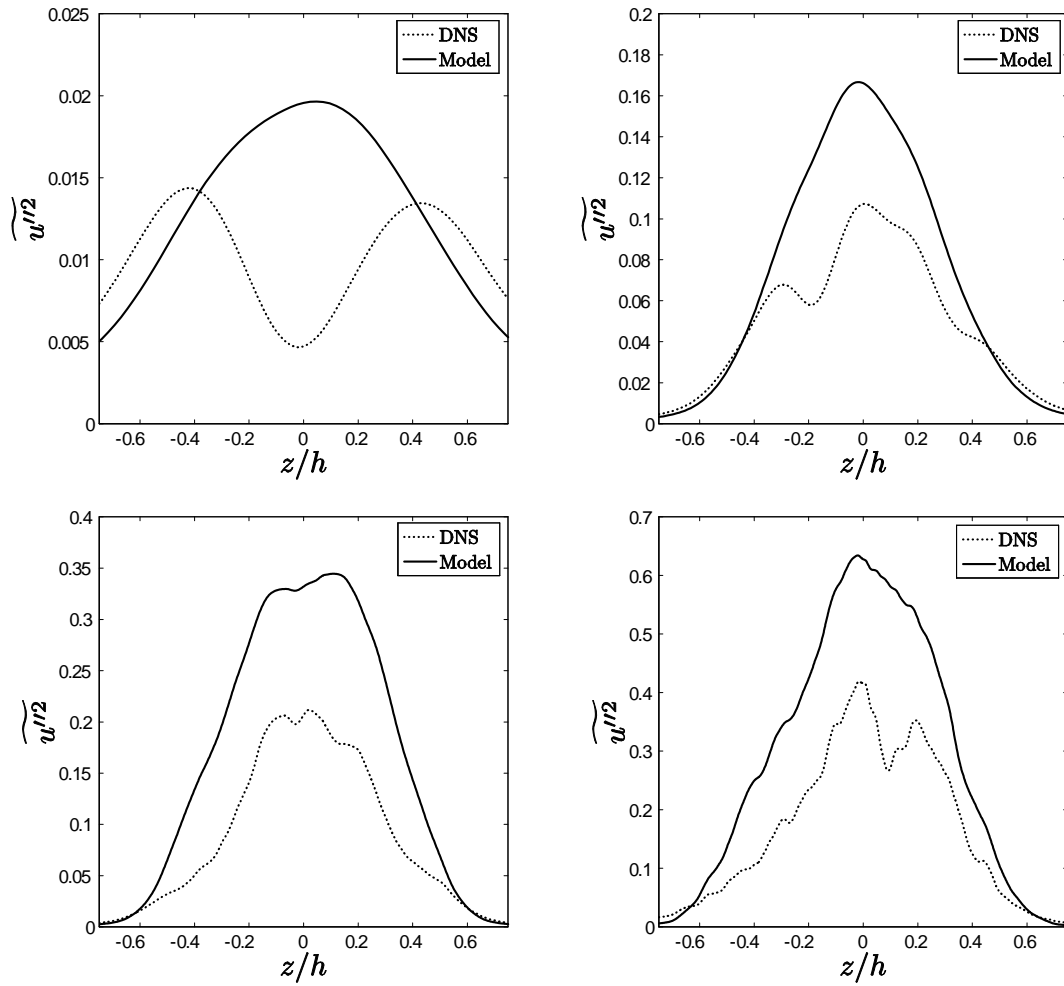


Figure 4.2 Profiles of the unclosed velocity variance $\overline{u''^2}$ and its eddy viscosity closure across the Rayleigh–Taylor mixing layer at $\tau = 0.21, 0.50, 1.01,$ and 1.52 (left-to-right, top-to-bottom).

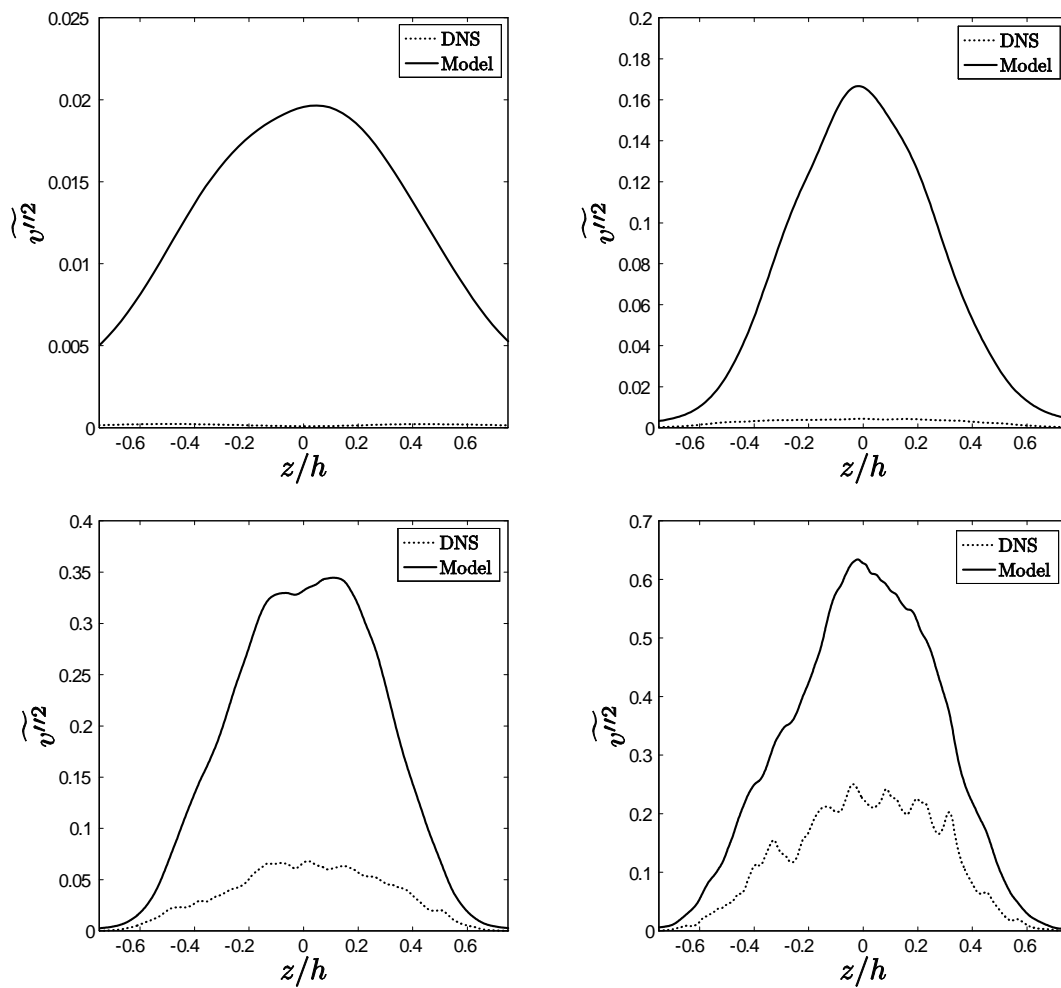


Figure 4.3 Profiles of the unclosed velocity variance $\widetilde{v''^2}$ and its eddy viscosity closure across the Rayleigh–Taylor mixing layer at $\tau = 0.21, 0.50, 1.01,$ and 1.52 (left-to-right, top-to-bottom).

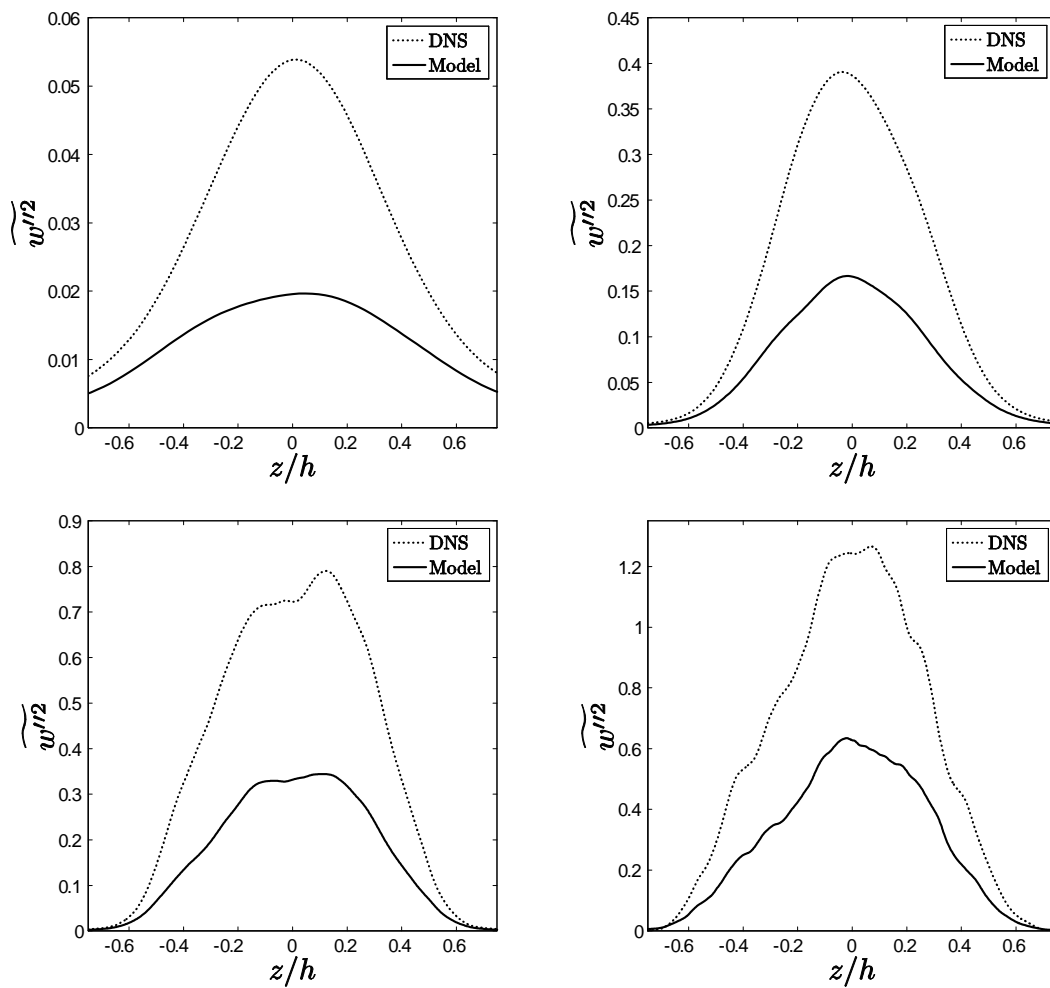


Figure 4.4 Profiles of the unclosed velocity variance $\overline{w'^2}$ and its eddy viscosity closure across the Rayleigh–Taylor mixing layer at $\tau = 0.21, 0.50, 1.01, \text{ and } 1.52$ (left-to-right, top-to-bottom).

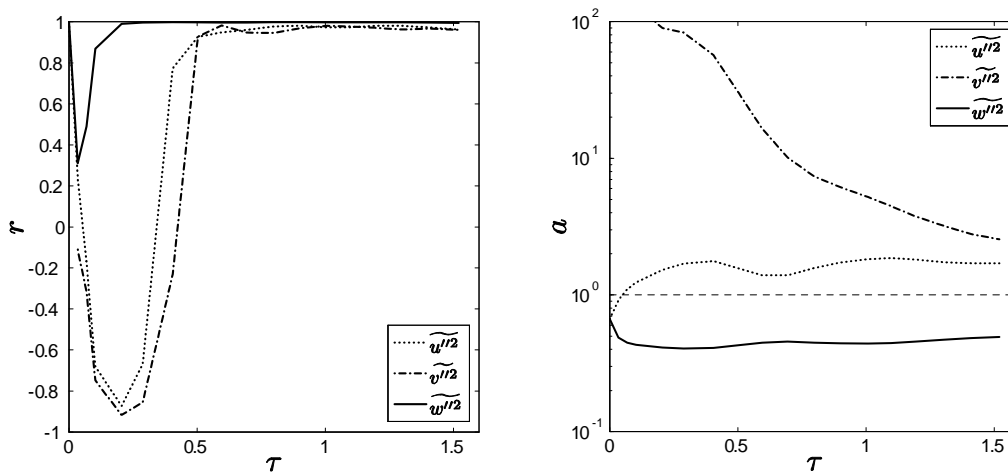


Figure 4.5 Evolution of correlation and amplitude coefficients for the Reynolds stress closures shown in figures 4.2–4.4.

4.3.3 Gradient-diffusion closures

Perhaps more important than an accurate prediction of the Reynolds stress tensor is the prediction of the turbulent flux of mass, energy, and other quantities of interest. The turbulent mass flux controls both the spreading rate of the mixing layer in the transport of \tilde{m}_1 and the production rates of $\widetilde{E''}$ and $\widetilde{m_1''^2}$. Furthermore, the conservative redistribution of transported quantities, such as $\widetilde{E''}$, $\bar{\epsilon'}$, $\widetilde{m_1''^2}$, and $\widetilde{\chi''}$, is not negligible and must be modeled by the gradient-diffusion hypothesis. Qualitative comparisons of the gradient-diffusion models for the turbulent fluxes $\bar{\rho} \widetilde{w'' m_1''}$, $\bar{\rho} \widetilde{w'' E''}$, $\bar{\rho} \widetilde{w'' \epsilon'}$, $\bar{\rho} \widetilde{w'' m_1''^2}$, and $\bar{\rho} \widetilde{w'' \chi''}$ are shown in figures 4.6–4.10. To minimize oscillations in the mean field gradients from the DNS used to construct the closures, a locally-weighted, linear, least-squares regression (Cleveland 1979; Cleveland & Devlin 1988) was applied to a 51-point stencil to filter the mean profiles before calculating gradients. Also, as noted by Spitz and Haas (1991), the density-velocity correlation in the turbulent mass flux $\overline{w''} = -\overline{\rho' w'} / \bar{\rho}$ is not shown as it is equivalent to the velocity-mass fraction correlation shown in figure 4.6.

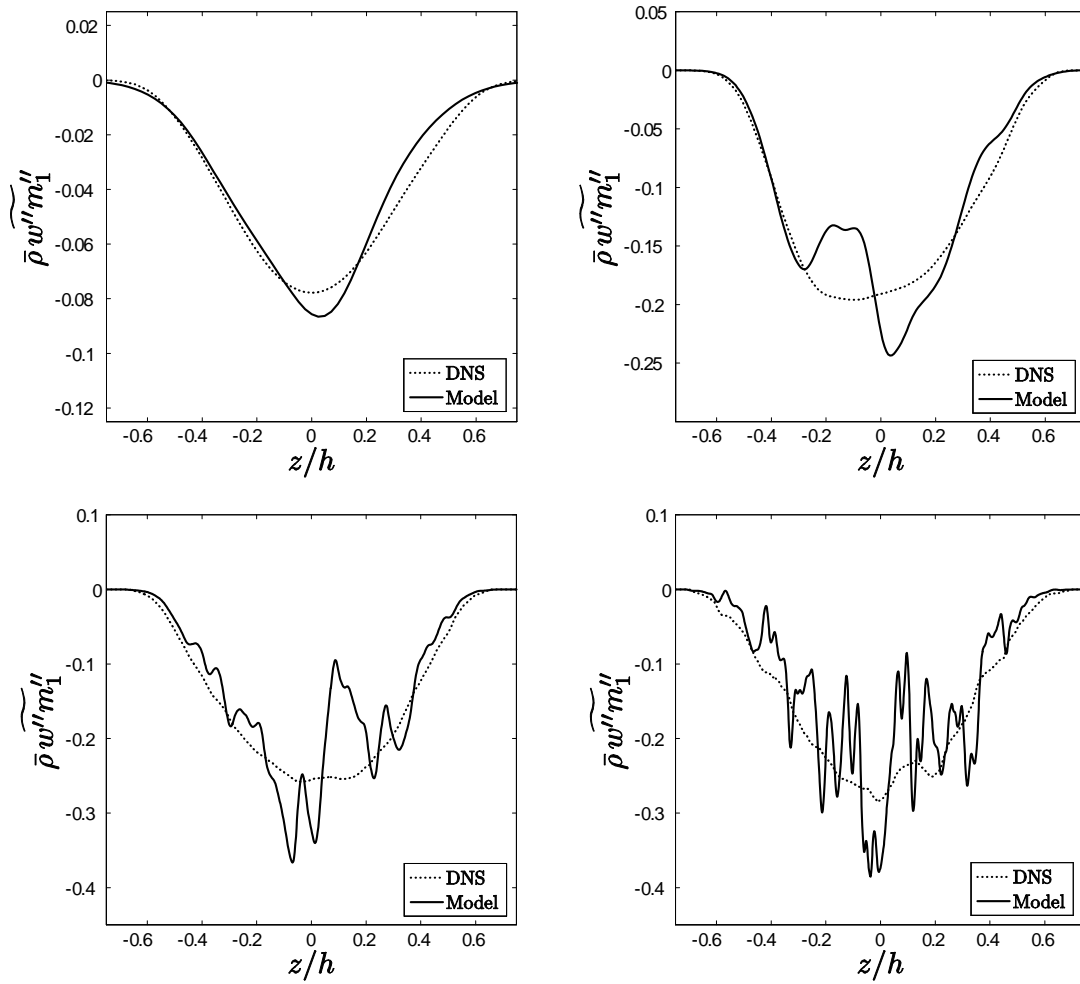


Figure 4.6 Profiles of the unclosed turbulent flux $\overline{\rho w'' m_1''}$ and its gradient-diffusion closure across the Rayleigh–Taylor mixing layer at $\tau = 0.21, 0.50, 1.01,$ and 1.52 (left-to-right, top-to-bottom).

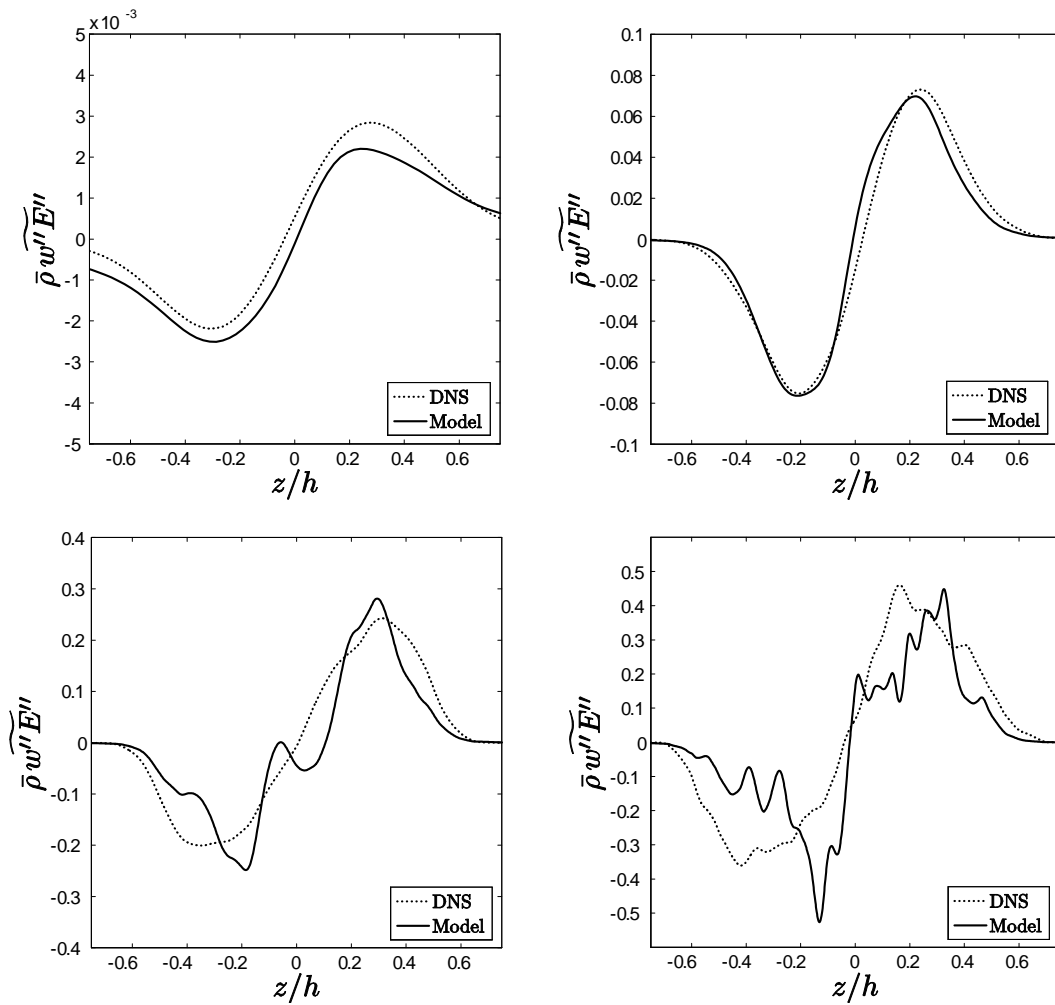


Figure 4.7 Profiles of the unclosed turbulent flux $\overline{\rho w'' E''}$ and its gradient-diffusion closure across the Rayleigh–Taylor mixing layer at $\tau = 0.21, 0.50, 1.01,$ and 1.52 (left-to-right, top-to-bottom).

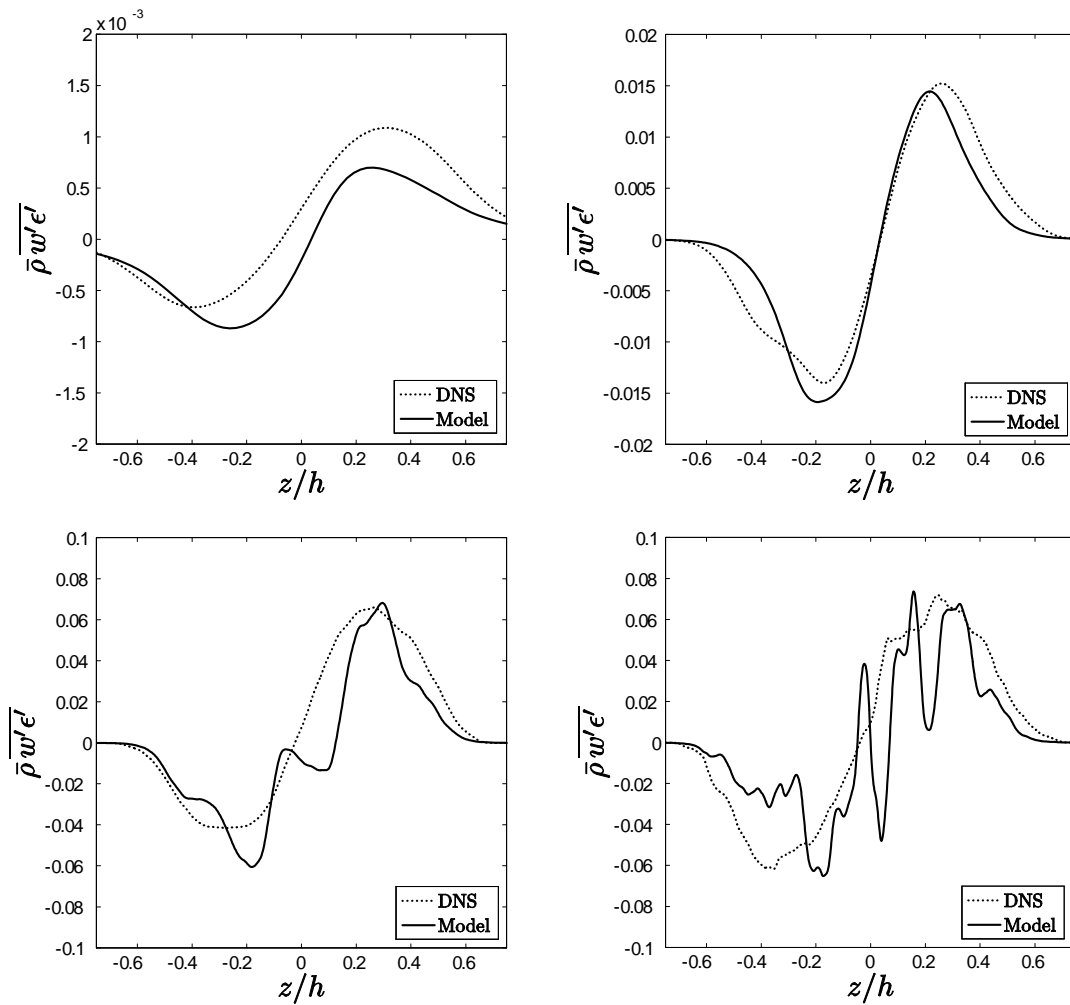


Figure 4.8 Profiles of the unclosed turbulent flux $\overline{\rho w' \epsilon'}$ and its gradient-diffusion closure across the Rayleigh–Taylor mixing layer at $\tau = 0.21, 0.50, 1.01,$ and 1.52 (left-to-right, top-to-bottom).

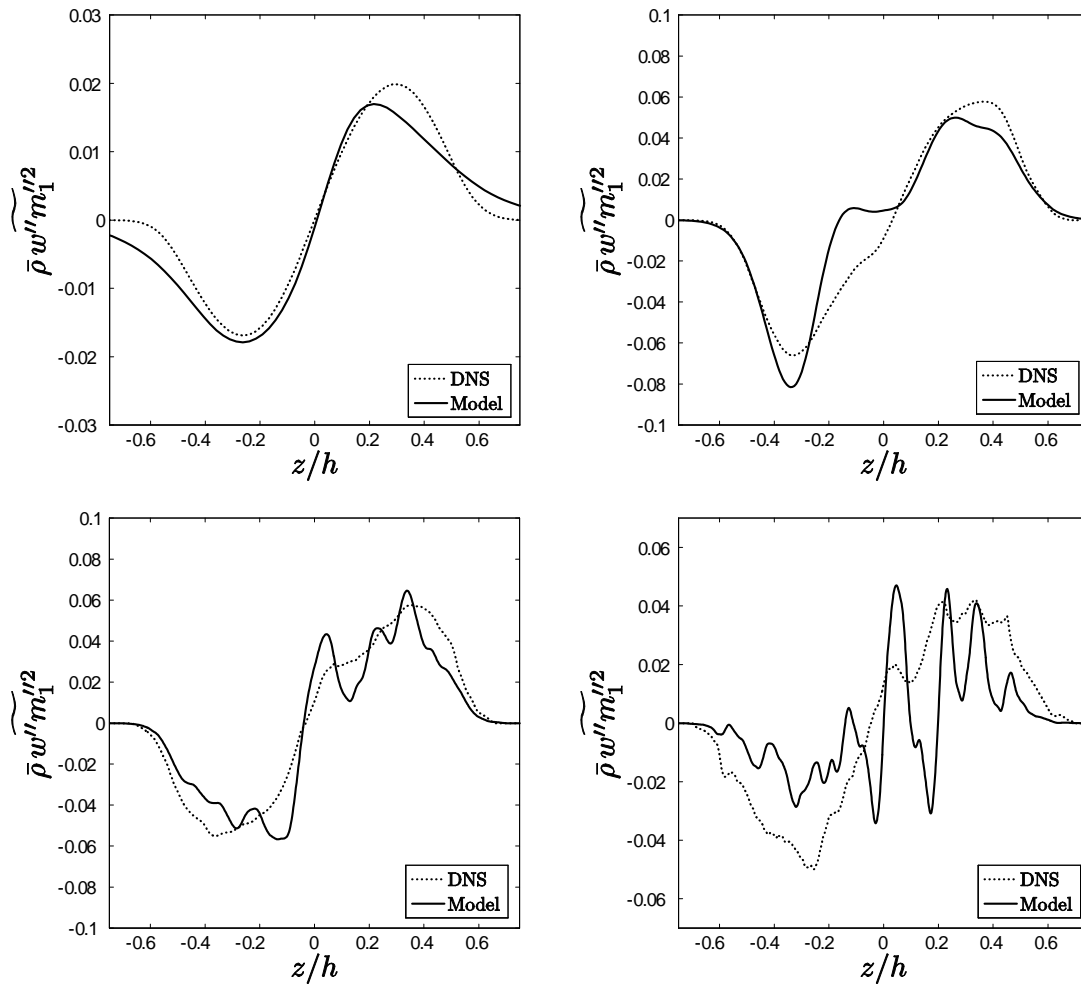


Figure 4.9 Profiles of the unclosed turbulent flux $\overline{\rho w'' m_1''^2}$ and its gradient-diffusion closure across the Rayleigh–Taylor mixing layer at $\tau = 0.21, 0.50, 1.01,$ and 1.52 (left-to-right, top-to-bottom).

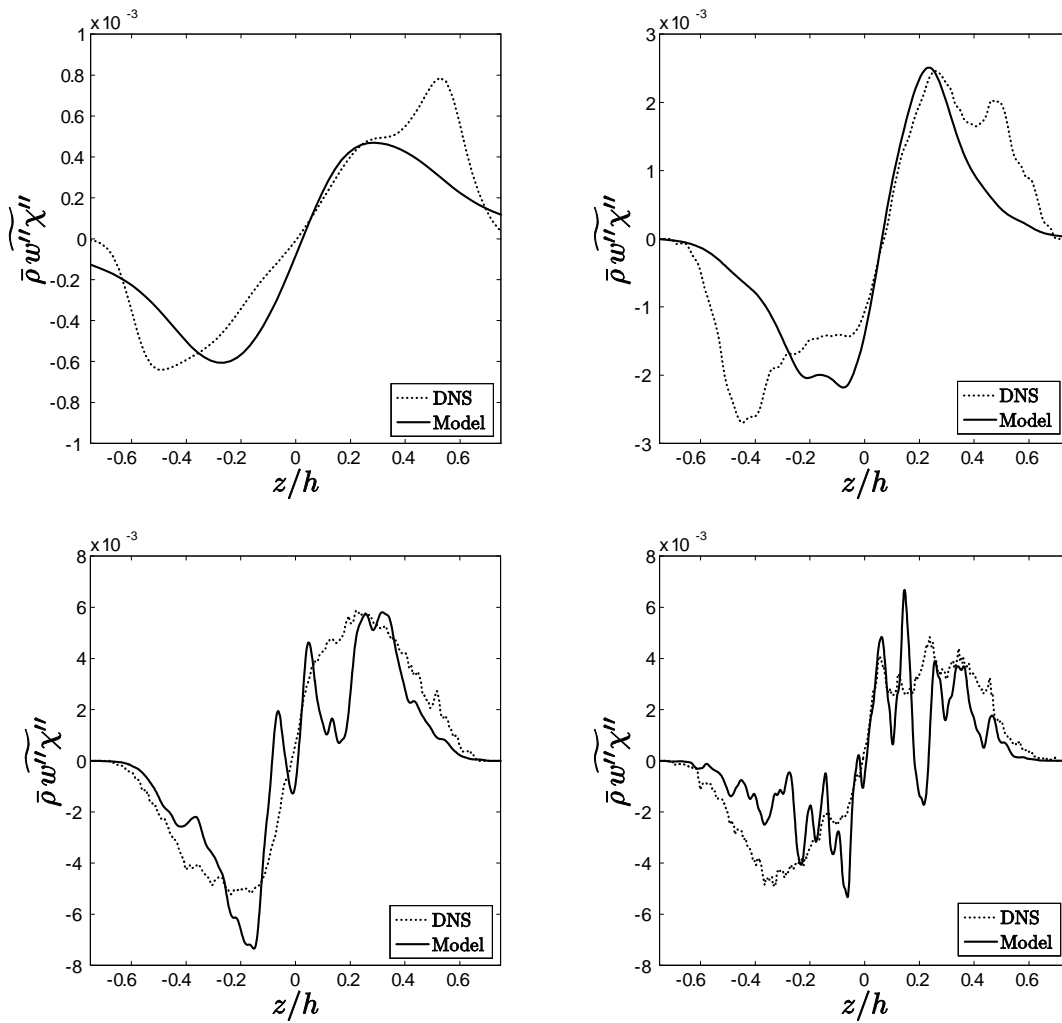


Figure 4.10 Profiles of the unclosed turbulent flux $\overline{\rho w'' \chi''}$ and its gradient-diffusion closure across the Rayleigh–Taylor mixing layer at $\tau = 0.21, 0.50, 1.01,$ and 1.52 (left-to-right, top-to-bottom).

The model profiles in figures 4.6–4.10 are plotted using the optimized turbulent Schmidt number $\sigma_\phi(Re_h)$ at each instance in time, calculated by minimizing the L_2 -norm difference between the DNS and model profiles. The evolution of the calibrated turbulent Schmidt numbers is shown in figure 4.11, and show some degree of variability in time. This is expected as the mixing transitions between linear growth, transitional, and turbulent regimes. To further illustrate this point, the evolution of the turbulent Schmidt numbers are plotted as a function of the integral-scale Reynolds number in figure 4.12. At early times ($\tau < 0.7$ or $Re_h < 500$), each σ_ϕ exhibits variations, as the production-to-dissipation ratios for each transport equation have yet to reach late-time steady values. Once the mixing layer becomes transitional ($Re_h \gtrsim 500$), the turbulent Schmidt numbers for the \widetilde{E}'' and $\bar{\epsilon}'$ transport equations relax to the late-time values $\sigma_\rho \approx 0.09$, $\sigma_k \approx 0.11$, and $\sigma_\epsilon \approx 0.15$; however, each exhibits a slight increase with Reynolds number. The turbulent Schmidt numbers for the scalar field exhibit a greater dynamic range and are more sensitive to Re_h . Both σ_{m2} and σ_χ show a more significant rise with Re_h at late time ($Re_h > 1000$). This may be due to the fact that the degree of molecular mixing and statistical composition of the mixed fluid have yet to reach steady-state values (see § 3.5).

All calibrated turbulent Schmidt numbers, which are at least weak functions of Re_h beyond the transitional threshold of $Re_h \approx 500$, exhibit much lower values than typically used to model shear-driven flows. Furthermore, all applications of RANS-type models to Rayleigh–Taylor mixing also have used larger turbulent Schmidt numbers. However, all of these cases have either cited other buoyancy-driven applications (Snider & Andrews 1996) or used a trial-and-error approach for selecting each turbulent Schmidt number (Besnard *et al.* 1992; Grégoire & Souffland 1999). The present work is the first to directly and systematically obtain turbulent Schmidt numbers for a Rayleigh–Taylor mixing layer from a DNS and determine the dependence of the model

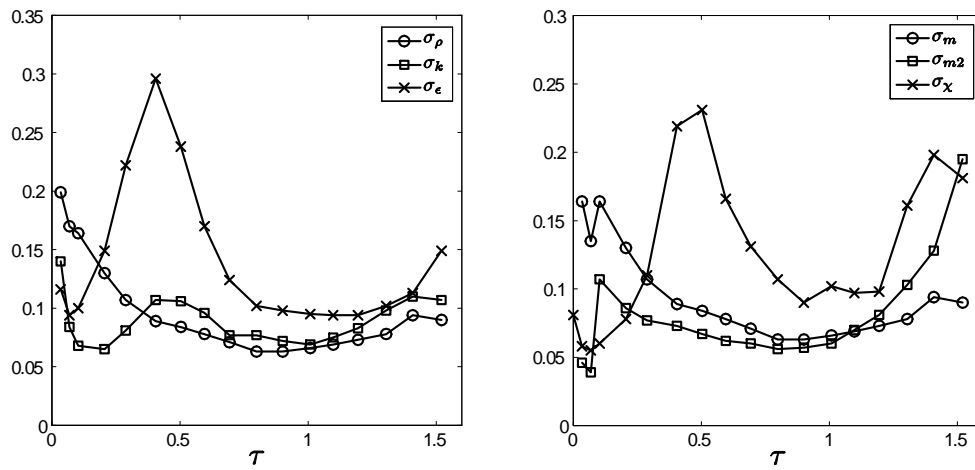


Figure 4.11 Evolution of calibrated turbulent Schmidt numbers as a function of dimensionless time.

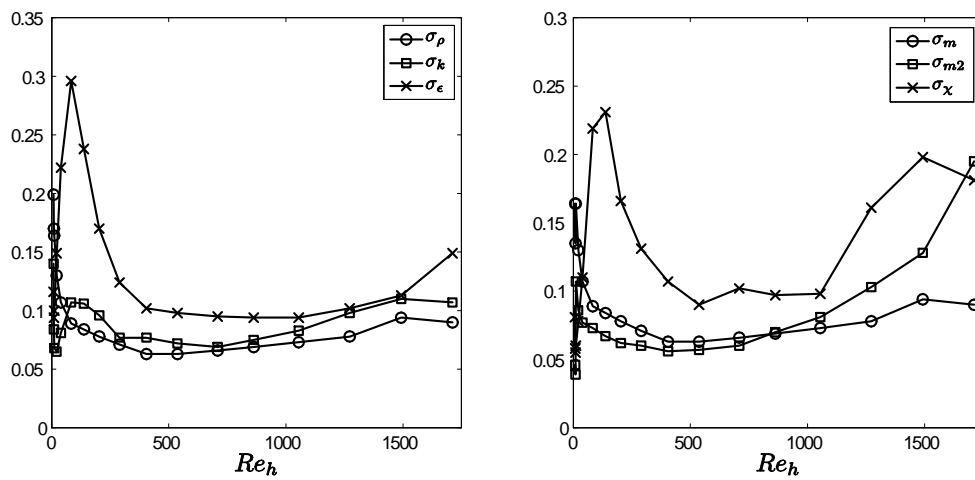


Figure 4.12 Evolution of calibrated turbulent Schmidt numbers as a function of integral-scale Reynolds number.

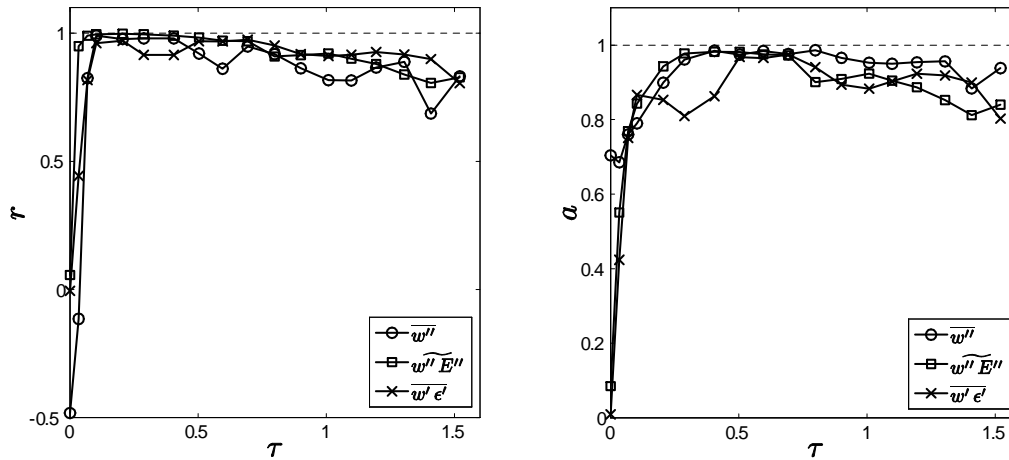


Figure 4.13 Evolution of the model correlation and magnitude coefficients for the turbulent flux terms in the \widetilde{E}'' and $\widetilde{\epsilon}''$ transport equations.

parameters on the Reynolds number. At late-time ($\tau \gtrsim 1.2$), the turbulent Schmidt numbers σ_ϵ , σ_{m2} , and σ_χ exhibit an increasing trend. For σ_{m2} , this is most likely due to the elevated degree of molecular mixing at late-time; however, it may also be due to the increased relative uncertainty in measured statistics at late-time. For the dissipative turbulent Schmidt numbers σ_ϵ and σ_χ , this rise is most likely due to the relative decrease in turbulent transport of $\widetilde{\epsilon}''$ and $\widetilde{\chi}''$ at late time, as shown in figures 3.53 and 3.69; however, this may also be due to the increased relative uncertainty at late-time.

To quantitatively assess the quality of the closures shown in figures 4.6–4.10, the model correlation and magnitude coefficients are shown in figures 4.13–4.14. Unlike the Boussinesq model of the Reynolds stress tensor, the gradient-diffusion models of the turbulent fluxes show favorable agreement for all closures beyond $\tau > 0.2$ when using the Reynolds number-dependent turbulent Schmidt numbers $\sigma_\phi(Re_h)$. At the latest times ($\tau \gtrsim 1.25$), the model correlation and magnitude coefficients deviate from values close to $r = 1$ and $a = 1$, indicating that the models do not agree as

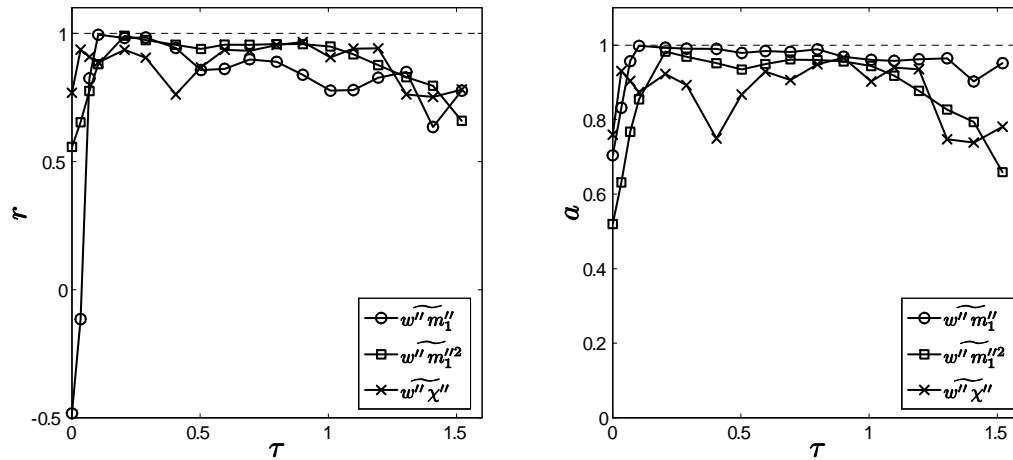


Figure 4.14 Evolution of the model correlation and magnitude coefficients for the turbulent flux terms in the scalar field transport equations.

well at these times. However, this is likely attributed to the increase in statistical oscillations in the mean profiles from the DNS, and hence increased oscillations in the mean profile gradients required to construct the gradient-diffusion closures.

4.3.4 Pressure transport closures

An interesting result from § 3.6.4 (see figures 3.46–3.48) was the finding that the pressure transport $\overline{p'w''}$ was non-negligible, has a complex profile shape, and has a bifurcation in its transport behavior at early times. Typical closure formulations either neglect the pressure transport (Daly & Harlow 1970) or group the pressure transport together with the closure of the turbulent kinetic energy flux $\widetilde{u_i''E''}$ (Lumley 1978). However, this is not appropriate for Rayleigh–Taylor driven mixing.

While the mathematical form of the pressure transport is similar to the canonical turbulent flux closed by the gradient-diffusion hypothesis (see § 4.2.1), such closures do not apply to pressure fluctuations. The first model investigated here was proposed by Lumley (1978), where the pressure transport simply subtracted from the overall

flux of $\widetilde{E''}$,

$$\overline{p' u_i''} = -C_{pu} \bar{\rho} \widetilde{u_i'' E''}, \quad (4.13)$$

where Lumley suggested a value of $C_{pu} = 2/5$ in homogeneous turbulence. Profiles of the unclosed and closed pressure transport are shown in figure 4.15. At very low Reynolds numbers ($Re_h < 100$), Lumley's model does not correctly predict the direction of the flux of $\widetilde{E''}$; however this may be rectified by a negative value of C_{pu} , as shown in the profile of $\overline{p' w''}$ at $\tau = 0.21$. At low and moderate Reynolds numbers ($100 < Re_h < 1500$), Lumley's model correctly predicts the flux direction of $\widetilde{E''}$ within the core of the mixing layer ($|z/h| \lesssim 0.5$). However, this model does not predict the shape of the profile very well, nor does it capture the change in sign of the flux at the boundaries of the mixing layer ($|z/h| \gtrsim 0.5$). This behavior is an important feature of the pressure transport that has significant effects at the mixing layer boundaries and should be captured by any realistic model.

Several researchers have also found Lumley's model to provide an inadequate description of the pressure transport in more complicated flows, and thus, alternate models have been proposed. Following the two-scale direct interaction approximation (TSDIA) of Yoshizawa (1982), Shimomura (1998) showed that

$$\overline{p' u_i'} = \frac{(\overline{E'})^2}{\overline{\epsilon'}} \left(C_{pu1} \frac{\partial \overline{E'}}{\partial x_i} + C_{pu2} \frac{\overline{E'}}{\overline{\epsilon'}} \frac{\partial \overline{\epsilon'}}{\partial x_i} \right), \quad (4.14)$$

where $C_{pu1} = 0.0136$ and $C_{pu2} = 0.00467$. Studying the wake flow past a rectangular trailing edge, Yao *et al.* (2002) proposed

$$\overline{p' u_i'} = -C_{pu} \frac{\overline{E'} u_i^*}{\overline{\epsilon'}} \frac{\partial}{\partial x_j} (\overline{E'} u_j^*), \quad (4.15)$$

where u_i^* is the difference between the velocity u_i and the trailing edge velocity U_{TE} . More closely related to Rayleigh–Taylor driven mixing, Chandra and Grötzbach

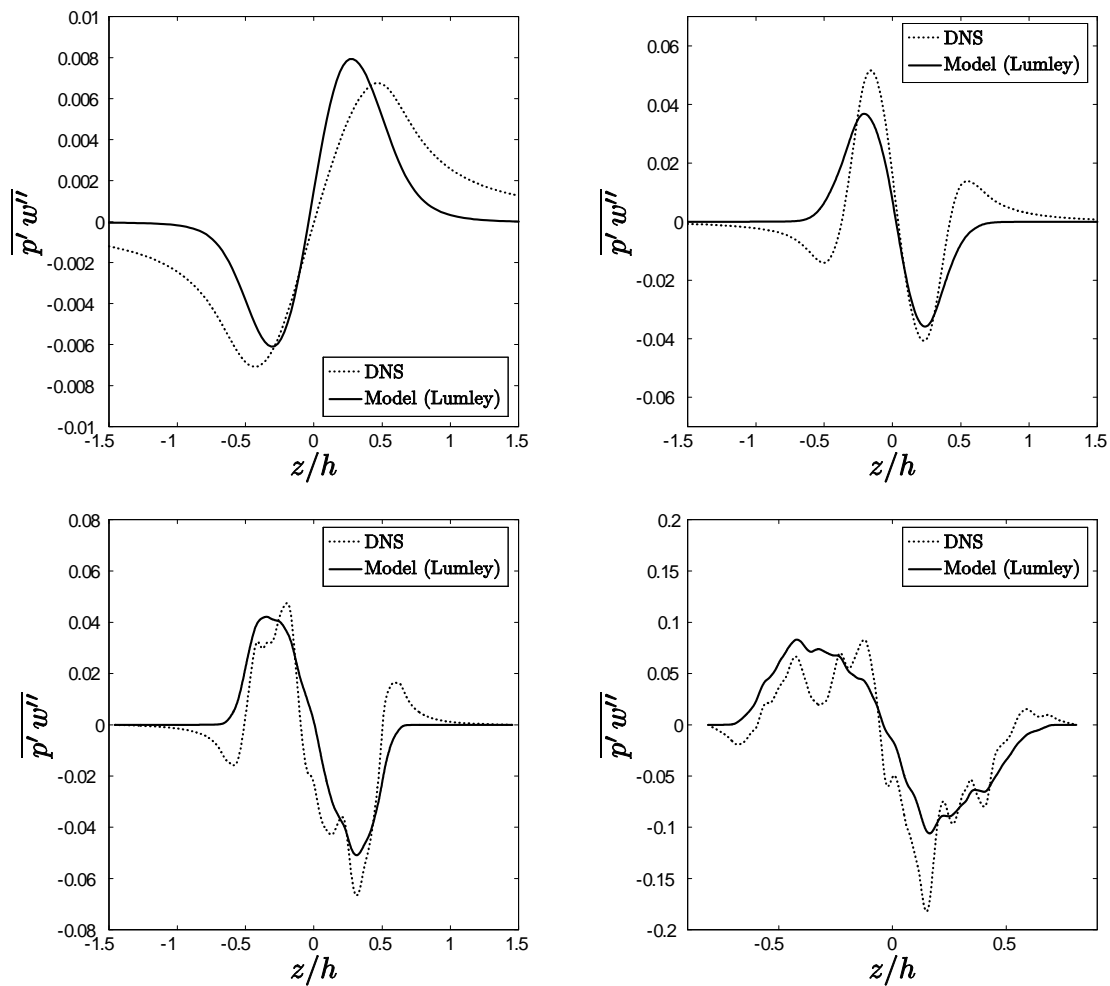


Figure 4.15 Profiles of the unclosed vertical pressure transport $\overline{p' w''}$ and Lumley's (1978) closure across the Rayleigh–Taylor mixing layer at $\tau = 0.21, 0.50, 1.01,$ and 1.52 (left-to-right, top-to-bottom).

(2007) found that the model proposed by Davidson (1969)

$$\overline{p' u'_i} = -\frac{2 C_{pu}}{Re_t^{0.8}} \frac{(\overline{E'})^2}{\overline{\epsilon'}} \frac{\partial \overline{E'}}{\partial x_i}, \quad (4.16)$$

where $Re_t = (\overline{E'})^2 / (\nu \overline{\epsilon'})$ is the turbulent Reynolds number, performed better in turbulent Rayleigh–Bénard and internally-heated natural convection problems. However, these more advanced turbulent flux models generate the same general profile shape as Lumley’s model. None of these models capture the transport of kinetic energy away from the mixing layer at the layer boundaries. The inability of pressure transport models to capture this particular effect will be discussed further in § 4.6.

Similar to the pressure transport of $\widetilde{E''}$, $\overline{\epsilon'}$ is also transported via pressure fluctuations. While the pressure transport of $\widetilde{E''}$ has received little attention in the literature, even less consideration has been given to the pressure transport of $\overline{\epsilon'}$. This is likely due to the notion that the modeled $\overline{\epsilon'}$ or $\widetilde{\epsilon''}$ transport equations are constructed on purely phenomenological grounds. However, a complete budget of the unclosed $\overline{\epsilon'}$ equation is available in § 3.6.5 for the evaluation of the turbulent dynamics. Using an analogous closure to Lumley’s (1978) pressure transport model, the pressure transport of $\overline{\epsilon'}$ is modeled as

$$2 \bar{\nu} \frac{\partial \overline{p'}}{\partial x_m} \frac{\partial \overline{u'_i}}{\partial x_m} = -C_{pu}^\epsilon \bar{\rho} \overline{u'_i \epsilon'}. \quad (4.17)$$

Both the unclosed and closed $\overline{\epsilon'}$ pressure transport profiles are shown in figure 4.16 at various times. Similar to $\overline{p' w''}$, the pressure transport of $\overline{\epsilon'}$ augments the turbulent flux $\bar{\rho} \overline{w' \epsilon'}$ at early times and then transitions to a profile that opposes $\bar{\rho} \overline{w' \epsilon'}$. Also, the pressure transport of $\overline{\epsilon'}$ shows the same complex behavior as $\overline{p' w''}$, where $\overline{\epsilon'}$ is transported away from the mixing layer at the boundaries of the layer. However, this particular effect is much smaller than the pressure transport of $\widetilde{E''}$ away from the layer by pressure fluctuations. This is expected as the velocity fluctuations induced

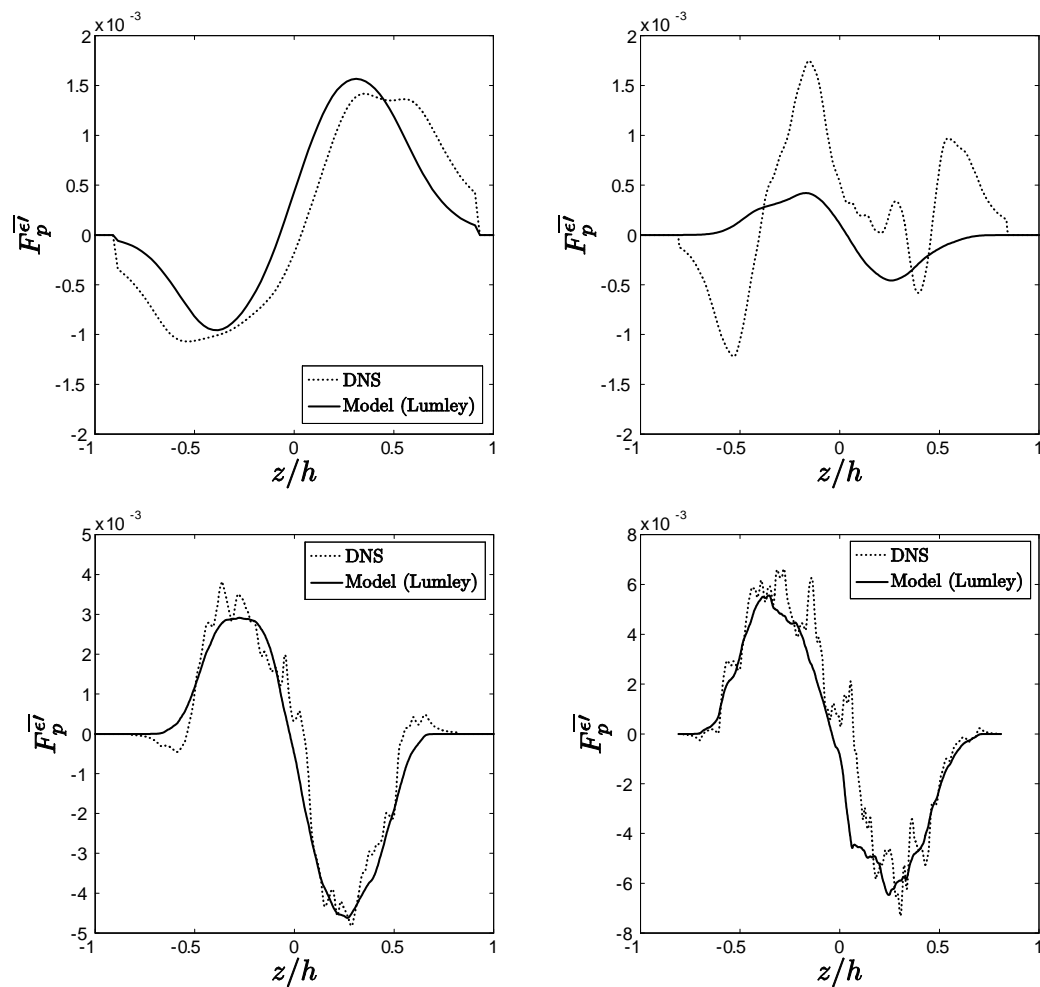


Figure 4.16 Profiles of the unclosed pressure transport $\overline{F_p^{e'}}$ and Lumley's (1978) closure across the Rayleigh–Taylor mixing layer at $\tau = 0.21, 0.50, 1.01, 1.52$ (left-to-right, top-to-bottom).

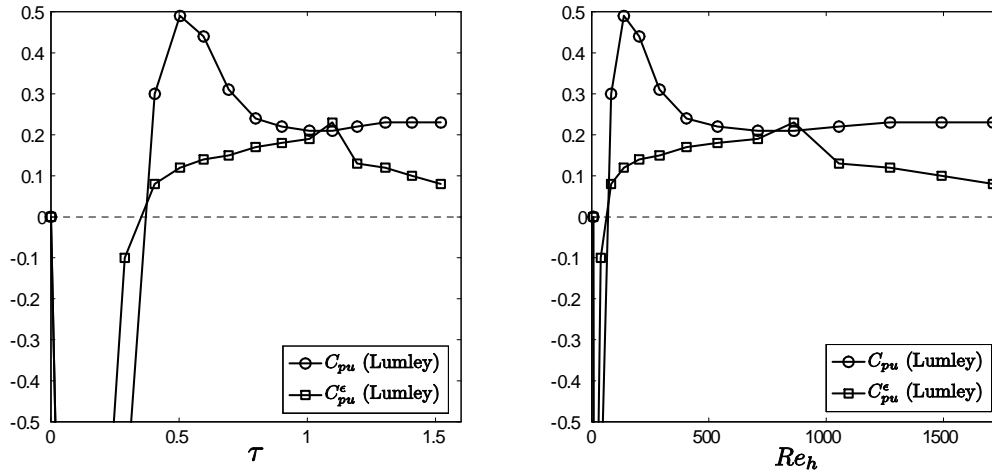


Figure 4.17 Evolution of calibrated pressure transport coefficients C_{pu} and C_{pu}^ϵ as a function of time (left) and integral-scale Reynolds number (right).

in the fluid around the mixing layer remains essentially irrotational, and hence, the dissipation rate of these fluctuations is nearly negligible.

Analogous to the turbulent Schmidt number calibrations in § 4.3.3, the pressure transport model coefficients may also be calculated. Figure 4.17 shows the evolution of C_{pu} and C_{pu}^ϵ for Lumley's model [see (4.13) and (4.17)] as a function of both time and integral-scale Reynolds number. As the pressure transport is non-negligible, even beyond the boundaries of the mixing layer, the L_2 norm minimization used to determine C_{pu} and C_{pu}^ϵ was modified such that the integral bounds were changed to $[-L_z/2, L_z/2]$. Both parameters have negative values before $\tau \approx 0.4$, when the mixing layer is at the beginning of its nonlinear transition regime. These negative values indicate that the pressure transport terms are aligned with the turbulent fluxes of \widetilde{E}'' and \bar{e}' . Once $Re_h \approx 500$ has been reached, $C_{pu} \approx 0.25$, or approximately half of Lumley's predicted value $C_{pu} = 0.4$. However, from figure 4.15, while $C_{pu} \approx 0.2$, it is evident that Lumley's model only captures the physics of $\overline{p'w''}$ within $|z/h| < 0.5$ and does not account for the flux away from the mixing layer at $|z/h| > 0.5$. The

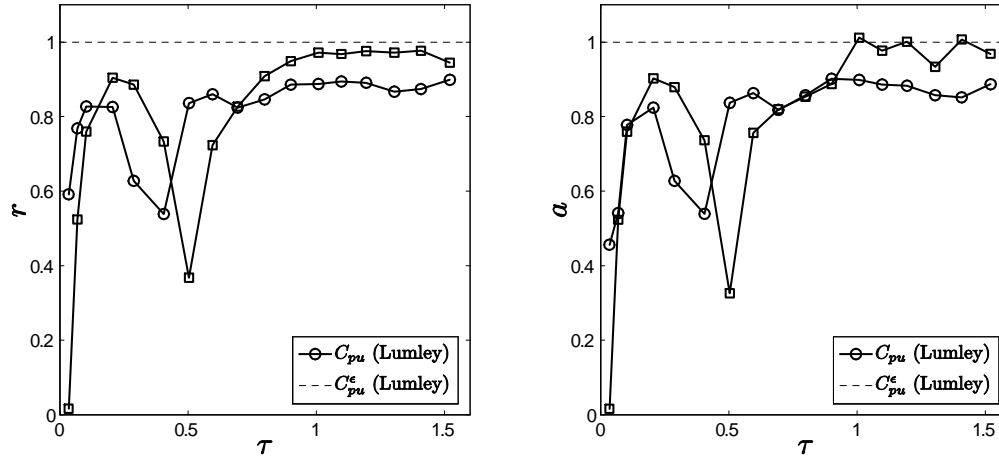


Figure 4.18 Evolution of the model correlation and magnitude coefficients for the Lumley pressure transport models in the \widetilde{E}'' and $\bar{\epsilon}'$ transport equations.

modeled form of the $\bar{\epsilon}'$ pressure transport in (4.17) performs better, as very little $\bar{\epsilon}'$ is transported away from the mixing layer by pressure fluctuations. In addition, as shown in figure 3.57, the turbulent flux of $\bar{\epsilon}'$ becomes more dominant with Re_h , while the pressure transport of $\bar{\epsilon}'$ remains relatively unchanged in magnitude. Thus, C_{pu}^ϵ continues to decrease with Re_h . It is plausible that at a sufficiently large Reynolds number, the pressure transport of $\bar{\epsilon}'$ may be negligible compared with the turbulent flux of $\bar{\epsilon}'$.

To quantify the predictive capability of the closures in figures 4.15 and 4.16, the model correlation and magnitude coefficients are shown in figure 4.18. Similar to the modified calculation of the L_2 -norm for the pressure transport, the correlation and magnitude coefficients were also calculated using integral bounds of $[-L_z/2, L_z/2]$. Before the early-time nonlinear transition at $\tau \approx 0.5$, both models capture the pressure transport of \widetilde{E}'' and $\bar{\epsilon}'$ given negative values of C_{pu} and C_{pu}^ϵ . During the nonlinear transition, $\tau \approx 0.3$ – 0.4 for \widetilde{E}'' and $\tau \approx 0.4$ – 0.6 for $\bar{\epsilon}'$, the correlation between the model and DNS profiles breaks down. After the transition, the model for the pressure

transport of \widetilde{E}'' is marginally adequate, while the model for the pressure transport of $\overline{\epsilon'}$ exhibits better agreement at $\tau > 1$. This is due to the fact that there is a negligible flux of $\overline{\epsilon'}$ away from the mixing layer boundaries for the model to capture.

4.3.5 Scale-similarity closures

The final set of closures examined are the scale-similarity closures used to model some of the more complex (non-flux type) correlations in the $\overline{\epsilon'}$, $\widetilde{m_1''^2}$, and $\widetilde{\chi''}$ transport equations. The first quantities examined are the production and destruction terms in the $\overline{\epsilon'}$ transport equation. The buoyancy production of $\overline{\epsilon'}$ was shown to be the dominant production mechanism of $\overline{\epsilon'}$ for $\tau < 1$ and is non-negligible over the range of Reynolds numbers examined here. The complex fluctuating velocity gradient-density gradient correlation is taken to be phenomenologically similar to the buoyancy production of \widetilde{E}'' , analogous to the scale-similarity closure for the shear production rate of $\overline{\epsilon'}$ (Jakirlić & Hanjalić 2002),

$$P_b^{\overline{\epsilon'}} = 2\bar{\nu} g_i \overline{\frac{\partial u'_i}{\partial x_j} \frac{\partial \rho'}{\partial x_j}} = C_{\epsilon 0} \frac{\overline{\epsilon'}}{\widetilde{E}''} P_b^{\widetilde{E}''}. \quad (4.18)$$

A comparison of the unclosed and closed profiles of $P_b^{\overline{\epsilon'}}$ is shown in figure 4.19. In general, the buoyancy production of $\overline{\epsilon'}$ is well-captured by the simple scale-similarity relationship with the buoyancy production of \widetilde{E}'' .

Even more complex than the buoyancy production term are the turbulent production and destruction of $\overline{\epsilon'}$ terms, which include triple fluctuating velocity gradient correlations and correlations of higher-order derivatives. Adopting the large Reynolds number closure (Jones & Launder 1972), the viscous destruction term and the turbulent production terms are grouped to form

$$D^{\overline{\epsilon'}} - P_t^{\overline{\epsilon'}} = -2\bar{\rho}\bar{\nu}^2 \overline{\left(\frac{\partial u'_i}{\partial x_k \partial x_m}\right)^2} + 2\bar{\mu} \overline{\frac{\partial u'_i}{\partial x_k} \frac{\partial u'_i}{\partial x_m} \frac{\partial u'_k}{\partial x_m}} = C_{\epsilon 2} \bar{\rho} \frac{(\overline{\epsilon'})^2}{\widetilde{E}''}. \quad (4.19)$$

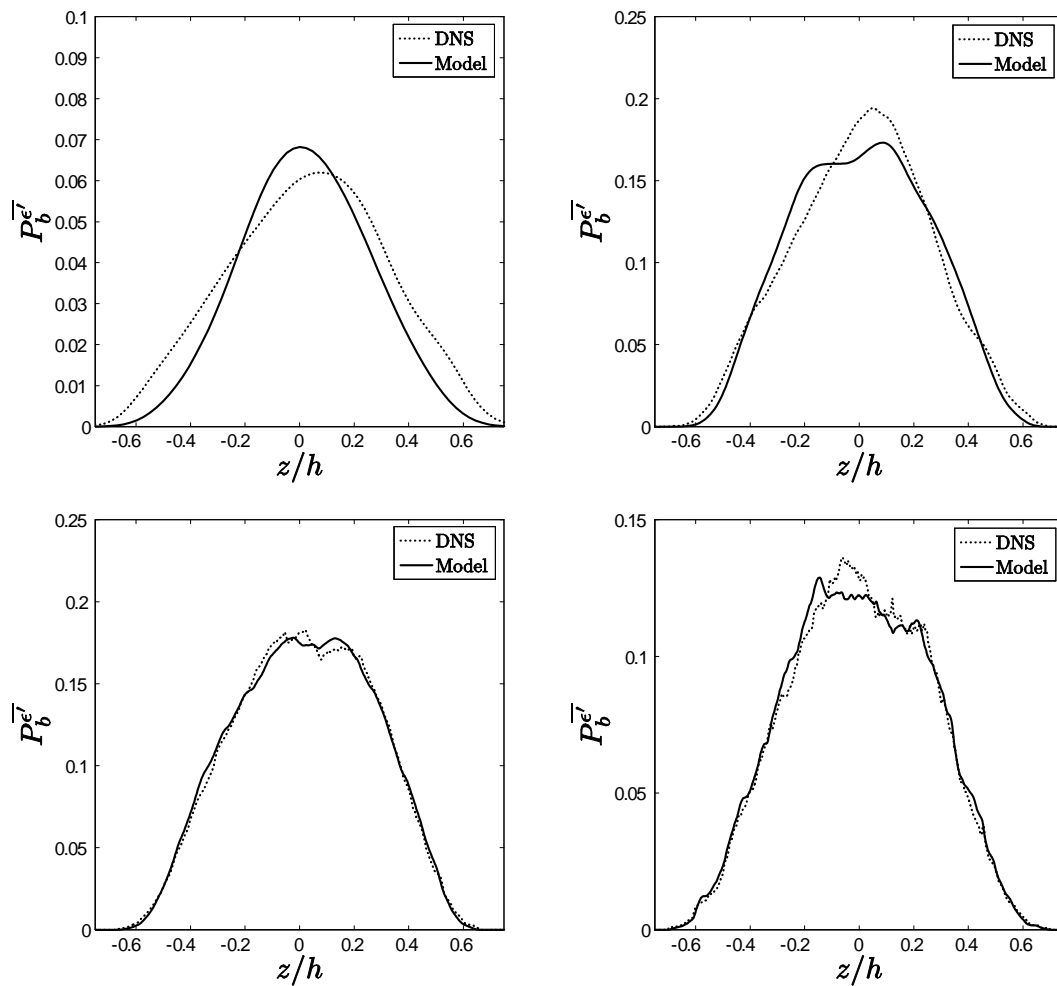


Figure 4.19 Profiles of the unclosed buoyancy production term $P_b^{e\tau}$ and its scale-similarity closure across the Rayleigh–Taylor mixing layer at $\tau = 0.21, 0.50, 1.01,$ and 1.52 (left-to-right, top-to-bottom).

Profiles of unclosed and closed forms of the difference $D^{\overline{\epsilon}} - P_t^{\overline{\epsilon}}$ are shown in figure 4.20 at various times. Similar to the buoyancy production model, the simple scale-similarity model shows good agreement with the DNS profiles.

Both the buoyancy production and turbulent production/destruction models shown in figures 4.19 and 4.20 have been plotted using the model parameters $C_{\epsilon 0}(Re_h)$ and $C_{\epsilon 2}(Re_h)$, shown in figure 4.21. The parameter $C_{\epsilon 0}$ changes before $\tau = 1$, after which a late-time steady value $C_{\epsilon 0} \approx 1.43$ is attained. This is larger than the value $C_{\epsilon 0} = 0.91$ determined from the self-similar analysis and *a posteriori* model evaluations of Snider and Andrews (1996), and $C_{\epsilon 0} = 0.95$ used by Grégoire and Souffland (1999) to model Rayleigh–Taylor and Richtmyer–Meshkov instability-driven mixing. However, both of these studies relied upon inductive testing to determine an appropriate value of $C_{\epsilon 0}$, whereas the present work uses the buoyancy production term in the $\overline{\epsilon}$ transport equation to directly determine $C_{\epsilon 0}$ for the first time.

The parameter for the combined turbulent production/destruction of $\overline{\epsilon}$ is also shown in figure 4.21, where $C_{\epsilon 2} \approx 2.8$ when the Rayleigh–Taylor mixing layer enters the transitional regime at $\tau \approx 0.5$. As Re_h increases, this parameter decreases to $C_{\epsilon 2} = 2.26$ at the latest time ($\tau = 1.52$). The final asymptotic value of $C_{\epsilon 2}$ remains unknown; however, it is possible that a late-time value of $C_{\epsilon 2}$ may be near the shear turbulence value 1.92. The dissipation rate $\overline{\epsilon}$ is physically related to the small-scale velocity fluctuations. However, from a turbulence modeling vantage point, $\overline{\epsilon}$ is better viewed as the rate of energy flux through the inviscid inertial subrange of scales. Thus, for $C_{\epsilon 0}$ and $C_{\epsilon 2}$ to reach late-time asymptotic values, it may be required that the Reynolds number be large enough that a sufficient separation of scales exists between the energy containing fluctuations and the dissipative fluctuations. As shown in figure 3.21, only a marginal portion of the wavenumbers form an inertial subrange, and a larger separation is required to satisfy the large Reynolds number criteria of

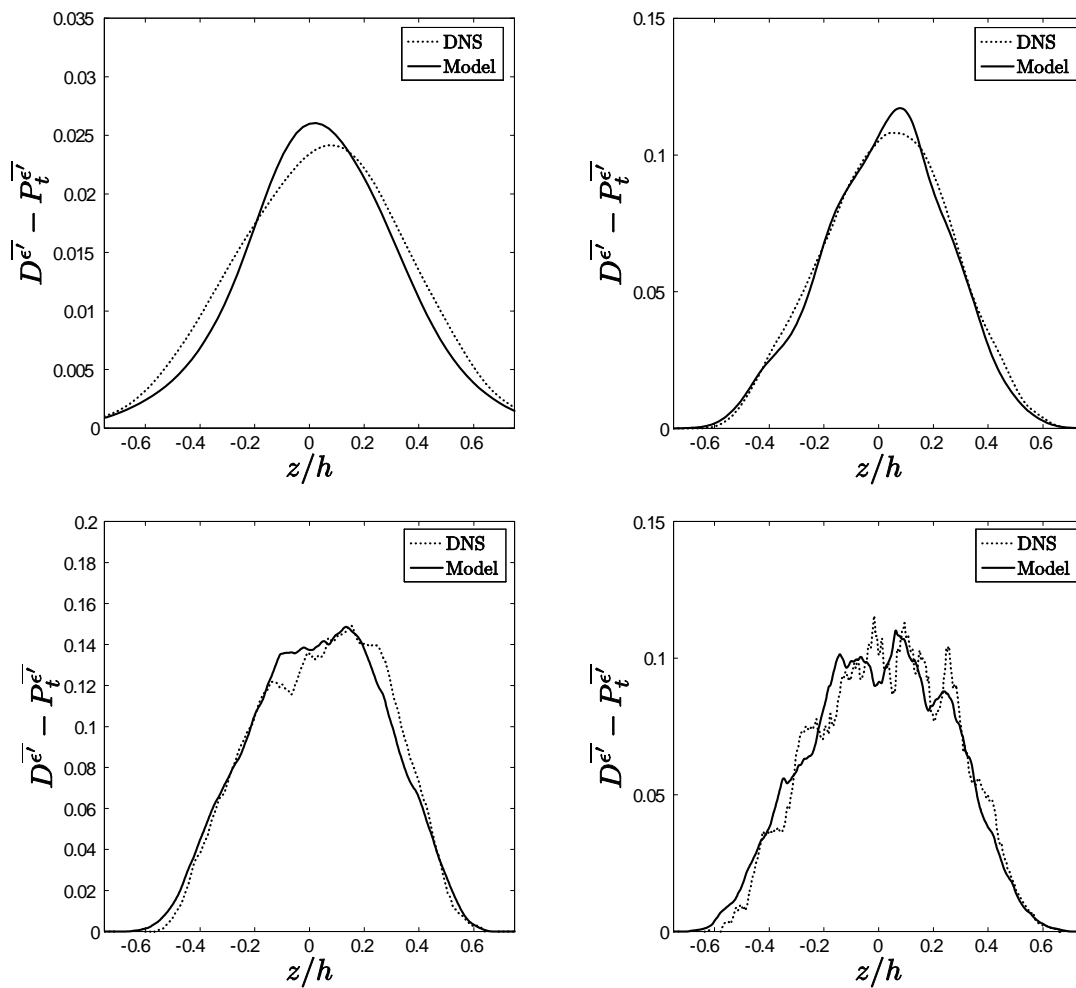


Figure 4.20 Profiles of the difference between the unclosed turbulent destruction and production term $D^{\overline{e}} - P_t^{\overline{e}}$ and its scale-similarity closure across the Rayleigh–Taylor mixing layer at $\tau = 0.21, 0.50, 1.01,$ and 1.52 (left–to–right, top–to–bottom).

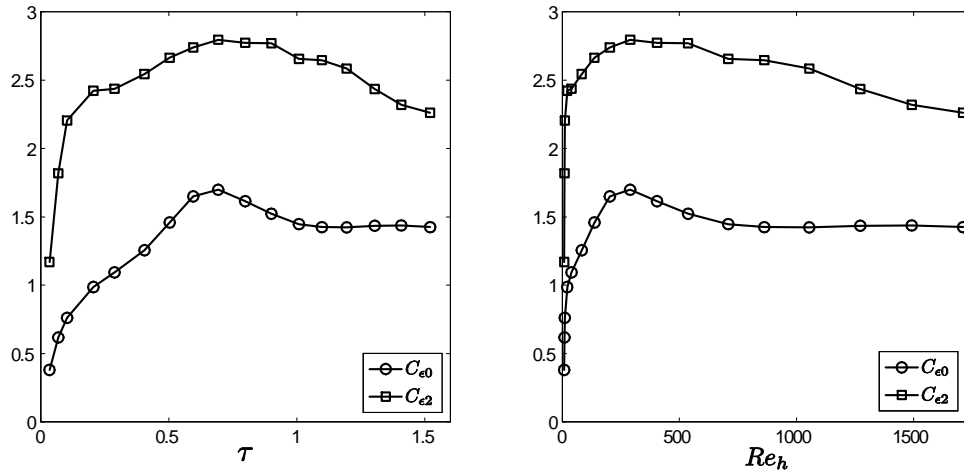


Figure 4.21 Evolution of calibrated scale-similarity coefficients for the $\overline{\epsilon'}$ transport equation as a function of time (left) and integral-scale Reynolds number (right).

the closures. Thus, $C_{\epsilon 2}$ is a weak function of Re_h until sufficient scale separation is achieved.

The evolution of the model correlation and magnitude coefficients is shown in figure 4.22. Despite utilizing the large Reynolds number form of the closed $\overline{\epsilon'}$ transport equation, the scale-similarity models for the buoyancy production and turbulent production/destruction terms exhibit good agreement with the unclosed DNS profiles after $\tau = 0.2$. Again, the models were computed using the Reynolds number-dependent model parameters $C_{\epsilon 0}(Re_h)$ and $C_{\epsilon 2}(Re_h)$. Thus, the closed form of the $\overline{\epsilon'}$ transport equation could be used to model Rayleigh–Taylor driven mixing, given a proper calibration in the small Reynolds number limit.

While the calibration and application of scale-similarity closures for the $\overline{\epsilon'}$ transport equation have been well-documented for a variety of flows, the modeling of the $\widetilde{m_1''^2}$ and $\widetilde{\chi''}$ transport equation closures has been primarily limited to combustion applications (Veynante & Vervisch 2002). The production of $\widetilde{m_1''^2}$, physically-represented

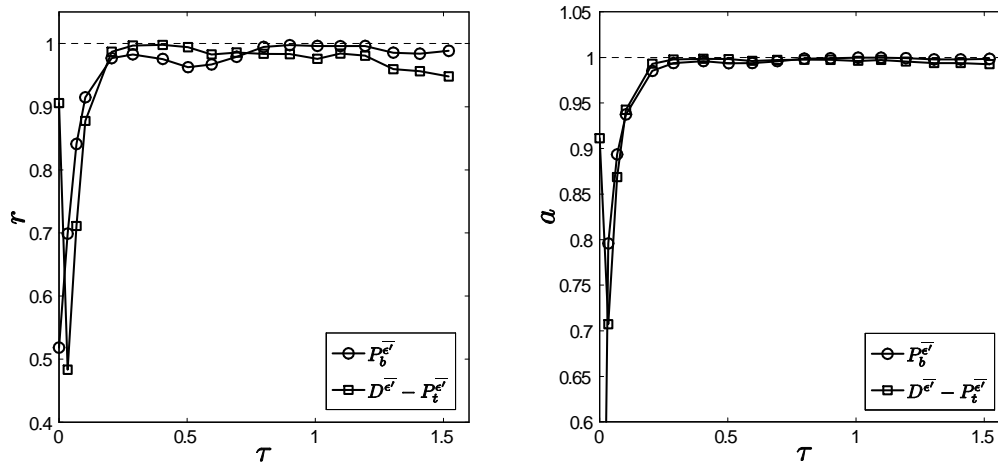


Figure 4.22 Evolution of the model correlation and magnitude coefficients for the scale-similarity models in the $\bar{\epsilon}'$ transport equation.

by the entrainment of unmixed fluid, is given by the gradient-diffusion closure of $\widetilde{w''m_1''}$ (see figure 4.6). However, the higher-order correlation of fluctuating mass fraction gradients governing the molecular destruction of $\widetilde{m_1''^2}$ (physically represented by the molecular mixing of fluids across a species interface) does not have a gradient-diffusion-based closure. Instead, the relationship between the turbulent mechanical time scale $\tau_m = \widetilde{E''}/\widetilde{\epsilon''}$ and the scalar mixing time scale $\tau_s = \widetilde{m_1''^2}/\widetilde{\chi''}$ is used to model the mass fraction dissipation rate $D^{\widetilde{m_1''^2}} = -2\bar{\rho}\widetilde{\chi''}$ (Corrsin 1951; Spalding 1971; Fox 2003). The ratio of the scalar-to-mechanical time scales may be used to model the mass fraction variance dissipation rate

$$\widetilde{\chi''} = C_{m2} \frac{\widetilde{\epsilon''}}{\widetilde{E''}} \widetilde{m_1''^2}, \quad (4.20)$$

where C_{m2} is a dimensionless parameter.

Profiles of the mechanical and scalar time scales are shown in figure 4.23. Once the mixing layer transitions into its nonlinear phase ($\tau \geq 0.5$), the mechanical time scale profiles are approximately constant across the mixing layer ($|z/h| < 0.5$). Sim-

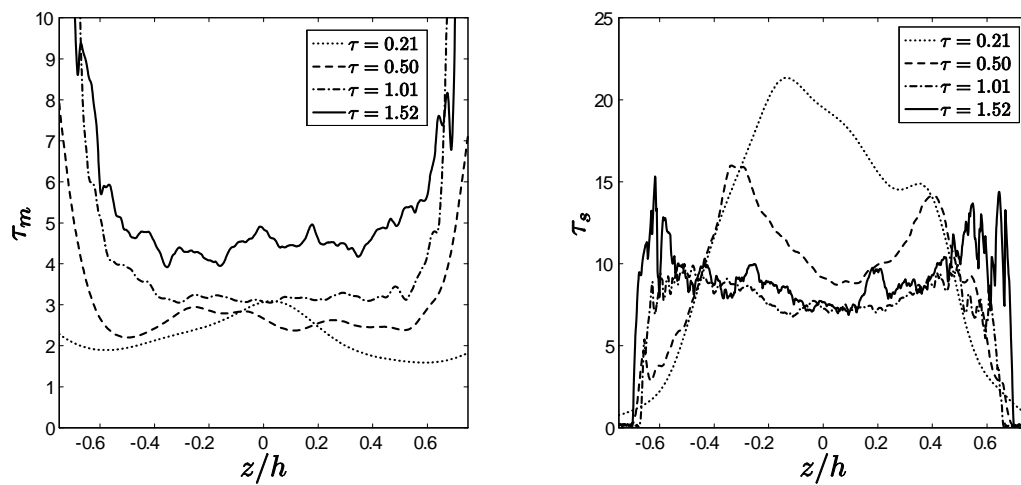


Figure 4.23 Profiles of the mechanical time scale τ_m (left) and the scalar mixing time scale τ_s (right) across the Rayleigh–Taylor mixing layer at various times.

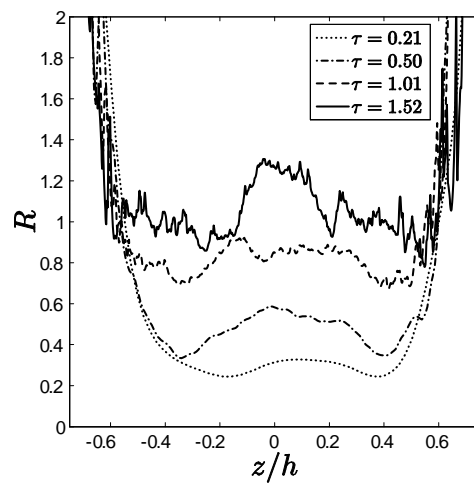


Figure 4.24 Profiles of the mechanical-to-scalar time scale ratio R across the Rayleigh–Taylor mixing layer at various times.

ilarly, the scalar time scale profiles are approximately constant across the mixing layer only after it becomes transitional at $\tau \approx 0.7$. Combining τ_m and τ_s gives the mechanical-to-scalar time scale ratio (Fox 2003)

$$R = \frac{2\tau_m}{\tau_s}, \quad (4.21)$$

where $C_{m2} = R/2$. Profiles of R across the mixing layer are shown in figure 4.24. The time scale ratio R is approximately constant across the layer, which indicates that the closure (4.20) is valid for this flow. In addition, the profiles in figure 4.24 show a continuous increase in R with time (and Re_h). This is important to note, in that many mixing models assume that this ratio is constant: typically $R \approx 2$ (Spalding 1971; Snider & Andrews 1996; Hanjalić 2002). At the latest time measured, $R \approx 2.0$ – 2.4 across the mixing layer, which is close to the values $R \approx 2.0$ – 2.2 for $Re_\lambda > 100$ predicted by Fox (2003) using a spectral equilibrium model. However, at earlier times, this is not the case, where a range $0.5 < R < 2.2$ is observed.

Profiles of the unclosed and closed mass fraction variance destruction term $D_1^{m''^2}$ at various times are shown in figure 4.25. At early times ($\tau \leq 0.5$), the model exhibits adequate agreement with the unclosed DNS profiles. As the mixing layer becomes more turbulent, the agreement improves, as seen in the profiles at $\tau = 1.01$ and 1.52 . The simple relationship between the mechanical and scalar time scales appears to be justified. The evolution of $C_{m2}(Re_h)$ used to create the model profiles in figure 4.25 is shown in figure 4.29.

The accuracy of a simple scale-similarity model for the mixing rate $\widetilde{\chi}''$ may be improved by solving an additional transport equation for $\widetilde{\chi}''$ as done in many studies where the degree of molecular mixing is important (Chidambaram *et al.* 2001; Veynante & Vervisch 2002; Fox 2003; Brinkman *et al.* 2007). However, the transport equation for $\widetilde{\chi}''$ contains more complicated terms which are not closed by either the

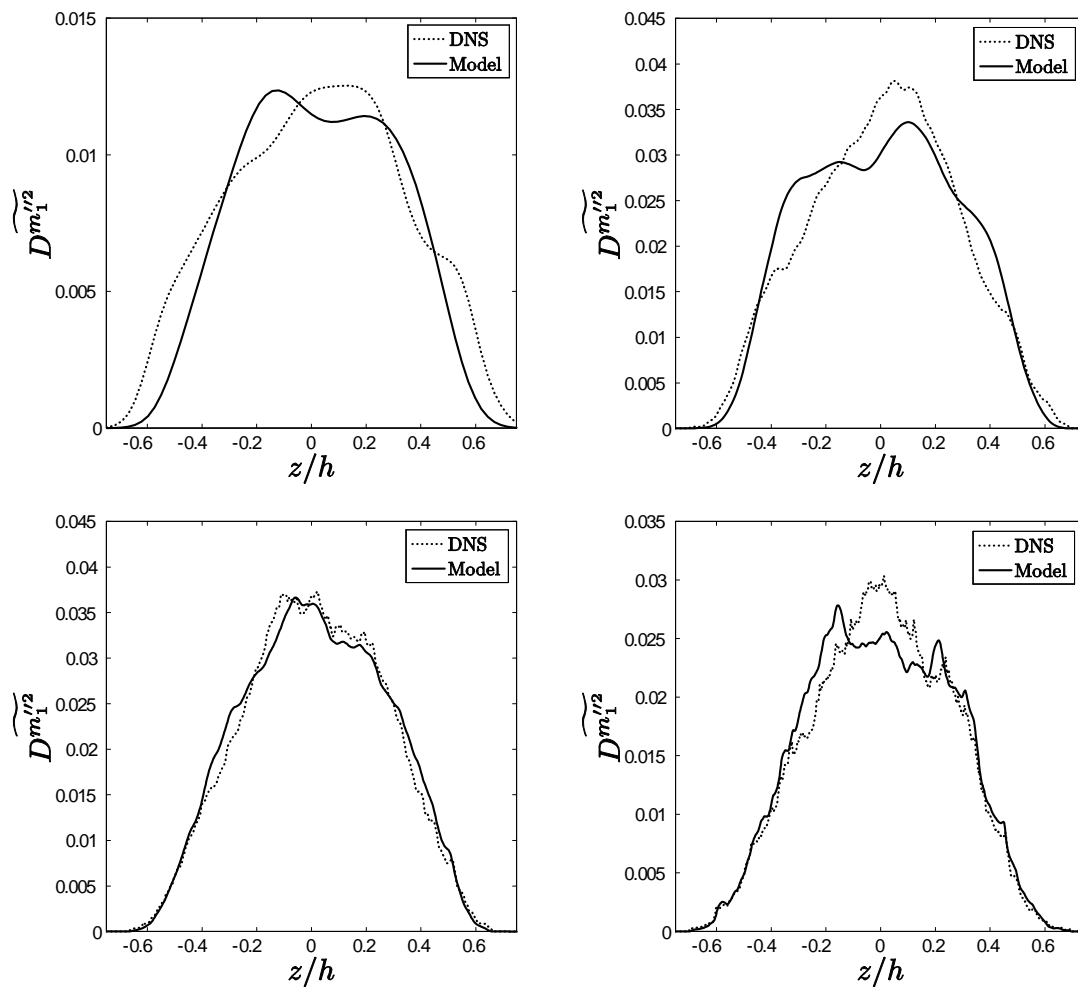


Figure 4.25 Profiles of the unclosed mass fraction variance destruction term $\widetilde{D^{m_1}{}^{1/2}}$ and its scale-similarity closure across the Rayleigh–Taylor mixing layer at $\tau = 0.21, 0.50, 1.01,$ and 1.52 (left-to-right, top-to-bottom).

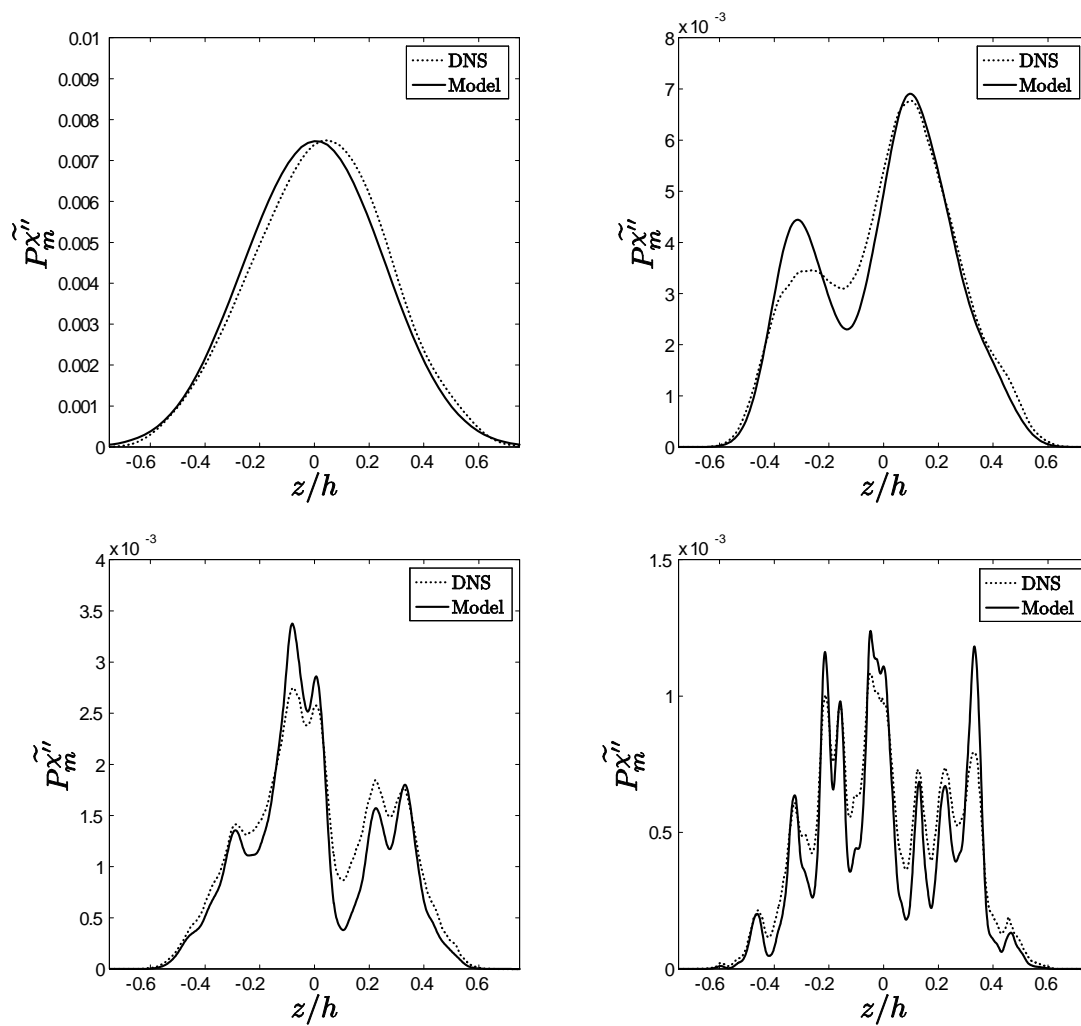


Figure 4.26 Profiles of the unclosed mass fraction variance dissipation rate mean gradient production term P_m'' and its scale-similarity closure across the Rayleigh–Taylor mixing layer at $\tau = 0.21, 0.50, 1.01,$ and 1.52 (left–to–right, top–to–bottom).

eddy viscosity approximation or the gradient-diffusion hypothesis. Thus, phenomenological scale-similarity closures must be invoked. First, the mean gradient production of $\widetilde{\chi}''$ is closed by (Mura & Borghi 2003; Mura *et al.* 2007)

$$P_m^{\widetilde{\chi}''} = -2\rho D \overline{\frac{\partial m_1''}{\partial x_i} \frac{\partial u_j''}{\partial x_i} \frac{\partial \tilde{m}_1}{\partial x_j}} = C_{\chi 0} \mu_t \frac{\widetilde{\epsilon}''}{\widetilde{E}''} \left(\frac{\partial \tilde{m}_1}{\partial x_j} \right)^2. \quad (4.22)$$

Profiles of the unclosed and closed mean gradient production of $\widetilde{\chi}''$ are shown in figure 4.26. In general, this closure shows good agreement with the unclosed profiles. At later times, the oscillations in the model are due to the gradient of \tilde{m}_1 . The calibrated model parameter $C_{\chi 0}$ is shown in figure 4.29 as a function of both time and integral-scale Reynolds number.

The mean gradient production term $P_m^{\widetilde{\chi}''}$ represents only a small fraction of the production of $\widetilde{\chi}''$, where the turbulent production $P_t^{\widetilde{\chi}''}$ is the dominant production mechanism. Similarly, the destruction of $\widetilde{\chi}''$ by molecular diffusion processes is also attributed to the fine-scale velocity fluctuations that drive the molecular mixing process. Thus, drawing an analogy to the closure of $D^{\overline{\epsilon}'} - P_t^{\overline{\epsilon}'}$, the difference of the two terms is modeled as (Mura *et al.* 2007)

$$\begin{aligned} D^{\widetilde{\chi}''} - P_t^{\widetilde{\chi}''} &= 2\rho D^2 \overline{\left(\frac{\partial^2 m_1''}{\partial x_i \partial x_j} \right)^2} + 2\rho D \overline{\frac{\partial m_1''}{\partial x_j} \frac{\partial m_1''}{\partial x_i} \frac{\partial u_j''}{\partial x_i}} \\ &= \bar{\rho} \widetilde{\chi}'' \left(C_{\chi 2} \frac{\widetilde{\epsilon}''}{\widetilde{E}''} - C_{\chi 3} \frac{\widetilde{\chi}''}{m_1''^2} \right), \end{aligned} \quad (4.23)$$

where $C_{\chi 2}$ is related to $P_t^{\widetilde{\chi}''}$ and $C_{\chi 3}$ is related to $D^{\widetilde{\chi}''}$. Profiles of the closed and unclosed forms of $P_t^{\widetilde{\chi}''}$ and $D^{\widetilde{\chi}''}$ are shown in figures 4.27 and 4.28. While the modeled $\widetilde{\chi}''$ shown in figure 4.25 appears to be valid for $\tau > 0.2$, the turbulent production and destruction of $\widetilde{\chi}''$ closures do not capture the flow physics until the mixing layer transitions into a pre-turbulent nonlinear stage at $\tau \approx 0.5$. However, once the nonlinear and turbulent regimes set in, the closures for $P_t^{\widetilde{\chi}''}$ and $D^{\widetilde{\chi}''}$ show good agreement

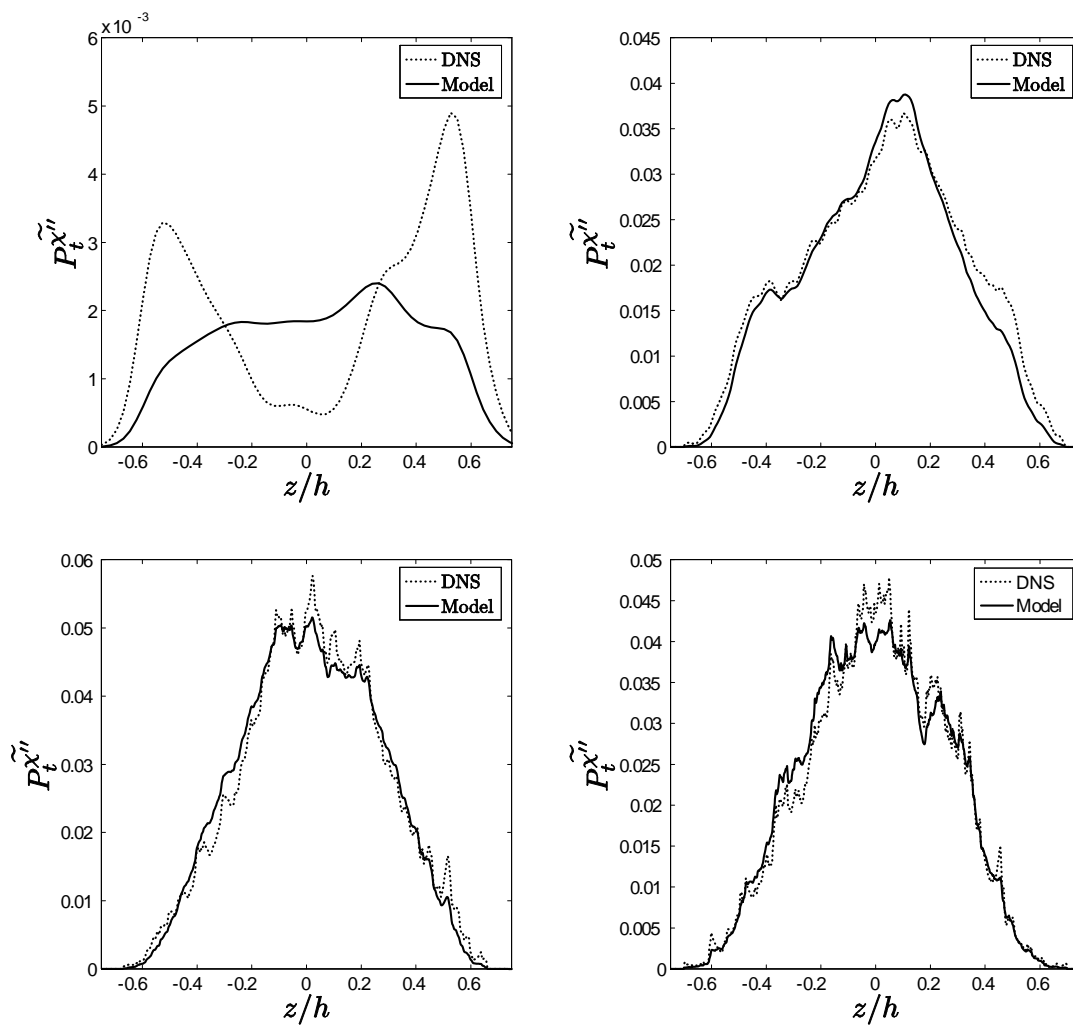


Figure 4.27 Profiles of the unclosed mass fraction variance dissipation rate turbulent production term $P_t^{\widetilde{x''}}$ and its scale-similarity closure across the Rayleigh–Taylor mixing layer at $\tau = 0.21, 0.50, 1.01,$ and 1.52 (left-to-right, top-to-bottom).

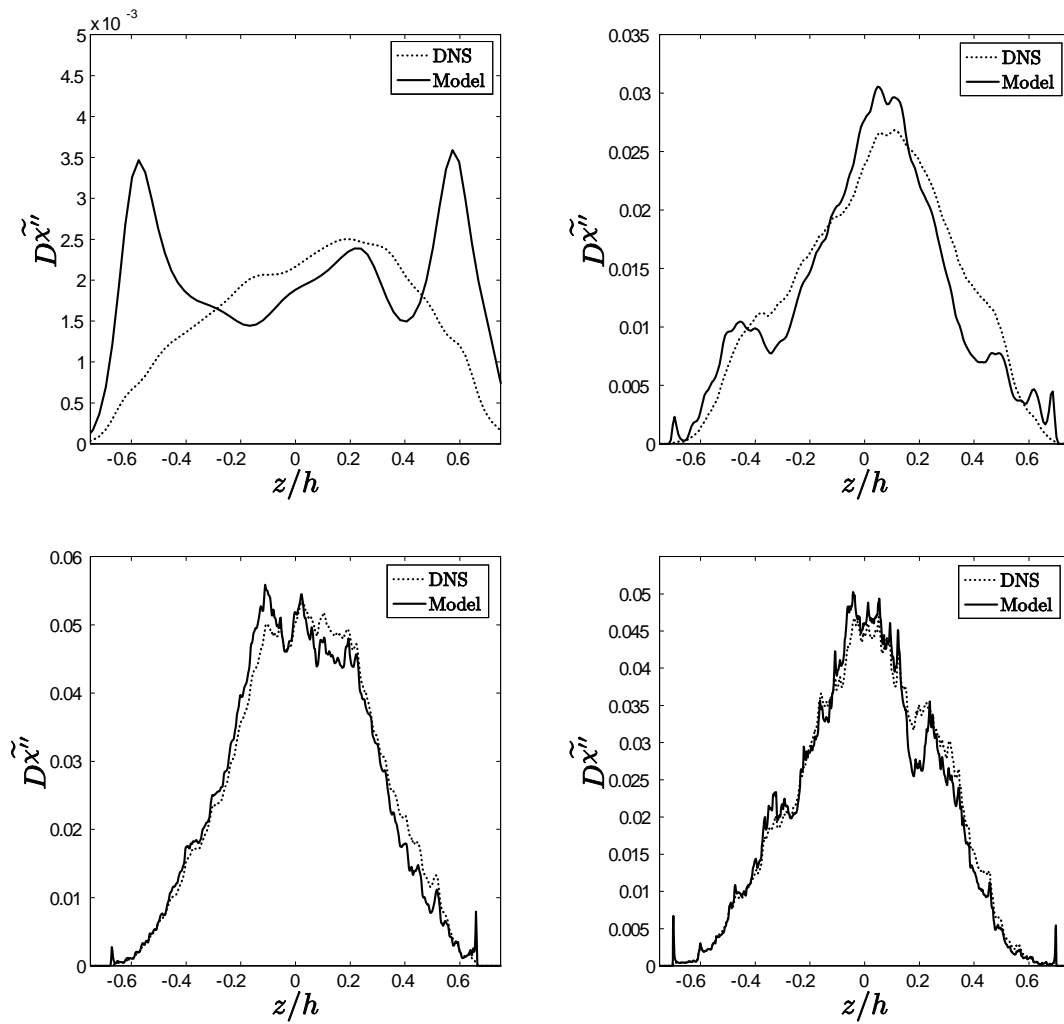


Figure 4.28 Profiles of the unclosed mass fraction variance dissipation rate destruction term $D\tilde{\chi}''$ and its scale-similarity closure across the Rayleigh–Taylor mixing layer at $\tau = 0.21, 0.50, 1.01,$ and 1.52 (left-to-right, top-to-bottom).

with the DNS profiles.

The time-dependent scale-similarity model parameters for the $\widetilde{m_1''^2}$ and $\widetilde{\chi''}$ transport equations are shown in figure 4.29 as both a function of time and integral-scale Reynolds number. For the case where $P_m^{\widetilde{\chi''}}$ is negligible (which is true for this flow beyond $\tau \approx 0.7$ as shown in figure 3.74), then $C_{m2} \equiv C_{\chi2}/C_{\chi3}$, which is evident in figure 4.29. Another important implication of measuring the time-evolution of C_{m2} and $C_{\chi2}/C_{\chi3}$ is noting that the parameter governing the mixing rate $\widetilde{\chi''}$ is not steady in time, as assumed in many models (Spalding 1971; Grégoire & Souffland 1999; Hanjalić 2002). Instead, there is a clear Reynolds number dependence across the entire range.

Finally, the quality of the scale-similarity closures for $\widetilde{m_1''^2}$ and $\widetilde{\chi''}$ is examined in figure 4.30, where the model correlation and magnitude coefficients are shown. The simple time scale ratio closure for the destruction of $\widetilde{m_1''^2}$ exhibits good agreement with the DNS profiles over all times shown when using the time-dependent value of C_{m2} shown in figure 4.29. Similarly, the buoyancy production of $\widetilde{\chi''}$ also shows excellent agreement with the DNS profiles over the range of Reynolds numbers examined. The turbulent production and molecular destruction of $\widetilde{\chi''}$ terms exhibit a poor correlation with the DNS data until $\tau \approx 0.5$, after which point turbulent fluctuations became more dominant, and the closures accurately reflect the flow physics.

4.4 Numerical Implementation of the $\widetilde{E''}$ - $\widetilde{\epsilon''}$ - $\widetilde{m_1''^2}$ - $\widetilde{\chi''}$ Model

To verify that the model calibrations presented in § 4.3 are able to reproduce the experimental and numerical results reported in § 2 and 3 *a posteriori*, the modeled transport equations were implemented in a one-dimensional code. In this section, the equations solved, numerical method, validation tests, and comparison with the

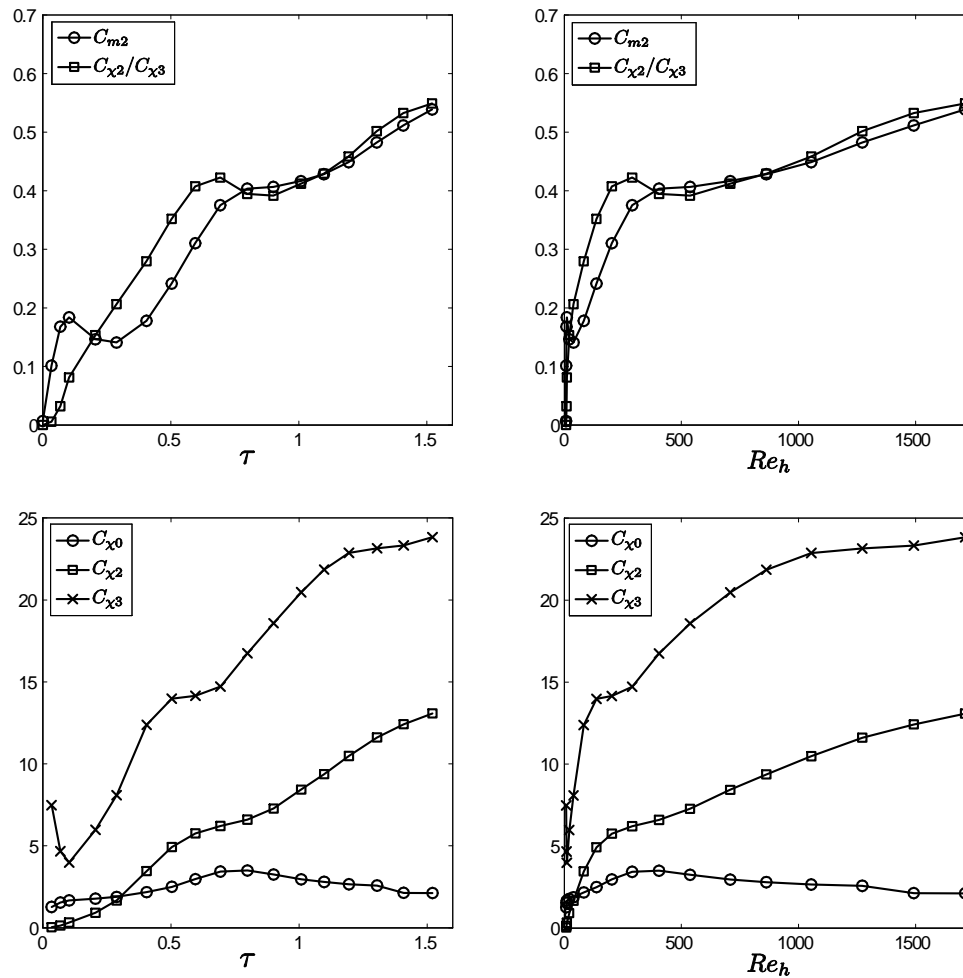


Figure 4.29 Evolution of calibrated scale-similarity parameters for the $\widetilde{m_1''^2}$ transport equation as a function of time (top-left) and the integral-scale Reynolds number (top-right). Evolution of calibrated scale-similarity parameters for the $\widetilde{\chi''}$ transport equation as a function of time (bottom-left) and the integral-scale Reynolds number (bottom-right).

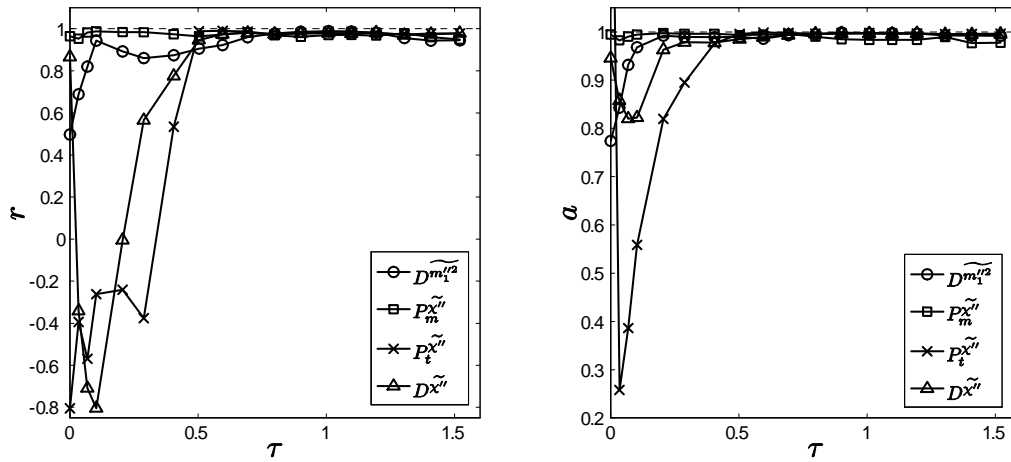


Figure 4.30 Evolution of the model correlation and magnitude coefficients for the scale-similarity models in the $\widetilde{m}_1''^2$ and $\widetilde{\chi}''$ transport equations.

experiments and DNS are presented. Next, the numerical algorithm is validated by comparing the current implementation with another $\overline{E'}-\overline{\epsilon'}$ model of Rayleigh–Taylor mixing (Snider & Andrews 1996) and with the analytical self-similar solutions of the modeled transport equations. The current model was used to demonstrate that the current calibration yields physically-realistic solutions of the transport equations. Finally, the experiment and DNS results were used to determine the necessary calibration required to reproduce measured quantities from the $Sc \sim 10^3$ water channel experiment.

4.4.1 Model equations

In the small Atwood number limit of a statistically one-dimensional Rayleigh–Taylor mixing layer, the transport equations can be simplified by neglecting the advection terms and all mean field gradients in the homogeneous directions. In this case, the following mean mass fraction, turbulent kinetic energy, turbulent kinetic energy dis-

sipation rate, and mass fraction variance transport equations are solved:

$$\bar{\rho} \frac{\partial \tilde{m}_1}{\partial t} = \frac{\partial}{\partial z} \left[\left(\frac{\bar{\mu}}{Sc} + \frac{\mu_t}{\sigma_m} \right) \frac{\partial \tilde{m}_1}{\partial z} \right], \quad (4.24)$$

$$\bar{\rho} \frac{\partial \widetilde{E''}}{\partial t} = -\frac{\nu_t}{\sigma_\rho \bar{\rho}} \frac{\partial \bar{\rho}}{\partial z} \frac{\partial \bar{p}}{\partial z} + \frac{\partial}{\partial z} \left\{ \left[\bar{\mu} + \frac{(1 - C_{pu}) \mu_t}{\sigma_k} \right] \frac{\partial \widetilde{E''}}{\partial z} \right\} - \bar{\rho} \widetilde{\epsilon''}, \quad (4.25)$$

$$\bar{\rho} \frac{\partial \widetilde{\epsilon''}}{\partial t} = -C_{\epsilon_0} \frac{\widetilde{\epsilon''}}{\widetilde{E''}} \frac{\nu_t}{\sigma_\rho \bar{\rho}} \frac{\partial \bar{\rho}}{\partial z} \frac{\partial \bar{p}}{\partial z} + \frac{\partial}{\partial z} \left\{ \left[\bar{\mu} + \frac{(1 - C_{pu}^\epsilon) \mu_t}{\sigma_\epsilon} \right] \frac{\partial \widetilde{\epsilon''}}{\partial z} \right\} - C_{\epsilon_2} \bar{\rho} \frac{(\widetilde{\epsilon''})^2}{\widetilde{E''}}, \quad (4.26)$$

$$\bar{\rho} \frac{\partial \widetilde{m_1''^2}}{\partial t} = 2 \frac{\mu_t}{\sigma_m} \left(\frac{\partial \tilde{m}_1}{\partial z} \right)^2 + \frac{\partial}{\partial z} \left[\left(\frac{\bar{\mu}}{Sc} + \frac{\mu_t}{\sigma_{m2}} \right) \frac{\partial \widetilde{m_1''^2}}{\partial z} \right] - 2 \bar{\rho} \widetilde{\chi''}, \quad (4.27)$$

where the turbulent viscosity is defined in (4.3). The pressure gradient in (4.25) and (4.26) is taken to be $\partial \bar{p} / \partial z = -\bar{\rho} g$, where the contribution of the gradient of the Reynolds stress component τ_{33} is negligible as shown in § 3.6.2. In (4.27), the mass fraction variance dissipation rate may be modeled as shown in (4.20) or a transport equation

$$\begin{aligned} \bar{\rho} \frac{\partial \widetilde{\chi''}}{\partial t} = & C_{\chi^0} \mu_t \frac{\widetilde{\epsilon''}}{\widetilde{E''}} \left(\frac{\partial \tilde{m}_1}{\partial z} \right)^2 + \frac{\partial}{\partial z} \left[\left(\frac{\bar{\mu}}{Sc} + \frac{\mu_t}{\sigma_\chi} \right) \frac{\partial \widetilde{\chi''}}{\partial z} \right] \\ & + \bar{\rho} \widetilde{\chi''} \left(C_{\chi^2} \frac{\widetilde{\epsilon''}}{\widetilde{E''}} - C_{\chi^3} \frac{\widetilde{\chi''}}{\widetilde{m_1''^2}} \right) \end{aligned} \quad (4.28)$$

may be solved.

The Favre-averaged mass fraction of fluid component r (where $r = 1, 2$) is related to the mean density field by $\bar{\rho} = (\tilde{m}_1 / \rho_1 + \tilde{m}_2 / \rho_2)^{-1}$, and $\tilde{m}_1 + \tilde{m}_2 = 1$ for the binary fluid system considered here. The Favre-averaged mass fraction of fluid r is related to the mean volume fraction \bar{f}_r by $\bar{\rho} \tilde{m}_r = \rho_r \bar{f}_r$. The viscosity difference between fluids 1 and 2 is assumed to be small and μ is taken to be a linear combination of μ_1 and μ_2 , such that $\bar{\mu} = \tilde{m}_1 \mu_1 + \tilde{m}_2 \mu_2$.

4.4.2 Spatial discretization

Equations (4.24)–(4.28) form a system of unsteady, parabolic partial differential equations. The spatial discretization of each equation can be written in general form, assuming a three-point, second-order finite difference stencil (Ferziger & Perić 2002)

$$\frac{\partial \phi}{\partial t} = A_W^\phi \phi_W + A_P^\phi \phi_P + A_E^\phi \phi_E + S^\phi. \quad (4.29)$$

The coefficients for each equation are

$$\bar{\rho} \tilde{m}_1 : \left\{ \begin{array}{l} A_W^{\tilde{m}_1} = \frac{1}{\bar{\rho}_W (\Delta z)^2} \left(\frac{\bar{\mu}}{S_c} + \frac{\mu_t}{\sigma_m} \right)_w \\ A_E^{\tilde{m}_1} = \frac{1}{\bar{\rho}_E (\Delta z)^2} \left(\frac{\bar{\mu}}{S_c} + \frac{\mu_t}{\sigma_m} \right)_e \\ A_P^{\tilde{m}_1} = -\frac{1}{\bar{\rho}_P (\Delta z)^2} \left[\left(\frac{\bar{\mu}}{S_c} + \frac{\mu_t}{\sigma_m} \right)_w + \left(\frac{\bar{\mu}}{S_c} + \frac{\mu_t}{\sigma_m} \right)_e \right] \\ S^{\tilde{m}_1} = 0 \end{array} \right. \quad (4.30)$$

$$\bar{\rho} \tilde{E}'' : \left\{ \begin{array}{l} A_W^{\tilde{E}''} = \frac{1}{\bar{\rho}_W (\Delta z)^2} \left[\bar{\mu} + \frac{(1-C_{pu})\mu_t}{\sigma_k} \right]_w \\ A_E^{\tilde{E}''} = \frac{1}{\bar{\rho}_E (\Delta z)^2} \left[\bar{\mu} + \frac{(1-C_{pu})\mu_t}{\sigma_k} \right]_e \\ A_P^{\tilde{E}''} = -\frac{1}{\bar{\rho}_P (\Delta z)^2} \left\{ \left[\bar{\mu} + \frac{(1-C_{pu})\mu_t}{\sigma_k} \right]_w + \left[\bar{\mu} + \frac{(1-C_{pu})\mu_t}{\sigma_k} \right]_e \right\} \\ S_P^{\tilde{E}''} = \frac{g}{2\sigma_\rho \Delta z} (\nu_t)_P (\bar{\rho}_E - \bar{\rho}_W) - \bar{\rho}_P \tilde{\epsilon}_P'' \end{array} \right. \quad (4.31)$$

$$\bar{\rho} \tilde{\epsilon}'' : \left\{ \begin{array}{l} A_W^{\tilde{\epsilon}''} = \frac{1}{\bar{\rho}_W (\Delta z)^2} \left[\bar{\mu} + \frac{(1-C_{pu}^\epsilon)\mu_t}{\sigma_\epsilon} \right]_w \\ A_E^{\tilde{\epsilon}''} = \frac{1}{\bar{\rho}_E (\Delta z)^2} \left[\bar{\mu} + \frac{(1-C_{pu}^\epsilon)\mu_t}{\sigma_\epsilon} \right]_e \\ A_P^{\tilde{\epsilon}''} = -\frac{1}{\bar{\rho}_P (\Delta z)^2} \left\{ \left[\bar{\mu} + \frac{(1-C_{pu}^\epsilon)\mu_t}{\sigma_\epsilon} \right]_w + \left[\bar{\mu} + \frac{(1-C_{pu}^\epsilon)\mu_t}{\sigma_\epsilon} \right]_e \right\} \\ S_P^{\tilde{\epsilon}''} = \frac{C_{\epsilon 0} g}{2\sigma_\rho \Delta z} (\nu_t)_P \frac{\tilde{\epsilon}_P''}{E_P''} (\bar{\rho}_E - \bar{\rho}_W) - C_{\epsilon 2} \bar{\rho}_P \frac{\tilde{\epsilon}_P''^2}{E_P''} \end{array} \right. \quad (4.32)$$

$$\bar{\rho} \widetilde{m}_1''^2 : \left\{ \begin{array}{l} A_W^{\widetilde{m}_1''^2} = \frac{1}{\bar{\rho}_W (\Delta z)^2} \left(\frac{\bar{\mu}}{S_c} + \frac{\mu_t}{\sigma_{m2}} \right)_w \\ A_E^{\widetilde{m}_1''^2} = \frac{1}{\bar{\rho}_E (\Delta z)^2} \left(\frac{\bar{\mu}}{S_c} + \frac{\mu_t}{\sigma_{m2}} \right)_e \\ A_P^{\widetilde{m}_1''^2} = -\frac{1}{\bar{\rho}_P (\Delta z)^2} \left[\left(\frac{\bar{\mu}}{S_c} + \frac{\mu_t}{\sigma_{m2}} \right)_w + \left(\frac{\bar{\mu}}{S_c} + \frac{\mu_t}{\sigma_{m2}} \right)_e \right] \\ S_P^{\widetilde{m}_1''^2} = \frac{2(\mu_t)_P}{\sigma_m} \left[\frac{(\widetilde{m}_1)_E - (\widetilde{m}_1)_W}{2(\Delta z)^2} \right]^2 - 2\bar{\rho} \widetilde{\chi}_P'' \end{array} \right. \quad (4.33)$$

$$\bar{\rho} \widetilde{\chi}'' : \left\{ \begin{array}{l} A_W^{\widetilde{\chi}''} = \frac{1}{\bar{\rho}_W (\Delta z)^2} \left(\frac{\bar{\mu}}{S_c} + \frac{\mu_t}{\sigma_\chi} \right)_w \\ A_E^{\widetilde{\chi}''} = \frac{1}{\bar{\rho}_E (\Delta z)^2} \left(\frac{\bar{\mu}}{S_c} + \frac{\mu_t}{\sigma_\chi} \right)_e \\ A_P^{\widetilde{\chi}''} = -\frac{1}{\bar{\rho}_P (\Delta z)^2} \left[\left(\frac{\bar{\mu}}{S_c} + \frac{\mu_t}{\sigma_\chi} \right)_w + \left(\frac{\bar{\mu}}{S_c} + \frac{\mu_t}{\sigma_\chi} \right)_e \right] \\ S_P^{\widetilde{\chi}''} = C_{\chi 0} \mu_t \frac{\widetilde{\epsilon}_P''}{E_P''} \left[\frac{(\widetilde{m}_1)_E - (\widetilde{m}_1)_W}{2(\Delta z)^2} \right]^2 + \bar{\rho} C_{\chi 2} \frac{\widetilde{\epsilon}_P''}{E_P''} \widetilde{\chi}_P'' - \bar{\rho} C_{\chi 3} \frac{\widetilde{\chi}_P''^2}{(\widetilde{m}_1''^2)_P} \end{array} \right. \quad (4.34)$$

In (4.33), the mass fraction variance dissipation rate $\widetilde{\chi}''$ can be either included directly as

$$\widetilde{\chi}_P'' = C_{m2} \frac{\widetilde{\epsilon}_P''}{E_P''} \left(\widetilde{m}_1''^2 \right)_P, \quad (4.35)$$

or the transport equation for $\widetilde{\chi}''$ may be evolved independently. In this case, the value of $\widetilde{\chi}_P''$ is used in (4.33). Intermediate values of $\bar{\rho}$, \widetilde{E}'' , $\widetilde{\epsilon}''$, and ν_t were interpolated using a second-order, linear interpolation scheme and are denoted by the standard ‘west’ and ‘east’ convention of Ferziger and Perić (2002) with subscripts ‘w’ and ‘e’.

Dirichlet boundary conditions were imposed for the mean mass fraction transport equation,

$$\widetilde{m}_1(z = -L_z/2, t) = 0, \quad \widetilde{m}_1(z = L_z/2, t) = 1. \quad (4.36)$$

Neumann boundary conditions were imposed for the \widetilde{E}'' , $\widetilde{\epsilon}''$, $\widetilde{m}_1''^2$, and $\widetilde{\chi}''$ transport equations,

$$\left. \frac{\partial \widetilde{E}''}{\partial z} \right|_{z=\pm L_z/2} = \left. \frac{\partial \widetilde{\epsilon}''}{\partial z} \right|_{z=\pm L_z/2} = \left. \frac{\partial \widetilde{m}_1''^2}{\partial z} \right|_{z=\pm L_z/2} = \left. \frac{\partial \widetilde{\chi}''}{\partial z} \right|_{z=\pm L_z/2} = 0, \quad (4.37)$$

4.4.3 Time integration

To minimize stability concerns that arise when using explicit time integration, an implicit, second-order accurate Crank–Nicholson time integration scheme was implemented (Ferziger & Perić 2002),

$$\begin{aligned} \phi_P^{n+1} = & \phi_P^n + \frac{\Delta t}{2} \left(A_W^\phi \phi_W + A_P^\phi \phi_P + A_E^\phi \phi_E + S^\phi \right)^{n+1} \\ & + \frac{\Delta t}{2} \left(A_W^\phi \phi_W + A_P^\phi \phi_P + A_E^\phi \phi_E + S^\phi \right)^n. \end{aligned} \quad (4.38)$$

The current model consists of a system of four (or five) coupled partial differential equations, and each equation is advanced in time sequentially using an iterative quasi-minimal residual method (Freund & Nachtigal 1991). Multiple outer iterations were required for each time step to ensure the convergence of the system of equations to the final solution at t^{n+1} . For the first outer iteration, the coefficients A^ϕ at the next time step t^{n+1} are approximated with the coefficients at the current time step t^n . Each inner iteration, which advanced one transport equation in time, was iterated until the relative residual norm of the linear system of equations satisfied $\epsilon_{inner} < 1 \times 10^{-12}$. Outer iterations, which solved one inner iteration per transport equation, were performed until the maximum difference between the predictions of ϕ^{n+1} at the previous and current outer iterations was $\epsilon_{outer} < 1 \times 10^{-18}$.

4.5 Model Validation

4.5.1 Comparison with Snider and Andrews (1996)

The first validation test compared results from the current model with those of the $\overline{E'}-\overline{\epsilon'}$ model of Snider and Andrews (1996), in which the incompressible, Reynolds-averaged \overline{T} , $\overline{E'}$, and $\overline{\epsilon'}$ transport equations were solved to model Rayleigh–Taylor mixing layer growth in the water channel experiment. For this validation case, the

Parameter	Snider and Andrews	Current Validation Case
C_μ	0.09	0.09
σ_m	–	0.6
σ_ρ	–	0.6
σ_T	0.6	–
σ_k	1.0	1.0
σ_ϵ	1.314	1.314
$C_{\epsilon 0}$	0.90	0.90
$C_{\epsilon 2}$	1.92	1.92
C_{pu}	–	0
C_{pu}^ϵ	–	0

Table 4.2 Model parameters used by Snider and Andrews (1996) and for the current model validation.

parameters were set to those used by Snider and Andrews and are listed in table 4.2. Instead of solving a mean mass fraction or mean density transport equation, Snider and Andrews solved a mean temperature equation, where the buoyancy driving was given by the thermal expansion coefficient $\beta = -(1/\rho_0)(\partial\rho/\partial T)$. Accordingly, the turbulent Schmidt number σ_T is equivalent to the turbulent Schmidt numbers σ_ρ and σ_m used in the current model.

The one-dimensional, transient calculations of Snider and Andrews (1996) showed that, using the coefficients in table 4.2, the self-similar growth parameter converged to $\alpha = 0.062$ as the grid spacing was decreased. Along with using the same parameters as Snider and Andrews, the same densities and domain size were used, where the densities of the heavy and light fluids were $\rho_1 = 0.9985986$ and $\rho_2 = 0.9971018$, $L_z = 50$ cm, and $g_z = 981$ cm/s². A series of calculations were performed to test

	$\Delta t = 0.1$ s	0.05 s	0.02 s	0.01 s	0.005 s
$N_z = 50$	0.097	0.0968	0.095	0.0944	0.0938
75	0.0591	0.0596	0.0601	0.0602	0.0602
100	0.063	0.0632	0.0633	0.0634	0.0634
150	0.0616	0.0619	0.0621	0.0622	0.0621
200	0.0609	0.0613	0.0615	0.0616	0.0616
250	0.0606	0.061	0.0613	0.0614	0.0613
300	0.0605	0.061	0.0612	0.0613	0.0613
400	0.0606	0.061	0.0613	0.0614	0.0614
500	–	0.0611	0.0613	0.0614	0.0614

Table 4.3 Convergence of self-similar growth parameter α for various grid spacings and time steps. Model parameters were chosen to match Snider and Andrews (1996).

the dependence of the numerical algorithm on the grid spacing and time step. Table 4.3 shows the late-time values of α obtained by calculating the late time slope of $(h_b - h_s)/2$ versus $Ag t^2$. As shown by Snider and Andrews, the model yields a grid spacing and time step-independent solution for approximately $N_z \gtrsim 250$ ($\Delta x \lesssim 0.2$ cm) and $\Delta t \lesssim 0.02$ s. Also, the current numerical implementation of the \tilde{m}_1 , \tilde{E}'' , and $\tilde{\epsilon}''$ equations yields a late-time value $\alpha = 0.0614$ using the parameters of Snider and Andrews, which agrees well with their value $\alpha = 0.062$. The slight difference in the late-time value of α may be attributed to the difference in numerical algorithms: finite difference versus finite volume, Favre-averaged versus Reynolds-averaged, and second-order Crank–Nicholson time integration versus first-order Euler-explicit time integration.

4.5.2 Self-Similar analysis

Another validation of the numerical implementation of (4.24)–(4.28) is given by a comparison of the modeled profiles \tilde{m}_1 , \widetilde{E}'' , $\tilde{\epsilon}''$, $\widetilde{m}_1''^2$, and $\widetilde{\chi}''$ with the analytical, self-similar solutions. Given the assumptions:

- small density difference,
- quiescent, pure fluid outside mixing layer ($\widetilde{E}'' = \tilde{\epsilon}'' = 0$ and $\widetilde{m}_1''^2 = \widetilde{\chi}'' = 0$),
- no mean velocity field within a Galilean reference frame moving with the mixing layer ($\tilde{u}_i = 0$),
- pressure transport of \widetilde{E}'' and $\tilde{\epsilon}''$ are neglected,
- physical viscosity and diffusivity contributions to the overall flux of each term neglected, *i.e.* $T^\phi = \frac{\partial}{\partial z} \left(\frac{\nu_t}{\sigma_\phi} \frac{\partial \tilde{\phi}}{\partial z} \right)$,

the partial differential equations in (4.24)–(4.28) have self-similar solutions (Andrews 1984; Spitz & Haas 1991; Snider & Andrews 1996; Dimonte & Tipton 2006). Given the similarity variable

$$\eta = \frac{z}{h(t)}, \quad (4.39)$$

the self-similar density (and hence, mass fraction) profiles are linear in η and the remaining turbulent quantities are all parabolic in η ,

$$\tilde{m}_1(\eta) = \eta + \frac{1}{2}, \quad (4.40)$$

$$\widetilde{E}''(\eta) = C_{\widetilde{E}''} (1 - 4\eta^2), \quad (4.41)$$

$$\tilde{\epsilon}''(\eta) = C_{\tilde{\epsilon}''} (1 - 4\eta^2), \quad (4.42)$$

over $-1/2 \leq \eta \leq 1/2$. Analogous self-similar solutions are assumed for the modeled $\widetilde{m}_1''^2$ and $\widetilde{\chi}''$ transport equations, given the similar form of the partial differential

equations,

$$\widetilde{m}_1''(\eta) = C_{\widetilde{m}_1''} (1 - 4\eta^2) , \quad (4.43)$$

$$\widetilde{\chi}''(\eta) = C_{\widetilde{\chi}''} (1 - 4\eta^2) . \quad (4.44)$$

However, due to the assumptions implicit in the formulation of the self-similar solutions, such profiles are taken to be approximations only.

Before the current numerical implementation of the model is tested, the approximate self-similar solutions are compared with the DNS results. To facilitate such a comparison, the definition of the self-similar profiles must be altered to match the definition of $h(t)$ used here, where $\widetilde{m}_1(\eta = -1/2) = 0.05$ and $\widetilde{m}_1(\eta = 1/2) = 0.95$ (not zero and one, respectively). Accordingly, the similarity variable is slightly altered to

$$\eta = \frac{0.9 z}{h(t)} , \quad (4.45)$$

where $h(t)$ is defined on a 5–95% threshold basis. A comparison of the normalized, self-similar profiles and the DNS profiles at various times is shown in figure 4.31. This comparison shows that the self-similar profiles are fair approximations of the DNS profiles; however, the DNS profiles do not match the quiescent boundary conditions at the edges of the mixing layer and the profiles of \widetilde{E}'' , \widetilde{e}'' , and $\widetilde{\chi}''$ are over-predicted by self-similar parabolic profiles within the core of the mixing layer ($|z/h| < 0.5$).

Next, the numerical implementation of the model is compared with the self-similar profiles as done by Snider (1994) and Dimonte and Tipton (2006). First, the model was run with the parameters used by Snider and Andrews (1996) (see table 4.2). A comparison of the model and self-similar profiles is shown in figure 4.32. The numerical implementation of the modeled transport equations is free from the statistical convergence criteria of the DNS (see § 3.4.3), so that much smoother profiles are obtained, allowing easier comparisons with the self-similar profiles. All

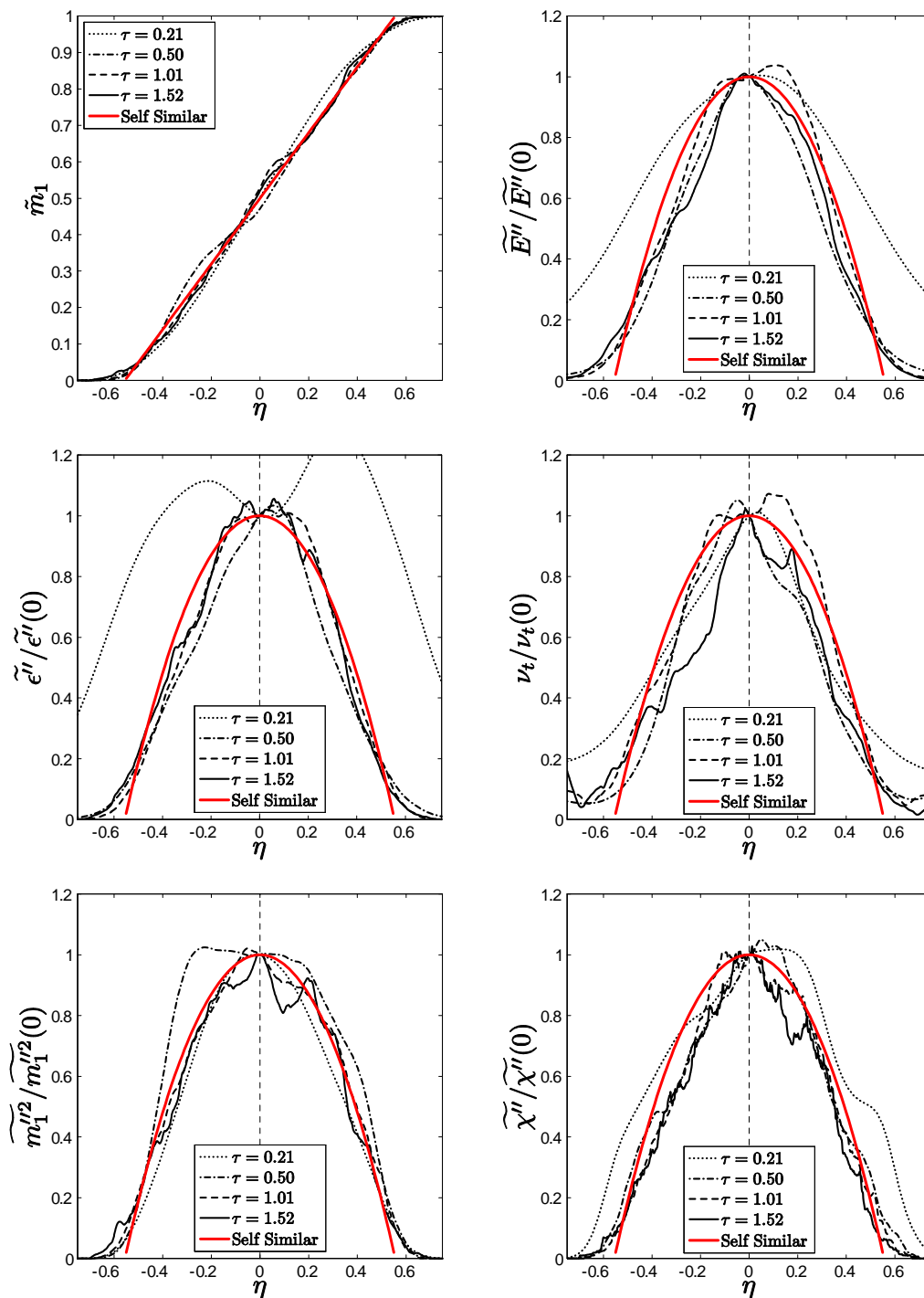


Figure 4.31 Comparison of DNS profiles (black) with self-similar solutions (red) across the mixing layer at various times. All parabolic profiles are normalized by their respective centerplane value.

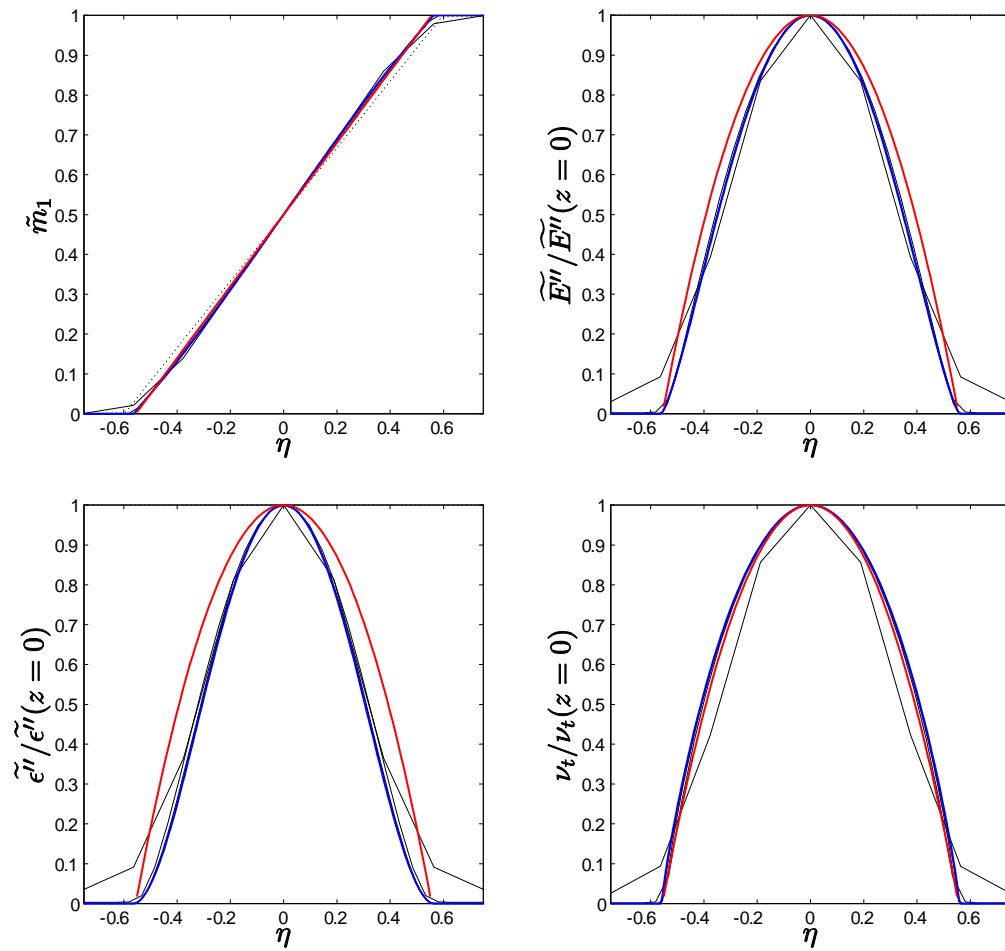


Figure 4.32 Comparison of profiles from the model with their self-similar solutions (red). The initial model profile is denoted by a dotted line and the final profile is denoted by a blue line. All parabolic profiles have been normalized by their respective centerplane value. The model parameters are taken from Snider and Andrews (1996).

profiles exhibit good agreement with the linear and parabolic predictions. As noted in the comparisons of the DNS and self-similar profiles in figure 4.31, the profiles of $\tilde{\epsilon}''$ are over-predicted by the self-similar profile.

Two additional tests were performed to examine the predictions of the model when using the Reynolds number-dependent parameters (see figures 4.12, 4.21, and 4.29) for the three-equation $\widetilde{E}''-\widetilde{\epsilon}''-\widetilde{m}_1''^2$ and four-equation $\widetilde{E}''-\widetilde{\epsilon}''-\widetilde{m}_1''^2-\widetilde{\chi}''$ models. A comparison of the self-similar profiles and the three-equation model predictions is shown in figure 4.33. The same comparison for the four-equation model is shown in figure 4.34. Both the three- and four-equation models reproduced the approximate self-similar profiles, as shown in the constant parameter case.

4.6 *Mixing Model: $Sc = 7$ Case*

In § 4.3, the gradient-diffusion and scale-similarity models were calibrated for a set of transport equations. To validate the model parameters obtained from the DNS, the numerical implementation of the model is tested *a posteriori*. In § 4.6.1–4.6.3, the numerical tests of the model were run using the Reynolds number-dependent parameters and are compared directly with the experimental and DNS results of § 2 and 3. The model was also run using a set of constant parameters to compare with Reynolds number-dependent parameter tests.

4.6.1 *Evolution of model profiles*

To model the growth of the Rayleigh–Taylor mixing layer in the water channel experiment, the numerical implementation of the modeled transport equations (4.24)–(4.28) was initialized with mean profiles from the DNS. Profiles from the DNS at $\tau = 0.1, 0.3, 0.5,$ and 0.7 were used to initialize the model, and are shown in figure 4.35. As

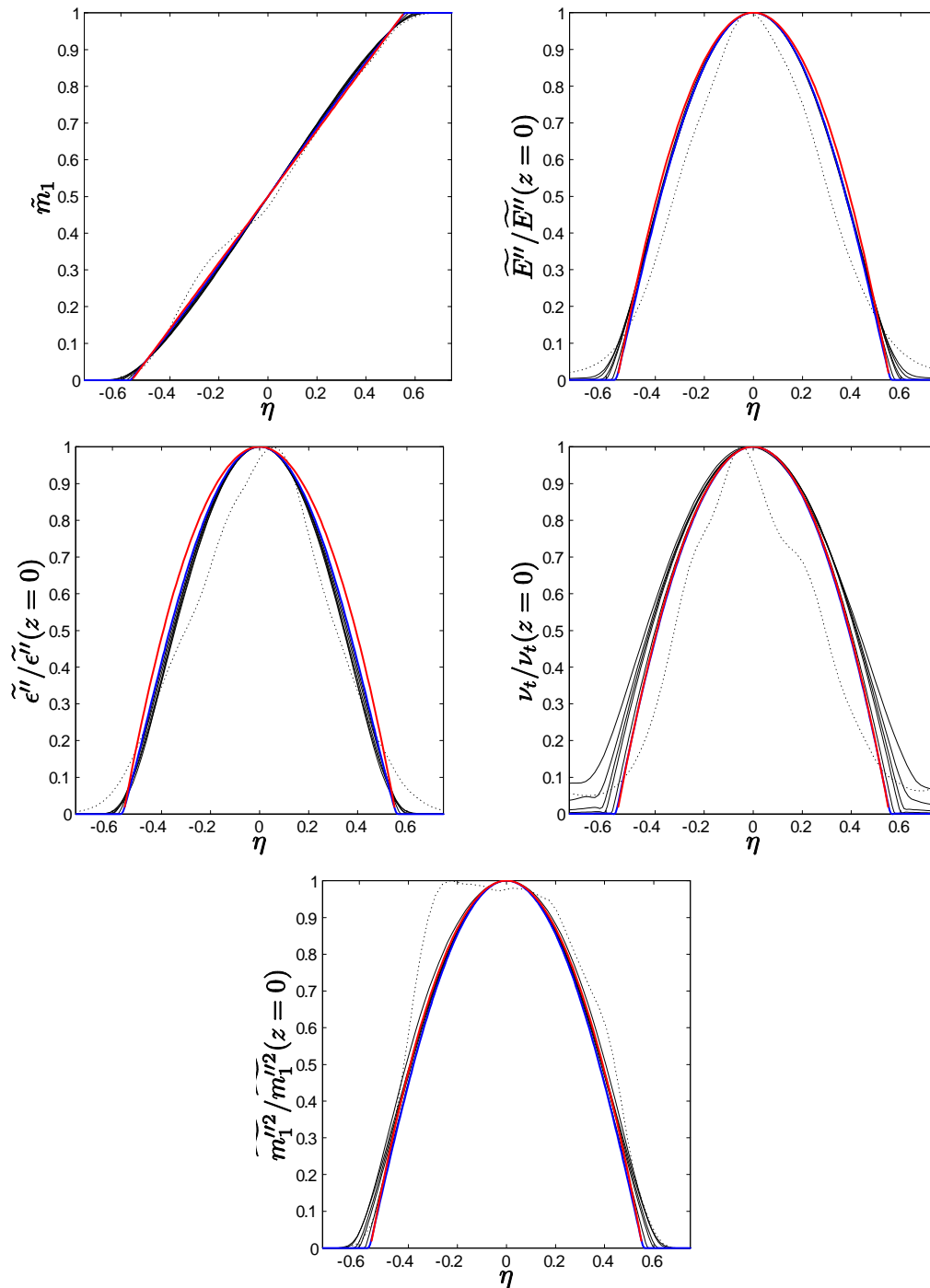


Figure 4.33 Comparison of profiles from the three-equation model with self-similar solutions (red). The initial profile is denoted by a dotted line and the final profile is denoted by a blue line. All parabolic profiles are normalized by their respective centerplane value. The model parameters are taken from the calibrations shown in figures 4.12, 4.21, and 4.29.

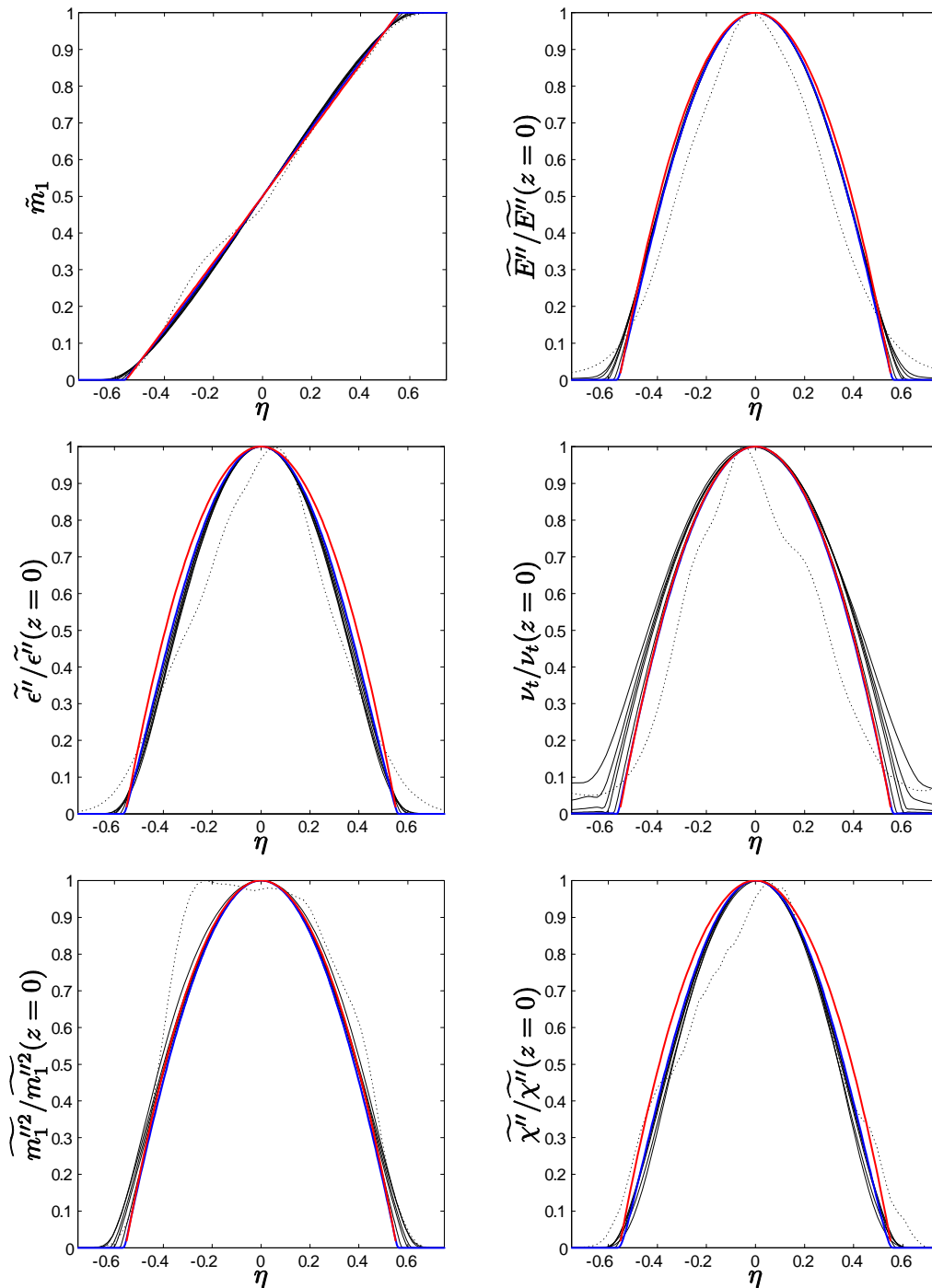


Figure 4.34 Comparison of profiles from the four-equation model with self-similar solutions (red). The initial profile is denoted by a dotted line and the final profile is denoted by a blue line. All parabolic profiles are normalized by their respective centerplane value. The model parameters are taken from the calibrations shown in figures 4.12, 4.21, and 4.29.

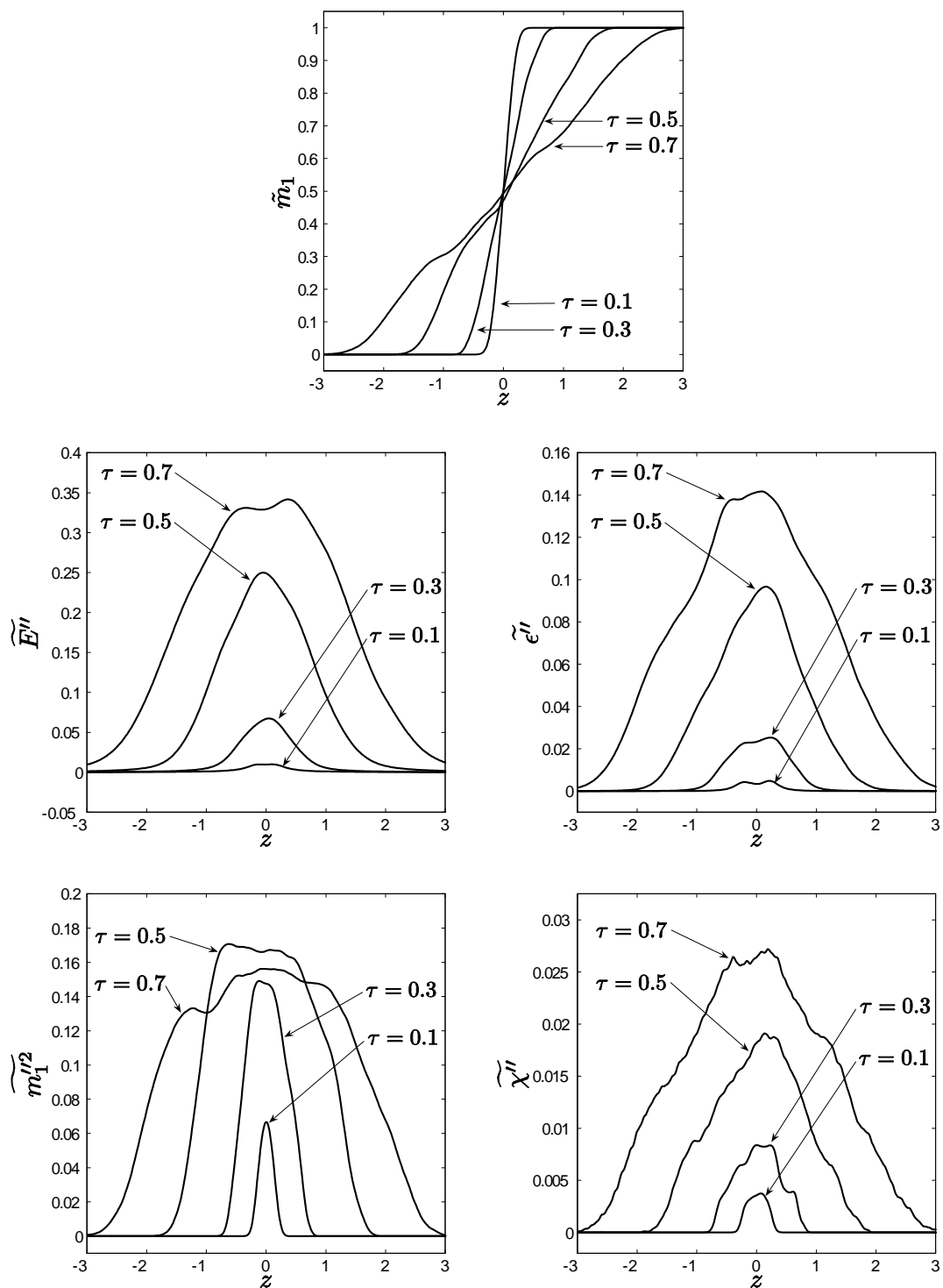


Figure 4.35 Profiles of \tilde{m}_1 , \tilde{E}'' , $\tilde{\epsilon}''$, $\tilde{m}_1''^2$, and $\tilde{\chi}''^2$ across the mixing layer from the DNS used as initial conditions in the model.

τ_{IC}	Re_h	Regime
0.1	10	Early-time, linear growth stage
0.3	39	Onset of nonlinearity and secondary instabilities; Peak P/D ratios
0.5	137	
		Minimum value of θ ;
		P/D ratio relaxation period;
		Turbulent production terms become non-negligible
0.7	289	Approximately steady-state P/D ratios

Table 4.4 Dimensionless initialization times and integral-scale Reynolds numbers for the four initial conditions cases examined.

shown in figure 4.31, these profiles are fairly approximated by the linear and parabolic self-similar solutions; however, small statistical oscillations exist. The sensitivity of the model to the exact initial conditions will be examined further below and in § 4.6.2.

The evolution of the modeled profiles of \tilde{m}_1 , \tilde{E}'' , \tilde{e}'' , $\tilde{m}_1''^2$, and $\tilde{\chi}''$ are shown in figures 4.36–4.40 as a function of the initial conditions. The evolution of each profile is shown for four different initial conditions, corresponding to four different regimes of development of the mixing layer, as listed in table 4.4. These specific initialization times were examined to test the ability of the model to capture the early-time, transient, and late-time dynamics of the mixing layer.

For an initialization time $\tau_{IC} = 0.7$ ($Re_h = 289$), the mixing layer is fully within the nonlinear transition stage. The production-to-dissipation ratios for all of the transport quantities have reached their respective approximate late-time steady value. This case represents a ‘best-case scenario’ for the model initialization, as very little of the initial transient dynamics must be captured by the model. For the case $\tau_{IC} = 0.5$ ($Re_h = 137$), the mixing layer is in a nonlinear transitional state, where

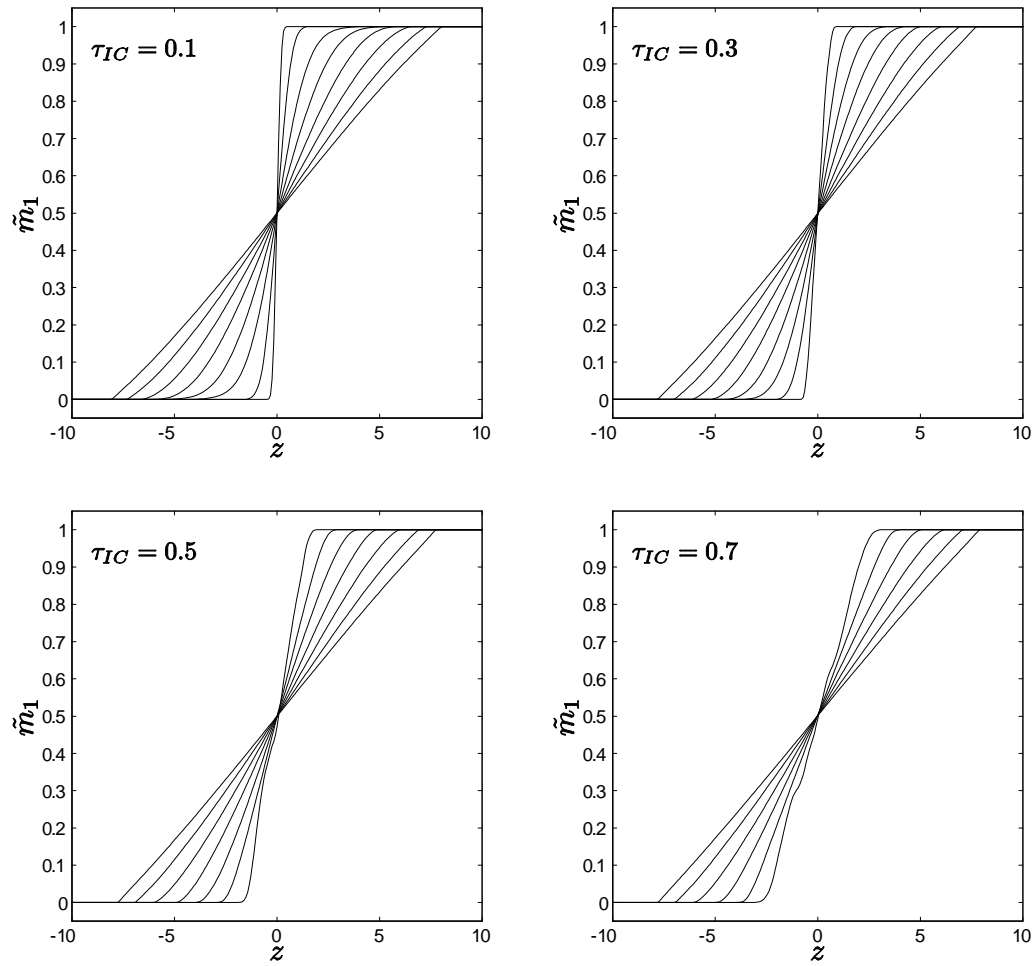


Figure 4.36 Evolution of \tilde{m}_1 profiles as a function of the initial conditions.

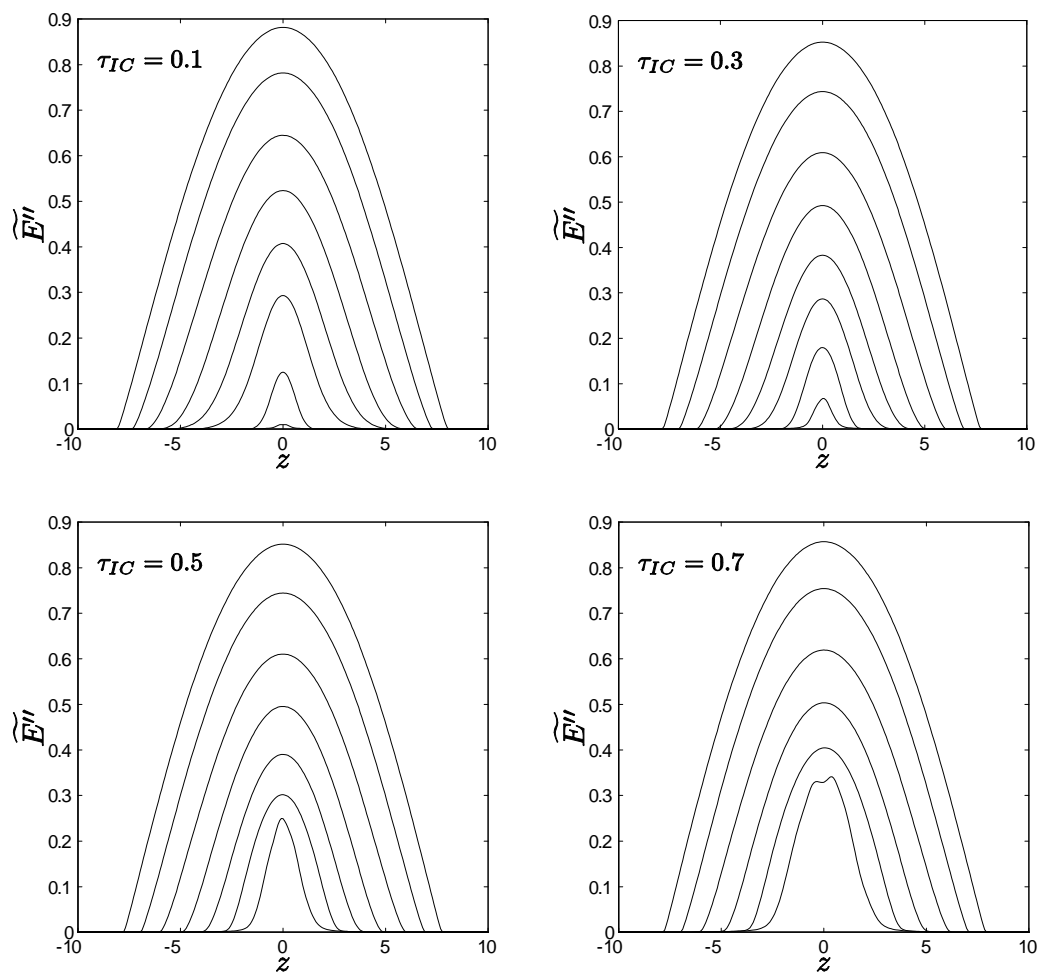


Figure 4.37 Evolution of \widetilde{E}'' profiles as a function of the initial conditions.

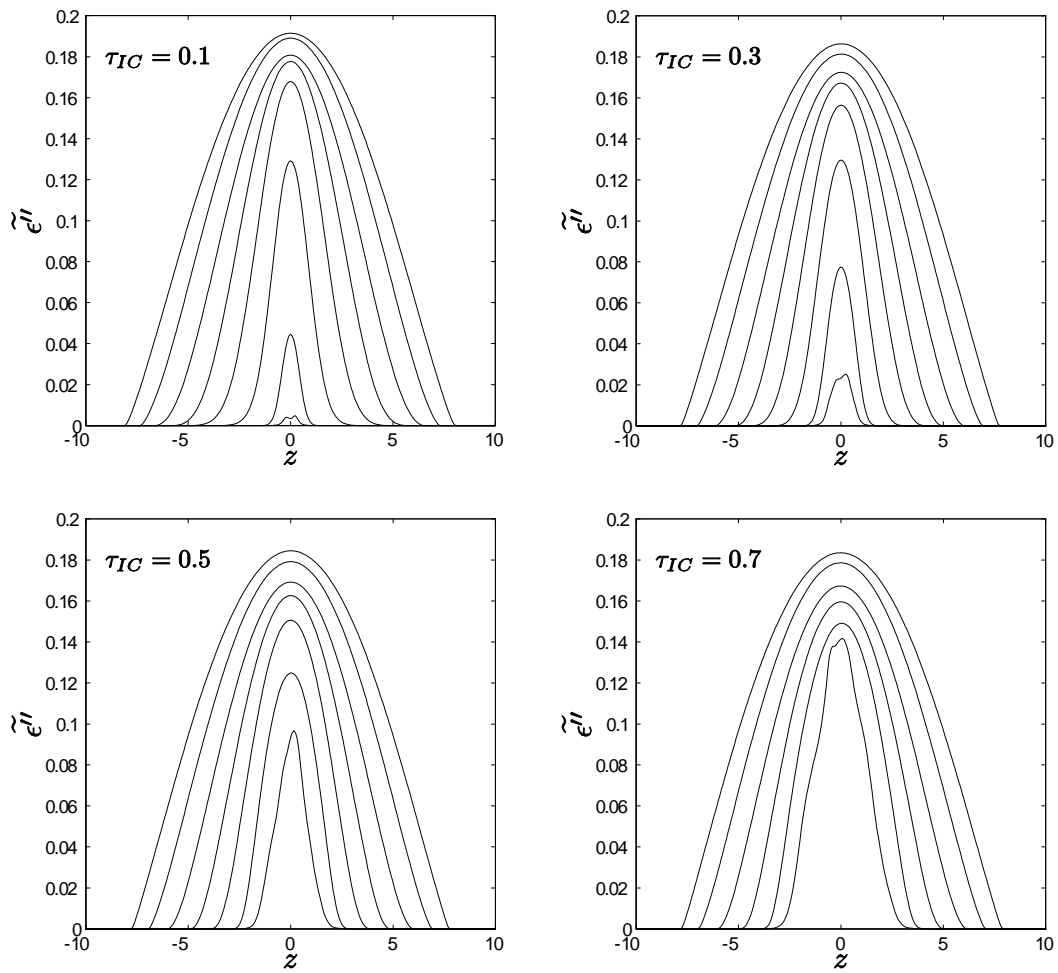


Figure 4.38 Evolution of $\tilde{\epsilon}''$ profiles as a function of the initial conditions.

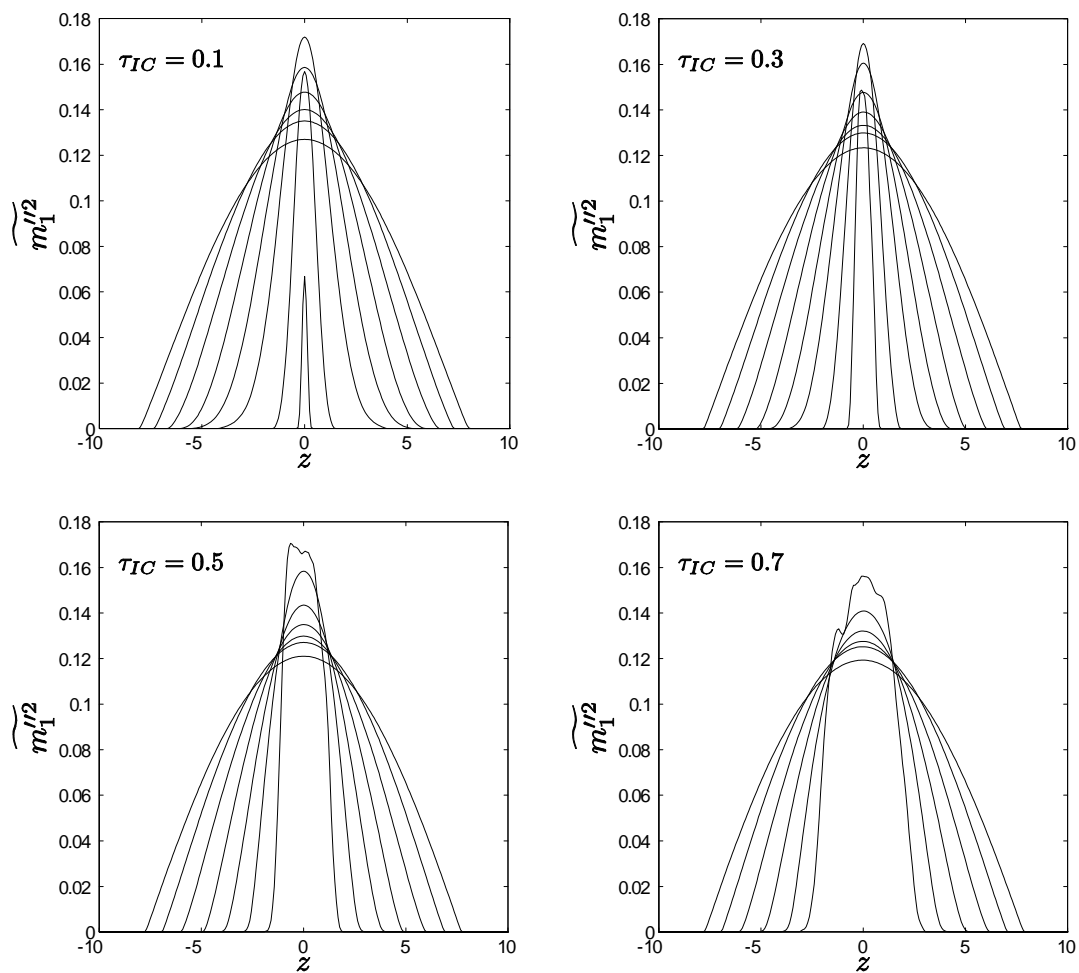


Figure 4.39 Evolution of $\widetilde{m}_1^{prime/2}$ profiles as a function of the initial conditions.

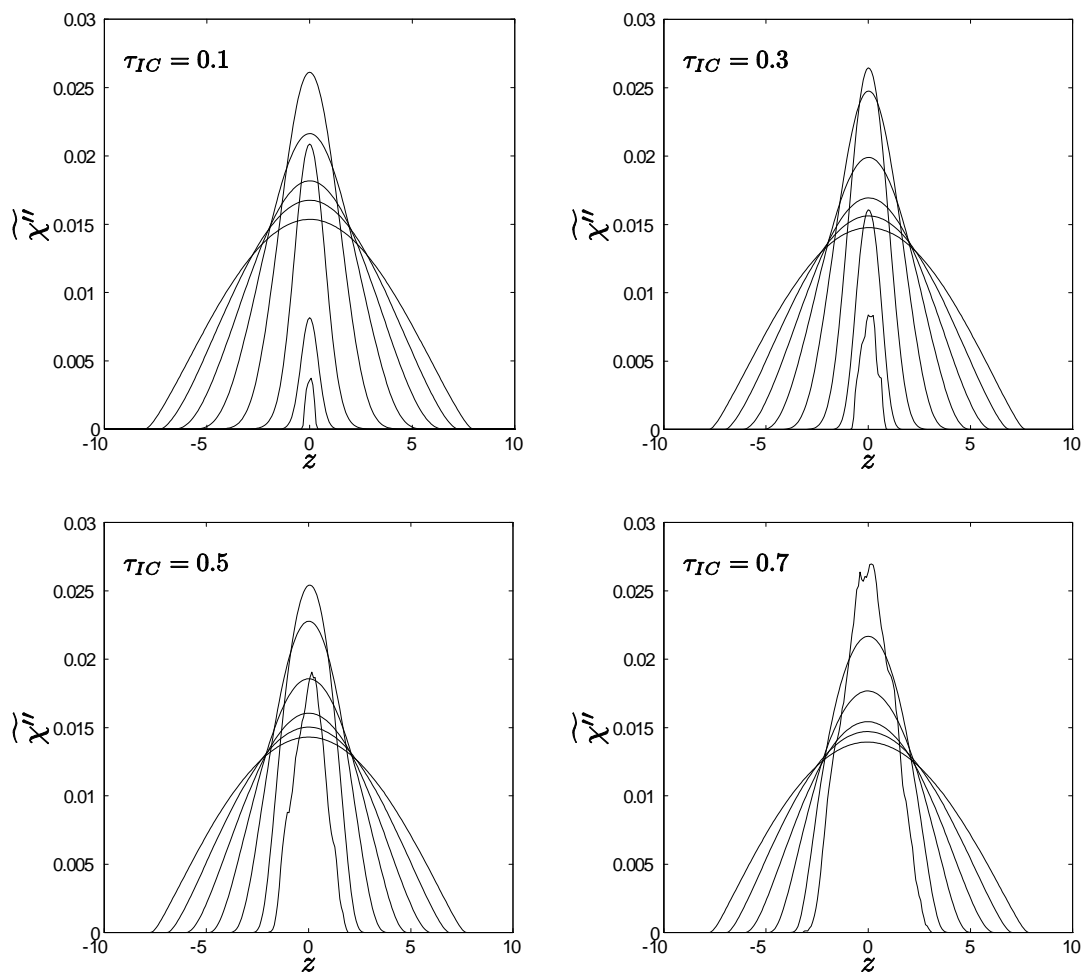


Figure 4.40 Evolution of $\widetilde{\chi}''$ profiles as a function of the initial conditions.

the production-to-dissipation ratios are relaxing towards their late-time steady values. This case represents a greater challenge to the model in that it requires the model to capture some of the weak, early-time transient dynamics as well as the late-time turbulent dynamics. The initialization profiles at $\tau_{IC} = 0.3$ ($Re_h = 39$) further increase the demands on the predictive capabilities of the model. For this case, the initial production-to-dissipation ratios are far from unity (see figures 3.51, 3.59, 3.67, and 3.74). The model must capture the low-Reynolds number, non-turbulent physics related to the onset of secondary instabilities and the initial formation of a broad range of scales across the turbulent spectrum of modes. Finally, the model is also initialized with profiles from the DNS at $\tau_{IC} = 0.1$. In this case, the ‘turbulence’ model must also account for the linear growth stage of the mixing layer, where the neglected pressure and viscous stress fluxes of \widetilde{E}'' , pressure transport of $\widetilde{\epsilon}''$, and curvature production of $\widetilde{\epsilon}''$ and $\widetilde{\chi}''$ are important.

The evolution of the profiles for each transport quantity is shown in figures 4.36–4.40. Despite the differences in the initial dynamic regimes and statistical oscillations present in the DNS profiles used as initial conditions, the model produced smooth, approximately symmetric profiles for each initialization case. Accordingly, the model appears to be qualitatively insensitive to small oscillations in the initial profiles. In addition, the magnitude of the final \widetilde{E}'' , $\widetilde{\epsilon}''$, $\widetilde{m_1''^2}$, and $\widetilde{\chi}''$ profiles are similar, despite the strong differences in the initial conditions. This suggests that the time-history of the transported quantities is insensitive to the initial conditions, when using the Reynolds number-dependent model parameters. This is important as it shows that the model does not require high-Reynolds number initial conditions to capture the time-evolution of the mixing dynamics.

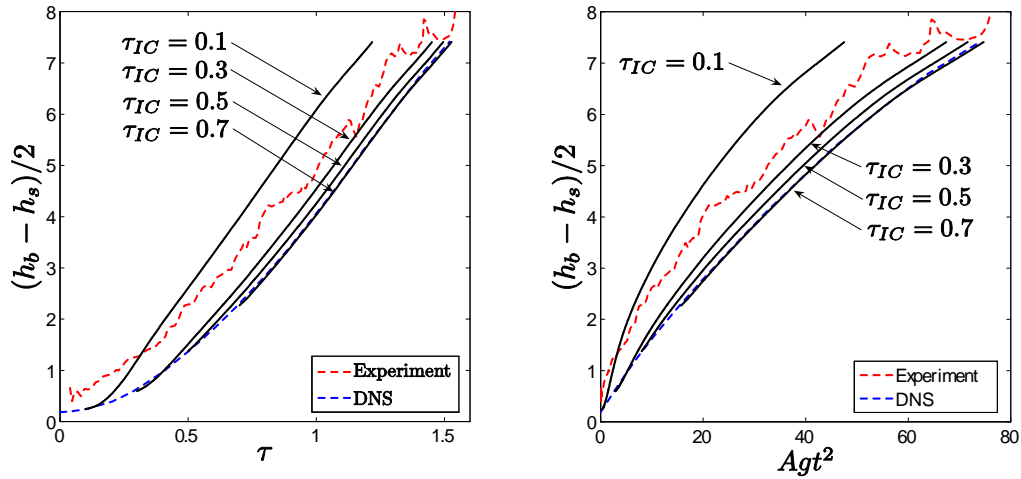


Figure 4.41 Comparison of the growth of the mixing layer (left) and late-time growth rate (right) from the model, DNS, and experiment using various initial conditions.

4.6.2 Comparison of model with DNS and experiments

The profiles presented above in § 4.5.2 and 4.6.1 only indicate that the model qualitatively predicts profiles expected for small Atwood number, Rayleigh–Taylor driven mixing layers. Further comparisons with the water channel experiments and DNS follow to quantitatively assess the model predictions. Figure 4.41 shows the evolution of the mixing layer width for the water channel experiment (Wilson 2002), the DNS, and the model using various initial conditions. For the cases $\tau_{IC} = 0.5$ and $\tau_{IC} = 0.7$, the model exhibits good agreement with the DNS. The model initialized at $\tau_{IC} = 0.3$ exhibits fair agreement with the DNS, but slightly over-predicts the mixing layer width. However, this discrepancy is small and the model still predicts the same late-time growth rate. Using $\tau_{IC} = 0.1$, the model demonstrates only fair agreement with the experiment and the DNS: the reasons for this discrepancy will be discussed in § 4.6.3. While the model exhibits good agreement with the DNS, it may be possible to improve the agreement with the experiment by manually decreasing

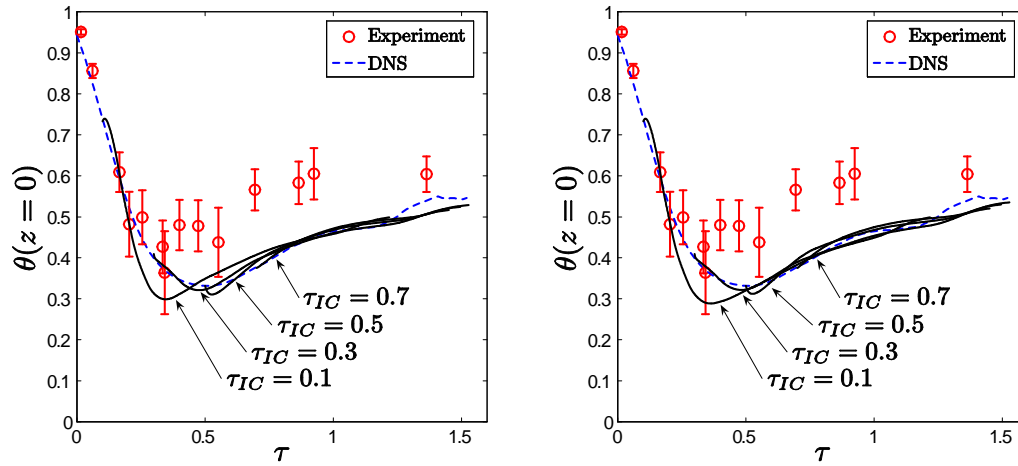


Figure 4.42 Comparison of $\theta(z = 0)$ from the model, DNS, and experiment using various initial conditions: three-equation model (left) and four-equation model (right).

the calibrated value of σ_ρ and σ_m or by decreasing the calibrated value of $C_{\epsilon 2}$.

In addition to comparing the growth of the mixing layer, the evolution of the mixing parameters $\theta(z = 0)$ and Θ are also compared. This is a novel comparison, in that such results have not been shown by any previous RANS model of Rayleigh–Taylor mixing. Figure 4.42 shows the evolution of $\theta(z = 0)$ for the water channel experiments (Mueschke *et al.* 2006), the DNS, and the model using various initial conditions. Both the three-equation model $\widetilde{E}''-\widetilde{\epsilon}''-\widetilde{m}_1''^2$ [figure 4.42 (left)] and the four-equation model $\widetilde{E}''-\widetilde{\epsilon}''-\widetilde{m}_1''^2-\widetilde{\chi}''$ [figure 4.42 (right)] were tested to determine if the inclusion of an additional transport equation yielded better accuracy. Both models show very good agreement with the DNS. Even for the case of $\tau_{IC} = 0.1$, the models show reasonable agreement with the DNS. Similar trends are also observed in the evolution of Θ , shown in figure 4.43, where the models show good agreement for $\tau_{IC} \geq 0.3$ and adequate agreement for $\tau_{IC} = 0.1$. Again, the model may be manually adjusted to exhibit better agreement with the experiment by increasing the calibration

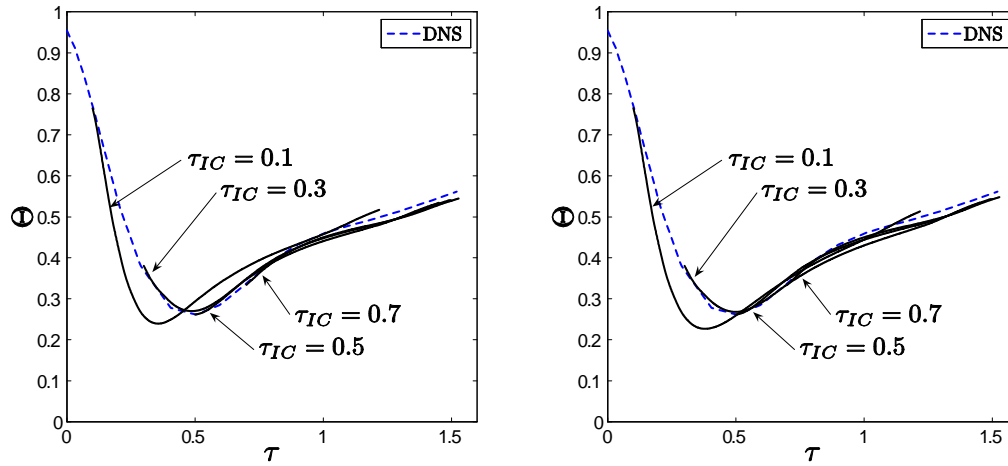


Figure 4.43 Comparison of Θ from the model and DNS using various initial conditions: three-equation model (left) and four-equation model (right).

of C_{m2} , which would increase the rate at which mixed fluid is produced resulting in larger values of θ .

4.6.3 Production-to-dissipation ratios

In general, the model shows fair-to-good agreement with the experiment and the DNS from which the model was calibrated. However, the discrepancy between the model and DNS increases as τ_{IC} decreases. This is primarily a result of applying a turbulence transport and mixing model to a flow which is not yet turbulent. Furthermore, RANS models are limited to applications where the turbulent dynamics of the flow are roughly in equilibrium with the mean flow dynamics, such that the turbulent flow exhibits slow changes with respect to changes in the mean field velocity or density field. However, for the mixing layer examined here, the mean mass fraction is expanding relatively quickly compared with changes in the turbulence. Accordingly, the production-to-dissipation ratios exhibit large variability during this time. In general, standard RANS-type models do not perform well under the conditions

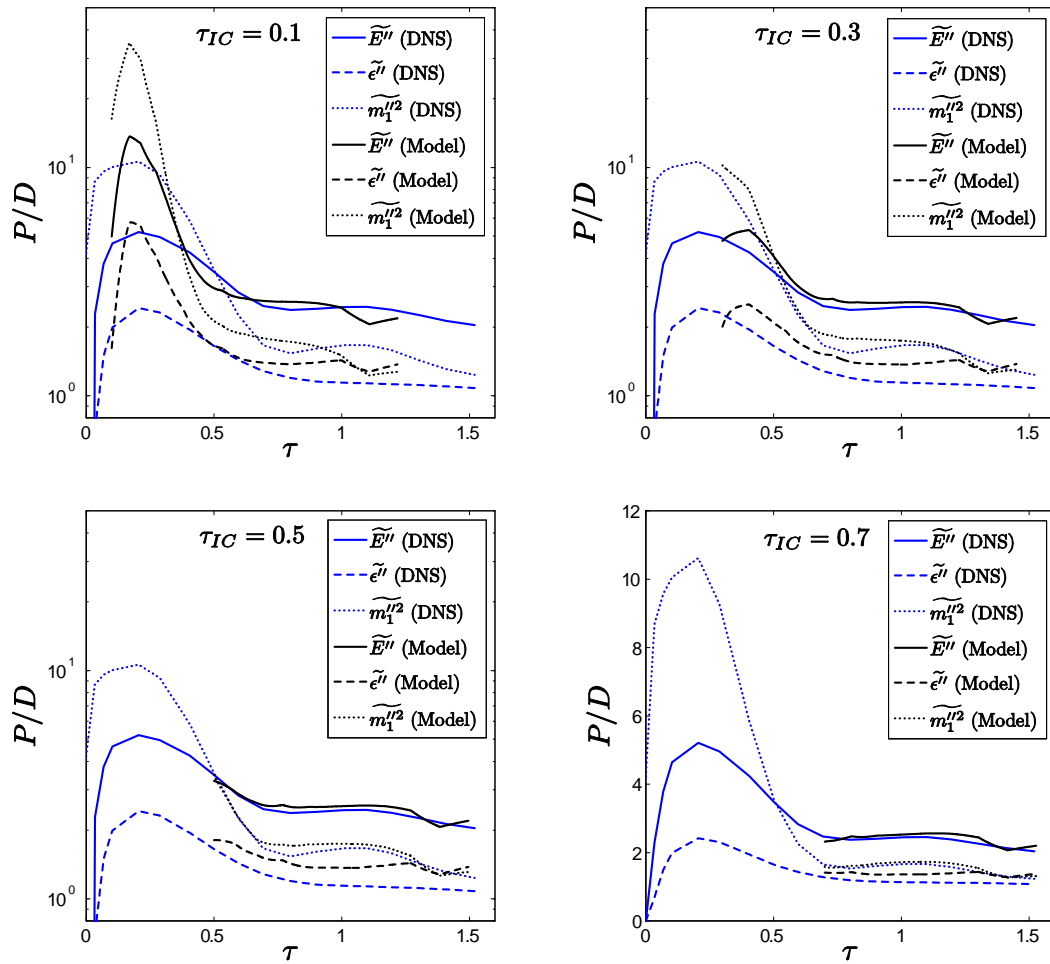


Figure 4.44 Comparison of production-to-dissipation ratios from the DNS (blue) and three-equation model (black) for various initial conditions.

of highly-variable production-to-dissipation ratios (Pope 2000). However, the early-time, dynamic production-to-dissipation ratios observed in the low-Reynolds number and transitional regimes can be recovered when using functional model parameters, and is analogous to the formulation of low Reynolds number modifications to standard \widetilde{E}'' - $\widetilde{\epsilon}''$ models for wall-bounded flows (Wilcox 2006).

The evolution of the production-to-dissipation ratios for both the DNS and model are shown in figures 4.44 and 4.45. For the case $\tau_{IC} = 0.1$, the model qualitatively

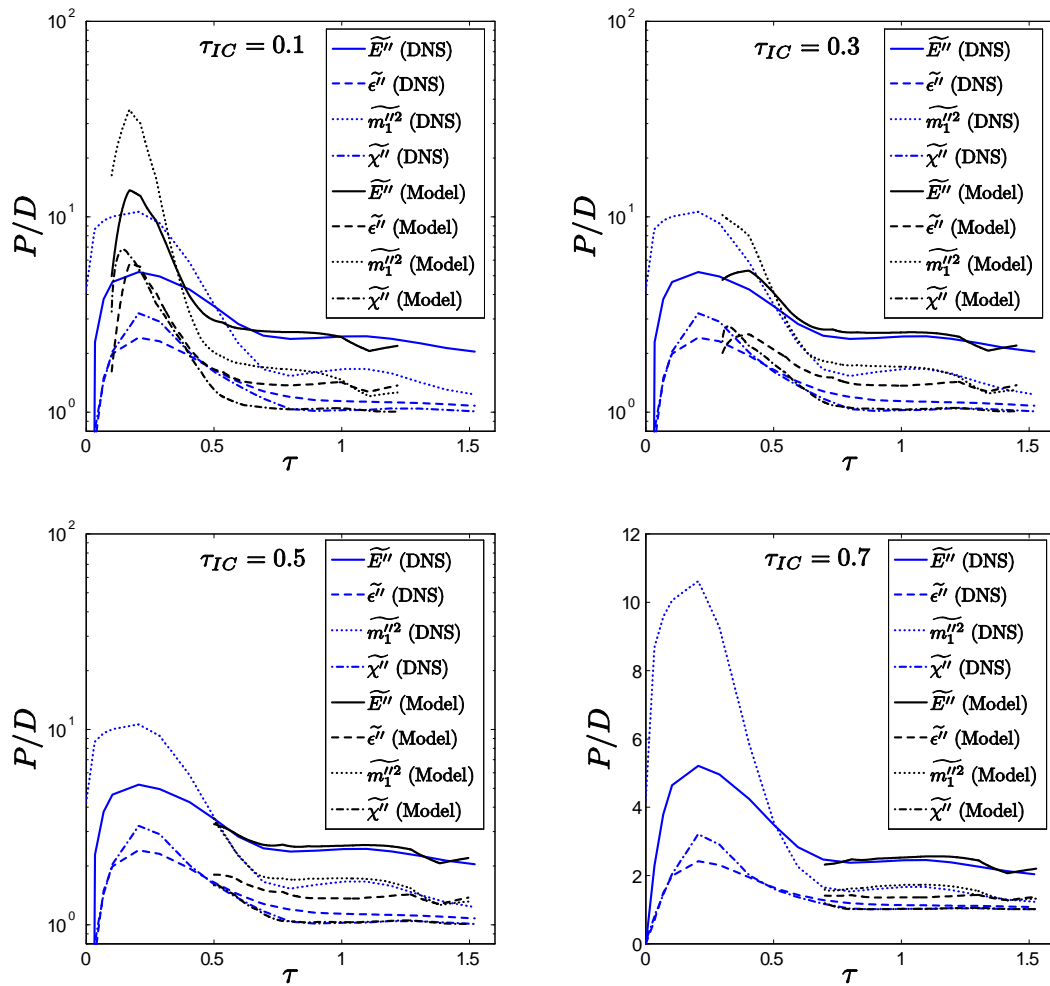


Figure 4.45 Comparison of production-to-dissipation ratios from the DNS (blue) and four-equation model (black) for various initial conditions.

captures the rise and fall of the different production-to-dissipation ratios, but does not accurately capture the magnitudes or time-history of the relaxation process. The agreement between the DNS and model production-to-dissipation ratios improve as the initial conditions are taken from the DNS at later times. This includes the cases $\tau_{IC} = 0.3$ and $\tau_{IC} = 0.5$, where the relaxation of the production-to-dissipation ratios to their respective late-time steady values is relatively well-captured.

4.6.4 Comparison with constant model parameters

While it is possible to model the mixing layer dynamics using variable model parameters, this practice has not been adopted for Rayleigh–Taylor driven mixing, whether using \widetilde{E}'' - $\widetilde{\epsilon}''$ type models (Spitz & Haas 1991; Snider & Andrews 1996; Grégoire & Souffland 1999) or other RANS-type models (Besnard *et al.* 1992; Youngs 1995; Dimonte & Tipton 2006). To illustrate the difference between the dynamics of the model using Reynolds number-dependent and constant model parameters, the model was run using the constant parameters shown in table 4.5, which are the average values of each parameter from the last three measurements in time.

A comparison of the mixing layer growth rate is shown in figure 4.46, where the late-time growth rate of the model, DNS, and experiment show good agreement. However, the model exhibits a time-lag depending upon the exact initial conditions used. This is due to the fact that the closures do not accurately model the early-time physics of the mixing layer. Figure 4.46 also shows the development of the centerplane molecular mixing parameter θ . Again, the model, DNS and experiment show fair agreement; however, the model approached the late-time steady value of $\theta \approx 0.6$ faster than the DNS. Both the time-lag in h and discrepancy in θ are discussed below.

For the constant-parameter case examined here, the late-time growth rate of the

Parameter	Constant parameters case
C_μ	0.09
σ_m	0.087
σ_ρ	0.087
σ_k	0.105
σ_ϵ	0.121 [†]
σ_{m2}	0.120 [†]
$C_{\epsilon0}$	1.432
$C_{\epsilon2}$	2.339 [†]
C_{m2}	0.511 [†]
C_{pu}	0
C_{pu}^ϵ	0

Table 4.5 Model parameters used in the constant parameters case taken from an average of the final three Reynolds-number dependent parameter values. Calibrated model parameters that are still changing at the latest times calculated are denoted by †.

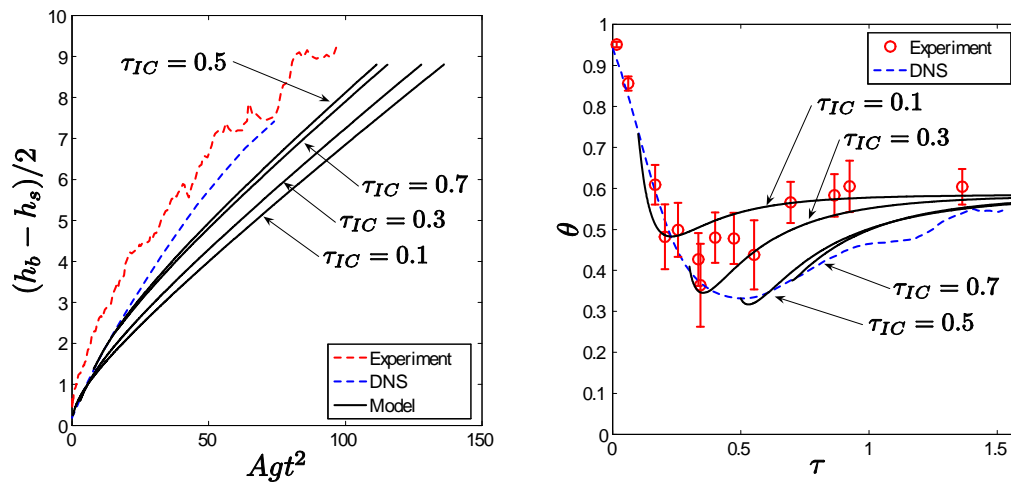


Figure 4.46 Comparison of the mixing layer growth rate (left) and $\theta(z = 0)$ from the model, DNS, and experiment for the constant parameters case.

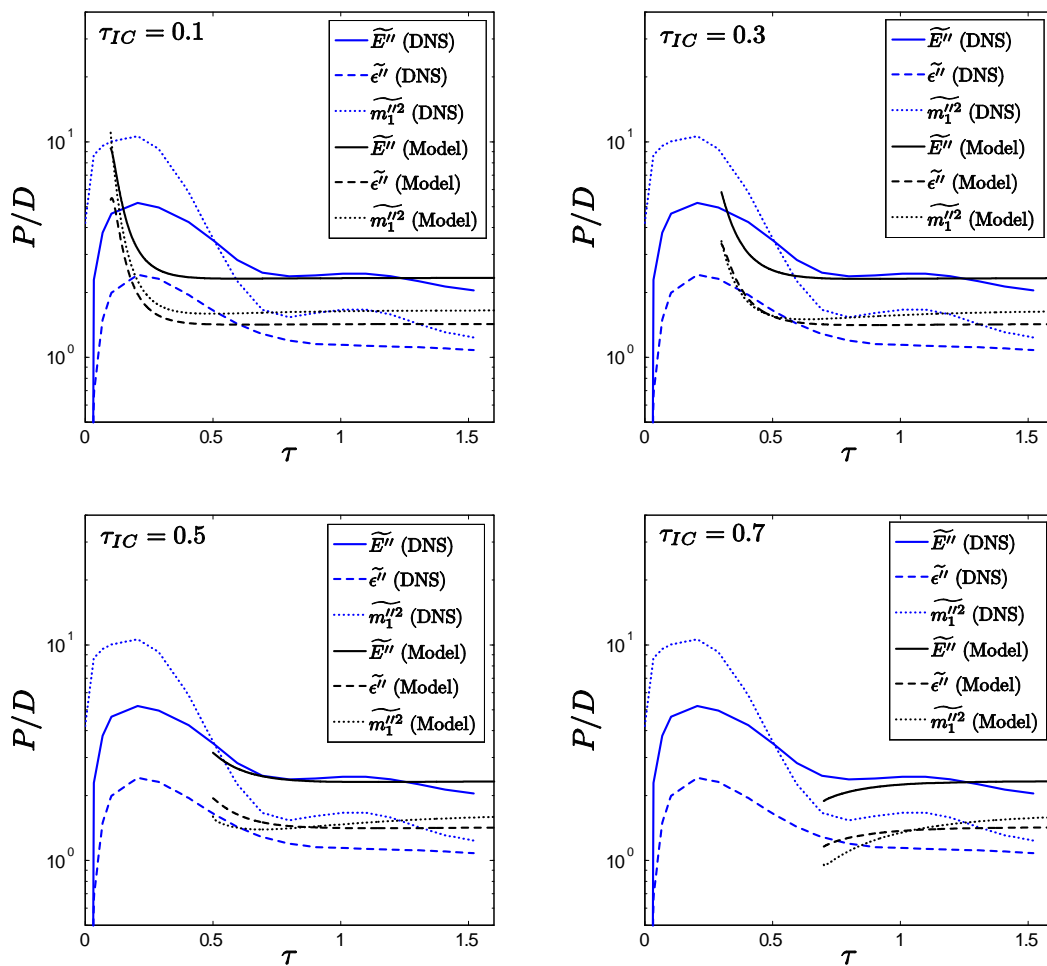


Figure 4.47 Comparison of the production-to-dissipation ratios from the model and the DNS for the constant parameters case.

mixing layer and $\theta(z = 0)$ is recovered; however, the early-time dynamics are poorly captured because the model does not accurately predict the early-time production-to-dissipation ratios. This is clearly demonstrated in figure 4.47, where the production-to-dissipation ratios for the constant parameters case do not resemble the evolutions from the DNS during the initial transition stages of the mixing layer. However, by selecting the parameters shown in table 4.5, the late-time asymptotic ratios are recovered.

4.7 Mixing Model: $Sc \sim 10^3$ Case

4.7.1 Calibration of C_{m2} for $Sc \sim 10^3$ experiments

The model calibration of C_{m2} shown in figure 4.29 is representative of the mixing dynamics for the $Sc = 7$ case. However, the calibration of the mass fraction variance transport equation must change to properly reproduce the $Sc \sim 10^3$ experiments. Neither the production nor transport terms of $\widetilde{m_1''^2}$ are explicitly functions of the mass diffusivity \bar{D} . Note that both the growth of the mixing layer (given by \tilde{m}_1) and the production rate of $\widetilde{m_1''^2}$ are functions of $\widetilde{w''m_1''}$. In § 2.4.4, it was reported that the growth rate of the $Sc \sim 10^3$ mixing layer was slightly larger than measured for the $Pr = 7$ case. Thus, $\widetilde{w''m_1''}$ may be a weak function of the Schmidt number; however, the results in § 2.4.4 indicate that this functional dependence is very weak. The final term in the transport equation of $\widetilde{m_1''^2}$ is the turbulent dissipation term

$$D^{\widetilde{m_1''^2}} = -2\bar{\rho}\widetilde{\chi''}, \quad (4.46)$$

where the mass fraction dissipation rate is clearly a function of the mass diffusivity:

$$\widetilde{\chi''} = \bar{D}^2 \left(\frac{\partial^2 \widetilde{m_1''}}{\partial x_i \partial x_j} \right)^2 \approx C_{m2} \frac{\widetilde{\epsilon''}}{\widetilde{E''}} \widetilde{m_1''^2}. \quad (4.47)$$

Accordingly, the parameter C_{m2} must account for variations in \bar{D} to reproduce experimental results at various Schmidt numbers.

It is possible to estimate C_{m2} for the high Schmidt number experiments by combining the experimental measurements in § 2.4 with the transport equation budgets reported in § 3.6. Integrating the transport equation for $\widetilde{m_1''^2}$ across the vertical domain eliminates the conservative transport term $T^{\widetilde{m_1''^2}}$, resulting in

$$\int_{-L_z/2}^{L_z/2} \bar{\rho} \frac{\partial \widetilde{m_1''^2}}{\partial t} dz = \int_{-L_z/2}^{L_z/2} P^{\widetilde{m_1''^2}} dz - \int_{-L_z/2}^{L_z/2} D^{\widetilde{m_1''^2}} dz. \quad (4.48)$$

Inserting the scale-similarity model for the dissipation term and rearranging gives

$$C_{m2} = \frac{\int_{-L_z/2}^{L_z/2} P^{\widetilde{m_1''^2}} dz - \int_{-L_z/2}^{L_z/2} \bar{\rho} \frac{\partial \widetilde{m_1''^2}}{\partial t} dz}{\int_{-L_z/2}^{L_z/2} \frac{\widetilde{\epsilon''}}{\widetilde{E''}} \widetilde{m_1''^2} dz}. \quad (4.49)$$

As a validation, using the $Sc = 7$ DNS data to evaluate (4.49) results in the same C_{m2} as shown in figure 4.29.

To calculate (4.49) and obtain a calibration of C_{m2} for the $Sc \sim 10^3$ experiments, the fluctuating density statistics from the $Sc \sim 10^3$ experiments (see § 2.4) must be used to calculate the integrals $\int_{-L_z/2}^{L_z/2} \bar{\rho} \widetilde{m_1''^2} dz$ and $\int_{-L_z/2}^{L_z/2} \frac{\widetilde{\epsilon''}}{\widetilde{E''}} \widetilde{m_1''^2} dz$. For the small Atwood number case considered here, the substitution $\widetilde{m_1''^2} \equiv \overline{f_1''^2}$ is accurate to within $\pm 0.2\%$ (see § 3.6.6). However, several terms remain in (4.49), which require approximations. The growth of the mixing layer is given by the mean mass fraction transport equation, which is explicitly a function of the mass fraction-velocity correlation $\widetilde{w''m_1''}$. As noted above, $\widetilde{w''m_1''}$ may be considered to be independent of Schmidt number. Using the same physical argument, the gradient-diffusion closure of $\widetilde{w''m_1''}$ depends upon $\widetilde{E''}$, $\widetilde{\epsilon''}$, and $\partial \widetilde{m_1}/\partial z$. Thus, if both the $Sc = 7$ and $Sc \sim 10^3$ mixing layers grow at the same rates, then to a first-order approximation, the profiles and evolutions of $\widetilde{E''}$ and $\widetilde{\epsilon''}$ must be the same. Accordingly, the profiles of $P^{\widetilde{m_1''^2}}$, $\widetilde{E''}$, and

$\widetilde{\epsilon}''$ from the $Sc = 7$ DNS are used as an ansatz to calculate the remaining unknown terms in (4.49).

Given the profiles of $P\widetilde{m}_1''^2$ from the DNS and the profiles of $\widetilde{m}_1''^2$ from the $Sc \sim 10^3$ experiments, the integrated dissipation profiles [see (4.48)] may be calculated. As expected, the molecular mixing rate during the early stages of the mixing layer is very small. Similar observations were made in high Schmidt number shear layer studies, where there is very little mixed fluid before the onset of three-dimensional, secondary-instabilities (Breidenthal 1981). For the early time development of the mixing layer ($\tau < 0.5$), the $Sc = 7$ and $Sc \sim 10^3$ cases exhibit similar integrated dissipation rates because the Reynolds number is small enough that turbulent fluctuations have yet to create sufficient surface area between pockets of unmixed fluid to allow significant rates of mixing to occur. However, once the mixing layer enters a nonlinear (or pre-turbulent) state, the dissipation rate increases and a difference between the $Sc = 7$ and $Sc \sim 10^3$ cases is observed. For all times $\tau > 0.5$, the $Sc = 7$ case has a higher dissipation rate. The dissipation term $D\widetilde{m}_1''^2$ is clearly a function of the Schmidt number and not the Reynolds number, as the mixing layers are essentially the same width.

Using the \widetilde{E}'' and $\widetilde{\epsilon}''$ profiles from the DNS, the final calibration of C_{m2} for the $Sc \sim 10^3$ case can be obtained using (4.49). As the dissipation rate for the $Sc \sim 10^3$ case is small for $\tau < 0.5$, the calibration in (4.49) is ill-posed as the denominator approaches zero. However, C_{m2} was calculated for later times ($\tau > 0.5$) and is shown in figure 4.49. While the calibration cannot be calculated directly for the initial low Reynolds number regime of mixing, it possible to postulate a low Reynolds number calibration. As observed in the $Sc = 7$ DNS and in the spectral-equilibrium model of Liu and Fox (2006), $C_{m2} \rightarrow 0$ as $Re_h \rightarrow 0$. Accordingly, C_{m2} was set to zero at $Re_h = 0$, which captures the dissipation term $D\widetilde{m}_1''^2 \rightarrow 0$ for small Reynolds numbers.

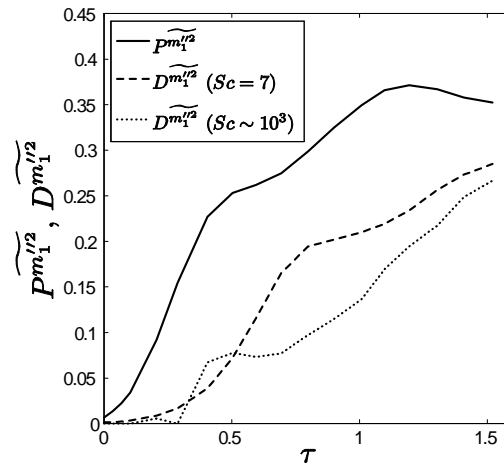


Figure 4.48 Evolution of the integrated production and dissipation profiles for the $Sc = 7$ and $Sc \sim 10^3$ cases.

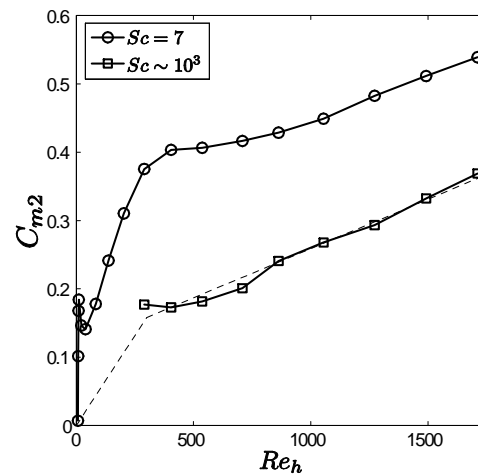


Figure 4.49 Comparison of C_{m2} calibration for the $Sc = 7$ and $Sc \sim 10^3$ cases. The approximate model for the $Sc \sim 10^3$ case is shown by the dashed line.

Comparison with the $Sc = 7$ calibration shows that C_{m2} for the large Schmidt number case shows the same increasing trend with Reynolds number; however the magnitude of C_{m2} is smaller for the range of Reynolds numbers examined. This is expected, as the dissipation rate of $\widetilde{m_1''^2}$ is shown to be lower for the $Sc \sim 10^3$ case in figure 4.48.

4.7.2 Comparison with experiment

The model calibrations presented in § 4.3 have been directly obtained from the DNS, and thus, have been used explicitly in the numerical tests in § 4.6. However, for the $Sc \sim 10^3$ case, approximations were required to obtain a calibration of C_{m2} . Thus, the evolution of C_{m2} shown in figure 4.49 has not been directly implemented in the current numerical algorithm. Rather, the calibration curve was fitted with a straight line over the range of Reynolds numbers and then forced to zero at $Re_h = 0$:

$$C_{m2} = \begin{cases} 0.000527 Re_h & Re_h \leq 300 \\ 0.1148 + 0.0001442 Re_h & Re_h > 300 \end{cases}, \quad (4.50)$$

which is shown in figure 4.49 by the dashed line.

The C_{m2} calibration in (4.50) has been tested using the current numerical implementation of the $\widetilde{E''}-\widetilde{\epsilon''}-\widetilde{m_1''^2}$ transport equations. For the same reasons discussed in § 4.7.1, the same initial profiles of \widetilde{m}_1 , $\widetilde{E''}$, and $\widetilde{\epsilon''}$ as used in the $Sc = 7$ case were used. However, the initial profiles of $\widetilde{m_1''^2}$ were taken from the experimental measurements in § 2.4. All of the Reynolds number-dependent model coefficients remained unchanged with the exception of C_{m2} . Accordingly, the same mixing layer growth was achieved as shown in § 4.6.2; however the degree of molecular mixing was reduced using the new C_{m2} calibration. A comparison of the molecular mixing parameter $\theta(z = 0)$ from the high Schmidt number model and the reacting flow measurements is shown in figure 4.50. The model and the experiment show favorable agreement,

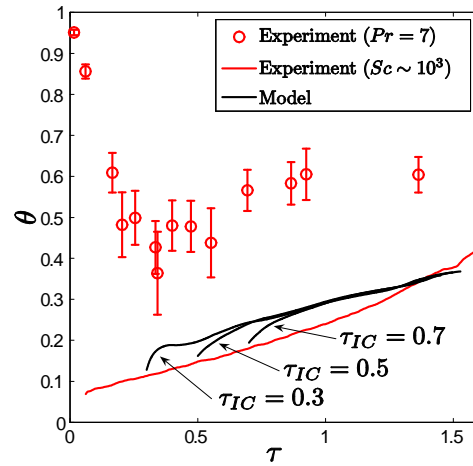


Figure 4.50 Comparison of $\theta(z = 0)$ from the model using the high Schmidt number calibration of C_{m2} and the $Pr = 7$ and $Sc \sim 10^3$ experiments.

despite the approximations required to generate the calibration in (4.50).

As shown from the previous results, a good indicator of the physical accuracy of a model is the ability to correctly predict the total amount of production and dissipation for a given transport equation. Accordingly, the evolution of the integrated dissipation profiles from figure 4.48 and the model are compared in figure 4.51. Again, the model is capable of capturing the evolution of the integrated dissipation rate. The discrepancy at early times ($\tau \approx 0.3$ – 0.6) is due to the required approximation of C_{m2} below $Re_h = 300$.

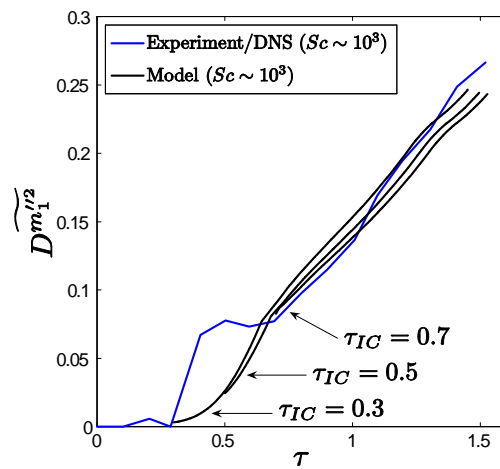


Figure 4.51 Comparison of the integrated dissipation rate profiles from the model and estimated integrals from figure 4.48.

5. CONCLUSIONS

5.1 Summary

This work combined experimental measurements, DNS, and the development of a three- or four-equation RANS model to examine the turbulent mixing dynamics of a small Atwood number Rayleigh–Taylor mixing layer at moderate and large Schmidt numbers. A summary of the significant accomplishments and conclusions from this work is given below.

1. A hot/cold water ($Pr \equiv Sc = 7$) arrangement of the Texas A&M Rayleigh–Taylor water channel and a high-resolution thermocouple system were used to make high-fidelity measurements of density statistics, the molecular mixing parameter $\theta(z = 0)$ (see § 2.3.2), probability density functions of the centerplane density fluctuations (see § 2.3.3), and density variance spectra (see § 2.3.4). A minimum value $\theta(z = 0) = 0.375 \pm 0.125$ was measured at $\tau \approx 0.35$ ($Re_h \approx 200$) and a late-time ($\tau = 1.36$) value $\theta(z = 0) = 0.6 \pm 0.05$ was also measured. A transition in θ was observed at $\tau \approx 0.35$ or $Re_h \approx 200$, where the laminar stirring motions of the mixing layer became more three-dimensional and θ changed from decreasing to increasing in time (see figure 2.3).
2. Experimental measurements of the PDF of the density fluctuations (see figure 2.4) on the centerplane of the mixing layer exhibited a bimodal shape at early times ($\tau < 0.8$), indicating that the two fluids in the layer exist in a ‘stirred’ state (*i.e.* as separate fluids), with little fluid existing in a ‘mixed’ state (*i.e.* molecularly mixed). After $\tau = 0.8$, the PDF is more complex, with an approximate combination of a bimodal distribution similar to the early-time PDF and a Gaussian distribution centered about $f_1 = 0.5$, indicating a greater production of molecularly-mixed fluid at later times. The symmetry of $P(f_1)$ also indicates

that the composition of mixed fluid on the centerplane is not biased to either the heavy or light fluid side.

3. A salt/fresh water arrangement in the water channel was used to study a diffusion-limited, chemically-reactive, $Sc \sim 10^3$ Rayleigh–Taylor mixing layer. Experimental diagnostics were developed and validated to measure the amount of chemical product formed within the mixing layer (see § 2.4.1–2.4.7). Measurements of the chemical product profiles and the equivalent product thickness P/h were obtained for various neutralization equivalence ratios φ_n (see § 2.4.5). For $\varphi_n \rightarrow 0$, the evolution of P/h was found to follow a similar nonlinear transition process to that of shear-driven mixing layers, where P/h is small at $Re_h \lesssim 200$. Once the mixing layer enters a nonlinear transitional regime, P/h begins to increase; however a final, late-time value of P/h was not observed for the facility-limited Reynolds number $Re_h \approx 3000$ or $\tau \approx 1.9$ (see figure 2.19).
4. Analysis techniques for the experimental data were developed to obtain the density variance $\overline{\rho^2}$ from the chemical product formation measurements (see § 2.4.9), and therefore the molecular mixing parameters θ and Θ . The first resolution-independent measurements of θ , Θ , and Ξ were reported for a $Sc \sim 10^3$ Rayleigh–Taylor mixing layer (see figures 2.24, 2.26 and 2.27). Similar to the early-time transition in P/h , both $\theta(z=0)$ and Θ demonstrated a transitional behavior at $Re_h \approx 200$, before which $\theta(z=0) \approx \Theta \approx 0.1$. After the transition to a more three-dimensional mixing layer, both $\theta(z=0)$ and Θ continued to increase (see figures 2.26 and 2.27), indicating that the mixing layer contained increasingly more mixed fluid with respect to the Reynolds number.
5. Comparison of the hot/cold ($Pr \equiv Sc = 7$) and salt/fresh ($Sc \sim 10^3$) water experiments with the $Sc = 0.7$ gas-phase experiments of Banerjee (2006) (see

figure 2.28) showed that the Schmidt number strongly influences the degree of molecular mixing at small and moderate Reynolds numbers. At later times, the dependence of $\theta(z = 0)$ on the Schmidt number persists, but is reduced at higher Reynolds numbers, where all Schmidt number experiments fall within $\theta(z = 0) = 0.5\text{--}0.7$.

6. To further examine the dynamics in a Rayleigh–Taylor mixing layer, a three-dimensional DNS model of the $Sc = 7$ water channel experiment was developed (see § 3.2). In addition, a methodology for implementing experimentally-measured density, interfacial, and velocity perturbations within the simulation was also developed (see Appendix D). This is the first reported DNS of a Rayleigh–Taylor mixing layer for $Sc > 1$, and late-time Reynolds numbers of $Re_h = 1712$ and $Re_\lambda^w \approx 95$ were achieved. Good agreement was demonstrated between the simulation and experimental measurements of h , $\theta(z = 0)$, $\overline{u_i^2}$, $E_w(k)$, and $E_\rho(k)$ (see § 3.4).
7. In addition to the comparison with experimental measurements, statistics quantifying the degree of molecular mixing were obtained from the DNS. The evolution of Θ , $\Xi(\varphi)$, and the PDF $P(f_1)$ were obtained. Comparison of $\Xi(\varphi \rightarrow 0)$ obtained from the $Sc = 7$ DNS with the $Sc \sim 10^3$ experiments indicates that the Schmidt number has a significant influence on the production of chemical product for all Reynolds numbers examined (see figure 3.23). At the latest times measured, $\Xi(\varphi \rightarrow 0)$ approaches the small Reynolds number limit of $\Xi(\varphi \rightarrow 0)$ measured in $Sc = 0.7$ shear-driven mixing layers.
8. Comparing the $Sc = 7$ DNS with the measurements of $P(f_1)$ from the $Pr = 7$ experiments (see figures 2.4 and 3.28), the same bimodal structure of $P(f_1)$ was observed for $\tau < 1$, with a more complex structure observed for $\tau \gtrsim 1$.

Measurements of $P(f_1)$ and the mean mixed fluid composition \bar{f}_1^m across the mixing layer from the DNS indicate that $P(f_1)$ has an approximate ‘tilted’ shape, where the mixed fluid contains more lighter fluid above the centerplane and more heavy fluid below the centerplane.

9. The DNS data set was also used to obtain budgets for the mean heavy fluid mass fraction, mean momentum, turbulent kinetic energy, turbulent kinetic energy dissipation rate, mass fraction variance, and mass fraction variance dissipation rate transport equations (see § 3.6.1–3.6.7). This work presents the first budgets of the $\bar{\epsilon}'$, $\widetilde{m_1''^2}$, and $\widetilde{\chi''}$ transport equations for this flow. The analysis has explicitly shown which terms are dominant and which have a negligible contribution to the overall dynamics: the shear-driven production terms and dilatational terms were shown to be negligible, whereas buoyancy and turbulent production terms were not. The evolution of the production-to-dissipation ratios for each transport equation were calculated, where the late time-values $P^{\widetilde{E''}}/D^{\widetilde{E''}} \approx 2$, $P^{\bar{\epsilon}'}/D^{\bar{\epsilon}'} \approx 1.1$, $P^{\widetilde{m_1''^2}}/D^{\widetilde{m_1''^2}} \approx 1.2$, and $P^{\widetilde{\chi''}}/D^{\widetilde{\chi''}} \approx 1$ were obtained (see figures 3.51, 3.59, 3.67, and 3.74).
10. From the *a priori* budget analysis, the pressure transport of $\widetilde{E''}$ was found to be non-negligible and complex in behavior (see figures 3.46 and 3.47). A bifurcation point was observed (see figure 3.48) at the onset of nonlinear, secondary instabilities, where the pressure fluctuations transported $\widetilde{E''}$ in a down-gradient manner, away from the centerplane at early times ($\tau \leq 0.29$). After this transition point ($\tau > 0.29$), the pressure transport developed a more complex profile that opposed the down-gradient turbulent flux of $\widetilde{E''}$ within the turbulent core of the mixing layer ($|z/h| < 0.5$), but augmented the turbulent flux of $\widetilde{E''}$ outside the boundaries of the layer ($|z/h| > 0.5$).

11. Budgets of the transport equations taken from the DNS were compared *a priori* with their respective gradient-diffusion and scale-similarity closures to test the predictive accuracy of RANS-type models for turbulent Rayleigh–Taylor mixing (see § 4.3). The Boussinesq eddy viscosity model was found to predict the overall shape of the diagonal Reynolds stress components; however, the intrinsic assumption of isotropy prevented the model from accurately predicting the magnitudes of the stresses (see § 4.3.2). Furthermore, the contribution of the Reynolds stress tensor to the mean momentum equations was negligible for this small Atwood number mixing layer.

12. The *a priori* comparison of turbulent fluxes with their respective gradient-diffusion closures showed that these closures captured the turbulent redistribution in the different transport equations (see § 4.3.3). From this comparison, the turbulent Schmidt numbers were calibrated by minimizing the L_2 norm difference between the DNS and model profiles. The values obtained were lower than the values implemented in ‘standard’ \widetilde{E}'' - $\widetilde{\epsilon}''$ models for Rayleigh–Taylor mixing, where late-time values $\sigma_\rho \equiv \sigma_m = 0.09$, $\sigma_k = 0.11$, $\sigma_\epsilon = 0.15$, $\sigma_{m2} = 0.19$, and $\sigma_\chi = 0.18$ were obtained.

13. Calibrations of the scale-similarity models used to close terms in the $\overline{\epsilon'}$, $\widetilde{m_1''^2}$, and $\widetilde{\chi''}$ transport equations were examined *a priori* (see § 4.3.5). The calibration of the buoyancy production of $\overline{\epsilon'}$ resulted in a model parameter $C_{\epsilon 0} = 1.43$ at late time, which is larger than the typically-reported value $C_{\epsilon 0} \approx 0.9$. Similarly, the calibration of the turbulent destruction model parameter $C_{\epsilon 2} = 2.26$ was also larger than the canonical value $C_{\epsilon 2} = 1.92$; however, this parameter was still changing at the end of the DNS (see figure 4.21). The scale-similarity closures in the $\widetilde{m_1''^2}$ and $\widetilde{\chi''}$ transport equations also exhibited good agreement with the

DNS; however, the calibrated parameters also exhibited a similar low Reynolds number dependence as C_{e0} and C_{e2} . At late times ($\tau \geq 1.3$ or $Re_h \geq 1200$), the calibrated parameter corresponding to the turbulent destruction of $\widetilde{m_1''^2}$ approached the expected high-Reynolds number value $C_{m2} = 0.5$ (see figure 4.29).

14. The parameter calibrations obtained from the *a priori* analysis were validated by an implementation of the modeled transport equations in a one-dimensional numerical code (see § 4.4). *A posteriori* comparisons of the model predictions with experimental measurements and DNS showed good agreement when the Reynolds number-dependent parameters were used (see § 4.6). The model was able to capture the early-time, low-Reynolds number dynamics of a transitional mixing layer, as shown in the comparison of the DNS and model production-to-dissipation ratios in figures 4.44 and 4.45. When only the late-time parameters were used, the model showed only fair agreement with the DNS and experiment, and was not able to capture the early-time dynamics.
15. A combination of high Schmidt number measurements of \bar{f}_1 and $\overline{f_1'^2}$ with the DNS transport equation budgets were used to calibrate C_{m2} for the $Sc \sim 10^3$ case [see (4.50)]. The calibration of C_{m2} was found to be phenomenologically similar to the $Sc = 7$ calibration, but lower in magnitude (see figure 4.49). Using the parameters from the $Sc = 7$ calibration along with the high Schmidt number C_{m2} calibration, the model was able to also reproduce the evolution of $\theta(z = 0)$ measured in the experiment (see figure 4.50).

5.2 Future Work

The future implications for this work are listed below.

1. The measurements of the equivalent product thickness P/h and the molecular mixing parameters $\theta(z = 0)$ and Θ from the $Sc \sim 10^3$ experiments have yet to reach their respective late-time asymptotic values by $Re_h \approx 3000$. A larger facility, approximately 70 cm in height, could achieve $Re_h > 12000$, and likely observe late-time, entrainment-limited dynamics.
2. A second method of measuring the degree of mixing in a high Schmidt number mixing layer may be achieved by using the existing laser system in conjunction with a fluorescing dye. Calibrated planar-laser induced fluorescence techniques may be applied directly to the water channel experiments to measure instantaneous dye concentrations, which in turn may be related to the local volume fraction of the fluid containing the dye. However, this technique is not free of resolution requirements. The Batchelor scale in the large Schmidt number experiments is approximately $\eta_B \approx 0.15 \mu\text{m}$ at $Re_h \approx 12000$, which must be resolved by the optical measurement system. In addition, such techniques are more sensitive to experimental errors associated with the index of refraction difference between the salt and fresh water, as opposed to the reacting flow measurements presented in § 2.4. Thus, care must be taken to account for index of refraction differences.
3. The DNS of the water channel experiment was limited to the $Sc = 7$ case, and a DNS of the large Schmidt number case will not be feasible in the immediate future. However, relatively recent subgrid-scale models have been shown to capture the physics of Schmidt number-dependent subgrid-scale mixing (Pullin

2000; Burton 2008). These appear to be the only approaches presently available for simulating the high Schmidt number experiments. Subgrid-scale models for active scalars, as in Rayleigh–Taylor mixing layers, may be calibrated using the experimental results in § 2.

4. A small difference in the degree of molecular mixing on the centerplane of the mixing layer was observed between the DNS and $Sc = 7$ water channel experiment. Great care has been taken to implement experimentally-measured initial conditions; however, a complete understanding of the onset of secondary instabilities and turbulent dynamics with respect to the spectral content of the initial conditions is not fully understood. To obtain better agreement between the DNS and experiment, a more thorough understanding of the effects of initial spectral content on the time or Reynolds number at which nonlinear dynamics become significant is needed.
5. A DNS of the $Sc = 7$ water channel experiment was used to calibrate model parameters for a variety of transport equations in § 4.3. It was shown that some of the parameters exhibited low- and moderate-Reynolds number dependence. As this was the first work to calibrate the transport equations directly from a DNS, it remains to be seen how other physical parameters affect either the model calibrations or their late-time values. As an extension to this work, DNS with different Atwood numbers, Schmidt numbers, and initial conditions should be performed to fully-understand the Reynolds number dynamics and applicability of RANS-type models to Rayleigh–Taylor mixing.
6. As a second-order extension to the transport budget analysis and model calibration, additional closures and transport equations could be examined. An advanced formulation of the Reynolds stress tensor (algebraic or nonlinear)

should produce better agreement with the anisotropy observed within the mixing layer. Given an improved model for the Reynolds stress tensor, a form of the generalized gradient-diffusion hypothesis might yield even better correlation between the DNS and the model for the turbulent fluxes. With respect to the unresolved pressure transport closure, a derivation and analysis of the pressure transport equation may yield insight into closure models that could capture the complex physics of $\overline{p'w''}$. Finally, the full Reynolds stress transport equations should be considered for analysis and modeling due to the ability of such models to capture anisotropic and low Reynolds number effects.

REFERENCES

- Adkins, J. F., McIntyre, K. & Schrag, D. P. 2002 The salinity, temperature, and $\delta^{18}\text{O}$ of the glacial deep ocean. *Science* **298**, 1769–1773.
- Andrews, M. J. 1984 The k - ϵ model applied to the development of Rayleigh–Taylor instability. Phoenix Demonstration Report PDF/CFDU IC/13.
- Andrews, M. J. 1986 *Turbulent Mixing by Rayleigh–Taylor Instability*. Ph.D. dissertation. Imperial College of Science and Technology.
- Andrews, M. J. & Spalding D. B. 1990 A simple experiment to investigate two-dimensional mixing by Rayleigh–Taylor instability. *Phys. Fluids A* **2**, 922–927.
- Anuchina, N. N., Kucherenko, Y. A., Neuvazhaev, V. E., Ogibina, V. N., Shibarshov, L. I. & Yakovlev, V. G. 1978 Turbulent mixing at an accelerating interface between liquids of different densities. *Izv. Akad Nauk. SSSR, Mekh. Zhidk. Gaza* **6**, 157–160.
- Atzeni, S. & Meyer-ter-Vehn, J. 2004 *The Physics of Inertial Fusion: Beam Plasma Interaction, Hydrodynamics, Hot Dense Matter*, International Series of Monographs on Physics Vol. 125. Oxford University Press.
- Atzeni, S., Schiavi, A., Califano, F., Cattani, F., Cornolti, F., Del Sarto, D., Liseykina, T. V., Macchi, A. & Pegoraro, F. 2005 Fluid and kinetic simulation of inertial confinement fusion plasmas. *Comput. Physics Commun.* **169**, 153–159.
- Banerjee, A. 2006 *Statistically Steady Measurements of Rayleigh–Taylor Mixing in a Gas Channel*. Ph.D. dissertation, Texas A&M University.
- Banerjee, A. & Andrews, M. J. 2006 Statistically steady measurements of Rayleigh–Taylor mixing in a gas channel. *Phys. Fluids* **18**, 035107.

- Banerjee, A., Kraft, W. & Andrews, M. J. 2008 Detailed measurements of a Rayleigh–Taylor mixing layer from small to intermediate Atwood numbers. (*submitted*).
- Batchelor, G. K. 1949 Diffusion in a field of homogeneous turbulence. I. Eulerian analysis. *Aust. J. Sci. Res. A* **2**, 437–450.
- Batchelor, G. K. 1953 *The Theory of Homogenous Turbulence*. Cambridge University Press, Cambridge, U.K.
- Batt, R. G. 1977 Turbulent mixing of passive and chemically reacting species in a low-speed shear layer. *J. Fluid Mech.* **82**, 53–95.
- Benedict, L. H. & Gould, R. D. 1996 Towards better uncertainty estimates for turbulence statistics. *Exp. Fluids* **22**, 129–136.
- Besnard, D., Harlow, F. H., Rauenzahn, R. M. & Zemach, C. 1992 Turbulence transport equations for variable-density turbulence and their relationship to two-field models. Los Alamos National Laboratory Report LA-UR-12303-MS.
- Betti, R., Umansky, M., Lobatchev, V., Goncharov, V. N. & McCrory, R. L. 2001 Hot-spot dynamics and deceleration-phase Rayleigh–Taylor instability of imploding inertial confinement fusion capsules. *Phys. Plasmas* **8**, 5257–5267.
- Bishop, E. (editor) 1972 *Indicators*. International Series of Monographs in Analytical Chemistry: Indicators. Pergamon Press, New York.
- Boris, J. P., Grinstein, F. F., Oran, E. S. & Kolbe, R. L. 1992 New insights into large eddy simulation. *Fluid Dyn. Res.* **10**, 199–228.
- Boussinesq, J. 1877 Théorie de l'écoulement tourbillant. *Mem. Presentes par Divers Savants Acad. Sci. Inst. Fr.* **23**, 31–64.

- Boussinesq, J. 1903 *Theorie analytique de la chaleur* Vol. 2. Gauthier-Vellars, Paris, France.
- Bradshaw, P. 1994 Turbulence - the chief outstanding difficulty of our subject. *Exp. Fluids* **16**, 203–216.
- Breidenthal, R. 1981 Structure in turbulent mixing layers and wakes using a chemical reaction. *J. Fluid Mech.* **109**, 1–24.
- Breidenthal, R. E. 1979 *A Chemically Reacting Shear Layer*. Ph.D. dissertation, California Institute of Technology.
- Brinkman, K. W., Calhoun, W. H. & Dash, S. M. 2007 Scalar fluctuation modeling for high-speed aeropropulsive flows. *AIAA J.* **45**, 1036–1046.
- Britter, R. E. & Hanna, S. R. 2003 Flow and dispersion in urban areas. *Annu. Rev. Fluid Mech.* **35**, 469–96.
- Browand, F. K. & Weidman, P. D. 1976 Large scales in the developing mixing layer. *J. Fluid Mech.* **76**, 127–144.
- Brown, G. L. & Roshko, A. 1974 On density effects and large structure in turbulent mixing layers. *J. Fluid Mech.* **64**, 775–816.
- Burton, G. 2008 The nonlinear LES (nLES) method applied to $Sc \sim 1$ and $Sc \gg 1$ passive scalar mixing. *Phys. Fluids* **20**, 035103.
- Cabot, W. 2006 Comparison of two- and three-dimensional simulations of miscible Rayleigh–Taylor instability. *Phys. Fluids* **18**, 045101.
- Cabot, W. H. & Cook, A. W. 2006 Reynolds number effects on Rayleigh–Taylor instability with possible implications for type-Ia supernovae. *Nat. Phys.* **2**, 562–568.

- Cabot, W. H., Schilling, O. & Zhou, Y. 2004 Influence of subgrid scales on resolvable turbulence and mixing in Rayleigh–Taylor flow. *Phys. Fluids* **16**, 495–508.
- Calder, A. C., Fryxell, B., Plewa, T., Rosner, R., Dursi, L. J., Weirs, V. G., Dupont, T., Robey, H. F., Kane, J. O., Remington, B. A., Drake, R. P., Dimonte, G., Zingale, M., Timmes, F. X., Olson, K., Ricker, P., MacNeice, P. & Tufo, H. M. 2002 On validating an astrophysical simulation code. *Astro. J. Supp. Ser.* **143**, 201–229.
- Caldin, E. 1964 *Fast Reactions in Solution*. John Wiley & Sons. New York.
- Canuto, C. G., Hussaini, M. Y., Quarteroni, A. & Zang, T. A. 2007 *Spectral Methods: Evolution to Complex Geometries and Applications to Fluid Dynamics*. Springer-Verlag, New York.
- Chandra, L. & Grötzbach, G. 2007 Analysis and modeling of the turbulent diffusion of turbulent kinetic energy in natural convection. *Flow, Turb. Combust.* **79**, 133–154.
- Chandrasekhar, S. 1961 *Hydrodynamic and Hydromagnetic Stability*. Dover, New York.
- Chassaing, P. 2001 The modeling of variable density turbulent flows. *Annu. Rev. Fluid Mech.* **66**, 293–332.
- Chassaing, P., Antonia, R. A., Anselmet, F., Joly, L. & Sarkar, S. 2002 *Variable Density Fluid Turbulence*, Fluid Mechanics and its Applications Vol. 69. Kluwer Academic, Boston.
- Chen, C., Riley, J. J. & McMurtry, P. A. 1991 A study of Favre averaging in turbulent flows with chemical reaction. *Comb. Flames* **87**, 257–277.
- Chidambaram, N., Dash, S. M. & Kenzakowski, D. C. 2001 Scalar variance transport in the turbulence modeling of propulsive jets. *J. Propul. Power* **17**, 79–84.

- Chiravalle, V. P. 2006 The k - L turbulence model for describing buoyancy-driven fluid instabilities. *Las. Part. Beams* **24**, 381–394.
- Cleveland, W. S. 1979 Robust locally weighted regression and smoothing scatterplots. *J. Amer. Statist. Assoc.* **74**, 829–836.
- Cleveland, W. S. & Devlin, S. J. 1988 Locally weighted regression: An approach to regression analysis by local fitting. *J. Amer. Statist. Assoc.* **83**, 596–610.
- Colgate, S. A. & White, R. H. 1966 The hydrodynamic behavior of supernova explosions. *Astrophys. J.* **143**, 626–681.
- Cook, A. W. & Dimotakis, P. E. 2001 Transition stages of Rayleigh–Taylor instability between miscible fluids. *J. Fluid Mech.* **443**, 69–99. Corrigendum. *J. Fluid Mech.* **457**, 410–411 (2002).
- Cook, A. W. & Zhou, Y. 2002 Energy transfer in Rayleigh–Taylor instability. *Phys. Rev E* **66**, 026312.
- Cook, A. W., Cabot, W. & Miller, P. L. 2004 The mixing transition in Rayleigh–Taylor instability. *J. Fluid Mech.* **511**, 333–362.
- Corriveau, A. F. & Baines, W. D. 1993 Diffusive mixing in turbulent jets as revealed by a pH indicator. *Exp. Fluids* **16**, 129–136.
- Corrsin, S. 1951 On the spectrum of isotropic temperature fluctuations in isotropic turbulence. *J. Appl. Phys.* **22**, 469–473
- Cui, A. Q. & Street, R. L. 2004 Large-eddy simulation of coastal upwelling flow. *Envir. Fluid Mech.* **4**, 197–223.
- Dahm, W. J. A. 1985 *Experiments on Entrainment, Mixing and Chemical Reactions in*

- Turbulent Jets at Large Schmidt Number*. Ph.D. dissertation, California Institute of Technology.
- Daly, B. J. 1967 Numerical study of two fluid Rayleigh–Taylor instability. *Phys. Fluids* **10**, 297–307.
- Daly, B. J. & Harlow, F. H. 1970 Transport equations in turbulence. *Phys. Fluids* **13**, 2634–2649.
- Dalziel, S. B., Linden, P. F. & Youngs, D. L. 1999 Self-similarity and internal structure of turbulence induced by Rayleigh–Taylor instability. *J. Fluid Mech.* **399**, 1–48.
- Dankwerts, P. V. 1952 The definition and measurement of some characteristics of mixtures. *Appl. Sci. Res.* **3**, 279–296.
- Davidson, L. 1990 Second-order corrections of the k - ε model to account for non-isotropic effects due to buoyancy. *Int. J. Heat Mass Transfer* **33**, 2599–2608.
- Deardorff, J. W. 1966 The counter-gradient heat flux in the lower atmosphere and in the laboratory. *J. Atmos. Sci.* **23**, 503–506.
- Deardorff, J. W. 1972 Theoretical expression for the countergradient vertical heat flux. *J. Geophys. Res.* **77**, 5900–5904.
- Desai, M. A. & Vadgama, P. 1991 Estimation of effective diffusion coefficients of model solutes through gastric mucus: assessment of a diffusion chamber technique based upon spectrophotometric analysis. *Analyst* **116**, 1113–1116.
- Dimonte, G. 2000 Spanwise homogeneous buoyancy-drag model for Rayleigh–Taylor mixing and experimental evaluation. *Phys. Plasmas* **7**, 2255–2269.

- Dimonte, G. & Schneider, M. 2000 Density ratio dependence of Rayleigh–Taylor mixing for sustained and impulsive acceleration histories. *Phys. Fluids* **12**, 304–321.
- Dimonte, G. & Tipton, R. 2006 *K-L* turbulent model for the self-similar growth of the Rayleigh–Taylor and Richtmyer–Meshkov instabilities. *Phys. Fluids* **18**, 085101.
- Dimonte, G., Ramaprabhu, P., Youngs, D. L., Andrews, M. J. & Rosner, R. 2005 Recent advances in the turbulent Rayleigh–Taylor instability. *Phys. Plasmas* **12**, 056301.
- Dimonte, G., Youngs, D. L., Dimitis, A., Weber, S., Marinak, M., Wunsch, S., Garasi, C., Robinson, A., Andrews, M. J., Ramaprabhu, P., Calder, A. C., Fryxell, B., Biello, J., Dursi, L., MacNeice, P., Olson, K., Ricker, P., Rosner, R., Timmes, F., Tufo, H., Young, Y.-N. & Zingale, M. 2004 A comparative study of the turbulent Rayleigh–Taylor (RT) instability using high-resolution 3D numerical simulations: The Alpha-Group collaboration. *Phys. Fluids* **16**, 1668–1693.
- Dimotakis, P. E. 2000 The mixing transition in turbulent flows. *J. Fluid Mech.* **409**, 69–98.
- Dimotakis, P. E. 2005 Turbulent mixing. *Annu. Rev. Fluid Mech.* **37**, 329–356.
- Dittrich, T. R., Hammel, B. A., Keane, C. J., McEachern, R., Turner, R. E., Haan, S. W. & Suter, L. J. 1994 Diagnosis of pusher-fuel mix in indirectly driven Nova implosions. *Phys. Rev. Lett.* **73**, 2324–2327.
- Drazin, P. G. & Reid, W. H. 2004 *Hydrodynamic Stability*, 2nd ed. Cambridge University Press, New York.
- Ebbing, D. D. 1993 *General Chemistry*, 4th ed. Houghton Mifflin, Boston.
- Ferziger, J. H. & Perić, M. 2002 *Computational Methods for Fluid Dynamics*, 3rd ed. Springer-Verlag, New York.

- Freund, R. & Nachtigal, N. 1991 QMR: A quasi-minimal residual method for non-Hermitian linear systems. *Numer. Math.* **60**, 315–339.
- Frieler, C. E. 1992 *Mixing and Reaction in the Subsonic Two-Dimensional Turbulent Free Shear Layer*. Ph.D. dissertation, California Institute of Technology.
- Fox, R. O. 2003 *Computational Models for Turbulent Reacting Flows*. Cambridge University Press, New York.
- Gauthier, S. & Bonnet, M. 1990 A k - ϵ model for the turbulent mixing in shock-tube flows induced by Rayleigh–Taylor instability. *Phys. Fluids A* **2**, 1685–1694.
- Gerz, T. & Schumann, U. 1996 A possible explanation of countergradient fluxes in homogeneous turbulence. *Theoret. Comput. Fluid Dyn.* **8**, 169–181.
- Green, F. J. 1990 *The Sigma-Aldrich Handbook of Stains, Dyes, and Indicators*. Aldrich Chemical Co, Milwaukee.
- Grégoire, O. & Souffland, D. 1999 Simulations of compressible mixing flows using a second order turbulence model. *Proc. of the 7th International Workshop on the Physics of Compressible Turbulent Mixing*, July 1999, 252–258.
- Grinstein, F. F., Margolin, L. G. & Rider, W. G. (editors) 2007 *Implicit Large Eddy Simulation: Computing Turbulent Flow Dynamics*. Cambridge University Press, New York.
- Haan, S. W. 1989 Onset of nonlinear saturation for Rayleigh–Taylor growth in the presence of a full spectrum of modes. *Phys. Rev. A* **39**, 5812–5825.
- Haan, S. W. 1991 Weakly nonlinear hydrodynamic instabilities in inertial fusion. *Phys. Fluids B* **3**, 2349–2355.

- Hanjalić, K. 2002 One-Point Closure Models for Buoyancy-Driven Turbulent Flows. *Annu. Rev. Fluid Mech.* **34**, 321–347.
- Harris, D. C. 2003 *Quantitative Chemical Analysis*, 6th ed. W. H. Freeman and Company, New York.
- Hecht, E. 2002 *Optics*, 4th ed. Addison Wesley, New York.
- Helmholtz, H. L. F. 1868 Über discontinuierliche Flüssigkeits-Bewegungen. *Monatsberichte der Königlich-Preussische Akademie der Wissenschaften zu Berlin* **23**, 215.
- Hickel, S., Adams, N. A. & Mansour, N. N. 2007 Implicit subgrid-scale modeling for large-eddy simulation of passive scalar mixing. *Phys. Fluids* **19**, 095102.
- Jakirlić, S. & Hanjalić, K. 2002 A new approach to modelling near-wall turbulence energy and stress dissipation. *J. Fluid Mech.* **459**, 139–166.
- Jones, W. P. & Launder, B. E. 1972 The prediction of laminarization with a two-equation model of turbulence. *Int. J. Heat and Mass Transfer* **15**, 301–314. Corrigendum, *Int. J. Heat and Mass Transfer* **16**, 2128 (1973).
- Joseph, D. D. 1990 Fluid dynamics of two miscible liquids with diffusion and gradient stress. *Eur. J. Mech. B* **9**, 565–596.
- Kadau, K., Rosenblatt, C., Barber, J. L., Germann, T. C., Huang, Z., Carlès, P. & Alder, B. J. 2007 The importance of fluctuations in fluid mixing. *Proc. Nat. Acad. Sci.* **104**, 7741–7745.
- Karasso, P. S. & Mungal, M. G. 1996 Scalar mixing and reaction in plane liquid shear layers. *J. Fluid Mech.* **323**, 23–63.

- Kastrinakis, E. G. & Nychas, S. G. 1998 Mixing at high Schmidt numbers in the near wake of a circular cylinder. *Chem. Engr. Sci.* **53**, 3977–3989.
- Kawamura, H. & Kawashima N. 1995 A proposal of $k\text{-}\tilde{\epsilon}$ model with relevance to the near-wall turbulence. In *Turbulence, Heat and Mass Transfer* (ed. K. Hanjalić & J. C. F. Pereira), vol. 1, 197–202. Begell House, Redding, CT.
- Keane, C. J., Cook, R. C., Dittrich, T. R., Hammel, B. A., Levedahl, W. K., Landen, O. L., Langer, S., Munro, D. H. & Scott, H. A. 1995a Diagnosis of pusher-fuel mix in spherical implosions using x-ray spectroscopy. *Rev. Sci. Instr.* **66**, 689–696.
- Keane, C. J., Pollak, G. W., Cook, R. C., Dittrich, T. R., Hammel, B. A., Landen, O. L., Langer, S. H., Levedahl, W. K., Munro, D. H., Scott, H. A. & Zimmerman, G. B. 1995b x-Ray Spectroscopic Diagnostics of Mix in High Growth Factor Spherical Implosions. *J. Quant. Spectr. Rad. Transfer* **54**, 207–220.
- Kelvin, Lord 1871 Hydrokinetic solutions and observations. *Philos. Mag.* **42**, 362–377.
- Kolthoff, I. M. 1937 *Acid-Base Indicators*. Macmillan, New York.
- Konrad, J. H. 1977 *An Experimental Investigation of Mixing in Two-Dimensional Turbulent Shear Flows with Applications to Diffusion-Limited Chemical Reactions*. Ph.D. dissertation, California Institute of Technology.
- Koochesfahani, M. M. 1984 *Experiments on Turbulent Mixing and Chemical Reactions in a Liquid Mixing Layer*. Ph.D. dissertation, California Institute of Technology.
- Koochesfahani, M. M. & Dimotakis, P. E. 1986 Mixing and chemical reactions in a turbulent liquid mixing layer. *J. Fluid Mech.* **170**, 83–112.

- Koop, G. K. 1976 *Instability and Turbulence in a Stratified Shear Layer*. Ph.D. dissertation. University of Southern California.
- Kukulka, D. J. 1981 *Thermodynamic and Transport Properties of Pure and Saline Water*. M.S. thesis. State University of New York at Buffalo.
- Laney, D., Bremer, P.-T., Mascarenhas, A., Miller, P. & Pascucci, V. 2006 Understanding the structure of the turbulent mixing layer in hydrodynamic instabilities. *IEEE Trans. Vis. Comp. Graph.* **12**, 1053–1060.
- Launder, B. E. & Sharma, B. I. 1974 Application of the energy dissipation model of turbulence to the calculation of flow near a spinning disc. *Let. Heat and Mass Trans.* **1**, 131–138.
- Lele, S. K. 1992 Compact finite difference schemes with spectral-like resolution. *J. Comput. Phys.* **103**, 16–42
- Li, C. K., Séguin, F. H., Frenje, J. A., Kurebayashi, S., Petrasso, R. D., Meyerhofer, D. D., Soures, J. M., Delettrez, J. A., Glebov, V. Yu., Radha, P. B., Regan, S. P., Roberts, S., Sangster, T. C. & Stoeckl, C. 2002 Effects of fuel-shell mix upon direct-drive, spherical implosions on OMEGA. *Phys. Rev. Lett.* **89**, 165002.
- Lide, D. R. (editor) 2006 *CRC Handbook of Chemistry and Physics*, 87th ed. CRC Press, Cleveland, OH.
- Linden P. F. & Redondo, J. M. 1991 Molecular mixing in Rayleigh–Taylor instability. Part I: Global mixing. *Phys. Fluids A* **3**, 1269–1277.
- Linden, P. F., Redondo, J. M. & Youngs, D. L. 1994 Molecular mixing in Rayleigh–Taylor instability. *J. Fluid Mech.* **265**, 97–124.

- Lindl, J. 1995 Development of the indirect-drive approach to inertial confinement fusion and the target physics basis for ignition and gain. *Phys. Plasmas* **2**, 3933–4024.
- Lindl, J. D. 1998 *Inertial Confinement Fusion: The Quest for Ignition and Energy Gain Using Indirect Drive*. Springer-Verlag, New York.
- Ling, S. C. & Huang, T. T. 1970 Decay of weak turbulence. *Phys. Fluids* **13**, 2912–2924.
- Liu, Y. & Fox, R. O. 2006 CFD predictions for chemical processing in a confined impinging-jets reactor. *AIChE J.* **52**, 731–744.
- Livescu, D. & Ristorcelli, J. R. 2007 Buoyancy-driven variable-density turbulence. *J. Fluid Mech.* **591**, 43–71.
- Lumley, J. L. 1978 Computational modeling of turbulent flows. *Adv. Appl. Mech.* **18**, 123–176.
- Mantel, T. & Borghi, R. 1994 A new model of premixed wrinkled flame propagation based on a scalar dissipation equation. *Comb. Flame* **96**, 443–457.
- Marmottant, P. H. & Villermaux, E. 2004 On spray formation. *J. Fluid Mech.* **498**, 73–111.
- Mellado, J. P., Sarkar, S. & Zhou, Y. 2005 Large-eddy simulation of Rayleigh–Taylor turbulence with compressible miscible fluids. *Phys. Fluids* **17**, 076101.
- Meshkov, E. E. 1969 Instability of the interface of two gases accelerated by a shock wave. *Sov. Fluid Dyn.* **4**, 101–104.
- Meyer, T. R., Dutton, J. C. & Lucht R. P. 2006 Coherent structures and turbulent molecular mixing in gaseous planar shear layers. *J. Fluid Mech.* **558**, 179–205.
- Mills, A. F. 1999 *Heat Transfer*. Prentice Hall, Upper Saddle River, NJ.

- Molchanov, O. A. 2004 On the origin of low- and middle-latitude ionospheric turbulence. *Phys. Chem. Earth* **29**, 559–567.
- Mueschke, N. J. & Andrews, M. J. 2006 Investigation of scalar measurement error in diffusion and mixing processes. *Exp. Fluids* **40**, 165–175; Erratum. *Exp. Fluids* **40**, 176 (2006).
- Mueschke, N. J., Andrews, M. J. & Schilling O. 2006 Experimental characterization of initial conditions and spatio-temporal evolution of a small Atwood Rayleigh–Taylor mixing layer. *J. Fluid Mech.* **567**, 27–63.
- Mungal, M. G. & Dimotakis, P. E. 1984 Mixing and combustion with low heat release in a turbulent mixing layer. *J. Fluid Mech.* **148**, 349–382.
- Mungal, M. G. & Frieler, C. 1988 The effects of Damkohler number in a turbulent shear layer. *AIAA J.* **20**, 1418–1423.
- Mura, A. & Borghi, R. 2003 Towards an extended scalar dissipation equation for turbulent premixed combustion. *Comb. Flame* **133**, 193–196.
- Mura, A., Robin, V. & Champion, M. 2007 Modeling of scalar dissipation in partially premixed turbulent flames. *Comb. Flame* **149**, 217–224.
- Nakai, S. & Mima, K. 2004 Laser driven inertial fusion energy: present and prospective. *Rep. Prog. Phys.* **67**, 321–349.
- Nakai, S. & Takabe, H. 1996 Principles of inertial confinement fusion—physics of implosion and the concept of inertial fusion energy. *Rep. Prog. Phys.* **59**, 1071–1131.
- Ofer, D., Alon, U., Shvarts, D., McCrory, R. L. & Verdon, C. P. 1996 Modal model for the nonlinear multimode Rayleigh–Taylor instability. *Phys. Plasmas* **3**, 3073–3090.

- Orszag, S. A., Staroselsky, I. Flannery, W. S. & Zhang, Y. 1996 Introduction to renormalization group modeling of turbulence. In Gatski, T. B., Hussaini, M. Y. & Lumley, J. L. (editors) *Simulation and Modeling of Turbulent Flows*. Oxford University Press, New York.
- Pfalzner, S. 2006 *An Introduction to Inertial Confinement Fusion*, Series in Plasma Physics. CRC Press, New York.
- Poinsot, T. & Veynante, D. 2005 *Theoretical and Numerical Combustion*, 2nd ed. R. T. Edwards, Philadelphia.
- Pope, S. B. 2000 *Turbulent Flows*. Cambridge University Press, New York.
- Press, W. H., Teukolsky, S. A., Vetterling, W. T. & Flannery, B. P. 2002 *Numerical Recipes in C: The Art of Scientific Computing*, 2nd ed. Cambridge University Press, New York.
- Pruett, D. C & Adams, N. A. 2000 *A priori* analyses of three subgrid-scale models for one-parameter families of filters. *Phys. Fluids* **12**, 1133–1142.
- Pullin, D. I. 2000 A vortex-based model for the subgrid flux of a passive scalar. *Phys. Fluids* **12**, 2311–2319.
- Radha, P. B., Delettrez, J., Epstein, R., Glebov, V. Yu., Keck, R., McCrory, R. L., McKenty, P., Meyerhofer, D. D., Marshall, F., Regan, S. P., Roberts, S., Sangster, T. C., Seka, W., Skupsky, S., Smalyuk, V., Sorce, C., Stoeckl, C., Soures, J., Town, R. P. J., Yaakobi, B., Frenje, J., Li, C. K., Petrasso, R., Seguin, F., Fletcher, K., Padalino, S., Freeman, C., Izumi, N., Lerche, R. & Phillips, T. W. 2002 Inference of mix in direct-drive implosions on OMEGA. *Phys. Plasmas* **9**, 2208–2213.

- Ramaprabhu, P. 2003 *On the Dynamics of Rayleigh–Taylor Mixing*. Ph.D. dissertation. Texas A&M University.
- Ramaprabhu, P. & Andrews, M. J. 2004a Experimental investigation of Rayleigh–Taylor mixing at small Atwood numbers. *J. Fluid Mech.* **502**, 233–271.
- Ramaprabhu, P. & Andrews, M. J. 2004b On the initialization of Rayleigh–Taylor simulations. *Phys. Fluids* **16**, L59–L62.
- Ramaprabhu, P., Dimonte, G. & Andrews, M. J. 2005 A numerical study of the influence of initial perturbations on the turbulent Rayleigh–Taylor instability. *J. Fluid Mech.* **536**, 285–319.
- Rayleigh, Lord 1884 Investigation of the equilibrium of an incompressible heavy fluid of variable density. *Proc. London Math. Soc.* **14**, 170–177.
- Read, K. I. 1984 Experimental investigation of turbulent mixing by Rayleigh–Taylor instability. *Physica D* **12**, 45–58.
- Richtmyer, R. D. 1960 Taylor instability in shock acceleration of compressible fluids. *Commun. Pure Appl. Math.* **13**, 297–319.
- Rikanati, A., Oron, D., Alon, U. & Shvarts, D. 2000 Statistical mechanics merger model for hydrodynamic instabilities. *Astro. J. Sup. Series* **127**, 451–457.
- Ristorcelli, J. R. 2006 Passive scalar mixing: analytic study of time scale ratio, variance, and mix rate. *Phys. Fluids* **18**, 075101.
- Ristorcelli J. R. & Clark T. T. 2004 Rayleigh–Taylor turbulence: self-similar analysis and direct numerical simulations. *J. Fluid Mech.* **507**, 213–253.
- Ristorcelli, J. R., Livescu, D. & Hjelm, N. 2005 An eddy viscosity expression for Favre aver-

- aged Reynolds stresses in variable density turbulence. Los Alamos National Laboratory Report LA-UR-05-5837.
- Rogers, M. M. & Moin, P. 1987 The structure of the vorticity field in homogeneous turbulent flows. *J. Fluid Mech.* **176**, 33–66.
- Rogers, M. M. & Moser R. D. 1994 Direct numerical simulation of a self-similar turbulent mixing layer. *Phys. Fluids* **6**, 903–923.
- Sandoval, D. L. 1995 *The Dynamics of Variable Density Turbulence*. Ph.D. dissertation. University of Washington.
- Schmitt, F. G., Marci, B., Dick, E. & Hirsch, C. 2003 Direct investigation of the K -transport equation for a complex turbulent flow. *J. Turb.* **21**, 1–16.
- Schumacher, J., Sreenivasan, K. R. & Yeung, P. K. Very fine structures in scalar mixing. *J. Fluid Mech.* **531**, 113–122.
- Schurtz, G. P., Nicolaï, Ph. D. & Busquet., M. 2000 A nonlocal electron conduction model for multidimensional radiation hydrodynamics codes. *Phys. Plasmas* **10**, 4238–4249.
- Sharp, D. H. 1984 An overview of Rayleigh–Taylor instability. *Physica D* **12**, 3–18.
- Shea, J. R. 1976 *A Chemical Reaction in a Turbulent Jet*. Ph.D. dissertation, California Institute of Technology.
- Shimomura, Y. 1998 A theoretical study of the turbulent diffusion in incompressible shear flows and in passive scalars. *Phys. Fluids* **10**, 2636–2646.
- Shvarts, D., Alon, U., Ofer, D., McCrory, R. L. & Verdon, C. P. 1995 Nonlinear evolution of multimode Rayleigh–Taylor instability in two and three dimensions. *Phys. Plasmas* **2**, 2465–2472.

- Smarr, L., Wilson, J. R., Barton, R. T. & Bowers, R. L. 1981 Rayleigh–Taylor overturn in super-nova core collapse. *Astrophysical J.* **246**, 515–525.
- Smith, A. M. O. & Gamberoni, N. 1957 Transition, pressure gradient, and stability theory. *Proc. Ninth Internat. Cong. Appl. Mech.* **4**, 234–244.
- Snider, D. M. & Andrews, M. J. 1994 Rayleigh–Taylor and shear driven mixing with an unstable thermal stratification. *Phys. Fluids A* **6**, 3324–3334.
- Snider, D. M. & Andrews, M. J. 1996 The simulation of mixing layers driven by compound buoyancy and shear. *Trans. ASME J. Fluids Eng.* **118**, 370–376.
- Spalding, D. B. 1971 Concentration fluctuations in a round turbulent free jet. *Chem. Eng. Science* **26**, 95–107.
- Spitz, P. B. & Haas, J.-F. 1991 Numerical calibration of Rayleigh–Taylor induced turbulent flows with a k - ϵ mix model. *Proc. of the 3rd International Workshop on the Physics of Compressible Turbulent Mixing*, June 1991, 511–525.
- Stilling, D. C., Head, M. J., Helland, K. N. & Van Atta, C. W. 1983 A closed loop gravity-driven water channel for density stratified shear flow. *J. Fluid Mech.* **131**, 73–89.
- Takabe, H., Yamanaka, M., Mima, K., Yamanaka, C., Azechi, H., Miyanaga, N., Nakatsuka, M., Jitsuno, T., Norimatsu, T., Takagi, M., Nishimura, H., Nakai, M., Yabe, T., Sasaki, T., Yoshida, K., Nishihara, K., Kato, Y., Izawa, Y., Yamanaka, T. & Nakai, S. 1988 Scalings of implosion experiments for high neutron yield. *Phys. Fluids* **31**, 2884–2893.
- Tavoularis, S. & Corrsin, S. 1981 Experiments in nearly homogeneous turbulent shear flow with a uniform mean temperature gradient. Part 1. *J. Fluid Mech.* **104**, 311–347.
- Taylor, G. I. 1938 The spectrum of turbulence. *Proc. Royal Soc. London A* **164**, 476–490.

- Taylor, G. I. 1950 The instability of liquid surfaces when accelerated in a direction perpendicular to their planes. *Proc. Royal Soc. London* **201**, 192–196.
- Thomas, G. O. 2003 The aerodynamic breakup of ligaments. *Atom. Sprays* **13**, 117–129.
- Valerio, E., Jourdan, G., Houas, L., Zeitoun, D. & Besnard, D. C. 1999 Modeling of Richtmyer–Meshkov instability-induced turbulent mixing in shock-tube experiments. *Phys. Fluids* **11**, 214–225.
- Vandromme D. & Ha Minh, H. 1993 Solution of the compressible Navier–Stokes equations: applications to complex turbulent flows. In *Lecture Series on CFD*. Von Kármán Institute.
- Van Ingen, J. L. 1956 A suggested semi-empirical method for the calculation of boundary layer transition regime. Inst. of Tech., Dept. of Aeronautic and Engrg., Report VTH-74, Delft, Holland.
- Veynante, D. & Vervisch, L. 2002 Turbulent combustion modeling. *Prog. Energy Comb. Sci.* **28**, 193–266.
- Veynante, D., Trouvé, A., Bray, K. N. C. & Mantel, T. 1997 Gradient and counter-gradient scalar transport in turbulent premixed flames. *J. Fluid Mech.* **332**, 263–293.
- Warhaft, Z. 2000 Passive scalars in turbulent flows. *Annu. Rev. Fluid Mech.* **32**, 203–240.
- Wilcox, D. C. 2006 *Turbulence Modeling for CFD*, 3rd ed. DCW Industries, La Cañada, CA.
- Wilson, D. C., Scannapieco, A. J., Cranfill, C. W., Clover, M. R., Hoffman, N. M. & Collins, J. 2003 Degradation of radiatively driven inertial confinement fusion capsule implosions by multifluid interpenetration mixing. *Phys. Plasmas* **10**, 4427–4434.

- Wilson, P. N. 2002 *An Investigation into the Spectral Evolution of Turbulent Mixing by Rayleigh–Taylor Instability*. Ph.D. dissertation. Texas A&M University.
- Wilson, P. N. & Andrews, M. J. 2002 Spectral measurements of Rayleigh–Taylor mixing at low-Atwood number. *Phys. Fluids A* **14**, 938–945.
- Wunsch, C. & Ferrari R. 2004 Vertical mixing, energy, and the general circulation of oceans. *Annu. Rev. Fluid Mech.* **36**, 281–314.
- Yao, Y. F., Savill, A. M. Sandham, N. D. & Dawes, W. N. 2002 Simulation and modelling of turbulent trailing-edge flow. *Flow, Turb. Comb.* **68**, 313–333.
- Yeung, P. K., Xu, S., Donzis, D. A. & Sreenivasan, K. R. 2004 Simulations of three-dimensional turbulent mixing for Schmidt numbers of the order 1000. *Flow Turb. Combust.* **72**, 333–347.
- Yoshizawa, A. 1982 Statistical evaluation of the triple velocity correlation and the pressure-velocity correlation in shear turbulence. *J. Phys. Soc. Japan* **51**, 2326–2337.
- Young, Y.-N., Tufo, H., Dubey, A. & Rosner, R. 2001 On the miscible Rayleigh–Taylor instability: two and three dimensions. *J. Fluid Mech.* **447**, 377–408.
- Youngs, D. L. 1984 Numerical simulations of turbulent mixing by Rayleigh–Taylor instability. *Physica D* **12**, 32–44.
- Youngs, D. L. 1989 Modelling turbulent mixing by Rayleigh–Taylor instability. *Physica D* **37**, 270–287.
- Youngs, D. L. 1991 Three-dimensional numerical simulations of turbulent mixing by Rayleigh–Taylor instability. *Phys. Fluids A* **3**, 1312–1320.

- Youngs, D. L. 1994 Three dimensional numerical simulation of turbulent mixing by Rayleigh–Taylor instabilities. *Las. Part. Beams* **12**, 725–750.
- Younis, B. A., Speziale, C. G. & Clark, T. T. 2005 A rational model for the turbulent scalar fluxes. *Proc. Royal Soc. A* **461**, 575–594.
- Zhang, S. 1995 *Molecular-Mixing Measurements and Turbulent-Structure Visualizations in a Round Jet with Tabs*. Ph.D. dissertation. Purdue University.
- Zhang, S. & Schneider, S. P. 1995 Quantitative molecular-mixing measurements in a round jet with tabs. *Phys. Fluids* **7**, 1063–1070.
- Zhang, S., Schneider, S. P. & Collicott, S. H. 1995 Quantitative molecular mixing measurements using digital processing of absorption images. *Exp. Fluids* **19**, 319–327.
- Zhou, Y. 2007 Unification and extension of the similarity scaling criteria and mixing transition for studying astrophysics using high energy density laboratory experiments or numerical simulations. *Phys. Plasmas* **14**, 082701.
- Zhou Y., Remington, B. A., Robey, H. F., Cook, A. W., Glendinning, S. G., Dimits, A., Buckingham, A. C., Zimmerman, G. B., Burke, E. W., Peyser, T. A., Cabot, W. & Eliason, D. 2003 Progress in understanding turbulent mixing induced by Rayleigh–Taylor and Richtmyer–Meshkov instabilities. *Phys. Plasmas* **10**, 1883–1896.

APPENDIX A

REACTING FLOW EXPERIMENTAL PROCEDURES

The standard operating procedures for the reacting flow experiments are listed below.

1. Flush any old water out of the water tanks and water channel.
2. Fill each 500 gallon tank with water at the same temperature.
3. Using a steel tape measure, measure the depth of the water in the lighter fluid tank. The total volume of the tank can then be calculated by $\text{volume} = \text{depth} \times (\text{diameter}/2)^2$, where the diameter of the tank is 52 inches. This information will be needed to calculate the proper amount of chemical indicator to add.
4. Turn on the sump pumps.
5. Add 100–125 ml of sodium thiosulfate ($\text{Na}_2\text{S}_2\text{O}_3$) at 2.0 N ('normal' or molar) to the each 500 gallon tank to dechlorinate the water.
6. Put pH meter probe in tap water and let rest for 30 minutes.
7. Calibrate pH meter using standard reference buffer solutions at pH = 4, 7, and 10. These buffer solutions may be purchased from any chemical vendor, such as VWR.
8. Using any standard handheld thermocouple probe (a K-type digital thermocouple probe is available within the lab), check each tank to ensure that the water temperature is the same to within ± 0.2 °C.

9. Measure out approximately 1.5 L of salt (NaCl) in a beaker and add to heavy fluid tank by dissolving 200 ml of salt at a time within a gallon jug of water. Shake continuously until all 200 ml of salt is dissolved and then pour contents into heavy fluid tank. Repeat until all 1.5 L of salt have been added to heavy fluid tank.
10. Starting with a concentrated solution (30–40% w/w) of sodium hydroxide (NaOH), which can be purchased from any major chemical supplier such as VWR, pour the concentrated solution into heavy fluid tank and let mix until a final $\text{pH}_1 = 11.5 \pm 0.05$ is achieved.
11. Starting with a concentrated solution (30–40% w/w) of hydrochloric acid (HCl), which can be purchased from any major chemical supplier such as VWR, pour the concentrated solution into lighter fluid tank and let mix until a final $\text{pH}_2 = 7 \pm 0.05$ is achieved.
12. Measure the density of the fluid in each tank using the following sub-steps.
 - 12a. Confirm calibration of electronic balance by measuring calibration masses (available from MEEN department equipment room). Electronic balance should read same value of mass as listed in the `ScaleCalibration.m` (see DVD of Matlab analysis scripts for the reacting flow experiments).
 - 12b. Use a 10 ml pipette to siphon 50+ ml of fluid from each tank. Note that, to prevent contamination of fluid samples used to calculate the density of each fluid, a different pipette must be used for each tank.
 - 12c. Measure mass of empty class A 50 ml flask.
 - 12d. Place 50–55 ml of fluid in a class A 50 ml flask.

- 12e. Remove fluid from flask as necessary until only 50 ml exactly remains.
- 12f. Measure mass of fluid and flask and record.
- 12g. Add fluid to flask and then remove fluid until exactly 50 ml remains.
- 12h. Repeat steps 12d–12g until approximately 10–12 measurements have been recorded for each fluid.
- 12i. Calculate density of each fluid, where the density of the fluid is given by average of the 10–12 mass measurements recorded minus the mass of the flask, divided by the volume of fluid within a sample (50 ml). If density difference is less than desired, add more salt (approximately 200 ml) to heavy fluid as was done in step 9 and repeat measurement of heavy fluid density as listed in steps.
13. Turn on water channel backlighting.
14. Use hose to fill water channel with water.
15. Remove any bubbles trapped under the splitter plate, on the endscreen, and between the back wall and translucent velum either by hand or with a hose.
16. Calculate volume of concentrated phenolphthalein ($C_{20}H_{14}O_4$) to add to light fluid tank, where

$$V_{concentrate} [In]_{concentrate} = V_{tank} [In]_{tank} .$$

For a 1% phenolphthalein solution (purchased from VWR), $[In]_{concentrate} = 0.031415$ mol/L. The volume of the tank is calculated in step 3. The desired concentration of indicator in the lighter fluid tank is $[In]_{tank} = 6 \times 10^{-6}$. De-

pending upon the exact volume of the tank, typically $V_{concentrate} \approx 350$ ml of phenolphthalein will need to be added to the lighter fluid tank.

17. Using a 50 ml graduated cylinder, add phenolphthalein in 50 ml increments to a 1000 ml graduated cylinder until the total volume of phenolphthalein calculated in step 25 has been added to the 1000 ml cylinder.
18. Pour the phenolphthalein concentrate into the lighter fluid tank and let the sump pumps mix the tank.
19. Set up camera (Canon Powershot A80), tripod, and light filter (Hoya HMC green filter) as shown in instructional video.
20. Place reference ruler within water channel and capture reference image. This information will be required to calculate the pixel spacing for the image analysis scripts, specifically within `MSetImageProp.m`.
21. Check final pH and temperature of each fluid tank using the pH probe and handheld thermocouple probe and record.
22. To eliminate any possible electrical interference with the experiment, diagnostics, and backlighting, turn all unnecessary electronics off, *i.e.* sump pumps, air conditioning, lights, *etc.* with the exception of the background lighting and the camera system.
23. Set camera to ISO 100, shutter speed 1/60 s, aperture $f/7.1$, high-speed, continuous capture mode (see instructional video or camera manual).
24. Start recording images to capture baseline, background images. Record for approximately 1 minute.

25. Turn on heavy and light fluid pumps and open exit plenum valves.
26. Set fluid velocities for each stream to $U_m = 5$ cm/s, adjust rotameters as necessary to eliminate shear between the top and bottom streams, and record mean advective velocity.
27. Let experiment run. The camera will record images of mixing layer.
28. Run the experiment until each 500 gallon water tank has been emptied.
29. Upon completion of the experiment, turn off the water pumps, place water hose in upper portion of the entrance plenum, and turn on the water to flush any residual chemicals out of the water channel.
30. After approximately 5 minutes, place the water hose in the lower portion of the entrance plenum to flush any remaining residual chemicals out of the lower portion of the channel.
31. Refill each 500 gallon water tank with fresh water.
32. After flushing the water channel with the water hose, rinse all top plates and bottles that have come into contact with the acidic or alkaline fluids.
33. Once each 500 gallon water tank is half-way filled, turn the sump pumps back on to flush in residual chemicals from the sump pumps.
34. Upon filling the 500 gallon water tanks, turn on the main water pumps and flush the entire system with the fresh water.

APPENDIX B

FOURIER ANALYSIS OF DATA

Given a set of data points along a line $u(x)$, it is possible to decompose $u(x)$ into a Fourier series and calculate its energy density spectrum. The Fourier series can be written as

$$u(x) = \sum_k \hat{u}(k) e^{ikx}, \quad (\text{B.1})$$

where $\hat{u}(k)$ is the amplitude of each wavenumber and $k \equiv 2\pi/\lambda$ is the wavenumber for each wave. The amplitude of each wave $\hat{u}(k)$ is complex, and thus contains both amplitude and phase information. An alternate expression for the original trace is

$$u(x) = \sum_k \text{Re} [\hat{u}(k)] \cos(kx) + \text{Im} [\hat{u}(k)] \sin(kx) \quad (\text{B.2})$$

or

$$u(x) = \sum_k |\hat{u}(k)| \cos[kx + \varphi(k)], \quad (\text{B.3})$$

where

$$\varphi(k) = \tan^{-1} \left\{ \frac{\text{Im} [\hat{u}(k)]}{\text{Re} [\hat{u}(k)]} \right\} \quad (\text{B.4})$$

is the phase angle of the wave.

The amplitude of each wave $\hat{u}(k)$ is calculated by taking the Fourier transform

$$\hat{u}(k) = \frac{1}{L} \int_{-L}^L u(x) e^{-ikx} dx. \quad (\text{B.5})$$

The energy of each mode is calculated

$$\hat{E}_u(k) = \frac{\hat{u}(k) \hat{u}^*(k)}{2}, \quad (\text{B.6})$$

where $\hat{u}^*(k)$ is the complex conjugate of $\hat{u}(k)$. The total energy in $u(x)$ can be calculated by summing the energy over all wavenumbers

$$\frac{\overline{u'^2}}{2} = \sum_k \hat{E}_u(k). \quad (\text{B.7})$$

The energy density spectrum is calculated from the energy spectrum by normalizing $\hat{E}_u(k)$ by the width of each wavenumber bin

$$E_u(k) = \frac{\hat{E}_u(k)}{\Delta k}. \quad (\text{B.8})$$

The energy density spectrum has the property

$$\frac{\overline{u'^2}}{2} = \int_0^\infty E_u(k) dk. \quad (\text{B.9})$$

The total energy of $u(x)$ can be computed by the following means:

Variance of original trace	$E = \frac{\overline{u'^2}}{2} = \frac{1}{4L} \int_{-L}^L [u(x) - \bar{u}]^2 dx$	
Summation of $\hat{E}_u(k)$	$E = \sum_k \hat{E}_u(k)$	(B.10)
Integration of $E_u(k)$	$E = \int_0^\infty E_u(k) dk$	

All methods should result in the same value of total energy E to within the error limits of the numerical integration scheme used.

In two-dimensional space, a field of values $u(x, y)$ may be written in terms of a two-dimensional Fourier series

$$u(x, y) = \sum_{k_x, k_y} \hat{u}(k_x, k_y) e^{i(k_x x + k_y y)}, \quad (\text{B.11})$$

where $\hat{u}(k_x, k_y)$ is the amplitude of a wave. The magnitude of the wavevector is

$$|\mathbf{k}| = \sqrt{k_x^2 + k_y^2} \quad (\text{B.12})$$

and the wavelength is

$$\lambda = \frac{2\pi}{|\mathbf{k}|}. \quad (\text{B.13})$$

The wave is traveling in a direction θ from the x -axis, such that

$$\theta(k_x, k_y) = \tan^{-1} \left(\frac{k_y}{k_x} \right). \quad (\text{B.14})$$

The field $u(x, y)$ may also be expressed in an alternative manner

$$u(x, y) = \sum_{k_x, k_y} \hat{u}(k_x, k_y) \begin{pmatrix} \cos(k_x x) \cos(k_y y) \\ -\sin(k_x x) \sin(k_y y) \\ +i \cos(k_x x) \sin(k_y y) \\ +i \sin(k_x x) \cos(k_y y) \end{pmatrix} \quad (\text{B.15})$$

or

$$\begin{aligned}
 u(x, y) = & \sum_{k_x, k_y} \operatorname{Re} [\hat{u}(k_x, k_y)] \cos(k_x x) \cos(k_y y) \\
 & - \operatorname{Re} [\hat{u}(k_x, k_y)] \sin(k_x x) \sin(k_y y) \\
 & - \operatorname{Im} [\hat{u}(k_x, k_y)] \cos(k_x x) \sin(k_y y) \\
 & - \operatorname{Im} [\hat{u}(k_x, k_y)] \sin(k_x x) \cos(k_y y) .
 \end{aligned} \tag{B.16}$$

The phase of each wave is

$$\varphi(k_x, k_y) = \tan^{-1} \left\{ \frac{\operatorname{Im} [\hat{u}(k_x, k_y)]}{\operatorname{Re} [\hat{u}(k_x, k_y)]} \right\} . \tag{B.17}$$

The complex-valued amplitudes for each mode are calculated by taking the two-dimensional Fourier transform of $u(x, y)$,

$$\hat{u}(k_x, k_y) = \frac{1}{L_x L_y} \int_0^{L_x} \int_0^{L_y} u(x, y) e^{-i(k_x x + k_y y)} dy dx . \tag{B.18}$$

The energy in each mode is given by

$$\hat{E}(k_x, k_y) = \frac{\hat{u}(k_x, k_y) \hat{u}^*(k_x, k_y)}{2} , \tag{B.19}$$

where $\hat{u}^*(k_x, k_y)$ is the complex conjugate of $\hat{u}(k_x, k_y)$. The total energy in $u(x, y)$ can be calculated by summing the energy over all wavenumbers

$$\frac{\overline{u^2}}{2} = \sum_{k_x, k_y} \hat{E}_u(k_x, k_y) . \tag{B.20}$$

The energy density spectrum is calculated from the energy spectrum by normalizing $\hat{E}_u(k_x, k_y)$ by the area of each wavenumber bin

$$E_u(k_x, k_y) = \frac{\hat{E}_u(k_x, k_y)}{\Delta k_x \Delta k_y}. \quad (\text{B.21})$$

Once normalized, the energy density spectrum has the property

$$\frac{\overline{u'^2}}{2} = \int_0^\infty \int_0^\infty E_u(k_x, k_y) dk_y dk_x. \quad (\text{B.22})$$

Typically, the two-dimensional spectra can be reduced to one-dimensional form by summing the energy content $\hat{E}(k_x, k_y)$ within azimuthal rings of constant $k = \sqrt{k_x^2 + k_y^2}$ and width Δk , where Δk can be specified as desired. Typically, for the case $L_x = L_y$, the wavenumber bin width is chosen to be $\Delta k = \Delta k_x = \Delta k_y$. Summing the azimuthal energy content in $\hat{E}(k_x, k_y)$ gives

$$\hat{E}(k) = \sum_{k_x, k_y} \hat{E}(k_x, k_y) \delta\left(\sqrt{k_x^2 + k_y^2} \geq k - \frac{\Delta k}{2}\right) \delta\left(\sqrt{k_x^2 + k_y^2} < k + \frac{\Delta k}{2}\right), \quad (\text{B.23})$$

where

$$\delta(x) = \begin{cases} 1 & x = 1 \text{ (boolean true)} \\ 0 & x = 0 \text{ (boolean false)} \end{cases}. \quad (\text{B.24})$$

The one-dimensional energy density spectrum is calculated by normalizing $\hat{E}(k)$ by Δk ,

$$E(k) = \frac{\hat{E}(k)}{\Delta k}. \quad (\text{B.25})$$

Similar to the one-dimensional energy density spectrum in the previous section and the two-dimensional energy density spectrum, the total energy in $u(x)$ is

$$\frac{\overline{u^2}}{2} = \int_0^\infty E_u(k) dk. \quad (\text{B.26})$$

The code in `MFFT` and `MFFT2D` (written to compute Fourier transforms and properly format output for this work) accounts for two issues that arise from using Matlab proprietary `fft` and `fft2` algorithms. The first issue deals with the proper normalization of the amplitudes returned by `fft` and `fft2`. In `MFFT`, the Fourier coefficients calculated by `fft` are scaled by $2/N_x$, where N_x is the total number of data points in the original trace. The factor of two arises from the fact that the Fourier coefficients are symmetric about $k = 0$. Thus, $\hat{u}(k)e^{ikx} = \hat{u}(-k)e^{i(-k)x}$. The negative wavenumber portion of the spectrum is ignored due to this symmetry; however, to enforce the fact that $\hat{u}(k)$ is in fact the amplitude of each Fourier mode, the factor of two must be used. In two dimensions, the Fourier coefficients are normalized by $1/(N_x N_y)$, where N_x and N_y are the number of points in the x - and y -directions, respectively. The factor of 2 is not used in two dimensions as the symmetric portion is retained in this case, by choice.

The Fourier coefficients returned by Matlab are each associated with a particular wavenumber. However, the wavenumber axis of the coefficients returned by `fft` do not follow a monotonic pattern, such as $k = 2\pi m/\lambda$, where the mode number m is

$$m_{\text{monotonic}} = \{-N_k + 1 \quad \dots \quad -1 \quad 0 \quad 1 \quad \dots \quad N_k - 1\}, \quad (\text{B.27})$$

where N_k is the Nyquist mode number

$$N_k = \frac{N_x}{2}. \quad (\text{B.28})$$

Instead, the Fourier coefficients are arranged according to the following mode number array (Trefethen 2000)

$$m_{Matlab} = \{0 \quad 1 \quad \dots \quad N_k - 1 \quad 0 \quad -N_k + 1 \quad \dots \quad -1\}. \quad (\text{B.29})$$

Note that the zeroth mode is repeated. While it is trivial to avoid adding $E_u(k=0)$ to the total energy content with one-dimensional spectra, more caution must be exercised in two dimensions.

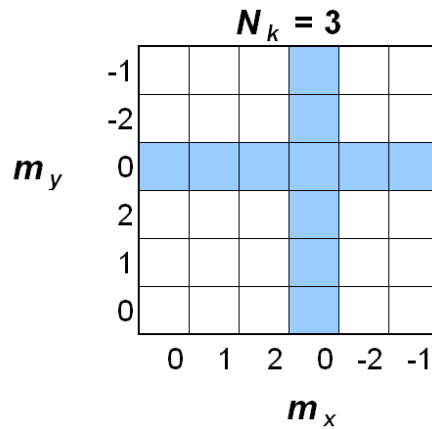
Similarly, in two-dimensions, the two-dimensional array of Fourier coefficients generated by `fft2` has mode numbers

$$\begin{aligned} m_{x,Matlab} &= \{0 \quad 1 \quad \dots \quad N_{k,x} - 1 \quad 0 \quad -N_{k,x} + 1 \quad \dots \quad -1\} \\ m_{y,Matlab} &= \{0 \quad 1 \quad \dots \quad N_{k,y} - 1 \quad 0 \quad -N_{k,y} + 1 \quad \dots \quad -1\}. \end{aligned} \quad (\text{B.30})$$

Now the issue of double counting energy values exists when calculating

$$\frac{\overline{u'^2}}{2} = \sum_{k_x, k_y} \hat{E}_u(k_x, k_y). \quad (\text{B.31})$$

The two dimensional array of Fourier coefficients is organized as shown in figure B. The blue regions represent Fourier coefficients that are repeated values.



Schematic representation of the two-dimensional matrix returned by `fft2`.

MFFT rearranges the output from Matlab so that

$$m = \{1 \quad \dots \quad N_k - 1 \quad -N_k - 1 \quad \dots \quad -1 \quad 0\}. \quad (\text{B.32})$$

For one-dimensional spectra, the aliased portion of symmetric values can be neglected by truncating the output arrays (as shown above) by the following code:

```
Nk = round(length(u_hat) / 2);
u_hat(Nk+1 : length(u_hat)) = [];
k(Nk+1 : length(k)) = [];
```

Similarly, MFFT2D reformats the output from Matlab so that the axes of the final two-dimensional array are

$$\begin{aligned} m_x &= \{-N_{k,x} + 1 \quad \dots \quad -1 \quad 0 \quad 1 \quad \dots \quad N_{k,x} - 1\} \\ m_y &= \{-N_{k,y} + 1 \quad \dots \quad -1 \quad 0 \quad 1 \quad \dots \quad N_{k,y} - 1\} \end{aligned} \quad (\text{B.33})$$

and no amplitudes or energy values are repeated.

APPENDIX C

NEUTRALIZATION CHEMISTRY

In aqueous solutions, the concentration of hydrogen and hydroxide ions satisfy the reversible reaction



with equilibrium constant

$$K_w = [\text{H}^+][\text{OH}^-] = 1 \times 10^{-14}. \quad (\text{C.2})$$

A mixture of two fluids with volume fractions f_1 , f_2 and hydrogen ions concentrations pH_1 , pH_2 , will reach a new equilibrium value pH_{mix} as determined by conservation of mass and equilibrium constraints. The initial, unmixed ion concentrations are given by

$$a_0 = f_1 [\text{H}^+]_1 + f_2 [\text{H}^+]_2, \quad (\text{C.3})$$

$$b_0 = f_1 [\text{OH}^-]_1 + f_2 [\text{OH}^-]_2, \quad (\text{C.4})$$

which may not necessarily satisfy the equilibrium constraint in (C.2). Upon mixing, a_0 and b_0 will decrease by an amount x , giving final concentrations $a_{mix} = a_0 - x$ and $b_{mix} = b_0 - x$. The new equilibrium concentrations a_{mix} and b_{mix} must then satisfy the equilibrium constraint (C.2), where

$$\begin{aligned} K_w &= [\text{H}^+][\text{OH}^-] & (\text{C.5}) \\ &= (a_0 - x)(b_0 - x) \\ &= a_0 b_0 - x(a_0 + b_0) + x^2. \end{aligned}$$

The change in ion concentrations, x , can be calculated by solving the quadratic equation in (C.5), giving

$$x = \frac{(a_0 + b_0) - \sqrt{(a_0 + b_0)^2 - 4(a_0 b_0 - K_w)}}{2} \quad (\text{C.6})$$

where the negative root provides the physical solution. Accordingly, the final pH of the mixture is given by $\text{pH}_{mix} = -\log_{10}(a_0 - x)$.

APPENDIX D

DNS INITIAL CONDITIONS

Many numerical simulations of Rayleigh–Taylor mixing have been performed to study the growth of turbulent mixing layers at various Atwood numbers. As much of this work has been focused on examining the late-time turbulent growth regime of a mixing layer, far less effort has been given to simulations representing physical experiments. As a result, most three-dimensional simulations are initialized with small *ad hoc*, isotropic perturbations to the initial interface separating the heavy and light fluids. Few simulations have used experimentally-measured initial conditions and, to date, no *direct numerical simulation* of a turbulent Rayleigh–Taylor experiment has been performed. Table D.1 lists an abbreviated list of pertinent Rayleigh–Taylor simulations and their respective numerical techniques and initial conditions used. The DNS presented in this work differs from all other numerical simulations in Table D.1 as the initial conditions implemented here come from measured initial perturbations in the water channel (Mueschke *et al.* 2006). An overview of the initial conditions and implementation methods is presented here.

The initial density field in the DNS is modeled as

$$\rho(x, y, z) = \frac{\rho_1 + \rho_2}{2} + \frac{\rho_1 - \rho_2}{2} \operatorname{erf} \left[\frac{z + \zeta(x, y)}{\varepsilon} \right], \quad (\text{D.1})$$

where $\zeta(x, y)$ is the two-dimensional interfacial perturbation, $\varepsilon = \delta/2 = 0.15$ cm is the half-width of the initially-diffuse interfacial thickness separating the heavier and lighter fluid, and $\operatorname{erf}(\cdot)$ is the error function. The initial interfacial perturbation $\zeta(x, y)$ is defined as the local vertical displacement of the point at which $\rho = (\rho_1 + \rho_2)/2$

Researcher	Numerical Technique	Interfacial	Velocity
Youngs (1991)	MILES	Isotropic	
Youngs (1994)	MILES	Isotropic	
Linden <i>et al.</i> (1994)	MILES		
Dalziel <i>et al.</i> (1999)	MILES	Isotropic	Anisotropic; Measured
Cook and Dimotakis (2001); Cook and Zhou (2002); Cabot <i>et al.</i> (2004)	DNS	Isotropic	
Cook <i>et al.</i> (2004)	LES	Isotropic	
Cabot and Cook (2006)	DNS	Isotropic	
Ristorcelli and Clark (2004)	DNS	Isotropic	
Ramaprabhu and Andrews (2004b)	MILES	Isotropic; Measured	
Ramaprabhu and Andrews (2004b)	MILES		Isotropic; Measured
Dimonte <i>et al.</i> (2004)	MILES; Euler PPM; DNS	Isotropic	
Current Work	DNS	Anisotropic; Measured	Anisotropic; Measured

Table D.1 Table of selected three-dimensional Rayleigh–Taylor simulations.

from the centerplane ($z = 0$) and has the same units as z and ε . While the interfacial perturbation $\zeta(x, y)$ is used to define the initial density field, the DNS does not directly track or evolve a numerical interface between the two fluid components.

The initial interfacial perturbations have been parameterized from measurements from a set of water channel experiments (Mueschke *et al.* 2006). To facilitate a comparison of experimental measurements and DNS data, a stochastic representation of the experimental initial perturbations is used to seed the initial conditions of the DNS. Spectra of interfacial perturbations from the experiment in the x - and y -directions, $\hat{\zeta}(k_x)$ and $\hat{\zeta}(k_y)$ respectively, are used to formulate the initial interfacial perturbation

$$\zeta(x, y) = \sum_{k_x=k_{\min}}^{k_{\max}} \hat{\zeta}(k_x) e^{ik_x x} + \sum_{k_y=k_{\min}}^{k_{\max}} \hat{\zeta}(k_y) e^{ik_y y}, \quad (\text{D.2})$$

where $k_x = 2\pi/\lambda_x$ and $k_y = 2\pi/\lambda_y$ are the wavenumbers in the x - and y -directions. The perturbation amplitudes in the x - and y -directions, $|\hat{\zeta}(k_x)|$ and $|\hat{\zeta}(k_y)|$, are taken from the experimentally-measured spectra shown in figure D.2:

$$|\hat{\zeta}(k_i)| = \sqrt{4 \Delta k E_{\zeta}(k_i)} \quad , \quad i = x, y. \quad (\text{D.3})$$

Phases for each mode were chosen from a uniform distribution of random values between $-\pi$ and π .

This initialization method is novel in that experimentally-measured perturbations have been used in both the x - and y -directions, and *no assumption of isotropy has been made*. While separate interfacial perturbation spectra are applied in the x - and y -directions, this method is still comparable to the commonly used methods of initialization using azimuthally-averaged (*i.e.* isotropic) energy spectra (Youngs 1994;

Cook & Dimotakis 2001; Ramaprabhu & Andrews 2004b; Dimonte *et al.* 2004). In wavenumber space, the current initialization of the interfacial perturbations limits fluctuations to those modes aligned with the x - and y -axes only. This differs from isotropic initializations where azimuthal rings of radius $k = \sqrt{k_x^2 + k_y^2}$ are populated with energetic modes.

The initial velocity fluctuations present in the mixing layer at the onset of the instability were measured using particle-image velocimetry (PIV) (Mueschke *et al.* 2006). An initial velocity field can then be constructed based on the initial vertical velocity variance spectrum at the centerplane ($z = 0$), shown in figure D.3. To apply the initial centerplane vertical velocity fluctuations to the entire computational domain, a velocity field must be parameterized based upon $E_w(k_x)$. This is accomplished by defining a velocity potential field similar to that used in the linear stability analysis of Kelvin–Helmholtz and Rayleigh–Taylor instabilities (Drazin & Reid 2004). The velocity potential in fluid $r = 1, 2$ is

$$\phi_r(\mathbf{x}, t = 0) = \sum_{k_x=k_{\min}}^{k_{\max}} \frac{\hat{w}(k_x)}{k_x} e^{ik_x x - k_x |z|}. \quad (\text{D.4})$$

The initial velocity field is the sum of the gradient of the potential field and a term proportional to the density gradient

$$u_i(\mathbf{x}, t = 0) = \frac{\partial \phi_r}{\partial x_i} - \frac{D}{\rho} \frac{\partial \rho}{\partial x_i}; \quad i = x, y, z, \quad (\text{D.5})$$

where $D = \nu/Sc$ is the species mass diffusivity, ν is the kinematic viscosity and $Sc = 7$ is the Schmidt number (see Table 3.1). The density gradient term in (D.5) accounts for the velocity field that exists due to the initial density gradient between the top

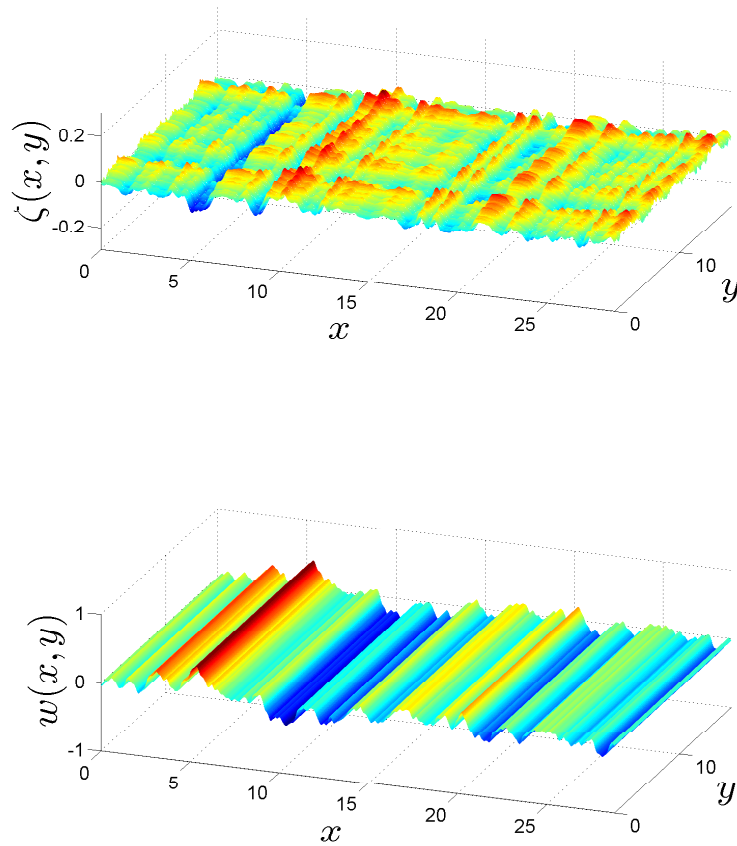


Figure D.1 Initial interfacial (top) and centerplane vertical velocity (bottom) perturbation isosurfaces.

and bottom fluids, as $\nabla \cdot \mathbf{u} \neq 0$ when $D \nabla \rho \neq 0$ (Joseph 1990; Sandoval 1995).

A visualization of the initial interfacial and vertical velocity perturbations is shown in figure D.1. As noted in Table D.1, the initial perturbations are anisotropic. In addition, there are no velocity perturbations in the y -direction. Thus, any three-dimensional turbulent structures that develop are due to the interfacial perturbations in the y -direction.

In developing the formulation of the initial conditions shown in (D.2) and (D.4), several issues arise which must be considered. First, the measurement of the initial interfacial perturbations in the x -direction $\hat{\zeta}(k_x)$ must be inferred from the density fluctuation measurements on the centerplane $\hat{\rho}(k_x)$. The density variance spectrum $\hat{\rho}(k_x)$ is not explicitly equivalent to the spectrum of interfacial perturbations $\hat{\zeta}(k_x)$; however, a relationship between $\hat{\rho}(k_x)$ and $\hat{\zeta}(k_x)$ does exist. This relationship relies upon Eq. (D.1) as an adequate model for the initial density field and ε assumed to be a constant. This parameterization assumes that diffusion occurs only in the z -direction, which is valid in this case where $\hat{\zeta}(k) \ll \lambda = 2\pi/k$. Also, when measuring the density fluctuations at a distance $x = 0.5$ cm from the splitter plate, the hot and cold water streams have been in contact for the same amount of time and, thus, an approximation of a constant ε is plausible.

To relate $E_\rho(k_x)$ to $E_\zeta(k_x)$ in the x -direction using (D.1), the fluctuating density field on the centerplane can be expressed as a sum of Fourier modes

$$\rho(x, z = 0)' = \rho(x, z = 0) - \frac{\rho_1 + \rho_2}{2} = \sum_{k_x=k_{\min}}^{k_{\max}} \hat{\rho}(k_x) e^{ik_x x}. \quad (\text{D.6})$$

Substituting (D.6) into (D.1) evaluated at $z = 0$ gives

$$\sum_{k_x=k_{\min}}^{k_{\max}} \hat{\rho}(k_x) e^{ik_x x} = \frac{\Delta\rho}{2} \operatorname{erf} \left[\frac{\zeta(x)}{\varepsilon} \right], \quad (\text{D.7})$$

where $\Delta\rho \equiv \rho_1 - \rho_2$, and the interfacial perturbation $\zeta(x, y)$ has been restricted to the x -axis. Solving for $\zeta(x)$ then gives

$$\zeta(x) = \varepsilon \operatorname{erf}^{-1} \left[\frac{2}{\Delta\rho} \sum_{k_x=k_{\min}}^{k_{\max}} \hat{\rho}(k_x) e^{ik_x x} \right]. \quad (\text{D.8})$$

The interfacial perturbation spectrum, $E_\zeta(k_x)$ can be computed by taking the one-dimensional Fourier transform of the reconstructed interfacial perturbation $\zeta(x)$ in (D.8). While this procedure is required to correctly implement the interfacial perturbation in the x -direction, the calculated spectrum $E_\zeta(k_x)$ exhibits negligible differences from the measured spectrum $E_\rho(k_x)$.

Another issue which must be examined arises because the numerical grid of the DNS is capable of supporting only a finite number of waves, where the total bandwidth is bounded by the total domain size

$$k_{min} = \frac{2\pi}{L_x}, \frac{2\pi}{L_y} \quad (\text{D.9})$$

and the grid resolution (Nyquist limit)

$$k_{max} = \frac{\pi}{\Delta x}, \frac{\pi}{\Delta y}. \quad (\text{D.10})$$

In general, the set of discrete wavenumbers supported by the numerical grid does not match the specific wavenumbers at which the experimentally-measured energy spectra are reported. Thus, a strategy is required to apply the experimentally-measured energy values to the discrete wavenumbers supported in the DNS.

Two means of implementing the initial energy spectra have been investigated. The most straight-forward method is to interpolate the energy from the experimental spectrum at each wavenumber supported by the numerical grid. This method, in the limit of sufficient numerical resolution, will give matching energy values for the

experimental and DNS spectra,

$$\int_{k_{min}}^{k_{max}} E_{exp}(k) dk = \int_{k_{min}}^{k_{max}} E_{DNS}(k) dk. \quad (\text{D.11})$$

However, a problem exists when using the interpolation method to implement initial conditions when detailed long wavelength information must be included, which is the case here. While a numerical grid might have a large enough domain to support the desired longer wavelengths, due to the discrete nature of the waves supported, the simulation spectrum may not fully resolve the shape of the experimental spectrum at these longer wavelengths. Energy values in the longer wavelengths, as a result of the interpolation procedure, were very sensitive to the exact domain size. To reduce this sensitivity of the DNS results on the choice of domain size, an alternate strategy of implementing the experimental spectra was investigated. The initial spectra were formulated based upon a local integration over individual wavepackets of the experimental spectrum, such that

$$E_{DNS}(k) = \frac{1}{\Delta k} \int_{k-\frac{\Delta k}{2}}^{k+\frac{\Delta k}{2}} E_{exp}(k) dk, \quad (\text{D.12})$$

where $\Delta k = 2\pi/L_x$. While the numerical grid resolution of the longer wavelengths remains the same, variations in the experimental spectral energy content can be captured more robustly. While the interpolation method may use a dramatically different value of long wavelength energy depending upon the exact size of the domain (see bandwidth definition again), the method of local wavepacket integration should yield more consistent results for minor changes in the domain size.

To examine the sensitivity of the DNS to the implementation of the longer wavelength perturbations, two separate DNS with resolution $1152 \times 720 \times 1280$ were per-

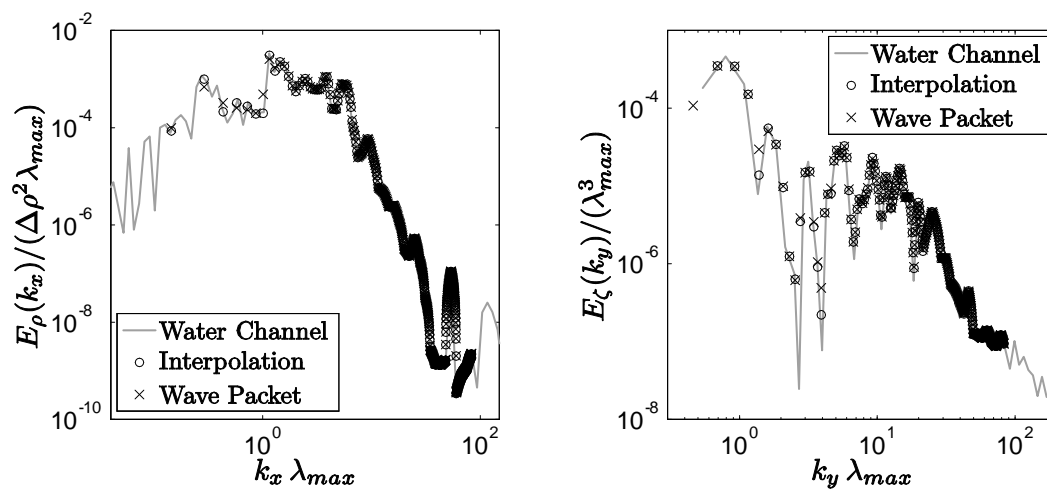


Figure D.2 Initial interfacial perturbation spectra in the x - and y -directions.

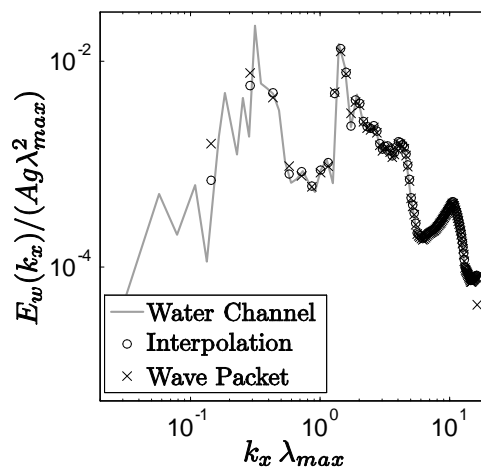


Figure D.3 Initial vertical velocity perturbation spectra at the centerplane of the mixing layer in the x -direction.

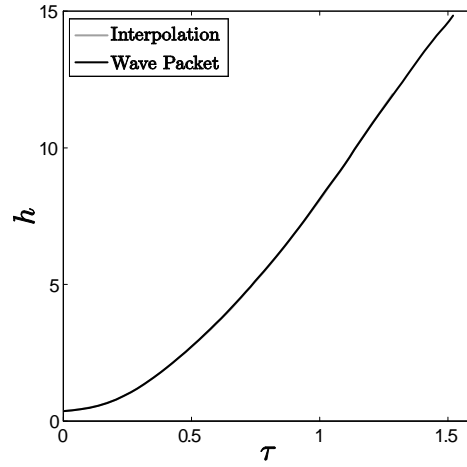


Figure D.4 Comparison of the mixing layer growth rates for different initialization methods.

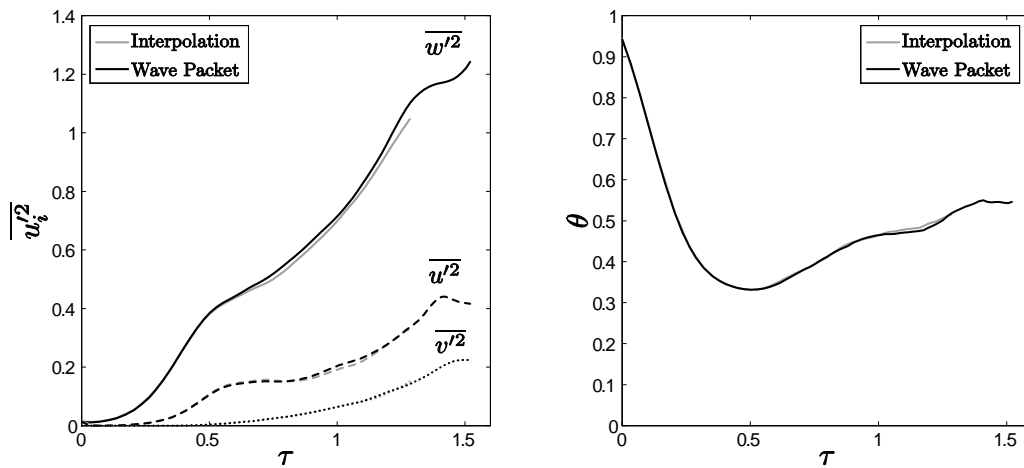


Figure D.5 Comparison of centerplane velocity variances and molecular mixing parameter θ for different initialization methods.

formed using the spectra shown in figures D.2 and D.3. The growth of the mixing layer for each DNS is shown in figure D.4, where the difference in the growth rates are negligible. In addition to a comparison of growth rates, the evolution of the center-plane velocity variances and θ are shown in figure D.5 for both DNS. While differences in $\overline{w'^2}$ and θ are perceptible, such a small difference remains negligible with respect to the analysis of presented in § 3–4.

APPENDIX E

TABLES OF SELECTED DATA

τ	Re_h (approximate)	$\theta(z = 0)$
0.016	22.5	0.951
0.061	31.8	0.856
0.166	55.9	0.609
0.204	68.4	0.482
0.255	89.2	0.499
0.334	124	0.427
0.342	119	0.364
0.400	158	0.480
0.473	197	0.478
0.552	270	0.438
0.694	377	0.566
0.865	649	0.583
0.924	665	0.605
1.363	1673	0.604

Table E.1 Molecular mixing parameters from $Pr = 7$ experiments.

τ	Re_h	$\theta(z = 0)$
0.1	33.1	0.096
0.2	64.6	0.114
0.3	113	0.128
0.4	180	0.144
0.5	265	0.162
0.6	367	0.176
0.7	487	0.194
0.8	621	0.213
0.9	769	0.234
1.0	930	0.252
1.1	1104	0.276
1.2	1290	0.300
1.3	1491	0.333
1.4	1708	0.367
1.5	1946	0.388
1.6	2210	0.428
1.7	2504	0.440
1.8	2480	0.470

Table E.2 Molecular mixing parameters from $Sc \sim 10^3$ experiments.

τ	Re_h	σ_m	σ_k	σ_ϵ	σ_{m2}	σ_χ
0	6.6	0.309	4.000	> 10	0.081	0.081
0.0339	7.4	0.164	0.140	0.116	0.046	0.058
0.0685	8.5	0.135	0.084	0.094	0.039	0.055
0.1031	10.2	0.164	0.068	0.100	0.041	0.060
0.2058	20.8	0.130	0.065	0.149	0.056	0.078
0.2878	38.9	0.107	0.081	0.222	0.065	0.110
0.4051	83.0	0.089	0.107	0.296	0.064	0.219
0.5034	137	0.084	0.106	0.238	0.061	0.231
0.5955	203	0.078	0.096	0.170	0.055	0.166
0.6928	289	0.071	0.077	0.124	0.054	0.131
0.7988	404	0.063	0.077	0.102	0.054	0.107
0.9005	537	0.063	0.072	0.098	0.055	0.090
1.0078	708	0.066	0.069	0.095	0.058	0.102
1.0978	863	0.069	0.075	0.094	0.064	0.097
1.1946	1055	0.073	0.083	0.094	0.074	0.098
1.3042	1273	0.078	0.098	0.102	0.089	0.161
1.4079	1492	0.094	0.110	0.113	0.104	0.198
1.5206	1712	0.090	0.107	0.149	0.166	0.181

Table E.3 Turbulent Schmidt numbers calculated from DNS.

τ	Re_h	$C_{\epsilon 0}$	$C_{\epsilon 2}$	C_{m2}	$C_{\chi 0}$	$C_{\chi 2}$	$C_{\chi 3}$
0	6.6	> 10	1.063	0.010	0.565	0.005	29.79
0.0339	7.4	0.381	1.170	0.102	1.280	0.045	7.485
0.0685	8.5	0.617	1.819	0.168	1.545	0.150	4.670
0.1031	10.2	0.761	2.205	0.184	1.680	0.325	3.990
0.2058	20.8	0.986	2.422	0.147	1.785	0.920	5.985
0.2878	38.9	1.094	2.437	0.141	1.890	1.670	8.090
0.4051	83.0	1.255	2.544	0.178	2.185	3.465	12.38
0.5034	137	1.459	2.664	0.242	2.510	4.925	13.98
0.5955	203	1.649	2.739	0.310	2.980	5.770	14.16
0.6928	289	1.698	2.796	0.376	3.440	6.220	14.72
0.7988	404	1.614	2.773	0.403	3.505	6.610	16.74
0.9005	537	1.523	2.770	0.407	3.260	7.280	18.58
1.0078	708	1.447	2.656	0.416	2.970	8.435	20.47
1.0978	863	1.425	2.647	0.429	2.810	9.380	21.86
1.1946	1055	1.422	2.585	0.449	2.670	10.49	22.88
1.3042	1273	1.435	2.435	0.482	2.590	11.62	23.16
1.4079	1492	1.437	2.320	0.512	2.140	12.43	23.33
1.5206	1712	1.425	2.262	0.539	2.130	13.08	23.84

Table E.4 Scale-similarity parameters calculated from DNS.

APPENDIX F

NOMENCLATURE

A	Atwood number
$a(t; C_\phi)$	Model amplitude coefficient for model parameter C_ϕ
B_0	Dimensionless measure of density variance
B_2	Dimensionless density variance for immiscible two-fluid case
b_{ij}	Reynolds stress anisotropy tensor
C	Normalized concentration of colored indicator, $[\text{In}_{IV}]/[\text{In}]_2$
$C_\phi(k)$	Normalized cumulative energy spectra of scalar ϕ
$C_{\epsilon 0}, C_{\epsilon 2}$	Scale-similarity parameters for $\overline{\epsilon'}$ transport equation
$C_{m 2}$	Scale-similarity parameter for $\widetilde{m_1''^2}$ transport equation
C_{pu}, C_{pu}^ϵ	Scale-similarity parameters for pressure transport closures
$C_{\chi 0}, C_{\chi 2}, C_{\chi 3}$	Scale-similarity parameters for $\widetilde{\chi''}$ transport equation
C_μ	Turbulent viscosity parameter
D	Mass diffusivity
D^ϕ	Turbulent destruction of scalar ϕ
DNS	Direct numerical simulation
$\overline{E'}$	Reynolds-averaged turbulent kinetic energy
$\widetilde{E''}$	Favre-averaged turbulent kinetic energy
$E(z, t)$	Exact (DNS) profile of unclosed quantity
$E_\phi(k)$	Variance spectrum for scalar ϕ
F_d^ϕ	Flux of ϕ due to molecular diffusion
F_t^ϕ	Flux of ϕ due to turbulent diffusion

F_p^ϕ	Flux of ϕ due to pressure fluctuations
f_r	Volume fraction of fluid $r = 1, 2$
$\overline{f_1^2}$	Variance of volume fraction fluctuations
$f_2^{50\%}$	f_2 value at which 50% of indicator exists in colored form for specified pH_1/pH_2 combination
\bar{f}_1^m	Mean mixed fluid composition
g	Gravity
H	Height of the water channel, 32 cm
h_b	Width of mixing layer on bubble side of mixing layer
h_s	Width of mixing layer on spike side of mixing layer
I	Intensity of light measured
I_0	Intensity of background lighting
In	Short-hand notation for phenolphthalein indicator
In_{IV}	Colored form of chemical indicator
$[\text{In}]_2$	Free-stream concentration of phenolphthalein
K_1, K_2, K_3	Equilibrium constants for indicator dissociation
K_{f_1}	Kurtosis of volume fraction fluctuations
K_w	Equilibrium constant for dissociation of water
K_ϕ	Kurtosis of scalar ϕ
k	Wavenumber $k = 2\pi/\lambda$ (implicitly defined as 1D wavevector for experiments)
k_*	Wavenumber of most unstable wavelength
L_x, L_y, L_z	Domain size
M	Molar concentration, moles per liter
$M(z, t)$	Profile of modeled quantity

m_r	Mass fraction of fluid $r = 1, 2$
$\widetilde{m_1''^2}$	Mass fraction variance
N_ϕ	Number of turbulent structures in DNS of scalar ϕ
P/D	Production-to-dissipation ratio
PDF	Probability density function
PE	Potential energy
P_b^ϕ	Production of ϕ by buoyancy forces
P_s^ϕ	Production of ϕ by shearing forces
P_t^ϕ	Production of ϕ by turbulent forces
P_c^ϕ	Production of ϕ by mean field curvature effects
P_m^ϕ	Production of ϕ by mean field gradient effects
$P(f_1)$	Probability density function of volume fraction fluctuations
pH	Local concentration of hydrogen ions
pH ₁	pH of top (heavy) fluid stream
pH ₂	pH of bottom (light) fluid stream
P/h	Integral product thickness for Rayleigh–Taylor mixing layer
P/δ	Integral product thickness for shear-driven mixing layer
Pr	Prandtl number, ν/Γ
Re_h	Integral-scale Reynolds number for Rayleigh–Taylor mixing layer
Re_δ	Integral-scale Reynolds number for shear-driven mixing layer
Re_λ	Taylor–Reynolds number
$R_{\widetilde{w''m_1''}}$	Turbulent mass flux correlation coefficient
r	Velocity ratio for shear-driven mixing layer
$r(t; C_\phi)$	Model correlation coefficient for model parameter C_ϕ
Sc	Schmidt number, ν/D

S_{ij}	Strain rate tensor
S_ϕ	Skewness of scalar ϕ
T	Temperature
T^ϕ	Turbulent transport of ϕ
t	Time
U_m	Mean advection velocity
w_ϕ	Absolute uncertainty in quantity ϕ
x	Downstream distance
z	Vertical height
α	Dimensionless growth parameter
α_{InIV}	Fraction of dissociation for colored form of indicator
α_{InIV}^{max}	Maximum value of α_{InIV} realized at pH = 11.3
Γ	Thermal diffusivity
ΔT	Temperature difference
$\Delta \rho$	Density difference, $\rho_1 - \rho_2$
$\Delta x, \Delta y, \Delta z$	Grid spacing
δ	Vorticity width of shear-driven mixing layer
δ_{vis}	Visual width of shear-driven mixing layer
ε	Molar absorptivity coefficient (In § 2)
ε	Half-width of the initially-diffuse interfacial thickness separating the heavier and lighter fluid (in Appendix D)
$\overline{\varepsilon'}, \widetilde{\varepsilon''}$	Reynolds- and Favre-averaged dissipation rate of $\widetilde{E''}$
ζ	Initial interfacial perturbation
η	Self-similarity variable
η_B	Batchelor scale

η_K	Kolmogorov scale
Θ	Global molecular mixing parameter
θ	Molecular mixing parameter
λ	Wavelength
λ_{max}	Most unstable wavelength
$\lambda_{\phi,x}, \lambda_{\phi,y}$	Dominant wavelength in x - and y -directions of scalar ϕ
μ	Dynamic viscosity
ν	Kinematic viscosity
ν_t	Turbulent viscosity
$\Pi^{\widetilde{E}''}$	Pressure dilatation of \widetilde{E}''
ρ	Density
ρ_1	Density of heavier fluid
ρ_2	Density of lighter fluid
$\overline{\rho'^2}$	Density variance
$\hat{\rho}(k, t)$	Fourier transform of density fluctuations
σ	Light absorption
σ_{ij}	Viscous stress tensor
σ_ϕ	Turbulent Schmidt number for scalar ϕ
τ	Dimensionless time
τ_{IC}	Dimensionless initial conditions time for model
φ	Chemical reaction equivalence ratio
φ_{In}	Reaction equivalence ratio for indicator reaction
φ_n	Reaction equivalence ratio for neutralization reaction
Ξ	Global molecular mixing parameter based on chemical product formation

$\widetilde{\chi''}$

Mass fraction variance dissipation rate

[•]

Square brackets denote molar concentration, moles per liter

APPENDIX G

EXPERIMENTAL FIGURE DATA FILES

Figure	Associated Figure Data File
2.3	Figure2.3_PlotData.dat
2.4 (top)	Figure2.4a_PlotData1.dat, Figure2.4a_PlotData2.dat, Figure2.4a_PlotData3.dat, Figure2.4a_PlotData4.dat
2.4 (bottom)	Figure2.4b_PlotData1.dat, Figure2.4b_PlotData2.dat, Figure2.4b_PlotData3.dat
2.5	Figure2.5_PlotData.dat
2.7 (top-left)	Figure2.7a_PlotData.dat
2.7 (top-right)	Figure2.7b_PlotData.dat
2.7 (bottom-left)	Figure2.7c_PlotData.dat
2.7 (bottom-right)	Figure2.7d_PlotData.dat
2.8 (top-left)	Figure2.8a_PlotData.dat
2.8 (top-right)	Figure2.8b_PlotData.dat
2.8 (bottom-left)	Figure2.8c_PlotData.dat
2.8 (bottom-right)	Figure2.8d_PlotData.dat
2.9	Figure2.9_PlotData.dat
2.10	Figure2.10_PlotData.dat

Table G.1 Figure data files.

Figure	Associated Figure Data File
2.11	Figure2.11_PlotData1.dat, Figure2.11_PlotData2.dat Figure2.11_PlotData3.dat
2.13	Figure2.13_PlotData.dat
2.14 (left)	Figure2.14a_PlotData1.dat, Figure2.14a_PlotData2.dat
2.14 (right)	Figure2.14b_PlotData.dat
2.16 (left)	Figure2.16a_PlotData.dat
2.16 (right)	Figure2.16b_PlotData.dat
2.17	Figure2.17_PlotData.dat
2.18	Figure2.18_PlotData1.dat, Figure2.18_PlotData2.dat Figure2.18_PlotData3.dat
2.19	Figure2.19_PlotData1.dat, Figure2.19_PlotData2.dat Figure2.19_PlotData3.dat, Figure2.19_PlotData4.dat Figure2.19_PlotData5.dat
2.21	Figure2.21_PlotData.dat
2.22 (left)	Figure2.22a_PlotData.dat
2.22 (right)	Figure2.22b_PlotData.dat
2.23	Figure2.23_PlotData1.dat, Figure2.23_PlotData2.dat Figure2.23_PlotData3.dat, Figure2.23_PlotData4.dat Figure2.23_PlotData5.dat, Figure2.23_PlotData6.dat Figure2.23_PlotData7.dat

Table G.2 Figure data files.

Figure	Associated Figure Data File
2.24	Figure2.24_PlotData1.dat, Figure2.24_PlotData2.dat Figure2.24_PlotData3.dat, Figure2.24_PlotData4.dat Figure2.24_PlotData5.dat, Figure2.24_PlotData6.dat Figure2.24_PlotData7.dat
2.25 (left)	Figure2.25a_PlotData1.dat, Figure2.25a_PlotData2.dat Figure2.25a_PlotData3.dat, Figure2.25a_PlotData4.dat Figure2.25a_PlotData5.dat, Figure2.25a_PlotData6.dat Figure2.25a_PlotData7.dat
2.25 (right)	Figure2.25b_PlotData1.dat, Figure2.25b_PlotData2.dat Figure2.25b_PlotData3.dat, Figure2.25b_PlotData4.dat Figure2.25b_PlotData5.dat, Figure2.25b_PlotData6.dat Figure2.25b_PlotData7.dat
2.26	Figure2.26_PlotData1.dat, Figure2.26_PlotData2.dat Figure2.26_PlotData3.dat
2.27	Figure2.27_PlotData.dat
2.28	Figure2.28_PlotData1.dat, Figure2.28_PlotData2.dat Figure2.28_PlotData3.dat
2.29 (left)	Figure2.29a_PlotData.dat
2.29 (right)	Figure2.29b_PlotData.dat

Table G.3 Figure data files.

VITA

Name: Nicholas J. Mueschke

Permanent Address: Dept. of Mechanical Engineering
c/o: Prof. Malcolm J. Andrews
M.S. 3123
College Station, TX 77843-3123

Education: B.S. (Mechanical Engineering), May 2002
University of Louisiana at Lafayette, Lafayette, LA

M.S. (Mechanical Engineering), December 2004
Texas A&M University, College Station, TX

Ph.D. (Mechanical Engineering), May 2008
Texas A&M University, College Station, TX